# Design of Nanostructured Materials for Advanced Lithium Ion Batteries

A thesis submitted in fulfilment of the requirements

for the award of the degree

**Doctor of Philosophy**

from

**University of Technology, Sydney**


by

**Ying Wang (B.Eng., M.Eng.)**

Principal supervisor: Guoxiu Wang
Co-supervisor: Alison Ung
Centre for Clean Energy Technology
Faculty of Science
2012

# DECLARATION

I, Ying Wang, declare that the work presented in this thesis is original unless otherwise referenced or acknowledged and has not been submitted for qualifications at any other academic institution. This thesis is in fulfilment of the requirements for the award of Doctor of Philosophy in the Centre for Clean Energy Technology, Faculty of Science, University of Technology, Sydney.

Ying Wang

Sydney, Australia

December, 2012

# DEDICATION

This dissertation is dedicated to my parents and my husband. Thank you for all of your love and support.

*(Translation from English to Chinese)*

## 致谢

本论文献给我的父亲，母亲和我的丈夫。感谢你们给予我的爱与支持。这份爱我将铭记于心。

# ACKNOWLEDGEMENTS

This dissertation is based on the results of my PhD project during the past four years, which were conducted in the Institute for Superconducting and Electronic Materials (ISEM) at the University of Wollongong (UOW) and the Centre for Clean Energy Technology, School of Chemistry and Forensic Science, Faculty of Science, University of Technology, Sydney (UTS). I would like to acknowledge all the staff and students in both organizations for sharing such an enjoyable and unforgettable period with me.

I would like express my deepest gratitude to my principle supervisor, Prof. Guoxiu Wang and co-supervisor, Assoc. Prof. Alison Ung, for their invaluable advice and supervision throughout this research work. Their innovative research ideas and inspiration enlightened and encouraged me during my PhD study.

I appreciate the technical and administrative support and assistance I received from Dr Ronald Shimmon, Dr Linda Xiao, Dr Jane Yao, Mrs Rochelle Seneviratne, Mrs Era Koirala, and staff in MAU. They have provided me with tremendous help.

I also would like to thank my colleagues Dr Hao Liu, Dr Bing Sun, Mr Bei Wang, Mrs Huimin Wu, Mr Dawei Su, Mr Kefei Li, Mr Shuangqiang Chen, Mr Anjon K. Mondal, Mr Jinqiang Zhang and Mr Yiying Wei for their encouragement and brilliant ideas during the period of this research.

Finally, I would like to express my sincere gratitude to my husband, Mr Zhou Tan, and my parents. Without their encouragement and support, it would have been impossible for me to complete the research. Their love is the mental strength that supported me while achieving my study abroad and it will hold a special place in my heart forever.

# TABLE OF CONTENTS

# LIST OF TABLES

# LIST OF FIGURES

# ABSTRACT

Among currently available rechargeable battery systems, Lithium-ion (Li-ion) batteries feature high energy density and operating voltage, and long cycle life. Since the 1990s, the development of Li-ion battery technology has been ongoing, owing to the ever-growing demand in portable electronics, electric vehicles (EV), hybrid electric vehicles (HEV) and stationary energy storage devices. Although the improvements in battery technology rely on achievements in electrode materials, separators, electrolytes and external management systems, electrode materials play the most important role as they control the electrochemical reaction and determine the properties of a battery system. Based on extensive literature reviews, the electrochemical performances of electrode materials are size- and morphology-dependent. In this study, several nanostructured materials with specifically designed morphologies were synthesized, characterized, and used as electrode materials for Li-ion battery applications.

First, spherical over-lithiated transition metal oxide was chosen as the high capacity cathode material. Through a modified co-precipitation method, this material exhibited relatively low irreversible capacity loss, high specific capacity, satisfactory cyclability and rate capability. These are suitable for large-scale application.

Secondly, two different carbon coating techniques were designed and applied in the synthesis of $LiFePO_4$ and $Li_2FeSiO_4$ cathode materials through *in-situ* polymerization and modified ball-milling methods respectively. Carbon-coated $LiFePO_4$ consists of primary particles (40-50 nm) and agglomerated secondary particles (100-110 nm). Each particle is evenly coated with an amorphous carbon layer, which has a thickness around 3-5 nm. Meanwhile, $Li_2FeSiO_4$/C nanoparticles

were coated with an amorphous carbon layer, owing to the carbonization of glycolic acid. Both materials exhibited much higher specific capacity, better capacity retention, and better rate capability than their pristine counterparts.

After that, a hydrothermal method was chosen and applied to synthesize hollow-structured $CoFe_2O_4$ nanospheres and $CoFe_2O_4$/mutiwalled carbon nanotubes (MWCNTs) hybrid material. The significant improvements in the electrochemical performances of these two materials, including high capacities, excellent capacity retentions and satisfactory rate capabilities could benefit from their unique nano architectures. $CoFe_2O_4$ demonstrated uniform hollow nanosphere architecture, with an outer diameter of 200-300 nm and the wall thickness of about 100 nm. Hybrid material resembled wintersweet flower “buds on branches”, in which $CoFe_2O_4$ nanoclusters, consisting of nanocrystals with a size of 5-10 nm, were anchored along carbon nanotubes. Both materials could be a promising high capacity anode material for lithium ion batteries.

# CHAPTER 1 Introduction

## 1.1 General Background

With increasing awareness of the need for low carbon emissions and the shortage of traditional fossil fuels, there is an ever-growing demand for renewable energy sources, including wind/solar energy, tidal power, nuclear energy, fuel cells and rechargeable batteries. The most widely used renewable energy sources are wind and solar energy, which can be converted into electricity for transmission to users or storage. However, they vary their availability as energy sources, which means alternative energy sources are in high demand.

Rechargeable batteries are among the most successful technologies that can be repeatedly used to provide an efficient storage of electrical energy [1]. As displayed in Figure 1.1, the history of the rechargeable battery began in the 1959, with Lead-acid and Ni-Cd being the most common secondary batteries [2]. In the 1970s, Ni-H batteries emerged as an alternative in the rechargeable battery market. Motivated by the demand for greener, more efficient and more durable batteries, extensive investigations on the lithium battery began in the 1960s and initially concentrated on nonaqueous primary batteries using lithium as the anode. However, their usage was limited because of safety concerns of lithium dendrites. Since the first commercial lithium-ion (Li-ion) batteries were developed in 1991 by the SONY Corporation, they have gradually become an alternative power source for traditional lead-acid and Ni-Cd batteries. Over the past two decades, with the development of battery technology, Li-ion batteries are currently the prevailing portable power source and are targeting wide-ranging applications in hybrid electric vehicle and stationary

energy storage, as it provides twice the energy density than nickel-cadmium or nickel-metal hydride batteries, in terms of both weight and volume.

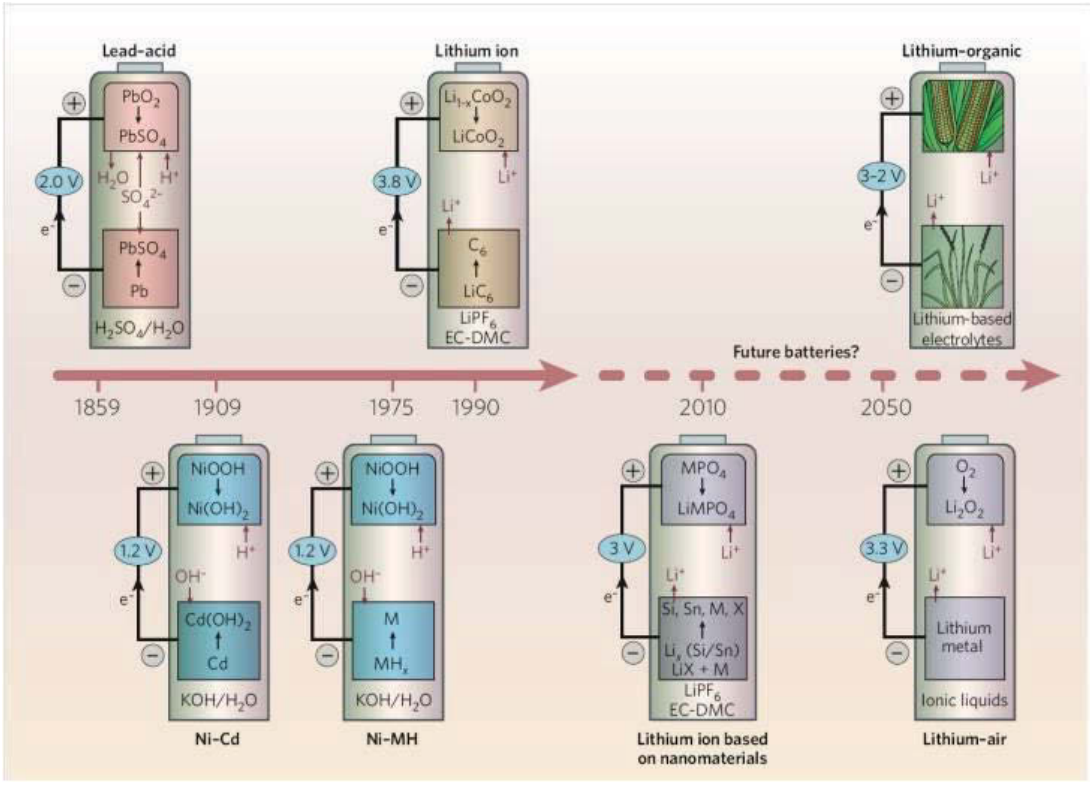


Figure 1.1 Battery histories over the years, showing the main electrode materials used [3]

There are several reasons why Li-ion batteries should meet considerable success in the market [4]. First, with the awareness of global warming, there is large demand for renewable energy sources to replace traditional fossil fuels. Second, the Li-ion battery offers high energy density (250 Wh $g^{-1}$, 2-3 times higher than Ni-MH, Ni-Cd, and Pb-acid batteries), long cycle life (more than 10000 cycles), high voltage output and no "memory effect", enabling them to meet the fast-growing requirements for newly emerged electronics and electrical vehicles. Furthermore, the chemistries involved in Li-ion batteries are versatile, which could offer more choice of electrode materials, ranging from layered oxides to polyanion compound, as well as some

suitable candidates from the organic field. This has provided many opportunities when searching for advanced electrode materials for Li-ion batteries.

## 1.2 Present Status and Remaining Challenges

The past twenty years have witnessed the continuous progress of Li-ion batteries, from first-generation test cells to mature mass production, which is dominating the current rechargeable battery market in portable electronic devices, such as computers, cell phones, power tools and camcorders. The new generation wireless and portable communication technologies require batteries of lighter weight, higher energy/power density and longer cycle life and in particular, the application of Li-ion batteries that will extend into the auto industry, with the goal to popularize fully battery-powered electric vehicles. Undoubtedly, the replacement of fossil fuels with renewable rechargeable batteries would solve some of the current serious problems, such as high carbon emission and scarcity of fossil fuels. However, at this stage, Li-ion batteries are no more practical and price competitive than fossil fuels for large-scale applications [5].

The ideal batteries for electric vehicles (PHEV, HEV and EV) and back electricity storage units will have attributes such as long life, low cost, environmental compatibility, high energy density, safety, compact size and light weight [1, 6]. Currently, none of these batteries fulfil all these critical requirements, and most of them operate below their theoretical value. The large-scale application of Li-ion batteries is still of prime concern.

## 1.3 Importance of Study

The popularity of Li-ion batteries for large-scale energy applications, such as low-emission electric vehicles, renewable power plants and stationary electric grids, requires safer batteries with high-rate charge-discharge capability and long cycle life. Under these circumstances, high demand for advanced energy storage devices with high energy and power densities has boosted extensive research in the development of novel electrode materials for Li-ion batteries. From the electrochemistry perspective, electrode materials are of great importance in the improvement of Li-ion battery technology, as the performance of a specific battery unit essentially relies on the thermodynamics and kinetics of the electrochemical reactions involved in a battery system. Today, nanomaterials with tunable morphology have drawn extensive attention because of their fascinating mechanical, electrical and optical properties compared with bulk counterparts. The development of Li-ion batteries could benefit from the application of nanomaterials. The aim of this study is to synthesize nanostructured electrode materials with enhanced battery performances through morphology control and process optimization. Also, the mechanism and principles involved the electrochemical redox reactions will be fully analysed, which will shed light on further on-going research. Improvements for electrode materials mainly focus on:

1) larger capacity and higher energy and power density;
2) higher reactivity, reversibility, structural stability during the de-lithiation/lithiation process;
3) faster ionic diffusion and electronic transfer at higher *C*-rates;
4) low cost, higher safety; and
5) facile synthesis of material and environmental benignity.

## 1.4 Outline of Study

This PhD study focuses on synthesizing the nanostructured electrode materials with diverse morphologies for rechargeable Li-ion battery application. The physical properties, crystal structures and electrochemical properties of the as-synthesized samples were systematically investigated, and the results and key findings are structured as follows:

1) Chapter 2 reviews the recent development in Li-ion batteries. Various cathode and anode materials were systematically summarized, especially the improvements in novel synthetic routes and electrochemical performances. The concise and useful investigations will shed light on my further research.
2) Chapter 3 lists the overall experimental methods, characterizations and electrochemical evaluations for various cathode and anode materials involved.
3) Synthesis of cathode materials via a precipitation method are presented in chapter 4 (over-lithiated transition metal oxide) and chapter 5 (lithium ion phosphate $LiFePO_4$) respectively.
4) Chapter 6 demonstrates the preparation of carbon-coated nanosized $Li_2FeSiO_4$ through solid-state reaction, and the effect of carbon-coating on the electrochemical performances of $Li_2FeSiO_4$ was evaluated through fully assembled Li-ion batteries.
5) Chapter 7 is divided into two parts, concentrating on the design of nanostructured $CoFe_2O_4$ nanospheres and the winter-sweet-flower-like $CoFe_2O_4$/MWCNTs nanocomposites respectively. A hydrothermal method was chosen to tailor the morphology of as-prepared samples. In addition, their

electrochemical performances were fully investigated when used as the anode materials in Li-ion batteries.

6) Finally, Chapter 8 summarizes the main achievements of this study, and outlook possible improvements. At the end of the thesis is a list of references, a list of nomenclature, and a list of materials and chemicals, followed by a list of publications during the period of the study.

# CHAPTER 2 Literature Review

## 2.1 Rechargeable Batteries

A battery is a device that converts the chemical energy contained in its active materials directly into electric energy by means of an electrochemical oxidation-reduction reaction [2]. The type of reaction involved is the transfer of electrons from one material to another through an electric circuit. In the case of a rechargeable system, the redox reaction inside the battery is reversible.

Rechargeable batteries are characterized by high power density, high rate capability, flat discharge voltage plateau, and good environmental endurance. They attract much attention worldwide as they have various applications, such as the following:

1) Energy-storage device: a rechargeable battery can be connected to, and charged by, a prime energy source, such as a un-interruptible power supply (UPS), wind/solar-power source, hybrid electric vehicle and stationary energy storage system.
2) Portable consumer electronics: for example, power tools, computers, cell phones, electric vehicles.

The history of rechargeable batteries began more than a century ago. Lead-acid batteries, invented in 1859 by a French physicist, are the oldest rechargeable battery, with corroded lead foils to form active material. Until the 1980s, the sealed valve-regulated batteries dominated the battery market for their applications in power tools, electronic back-up, and small cells for consumer and road usage because they were low cost, maintenance-free, and had moderate energy density [2]. Following on, the

rechargeable nickel-cadmium and nickel-hydrogen emerged as alternatives for lead-acid batteries. Soon after, lithium metal, as the most powerful reducing agent, became attractive as a battery anode material, owing to its superior conductivity, light weight, high voltage and high energy-density batteries. In the early 1970s, the first lithium batteries were used in selected military applications. However, their applications were restricted because of safety concerns [7]. Until 1983, Yoshino proposed an operational model of rechargeable battery, later named lithium ion battery, which contained $LiCoO_2$ as cathode and polyacetylene as anode, and was sealed in a test tube [8]. This cell functioned with the same cell principles as the Li-ion batteries in the market. Yoshino also developed an electrode fabrication method, using Al foil and Cu foil as current collectors for cathode and anode respectively. After immense pioneering work, SONY successfully commercialized the lithium-ion battery in 1991. Since then, they have revolutionized battery technology.

Today, there are several types of rechargeable batteries utilized successfully in all areas of life. Table 2.1 summarizes the key characteristics and applications of standard rechargeable battery systems.

Table 2.1 Major characteristics and applications of standard rechargeable battery systems (reproduced from [2, 3])

| Systems | Applications | Advantages | Disadvantages |
|---|---|---|---|
| Lead-acid | | | |
| Automotive | Automotive staring, lighting and ignition (SLI)<br>Golf carts<br>Lawn mowers<br>Tractors<br>Aircraft<br>Marine | Popular<br>Low cost<br>High rate and low-temperature performance<br>Maintenance-free designs | Poor energy density (30-40 Wh $kg^{-1}$)<br>Relatively low cycle life (50-500 cycles)<br>Limited high temperature cyclability<br>Difficult to manufacture in very small size<br>Toxic lead |
| Stationary | Emergency power<br>UPS | Long life<br>Stability | |

| | | | |
|---|---|---|---|
| | Energy storage<br>Load levelling | | |
| Portable | Portable tools<br>Small appliances | Maintenance-free<br>Low cost<br>Price competitive<br>Moderate cycle life | |
| Nickel-cadmium | | | |
| Portable | Consumer electronics<br>Memory backup | Maintenance-free<br>Sealed<br>Long cycle life<br>High-rate low-temperature performance<br>Long shelf life in any state of charge<br>Rapid recharge capability | Voltage depression or memory effect in certain applications<br>Higher cost than lead-acid batteries<br>Poor charge retention<br>Toxic Cd |
| Large-scale | Industrial and aerospace<br>Railroad equipment<br>Standby powers | Low maintenance<br>Reliable: no sudden death<br>Good charge retention<br>Excellent cycle life and long-term storage | Low energy density<br>Higher cost than lead-acid batteries<br>Toxic Cd |
| Nickel-metal hydride | | | |
| Portable | Consumer electronics<br>Other portable applications | Higher capacity then Ni-Cd batteries<br>Sealed<br>Maintenance free<br>Cd free, minimal environmental problems | Low voltage<br>Poor charge retention<br>Moderate memory effect<br>Limited recyclable |
| Nickel-hydrogen | | | |
| Aerospace | Primarily for aerospace applications | High specific energy (60 Wh $kg^{-1}$)<br>Long cycle life under shallow discharge<br>Long life | High initial cost<br>Self-discharge proportional to $H_2$ pressure<br>Low volumetric energy density |
| Zinc-$MnO_2$ | | | |
| Portable | Cylindrical cell applications<br>Rechargeable replacement for Zn-Carbon and alkaline primary batteries | Low cost<br>Good capacity retention<br>Sealed<br>Maintenance-free<br>No memory effect | Limited cycle life and rate capability<br>Higher internal resistance than Ni-Cd and Ni-MH batteries |
| Li-ion | | | |
| Portable | Portable electronic equipment<br>Power tools | High voltage<br>High specific energy/power density<br>Long cycle and shelf life<br>Rapid charge capability<br>High coulombic and energy | Moderate initial cost at this stage<br>Need for protective circuitry<br>Cobalt is not green, but can be replaced by |

| | | | |
|---|---|---|---|
| | | efficiency<br>No memory effect<br>Durable and compact | abundant and sustainable materials<br>Recycling feasible but at an extra energy cost |
| Large-scale | Electric and hybrid electric vehicles<br>Stationary power grid<br>Aerospace applications | High specific energy/power density<br>High rate capability<br>Long life<br>Maintenance-free | |
| Li-air (future) | | | |
| Large-scale | Large-scale<br>Stationary energy sources | Quite high energy density<br>Low cost if technology improves | Poor energy efficiency<br>Easy recycling |

## 2.2 An Introduction of Li-ion Batteries

Li-ion batteries comprise cells that employ lithium intercalation compounds as the positive and negative materials. When the cell is charged and discharged, $Li^+$ exchange between the positive and negative electrodes, forming the so-called rocking-chair batteries.

Lithium metal is the chosen anode material, based on Li being the most electronegative (-3.04 V *vs*. standard hydrogen electrode, SHE) as well as the lightest metal (equivalent weight M = 6.94 g $mol^{-1}$), and may deliver a theoretical capacity up to 3860 mAh $g^{-1}$ [9]. This provides lots of opportunity to tune the size of the battery down and enhance its energy density and power density.

The advantageous features of the Li-ion battery include the following:

1) High voltage: Li-ion batteries have voltages up to 4 V, depending on the active materials used
2) High specific energy and power density: the energy output of a lithium battery is 2 to 4 or more times better than that of conventional zinc anode batteries
3) Wide operation temperature range: most of the lithium batteries will perform over a temperature range from about 70 to -40 °C

4) High coulombic and energy efficiency
5) High rate and rapid charge capability
6) Long cycle life
7) Superior shelf life: Li-ion batteries can be stored for long periods, even at elevated temperatures, with no memory effect

Disadvantages for Li-ion batteries:

1) Degrade at high temperature
2) Capacity loss or thermal runaway when overcharged
3) Venting and possible thermal runaway when crushed
4) Moderate initial cost and extra cost for recycling

### 2.2.1 Basic concepts for Li-ion batteries

The following terms are frequently used in this study for evaluating the properties of Li-ion batteries.

#### 2.2.1.1 Cathode and anode

In chemistry, the cathode and anode of an electrochemical cell is where the reduction and oxidation occurs respectively. The cathode can be negative, as when the cell is electrolytic, or positive, as when the cell is galvanic. Since our studies were on the galvanic cell, the cathode was connected to the positive pole to allow the circuit to be completed. The anode was the negative electrode from which electrons flowed out towards the external part of the circuit.

#### 2.2.1.2 Charge-discharge

When the cell is connected to an external load, electrons flow from the anode through the external load to the cathode. The electric circuit is completed in the

electrolyte by the flow of anions and cations to the anode and cathode respectively. This process is called discharge, which is the exact reverse to the charge process [2]. During the recharge of a rechargeable battery, the current flow is reversed and oxidation occurs at the cathode and reduction at the anode.

### 2.2.1.3 Potential

The theoretical potential of the cell depends on the type of active materials selected in the cell. It can be calculated from free-energy data or the standard electrode potentials. Figure 2.1 summarizes the voltages and capacity for various electrode materials. The open circuit voltage is the voltage of a no-loaded cell and is usually close to the theoretical voltage. For a commercial battery, it is often evaluated by its nominal voltage, which is generally accepted as typical of the operating voltage of the battery.

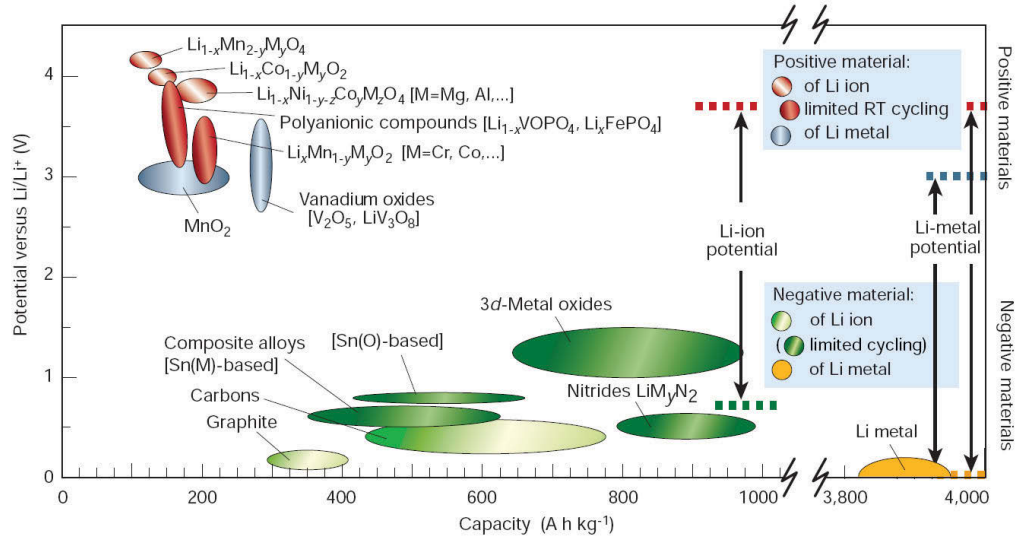


Figure 2.1 Voltages versus capacity for cathode and anode materials for the next generation of rechargeable Li-based cells [9]

### 2.2.1.4 Theoretical capacity

The theoretical capacity of materials is the total quantity of electricity involved in a specified electrochemical reaction, which is dependent on the electron transfer and molecular weight of active material. The specific capacity ($Q_s$ (Ah $g^{-1}$)) of electrode materials is theoretically determined by the electrode reactions according to the Faraday equation, and can be calculated from the equation below:

$$Q_s = 26.8 \times \frac{n}{M} \quad \text{(Eq. 2.1)}$$

Where $M$ is the molecular weight of the active material (g $mol^{-1}$)

$n$ is the number of electrons transferred during the redox reaction

2.2.1.5 Coulombic efficiency

The coulombic efficiency ($\eta$) of a battery is the ratio of the charge capacity ($Q_c$) during charging compared with the discharge capacity ($Q_d$) during discharging. It indicates the reversibility of a particular battery and can be defined by equation (2.2):

$$\eta = \frac{Q_c}{Q_d} \times 100\ \% \quad \text{(Eq. 2.2)}$$

2.2.1.6 *C*-rates

In this study, *C*-rate was used to indicate the charge-discharge current of a battery, which can be expressed as:

$$I = C \times Q_s \quad \text{(Eq. 2.3)}$$

Where I is the charge or discharge current (A), $Q_s$ represents the theoretical specific capacity of the cell (Ah $g^{-1}$). For example, a battery charge-discharged at 0.1 *C* rate represents 10 hours charge and discharge of this battery to its cut-off voltage, and the charge-discharge current can be calculated from equation 2.3.

2.2.2 Principles of Li-ion batteries

The prototype of a commercial Li-ion battery contains lithium cobalt oxide as cathode and graphite as anode respectively, with $LiPF_6$ dissolved in carbonate as electrolyte. The schematic operating principles of a typical Li-ion battery are shown in Figure 2.2. When charging the battery, Li-ions move from the cathode, through electrolyte, and insert into graphite layers, forming $LiC_6$. Upon discharging, the whole process is reversed. During charging-discharging, lithium ions flow between cathode and anode, forming the so called "rocking-chair" battery, enabling the conversion of chemical energy into electrical energy, which will be utilized by load.

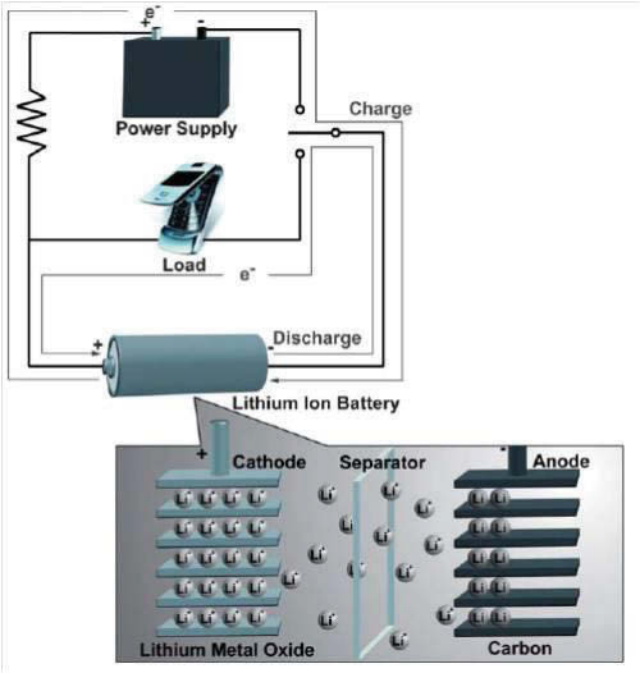


Figure 2.2 Schematic operating principles of a typical Li-ion battery [10]

The electrochemical reactions involved in the $LiCoO_2$/graphite cell are:

Anode:

$$Li_xC_6 \leftrightarrow 6C + xLi^+ + xe^- \qquad \varphi = -2.9\ V \qquad \text{(Eq. 2.4)}$$

Cathode:

$$Li_{1-x}CoO_2 + xLi^+ + xe^- \leftrightarrow LiCoO_2 \qquad \varphi = 1.2\ V \qquad \text{(Eq. 2.5)}$$

Overall:

$$Li_{1-x}CoO_2 + Li_xC_6 \leftrightarrow LiCoO_2 + 6C \qquad E^0 = 4.1\ V \qquad \text{(Eq. 2.6)}$$

### 2.2.3 Configurations of Li-ion batteries

The term battery is generally used, and the basic electrochemical unit is referred to as the 'cell'. The cell is composed of an assembly of cathode, anode, porous polyethylene separator, electrolyte, container and terminals. A battery consists of one or more of these electrochemical cells, connected in a series or parallel, or both, depending on the designed output voltage and capacity. The commercial Li-ion batteries consist of the same components inside, with different configurations (shown in Figure 2.3). The electrolyte of lithium ion batteries, usually liquid carbonate electrolyte containing lithium salt or solid electrolyte, is an ionic conductor, which provides the medium for the transfer of the charge. The separator is for physically separating the anode and cathode to prevent internal short-circuiting, and at the same time providing the desired ionic conductivity.

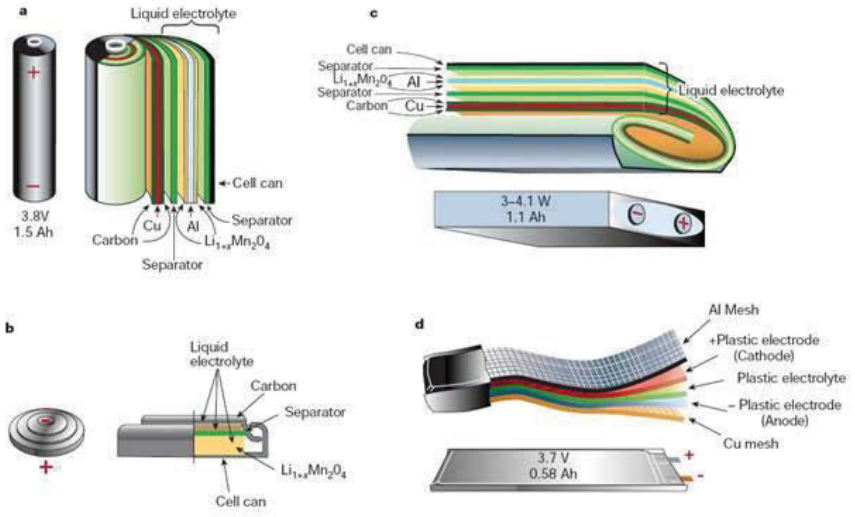


Figure 2.3 Schematic drawing of various Li-ion battery configurations (a) cylindrical (b) coin (c) prismatic and (d) thin and flat [9]

Hereafter, a detailed review on the electrode materials is presented, which will highlight the importance of electrode materials on the performance of state-of-the-art Li-ion batteries.

## 2.3 Cathode Materials for Li-ion Batteries

One of the critical properties for Li intercalation material is the potential at which Li can be extracted and inserted. Hence, knowledge of the thermodynamic potential is one critical aspect when determining whether new materials are used as cathode materials for Li-ion batteries. If the potential is too high, even though it will benefit the high energy density of the material, Li cannot be practically removed, and the electrolyte breakdown will deteriorate battery performance. By contrast, a low potential can lead to moisture sensitivity of the electrode material. In a practical system, the cathode must fulfil the following requirements

1) High free energy of reaction with lithium
2) Capable of hosting large quantities of lithium
3) Reversibly incorporates lithium without structural change
4) Have a useful working voltage
5) High lithium ion diffusivity
6) Good electronic conductivity
7) Be stable when in contact with the electrolyte
8) Low cost in terms of reagents and synthetic method

Based on these criteria, various cathode materials are proposed for Li-ion battery application. These range from conventional layered materials ($LiCoO_2$, $LiNiO_2$,

$LiMnO_2$ and $LiMO_2$ (M = Ni, Co, Mn and combination)), to the spinel materials and the recent polyanion materials. A brief review of these materials follows.

### 2.3.1 Layered transition metal oxides

The development of lithium ion batteries is through the continuous improvements in air stable Li-based intercalation compounds which can significantly improve battery technology. Early studies on $LiCoO_2$ [11] have emphasized the important applications of the layered transition metal oxide cathode materials. They provide several benefits, for example, the well-developed synthetic routes, high specific capacity, and the ability for facile processing for mass production [4].

#### 2.3.1.1 Conventional Layered Metal Oxides

$LiCoO_2$, first reported by Goodenough and co-workers in 1979 [11], offers a high theoretical capacity (274 mAh $g^{-1}$ assuming complete Li extraction) and an intercalating and deintercalating voltage around 3.9 V. $LiCoO_2$ exhibits two crystal structures (a cubic spinel-related structure and a hexagonal layered structure), depending on both the preparation method and synthesis temperatures [12]. Figure 2.4 displays a typical layered structure of $LiCoO_2$, with cubic-close-packed oxygen array providing a two-dimensional network of edge-shared $CoO_6$ octahedra for the lithium ions.

The conventional synthetic method for $LiCoO_2$ is solid-state reaction, where high calcination temperature is usually required to obtain $LiCoO_2$, owing to the insufficient mixing and the low reactivity of reagents. In this case, $LiCoO_2$ was predominantly composed of a layered structure. However, the high temperature calcination process is less energy-efficient, and normally causes the aggregation of

the nanoparticles and even the evaporation of lithium. Moreover, studies suggest that the capacity fading rate increases with increasing $LiCoO_2$ particle size [12]. Thus, other low temperature synthetic methods, such as sol-gel [13], spray-drying [14] and rotary evaporation method [15], are much more favourable in obtaining $LiCoO_2$ with ultrafine particles and controlled morphology. In particular, nanowire and mesoporous $LiCoO_2$ were prepared using a templating reaction under low temperature [16, 17]. These nanostructured $LiCoO_2$ exhibited superior capacity retention compared with normal $LiCoO_2$.

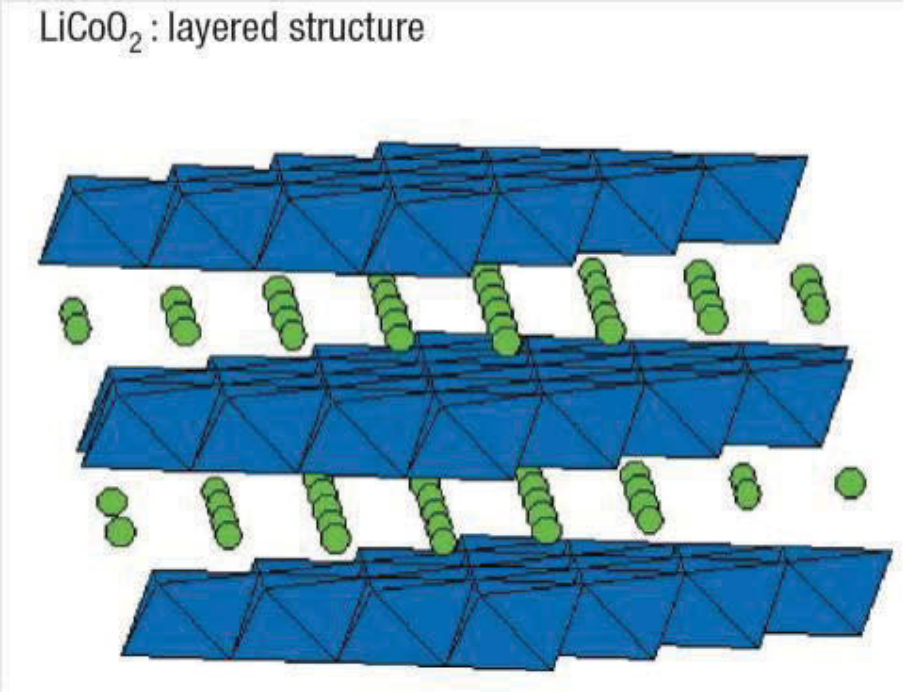


Figure 2.4 Structure of layered $LiCoO_2$ (dots: lithium ions; octahedra: $CoO_6$) [18]

Owing to extensive pioneer work on $LiCoO_2$, it was the most widely used commercial cathode material for Li-ion batteries during the 1990s. When pairing with graphite carbon anode, $LiCoO_2$/graphite batteries have dominated the Li-ion battery market for the last twenty years as they provide much improved safety over the lithium batteries, while maintaining high energy density, high capacity and high

voltage to meet consumers' demand. However, owing to the severe structural stability degradation of $LiCoO_2$ when in contact with organic electrolyte, the delithiation of $LiCoO_2$ beyond 0.5 Li is limited, which means $LiCoO_2$ can only deliver half of its theoretical capacity [19]. Even though this disadvantage could be compensated through doping with trivalent ions (such as Al, Cr) and coating with the metal oxides or phosphates (e.g. $ZrO_2$, $Al_2O_3$, $AlPO_4$ and $FePO_4$) [20-23], toxicity and high cost led us to search for alternative cathode materials.

$LiNiO_2$ is another choice of intercalated cathode material to replace $LiCoO_2$ as it has favourable specific capacity and is cheaper when compared with $LiCoO_2$. However, the preparation of $LiNiO_2$ is complicated, because the atomic radius of Li and Ni are similar, resulting in additional nickel ions on the lithium sites, and vice versa in the crystal structure of $LiNiO_2$ [24]. This structure makes the synthesis of the stoichiometric oxide, with all the lithium sites entirely filled by lithium, difficult. In addition, the structure of delithiated $LiNiO_2$ usually collapses, accompanying exothermic oxidation of the organic electrolyte [9]. These disadvantages hinder its commercial application.

Another candidate for cathode materials is $LiMnO_2$. Although $LiMnO_2$ exhibits 10 % less theoretical capacity than $LiCoO_2$, it has an advantage in terms of cost and non-toxicity. However, its implementation has been delayed because of limited cycling performance at elevated temperatures. The layered $LiMnO_2$ can be easily converted to the spinel structure during cycling [25-28].

None of the aforementioned layered cathode materials ($LiCoO_2$, $LiNiO_2$ and $LiMnO_2$) offer the satisfactory electrochemical properties required by the fast growing battery industry. Under such circumstances, layered transition metal oxides LMO (M = Ni,

Co, Mn combinations with various ratios) were proposed and investigated, such as $LiNi_{1/3}Co_{1/3}Mn_{1/3}O_2$ (NCM) [27, 29], $LiNi_{0.8}Co_{0.2}O_2$ [17, 30], and $LiNi_{0.5}Mn_{0.5}O_2$ [31-33], because the combination of transition metal provides advantages of milder thermal stability at charge state, lower cost and less toxicity than $LiCoO_2$. In particular, one paper published findings on a layered cathode material with a fascinating core-shell structure [34]. Figure 2.5 shows the $LiNi_{0.8}Co_{0.1}Mn_{0.1}O_2$ core surrounded by a concentration-gradient outer layer, with the purpose of increasing the thermal-abuse tolerance and cycle life of $LiNi_{0.8}Co_{0.1}Mn_{0.1}O_2$. The Ni-rich core features high capacity, whereas the Mn and Co-rich outer layer provides enhanced thermal stability. Under an aggressive test condition, this material exhibited a high capacity of 209 mAh $g^{-1}$ and a capacity retention of 96 % after 50 cycles.

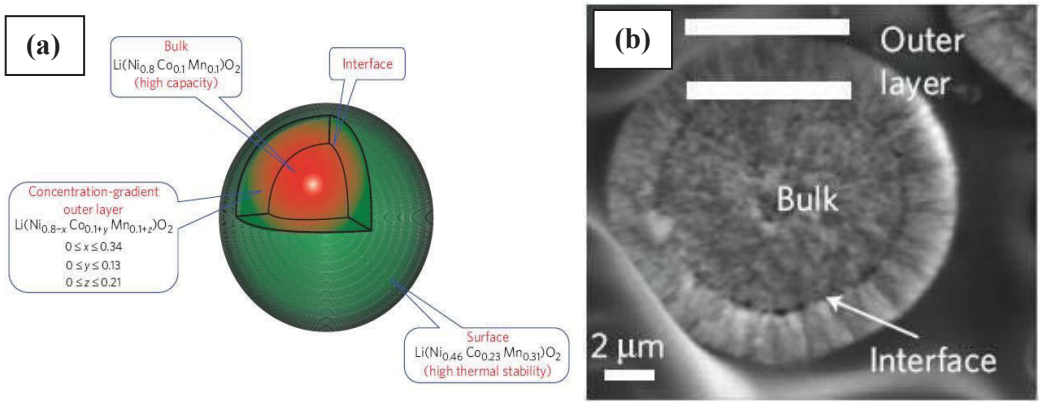


Figure 2.5 (a) Schematic diagram and (b) SEM images of cathode material with Ni-rich core surrounded by concentration-gradient outer layer (reproduced from [34])

Among those binary or ternary layered materials, $LiNi_{1/3}Co_{1/3}Mn_{1/3}O_2$ (NCM) is the most attractive alternative with a high theoretical capacity of 278 mAh $g^{-1}$ through redox couples of $Ni^{2+}/Ni^{3+}$, $Ni^{3+}/Ni^{4+}$ and $Co^{3+}/Co^{4+}$, almost zero phase change and superior thermal stability [35, 36]. Moreover, the decreased Co content in NCM

makes mass production feasible. Early reports on NCM show that although this material has superior initial capacity, a relatively high irreversible capacity and poor cyclability can be observed [37]. During the past ten years, significant improvements were achieved on NCM material, making it a promising candidate for large-scale Li-ion batteries. For example, carbon coated NCM, prepared through the pyrolysis of polyvinyl alcohol (PVA), exhibited better rate capability and higher discharge capacity compared with the pristine one [38]. Through a rheological phase reaction route, the as-synthesized NCM had a high tap density of 2.41 g $cm^{-3}$, resulting in a high volumetric energy density of this material [39]. P.G. Bruce group published that a porous NCM material synthesized through sol-gel method exhibited a quite high capacity of 195 mAh $g^{-1}$ at 1 *C* rate, superior capacity retention of 99.99 % and high volumetric density of 2244 and 2008 Wh $L^{-1}$ at 1 *C* and 10 *C* respectively [40]. In addition, a very recent publication also demonstrated the preparation of porous NCM materials, consisting of single crystal nanoparticles, through an optimized crystallization process [41]. As shown in Figure 2.6, metal acetates were dissolved in water to form solution A. This was added drop-wise into citric acid solution B. After adding nitric acid, the mixture was left to age and dry, forming a homogeneous gel. The gel was further dried and sintered to produce a porous NCM product. This material exhibited high surface area and well-defined layered structure, which gave improved electrochemical performances.

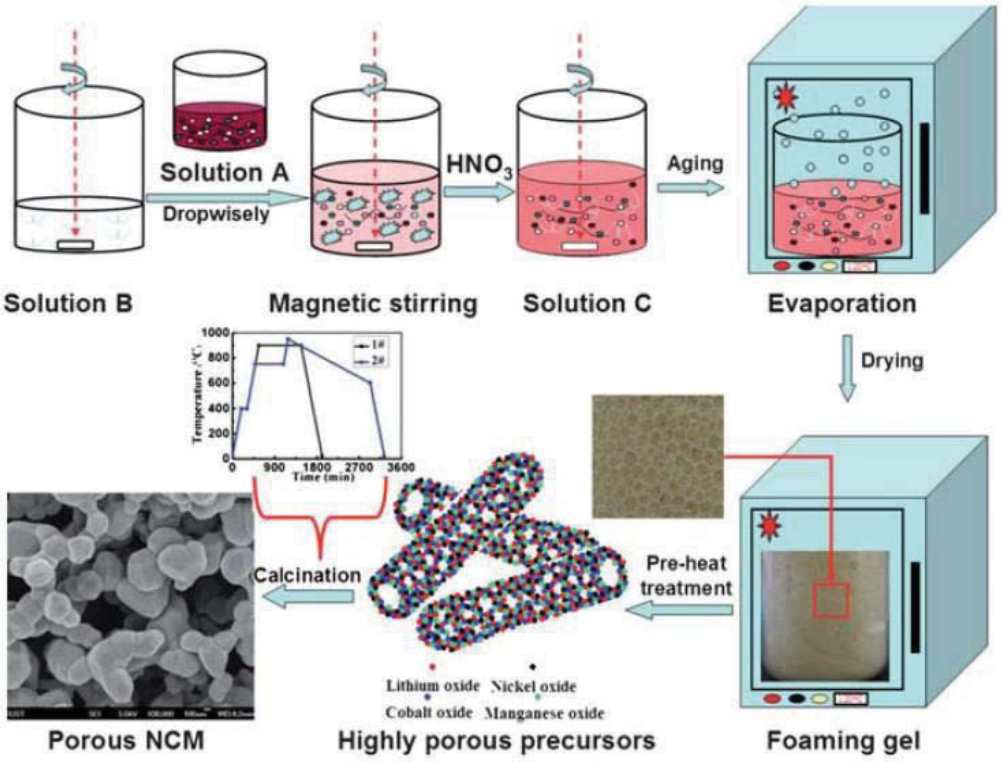


Figure 2.6 Schematic illustration of porous NCM prepared by modified sol-gel method [41]

2.3.1.2 Over-lithiated Layered Metal Oxides

Among the aforementioned cathode materials, $LiCoO_2$ can only deliver half of its theoretical capacity, owing to chemical and structural instabilities at deep charge, with $x<0.5$ in $Li_xCoO_2$ [19]. In addition, difficulties in the preparation of $LiNiO_2$ and its exothermic oxidation when in contact with organic electrolytes hinder its commercial application, while, as already discussed, the layered $LiMnO_2$ can be easily converted to the spinel structure during cycling [25-28]. Under such circumstances, lithium-rich (or over-lithiated) layered transition metal oxides emerged as promising alternatives, owing to their lower cost, higher discharge capacities and better thermal stability compared with previous conventional layered

materials [42-44]. Lithium excess compound is a series of $Li_2MnO_3$-LMO (M = Ni, Co, Mn combinations with various ratios) solid solution with different mole ratios between $Li_2MnO_3$ and LMO, and the ratios among Ni:Co:Mn in LMO may also vary in different cases. Literature shows that the excess lithium and manganese in the 'conventional' transition metal oxides ($LiNi_{1/2}Mn_{1/2}O_2$ and $LiNi_{1/3}Co_{1/3}Mn_{1/3}O_2$) can lead to the formation of $Li_2MnO_3$, which is capable of participating in the lithium intercalation and deintercalation process to deliver a discharge capacity greater than 200 mAh $g^{-1}$ [45-47].

Lithium-rich layered oxides mainly have three disadvantages: high irreversible capacity; poor cyclic performance; and rate capability [42, 48, 49]. The large irreversible capacity loss of 40-100 mAh $g^{-1}$ in the first charge-discharge cycle is due to the oxygen evolution during the first charging process, while the poor cycling performance and low rate capability can be ascribed to the low electronic conductivity induced by the insulating $Li_2MnO_3$ component [50, 51]. Some appealing approaches were proposed to overcome the problems. In particular, surface modification with conductive or protective agents proved to be an effective way to enhance the electrochemical performances of over-lithiated layered compounds. Table 2.2 summarizes recent publications on various coating agents and corresponding coating techniques of layered materials. The reasons that the surface-modified material exhibits better electrochemical performance are because the coated layer can suppress the SEI layer thickness, enhance the surface conductivity, and lower irreversible capacity by retaining more oxide ion vacancies in the lattice [52-54]. In some cases, a double layer coating was also applied on over-lithiated layered material (i.e. $AlPO_4$+$Al_2O_3$ [55], $Al_2O_3$+$RuO_2$ [56]).

Table 2.2 Summary of recent publications on surface-modified over-lithiated layered transition metal oxides

| Materials | Coating layer | Coating techniques | Functions | Refs |
|---|---|---|---|---|
| Surface coating with conductive agents | | | | |
| $Li[Li_{0.2}Mn_{0.54}Ni_{0.13}Co_{0.13}]O_2$ | Carbon | Thermal evaporation | Higher specific capacity, rate capability and capacity retention | [57] |
| | Al | | Higher rate capability<br>Lower $C_{irr}$ loss | [58] |
| | $RuO_2$ | Co-precipitate $RuCl_3$ with $NH_4OH$ followed by calcination | Higher specific capacity and rate capability<br>Lower charge transfer resistance | [56] |
| Surface coating with inert oxides | | | | |
| $Li[Li_{0.2}Mn_{0.54}Ni_{0.13}Co_{0.13}]O_2$ | $AlPO_4$<br>$CoPO_4$ | Co-precipitate corresponding metal nitrates /acetates /chlorides with $NH_4OH$ /$(NH_4)_2HPO_4$, followed by calcination | Higher rate capability and specific capacity<br>Lower $C_{irr}$ loss | [55, 59] |
| $(1-z)Li[Li_{1/3}Mn_{2/3}]O_2$-$(z)Li[Mn_{0.5-y}Ni_{0.5-y}Co_{2y}]O_2$ | $Al_2O_3$ | | Higher specific capacity and capacity retention<br>Lower $C_{irr}$ loss | [52, 60] |
| | $CeO_2$/$ZrO_2$/ ZnO | | Lower $C_{irr}$ loss | |
| $Li[Li_{0.2}Mn_{0.54}Ni_{0.13}Co_{0.13}]O_2$ | $AlF_3$ | Co-precipitate $AlNO_3$ with $NH_4F$ followed by calcination | Higher rate capability and capacity retention<br>Lower $C_{irr}$ loss<br>Suppress electrolyte decomposition | [61] |
| $Li[Li_{0.2}Mn_{0.6}Ni_{0.2}]O_2$ | $Al(OH)_3$ | Hydrolysis of $Al(C_3H_7O)_3$ | Lower area specific impedance<br>Higher capacity retention and thermal stability | [53] |
| $Li[Li_{0.2}Mn_{0.54}Ni_{0.13}Co_{0.13}]O_2$ | $TiO_2$ | | Higher thermal stability and capacity retention<br>Lower $C_{irr}$ loss | [62] |
| Doping strategies | | | | |
| $Li[Li_{0.17}Mn_{0.58}Ni_{0.25}]O_2$ | $Al^{3+}$ | Co-precipitation | Higher specific capacity<br>Lower $C_{irr}$ loss | [54] |
| | $F^-$ | Calcination pristine sample with $NH_4HF_2$ | Slightly higher capacity retention<br>Lower specific capacity | |
| $Li[Li_{0.2}Mn_{0.54}Ni_{0.13}Co_{0.13}]O_2$ | $Ti^{4+}$ | Solution-based method | Lower specific capacity<br>Suppress oxygen loss | [63] |

$C_{irr}$ :Initial irreversible capacity

Furthermore, Manthiram and co-workers also proposed a novel technique of blending $Li[Li_{0.2}Mn_{0.54}Ni_{0.13}Co_{0.13}]O_2$ cathode with other lithium insertion hosts, such as $V_2O_5$, $Li_4Mn_5O_{12}$, or $LiV_3O_8$ [64, 65]. It showed that the lithium insertion hosts can efficiently decrease the irreversible capacity loss of layered material by accommodating the extracted Li-ions which could not be reinserted back into the layered lattice.

In conclusion, the fully developed synthetic procedures for layered materials have fulfilled the mass production of Li-ion batteries for the application in small-scale portable electronics for the last two decades. However, their unavoidable shortcomings, including high cost, toxicity, scarcity, oxygen evolution and electrolyte decomposition at high charging potential, have limited their application in EVs/HEVs [3].

### 2.3.2 Spinel $LiMn_2O_4$ materials

Spinel materials have a three-dimensional framework or tunnelled structure based on λ-$MnO_2$ as illustrated in Figure 2.7. The cubic-close-packed oxygen array provides a three-dimensional array of edge-shared $MnO_6$ octahedra for the lithium ions.

Initially, $LiMn_2O_4$ is also of commercial interest, particularly for applications that are cost-effective, durable and robust. This material offers favourable safety and intrinsic rate capability, which arise from the chemically stable $Mn^{3+}/Mn^{4+}$ couple and a 3D framework for facile $Li^+$ mobility [66]. However, the commercialization of $LiMn_2O_4$ has ceased, owing to the gradual capacity loss resulting from the recognized John-Teller distortion of $Mn^{3+}$ and Mn dissolution in the electrolyte. John-Teller distortion happens when the cubic spinel crystal transforms into tetragonal with a $c/a \approx 1.16$,

and the volume of the unit cell increases by 6.5 %, which results in a low capacity and significant capacity fading at moderate temperature [67].

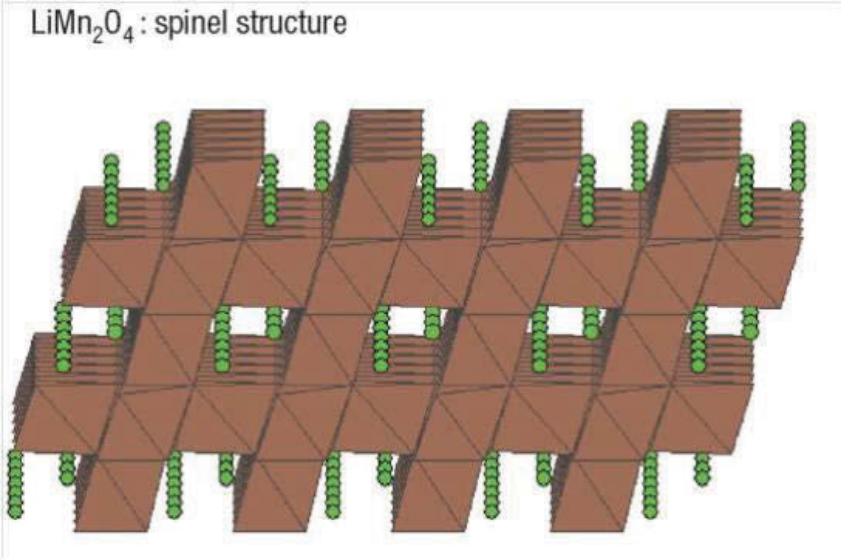


Figure 2.7 Structure of spinel $LiMn_2O_4$ (dots: lithium ions; octahedra: $MnO_6$) [18]

The development in novel nanomaterial synthesis allows us to improve the properties of $LiMn_2O_4$ by shifting from bulk to nanostructured electrode materials. Although nano-structured materials are not likely to suppress the structural change, they can accommodate better strains during this structure transformation than bulk counterparts. Particularly, one-dimensional (1D) $LiMn_2O_4$ nanowires showed enhanced power density, owing to its shorter $Li^+$ diffusion path [68]. Cho *et al.* also reported the rate capability and cycling performance of $LiMn_2O_4$ can be improved by coating with a $ZrO_2$ layer [69]

Doping with other elements in manganese site is an effective way to improve the cycling performance of $LiMn_2O_4$. In particular, Ni doped spinel compound showed the highest capacity and the most stable cyclability at higher potential. N. Kumagai demonstrated the easy substitution of Mn with Ni to form $LiNi_{0.5}Mn_{1.5}O_4$ through an emulsion drying method [70]. After optimizing the calcination condition at 750 °C

for 24 h, this material showed good cyclability. A modified Pechini method was employed to obtain nanostructured $Li_xMn_{1.5}Ni_{0.5}O_4$ (x = 0.95, 1.0, 1.05), which was sintered at different temperatures and resulted in two spinels with different symmetry groups [ordered $P4_332$(P) or disordered $Fd3m$(F)] [71]. The disordered spinel was shown to have two orders of magnitude higher electronic conductivity than the ordered sample. Thus, the disordered spinel exhibited higher rate capability than the ordered sample. Moreover, Hernan demonstrated the preparation of $LiNi_{0.5}Mn_{1.5}O_4$ with controlled crystallinity through polymer-assisted synthesis [72]. The nanorod-like $LiNi_{0.5}Mn_{1.5}O_4$, with nanocrystals in the size of 20 nm, was obtained using polyethylene glycol 400 (PEG400) as a sacrificial template. After calcination, high crystalline nanoparticles adopted a well-defined polyhedral morphology. The polymerization controlled the particle shape and maintained connectivity between nanocrystals during the synthesis. This material delivered an excellent coulombic efficiency and fast charge ability, which might have application in high-voltage lithium batteries.

### 2.3.3 Polyanion-based materials

Polyanion compounds are a class of materials in which tetrahedral polyanion structure units $(XO_4)^{n-}$ with strong covalent bonding combine with $MO_x$ (M denotes transition metal) polyhedral [4], resulting in a higher thermal stability than conventional layered transition metal oxides. Therefore, polyanion-based materials, such as phospho-olivines and lithium metal orthosilicates, are now the most promising cathode candidates for use in next-generation Li-ion batteries for large-scale applications, owing to their enhanced stability and safety, natural abundance

and no toxicity, compared with traditional transition metal oxides [73, 74]. To date, extensive studies have concentrated on lithium iron phosphate ($LiFePO_4$) and lithium iron/manganese silicate ($Li_2MSiO_4$ (M = Fe, Mn or combinations)), and they are addressed in the following review.

#### 2.3.3.1 Lithium Iron Phosphate

Since J.B. Goodenough's group did their breakthrough work on phospho-olivine polyanionic compound in 1997 [75], $LiFePO_4$ has emerged as the most promising cathode material for large-scale applications [76, 77]. As shown in Figure 2.8, olivine $LiFePO_4$ can be described as a slightly distorted hexagonal closed-packed (*hcp*) oxygen array resulting in an orthorhombic structure, in which the $FeO_6$ octahedra share common corners. The phosphorus atoms occupy tetrahedral sites; the iron and lithium atoms occupy octahedral 4*a* and 4*c* sites respectively [78].

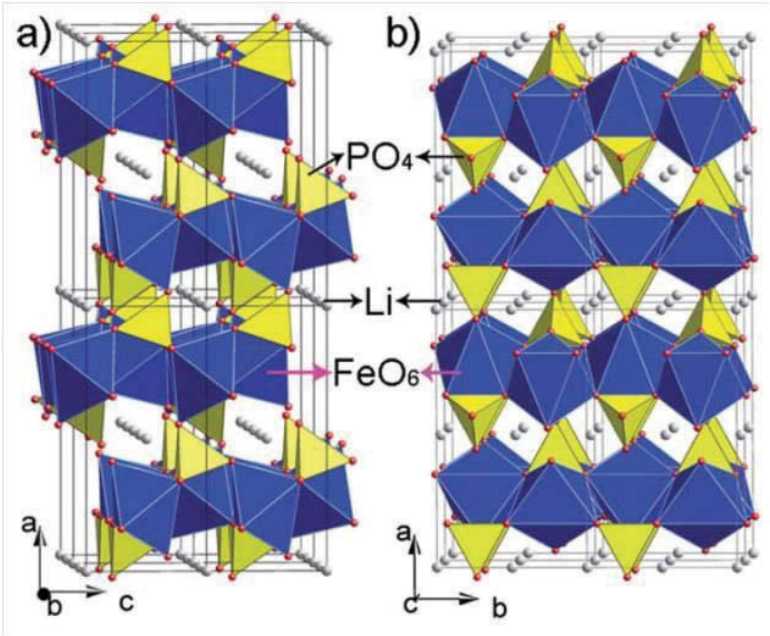


Figure 2.8 Crystal structure of olivine $LiFePO_4$viewed along the (a) *b*- and (b) *c*-axis respectively. tetrahedral, $PO_4$; octahedral, $FeO_6$ [4]

The electrochemical reaction of $LiFePO_4$ can be expressed as $LiFePO_4 \leftrightarrow FePO_4 + Li^+ + e^-$. During the charge-discharge processes, strong P-O covalent bonds in $(PO_4)^{3-}$ polyanion stabilize the oxygen. Thus, the delithiated phase $FePO_4$ essentially has the same structure as $LiFePO_4$ but the $FePO_4$ host framework deforms slightly to orthorhombic symmetry as displayed in Figure 2.9. Therefore, during the charge and discharge of the cell, $LiFePO_4$ electrodes are actually composed of two separate phases of $LiFePO_4$ and $FePO_4$.

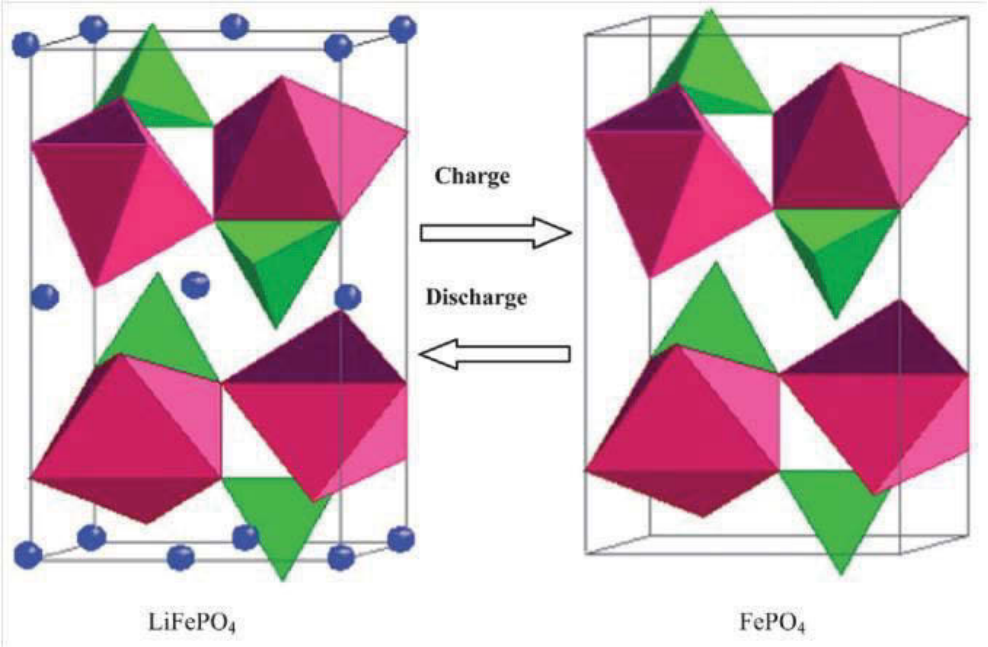


Figure 2.9 The olivine structure evolution during lithium insertion and extraction. dots, Li; tetrahedral, $PO_4$; octahedral, $FeO_6$ [79]

The prominent advantages of this compound include the abundance of iron phosphate, a relatively high theoretical capacity (170 mAh $g^{-1}$), good lithium storage reversibility, thermal stability at deeply charged state and high safety [80]. $LiFePO_4$ also features an extremely flat charge/discharge profile characterized by typical two-phase ($LiFePO_4/FePO_4$) reactions with lithium insertion voltage at 3.5 V, which lies

within the window of the carbonate electrolyte, resulting in an excellent electrochemical stability of $LiFePO_4$ with no apparent capacity fade [75, 81]. The disadvantages of this material include low electronic conductivity (~$10^{-9}$ S $cm^{-1}$) and lithium diffusivity (~$1.8\times10^{-14}$ $cm^2$ $s^{-1}$) [82, 83], resulting in a relatively poor rate performance. Over the last ten years, extensive studies showed that the electrochemical performances of $LiFePO_4$ could be dramatically improved through the following techniques.

The first approach is surface coating, particularly carbon coating, which can significantly increase the intrinsically poor electronic conductivity to around $10^{-1}$ S $cm^{-1}$ from around $10^{-8}$ S $cm^{-1}$ at room temperature, while serving as a barrier against detrimental surface reactions between active material and electrolyte [84, 85]. Previous publications showed that there were various methods to introduce a conductive carbon layer on the surface of $LiFePO_4$. Porous microspheres of $LiFePO_4$/C were synthesized through sol-gel and subsequent spray drying method [86]. The carbothermal reduction method was also adopted in the preparation of $LiFePO_4$/C composite from inexpensive raw materials [87]. A soft chemistry approach to coat $LiFePO_4$ with a conducting polymer Poly(3,4-ethylenedioxythiophene) (PEDOT) demonstrated it to be a facile, green and environmentally friendly method to prepare high-rate $LiFePO_4$ cathode materials [88]. $LiFePO_4$ nanoplates with a 5 nm thick amorphous carbon layer were synthesized by the solvothermal method and exhibited high rate lithium storage performances [89].

Furthermore, in terms of the carbon sources, polymers (e.g. polyaniline [90, 91], polypyrrole [92, 93], PEDOT [94], polyethylene [95], polyacene [96], polystyrene

[97], polyvinyl alcohol (PVA) [98]) and inexpensive organic materials [99, 100] offer lots of opportunities to achieve the mass production of high-performance $LiFePO_4$. In chapter 4, we demonstrate an example of carbon-coated $LiFePO_4$ through in-situ polymerization. The detailed review about various polymers as carbon precursor is presented. In this study, nanosized $LiFePO_4$/C is shown to have a high rate capability and excellent cyclability.

The second method to improve the rate capability of $LiFePO_4$ is by downsizing the particle size to nanoscale [101], because nanosized materials can provide a shorter distance for ionic and electronic transport and enhance lithium transport kinetics compared with bulk material. Carbon-free $LiFePO_4$ can still deliver satisfactory performance, with a discharge capacity of 147 mAh $g^{-1}$ at 5 *C* rate, by controlling its particle size between 100-200 nm [102]. Some efforts were made on reducing carbon content while maintaining the good rate capability of $LiFePO_4$/C [85, 103], as the presence of carbon usually lowers the specific capacity of $LiFePO_4$ and decreases its tap density, resulting in a relatively low energy density.

Another way is through substituting Fe with covalent ions, including Cr [104], F [105], V [106], Ti [107, 108], Cu [109], and Al [110] etc. These apart, one representative is Mn substituted $LiMn_{1-x}Fe_xO_4$ ($0 < x < 1$). Compared with $LiFePO_4$, $LiMnPO_4$, $LiCoPO_4$ and $LiNiPO_4$ have higher plateau voltages, because of the higher redox potentials of $Mn^{3+}/Mn^{2+}$ (≈ 4.1 V), $Co^{3+}/Co^{2+}$ (≈ 4.7 V) and $Ni^{3+}/Ni^{2+}$ (≈ 5.1 V) [111]. However, those materials demonstrated extremely low capacity retention and sluggish kinetics, which prohibited their practical applications [112]. In particular, $LiMnPO_4$ suffers from poor electronic conductivity (< $10^{-10}$ S $cm^{-1}$) and cycle life because of Mn dissolution. Partially substituting Mn with Fe to form mixed-metal

olivine compounds could balance the properties offered by the pure olivine compound. Examples are $LiMn_{0.8}Fe_{0.2}PO_4$ [113], $LiMn_{1-x}Fe_xPO_4$/graphene composites [114] and double-structured $LiMn_{0.85}Fe_{0.15}PO_4$ [115]. Those materials showed a much improved rate capability than those of $LiFePO_4$ or $LiMnPO_4$. In particular, double-structured $LiMn_{0.85}Fe_{0.15}PO_4$ was prepared by combining the bulk material $LiMn_{0.85}Fe_{0.15}PO_4$ with a $LiFePO_4$ outer layer to ensure the high energy density, as well as improve its overall rate capability. In comparison with bulk material, the double-structured $LiMn_{0.85}Fe_{0.15}PO_4$ showed a much improved rate capability at 0 °C and room temperature, high thermal stability and high tap density. The specific capacity approached the theoretical limit. These results indicate that the double-structured $LiMn_{0.85}Fe_{0.15}PO_4$ is suitable for large-scale battery applications. Aurbach [113] explained that the presence of Mn and Fe ions in the olivine material could increase the size of the solid-solution zone of $Li(MnFe)PO_4/(MnFe)PO_4$ compared with $LiMnPO_4$, and also improve the kinetic of $Li(MnFe)PO_4$. Alternatively, the electronic conductivity of this material could be enhanced though substituting Fe ions for some Mn ions.

Along this vein, $LiFePO_4$ nanocomposites also demonstrated a new insight into synthesizing electrode materials with improved electrochemical performances. For instance, porous $LiFePO_4/RuO_2$ nanocomposites were proposed for improved electrode performance. $RuO_2$ act as the interconnect between the carbon layer and $LiFePO_4$ (corresponding TEM images is shown in Figure 2.10). $RuO_2$ can maintain the contact between carbon and $LiFePO_4$ through surface-surface interactions [116], especially when the cell works at high current rates.

Approximately 0.9 wt% doping of NiP in the NiP/$LiFePO_4$ nanocomposites were prepared using a spraying technique. This approach increased the conductivity of bulk $LiFePO_4$ by nearly four orders of magnitude with improved reversible capacity and lithium insertion/extraction kinetics [117]. $LiFe_{0.9}Mn_{0.1}PO_4/Fe_2P$ composite [118], synthesized by mechanical alloying, showed higher electronic conductivity with the formation of conductive $Fe_2P$ and increased $Li^+$ mobility by substitution of $Mn^{2+}$ for $Fe^{2+}$, resulting in better electrochemical performance, compared with $LiFePO_4$.

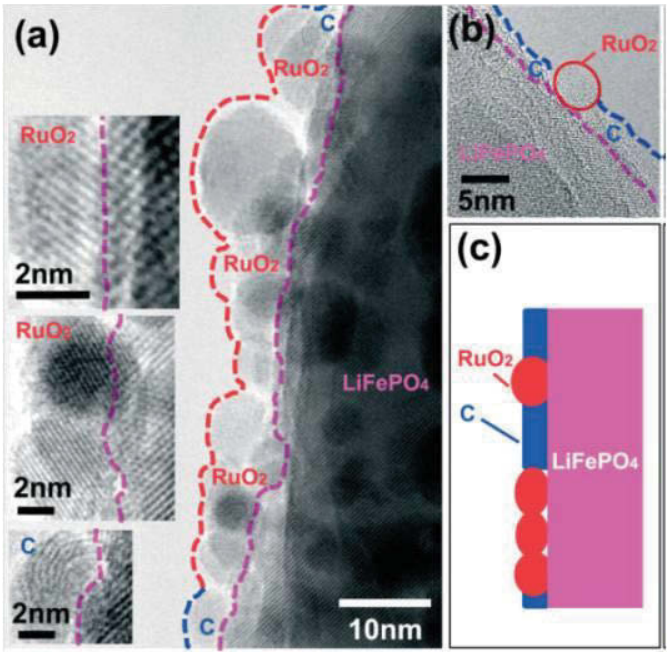


Figure 2.10 (a) and (b) Typical HRTEM images of C-$LiFePO_4$/$RuO_2$ nanocomposites; (c) scheme showing the repair of the electronically conducting network of carbon on porous $LiFePO_4$ by nanometer-sized $RuO_2$ [116]

The advances in materials preparation, particularly in nanostructured materials, have opened a new era for electrode materials preparation. In summary, the synthetic routes of $LiFePO_4$ are many. They range from a conventional solid-state reaction

[119, 120], to the hydrothermal [121-123], so-gel [124], microwave [94] and spray pyrolysis method [125]. There are also some novel techniques reported, such as ionothermal synthesis [126] and template method [127, 128]. The low-temperature ionothermal synthesis benefits from less energy demand, compared with conventional ceramic routes. One example is tailor-made $LiFePO_4$ with controlled size and morphology at low temperatures, prepared using ionic liquids as both solvent and template [126]. This material showed excellent electrochemical performances versus lithium. Fluorophosphates were also prepared via ionothermal synthesis and demonstrated effectiveness of this method in the preparation of nanometric $LiFePO_4F$ [105]. Hierarchically porous $LiFePO_4$ were prepared via a solution-based templating technique, using poly(methyl methacrylate) (PMMA) as the template [127]. Figure 2.11 summarizes the recent synthesis approaches in the preparation of $LiFePO_4$ by taking into account energy and material thrift.

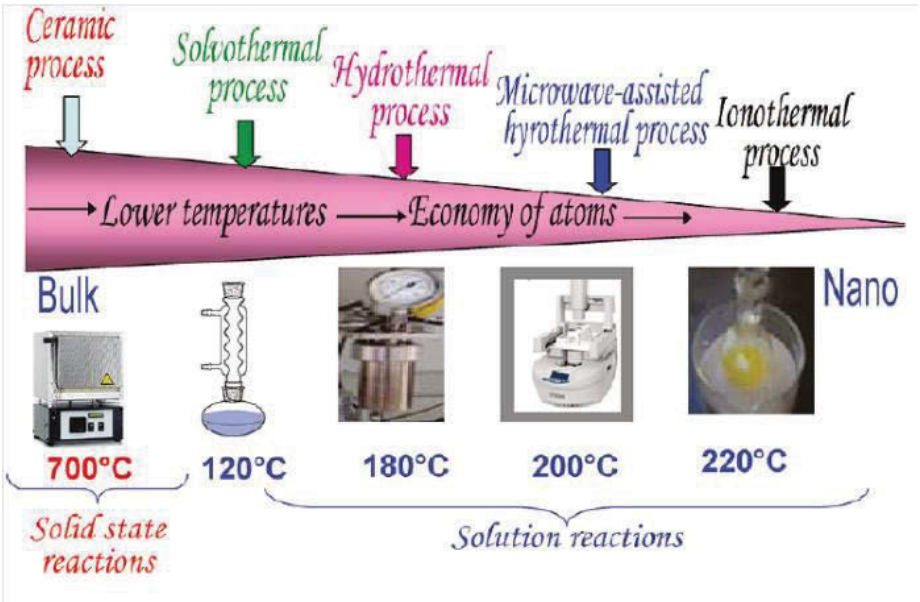


Figure 2.11 Summary of the current synthetic approaches towards the preparation of $LiFePO_4$ [129]

#### 2.3.3.2 Lithium Iron/Manganese Silicate

Theoretically, the orthosilicate family could afford more than one electron reversible exchange per transition metal I, as the group would allow the 3*d* metal to change its valence between +2 and +4, resulting in two lithium insertion/extraction per formula unit [4]. Early theoretical research showed the Li intercalation potential of orthosilicate ($Li_2MsiO_4$, M = Fe, Mn, Co, Ni) compounds approaching 5 V [130]. Apart from the high theoretical capacity and high voltage potential, orthosilicates also have remarkable privileges in their natural abundance and non-toxicity. Thus, they emerge as another class of polyanion-type cathode materials and attract considerable interests.

$Li_2FeSiO_4$ has a theoretical capacity of 166 mAh $g^{-1}$ through the $Fe^{3+}/Fe^{2+}$ redox couple, as the $Fe^{4+}/Fe^{3+}$ is hard to access. Through *in-situ* X-ray adsorption spectroscopy (XAS) study, the changes in the local environment of Fe were monitored, revealing the electrochemical reversibility of $Li_2FeSiO_4$, which can be expressed as $Li_2FeSiO_4 \leftrightarrow LiFeSiO_4 + Li^+ + e^-$ [131]. Early research evaluated the possibility of the application of $Li_2FeSiO_4$ in Li-ion batteries. Nyten et al. first reported the application of $Li_2FeSiO_4$ as a new cathode material for Li-ion batteries, which can deliver a reversible capacity of 130 mAh $g^{-1}$ at 60 °C at *C*/16 [132]. When $Li_2FeSiO_4$ was used as the cathode material for Li-ion batteries, it was suggested that an obvious voltage drop (usually in the range of 0.18-3.0 V after the initial cycle, shown in Figure 2.12) was associated with the structure arrangement from $Li_2FeSiO_4$ to $LiFeSiO_4$, in which some of the Li-ions (in the 4*b* site) and Fe ions (in the 2*a* site) became interchanged [132, 133].

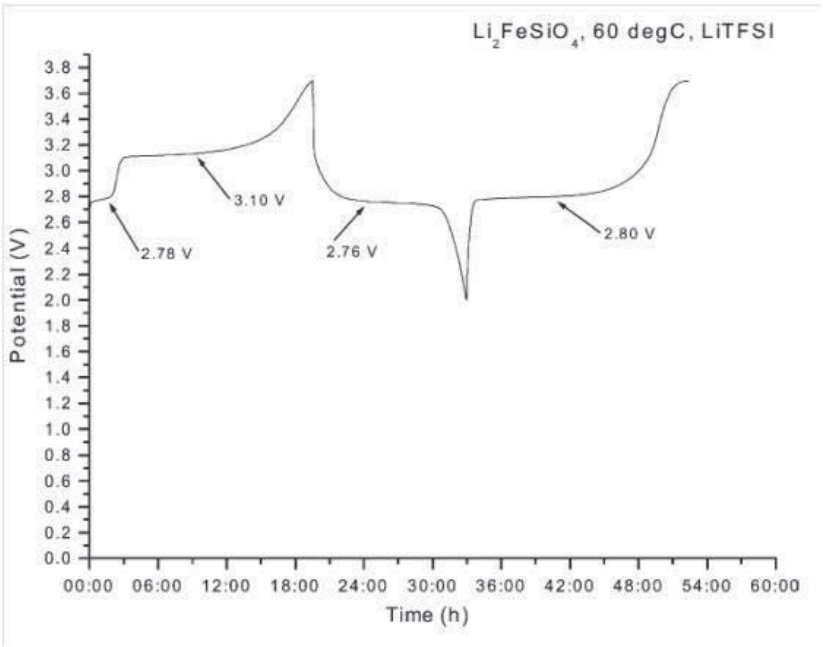


Figure 2.12 A voltage profile of pristine $Li_2FeSiO_4$ cycled at 60 °C at *C*/16 using 1M LiTFSI in EC:DEC 2:1 electrolyte [132]

In regards of structure, orthosilicates belong to the large family of tetrahedral structure materials which usually exhibit complex polymorphism [134]. The tetrahedral structures can be divided into two families, designated $\beta$ and $\gamma$ (related to the $\beta$ and $\gamma$ polymorphs of $Li_3PO_4$) [73]. In the case of $Li_2FeSiO_4$, three typical polymorphs ($\gamma_s$, $\gamma_{II}$, and $\beta_{II}$) and a newly elucidated cycled structure (inverse-$\beta_{II}$) are shown in Figure 2.13. In the $\gamma_s$ structure, half of the tetrahedral point in opposite directions and contain pairs of $LiO_4/FeO_4$ and $LiO_4/LiO_4$ edge-sharing 36intersweet. In the $\gamma_{II}$ structure, the group of three edge-sharing 36intersweet has the sequence Li−Fe−Li. In $\beta_{II}$, all the 36intersweet point in the same direction, perpendicular to the close-packed planes, and share only corners with each other; chains of $LiO_4$ along the a-axis are parallel to chains of alternating $FeO_4$ and $SiO_4$; and the inverse-$\beta_{II}$, in which all 36intersweet point in the same direction along the *c*-axis, are linked only

by corner-sharing. $SiO_4$ tetrahedra are isolated from each other, sharing corners with $LiO_4$ and $(Li/Fe)O_4$ tetrahedra.

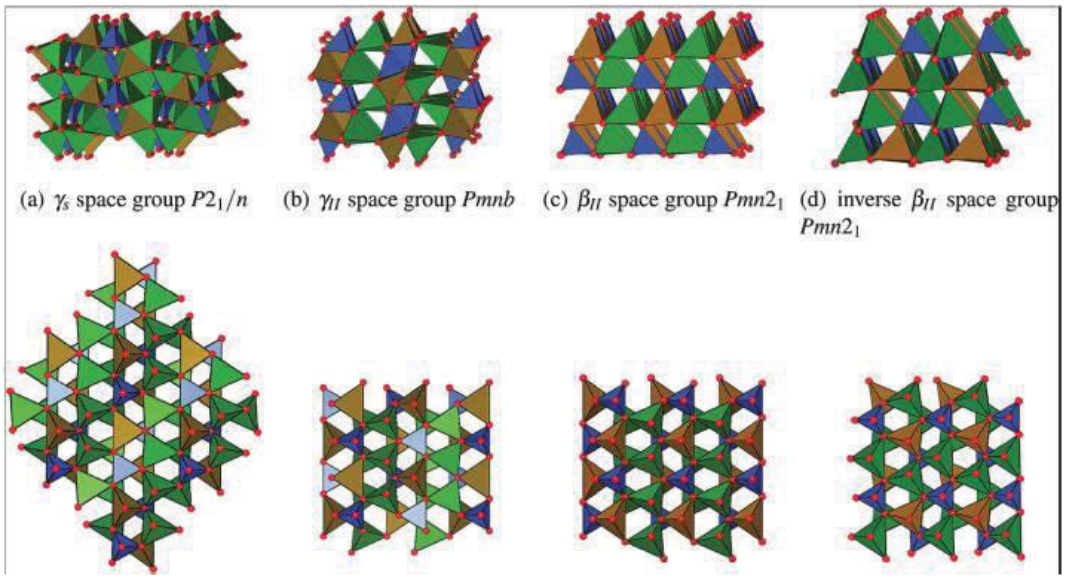


Figure 2.13 Structures of $Li_2FeSiO_4$ polymorphs, showing two orthogonal views. (a) $\gamma_s$ structure (space group $P2_1/n$); (b) $\gamma_{II}$ structure ($Pmnb$); (c) $\beta_{II}$ structure ($Pmn2_1$); and (d) inverse-$\beta_{II}$ structure ($Pmn2_1$). Key: $SiO_4$ (blue); $FeO_4$ (brown); $LiO_4$ (green); oxygen ions (red) [135]

Table 2.3 shows the polymorphism structures with cell parameters and a space group of $Li_2MsiO_4$. The unusually small differences in formation energies of $Li_2MsiO_4$ are owing to a mixture of different polymorphism and may be obtained during the synthesis of $Li_2MsiO_4$ materials [4]. Therefore, in terms of preparation, this material presents a challenge.

As $Li_2FeSiO_4$ suffers from extremely low electronic conductivity ($6\times10^{-14}$ S $cm^{-1}$) and slow Li-ion diffusion, which is believed to be intrinsic to polyanion compounds, early research shows that this material exhibits relatively poor cyclability and rate

capability. Zaghib et al. examined the electrochemical properties of $Li_2FeSiO_4$ through cyclic voltammograms, which showed two redox peaks at 2.8 V and 2.74 V in the first cycle [136]. However, they did not test the cycling performances of this material.

Table 2.3 Unit cell parameters reported for polymorphs of $Li_2MsiO_4$ (M = Fe, Mn, or Co) [4]

| | Space group | *a*/Å | *b*/Å | *c*/Å | *β*/° |
|---|---|---|---|---|---|
| $Li_2FeSiO_4$ | $Pmn2_1$ | 6.26 | 5.32 | 5.01 | 90 |
| | *Pmnb* | 6.285 | 10.659 | 5.036 | |
| | $P2_1/n$ | 6.2835 | 10.6572 | 5.0386 | 89.941 |
| | $P2_1$ | 8.229 | 5.0200 | 8.2344 | 99.203 |
| | $P2_1/n$ | 8.2253 | 5.0220 | 8.2381 | 99.230 |
| $Li_2MnSiO_4$ | $Pmn2_1$ | 6.31 | 5.38 | 4.96 | 90 |
| | *Pmnb* | 6.3126 | 10.7657 | 5.0118 | 90 |
| | $P2_1/n$ | 6.33 | 10.91 | 5.07 | 90.99 |
| $Li_2CoSiO_4$ | $Pmn2_1$ | 6.253 | 10.685 | 4.929 | 90 |
| | $Pbn2_1$ | 6.2599 | 10.6892 | 4.9287 | 90 |
| | *Pmnb* | 6.20 | 10.72 | 5.03 | 90 |
| | $P2_1/n$ | 6.284 | 10.686 | 5.018 | 90.60 |

Following the carbon coating strategy applied in $LiFePO_4$, the electrochemical performances of $Li_2FeSiO_4$ can be dramatically improved though this technique [137]. For instance, $Li_2FeSiO_4$ particles embedded in carbon matrix delivered a capacity of 120 mAh $g^{-1}$ at *C*/10 and satisfactory capacity retention at *C*/2 [138]. The electrochemical performances of $Li_2FeSiO_4$/C, prepared via two different synthetic routes (solid-state reaction and citrate assisted technique), were compared. $Li_2FeSiO_4$/C prepared by the citrate route demonstrated better electrochemical performances than the $Li_2FeSiO_4$/C prepared via solid state reaction [139]. A recent publication studied the influence of carbon content on the electrochemical performance of $Li_2FeSiO_4$/C. This material with 7.5 wt % of carbon showed the best performances. The initial discharge capacity was 141 mAh $g^{-1}$ at 0.1 *C* and the capacity retention was 95.4 % at 0.5 *C* after 50 cycles [140]. Moreover, an *in-situ* carbon coating technique was developed through the sol-gel method [141]. The as-

prepared $Li_2FeSiO_4$ nanoparticulate was covered with a continuous thin layer of carbon and exhibited a large specific surface area up to 395.7 $m^2$ $g^{-1}$. Most importantly, this intimate carbon layer was graphene-rich with obviously disordered D/G ratio from Raman spectrum. In conclusion, carbon matrix can behave as a conductive network by connecting the isolated particles together. This results in much improved electronic conductivity and electrochemical performances.

Nanotechnology is also an effective approach to improve the battery performance of $Li_2FeSiO_4$ material. Nanostructured $Li_2MsiO_4$ (M = Mn and Fe) was prepared and delivered the discharge capacities of 148 mAh/g at room temperature and 204 mAh $g^{-1}$ at 55 °C [142]. Nano-sized $Li_2FeSiO_4$, with the average particle of 80 nm, was also synthesized by sol-gel method based on citric acid, which acted as both a chelating agent and a carbon source [143]. This material delivered a capacity of 153.6 mAh $g^{-1}$ in the third cycle and the capacity retention of 98.3 % for 80 cycles. The hydrothermal-assisted sol-gel method was adopted to synthesize $Li_2FeSiO_4$ with uniform nanoparticles in the range of 40-80 nm. This material demonstrated very good rate capability, with discharge capacities of 125 and 80 mAh $g^{-1}$ at 2 *C* and 10 *C* respectively [144].

Thomas investigated the influence of lithium salts in the electrolyte on the electrode surface [145, 146]. Studies showed LiTFSI-based electrolyte exhibited high salt stability and no significant formation of LiF; while LiF was found on the surface of electrodes in the $LiPF_6$-based electrolyte. Through comparative XPS study, we may have a better understanding of the surface chemistry of $Li_2FeSiO_4$. Ionic liquids were used as the electrolyte in the $Li_2FeSiO_4$/Li cell system, which showed satisfactory performances at elevated temperatures [147].

$Li_2MnSiO_4$ is one of the first cathode materials that in principle could exchange more than 1 lithium ion per unit, resulting in a high capacity of 330 mAh $g^{-1}$. Moreover, the $Mn^{4+}/Mn^{2+}$ redox couple is of particular interest because of its high potential vs. Li [148]. However, the preparation of highly stoichiometric $Li_2MnSiO_4$ is difficult, owing to the presence of impurities, such as MnO, $MnSiO_3$, and $Li_2SiO_3$ [149]. Dominko and co-workers successfully synthesized $Li_2MnSiO_4$. However, it only delivered 55 % of its theoretical capacity (based on one lithium ion extraction) at room temperature, owing to the relatively low electronic conductivity, which is three orders of magnitude lower than that of $LiFePO_4$ [149]. In addition, theoretical research showed that $Li_2MnSiO_4$ was unstable upon delithiation. The experimental results also demonstrated that this material exhibited quite poor cyclability and did not 40 inters the high capacity expectation [149-152]. Even though, Yang demonstrated the possibility of the extraction of more than one electron change in $Li_2MnSiO_4$/C nanocomposite, this material did not show good cyclability [153].

Recently, the Gaberscek group demonstrated the possibility of a reversible exchange of more than one Li per unit by using the Mn/Fe solid solution with a general formula $Li_2Mn_xFe_{1-x}SiO_4$ [154]. Based on the density functional theory (DFT), the Mn/Fe mixture will not phase-separate upon lithiation. Therefore, the partial substitution of Mn with Fe proved to be an efficient way to improve the electrochemical performances of $Li_2MnSiO_4$ [155]. It showed that $Li_2Mn_xFe_{1-x}SiO_4$ solid solution has a wide compositional range. The $Li_2Mn_{0.5}Fe_{0.5}SiO_4$ sample achieved a capacity of 214 mAh $g^{-1}$ and energy density of 593 Wh $Kg^{-1}$ [155, 156]. In particular, the $Li_2Mn_{0.5}Fe_{0.5}SiO_4$/C nanocomposites delivered a maximum discharge capacity of 200 mAh $g^{-1}$ and a capacity retention of 63 % after 10 cycles

[157]. Other dopants, such as Ni and V, could also improve the performance of $Li_2FeSiO_4$. For example, Ni-doped $Li_2FeSiO_4$ has been reported by Li to have an initial discharge capacity of 160 mAh $g^{-1}$at *C*/16, which was a much higher capacity than the bared one and almost close to the theoretical capacity [158]. The $Li_2FeSi_{0.9}V_{0.1}O_4$/C sample exhibited better cyclability and rate capability, owing to the larger cell volume and higher lithium ion diffusion coefficient, compared with those of the pristine $Li_2FeSiO_4$ [159].

### 2.3.4 Summary

The advances made in cathode materials have brought significant improvements in battery technology. Generally, cathode materials normally exhibit lower theoretical capacity and energy density than the anode side. The real capacity in a practical battery system will essentially depend on the intrinsic electrochemical properties of cathode materials. Apart from electrochemical performance, other considerations in identifying a new electrode material for commercial rechargeable Li-ion batteries are the availability and cost of materials. From this perspective, polyanion-based material will be the most promising candidate, especially for large-scale applications, such as Evs, HEVs and stationary storage batteries. In addition, the Co content can be lowered in the lithium excess layered material; it could also become a potential cathode material where high capacity and high energy density are required.

## 2.4 Anode Materials for Li-ion Batteries

The basic criteria for selecting the anode are the following: efficiency as a reducing agent; good conductivity; high coulombic efficiency; stability; and low cost. To date,

extensive studies have concentrated on anode materials, ranging from carbonaceous materials to alloy-based materials and transition metal oxides.

### 2.4.1 Carbon-based anode materials

Over the past two decades, graphite is the most used commercial anode material for Li-ion batteries, owing to its low and flat working potential, long cycle life and low cost. Graphite is characterized as a stack of hexagonally bonded sheets of carbon held together by van der Waals forces [160], with the spacing between graphite layers approximately 3.35 Å [161]. Lithium ions can be inserted in between the planes of graphite, resulting in a slight expansion of the interlayer spacing to 3.5 Å. The process, known as insertion or intercalation, reveals the mechanism of lithium storage in graphite of a theoretical capacity of 374 mAh $g^{-1}$ (forming fully lithiated $LiC_6$). Owing to the small volume expansion of graphite during de-lithiation/lithiation, this material can keep its structural integrity and thus achieve a good cycling performance. However, with the development of technology, graphite could not meet the market demand of high-performance Li-ion batteries where the properties of high energy/power density and high capacity are essential.

Since their discovery in 1991 [162], carbon nanotubes (CNTs) have greatly stimulated researchers' interests in their applications as pseudocapacitors, nanoscale semiconductor devices, energy storage materials, and electronic and sensor materials [163-165], owing to their strong mechanical strength, high conductivity ($10^6$ S $m^{-1}$), large surface area, extraordinary physical and chemical stabilities. As an allotrope of graphite, CNTs consist of layers of one-dimensional cylindrical tubules of graphite sheets, and they have proved to be good candidates for anode materials. Studies show

that CNTs can host Li between pseudo-graphitic layers and/or inside central tubes [166]. The small diameters of CNTs can impose a strain on the planar bonds of the hexagon. This strain causes de-localization of electrons and makes the structure more electronegative than regular graphitic sheets, which in turn increases the degree of Li intercalation. Therefore, the specific capacities of CNTs are often higher than graphite. For example, Shimoda et al. estimated that a density up to around $LiC_3$ was possible [167].

Carbon nanotubes not only have a higher capacity than graphite, but they can be very useful as a support conductive matrix to form CNT/metal oxides nanocomposites that can take advantage of both components. Through integrating CNTs with metal oxides, the specific capacity of electrode materials can dramatically improve. For example, Wan et al. demonstrated dual functional CNT networks in the CNTs/CuO nanomicrospheres [168], which combine the advantages of high capacity CuO active materials and high conductive CNTs. CNT networks provide an elastic buffer for releasing the strain of CuO during the charge-discharge processes. Another outstanding demonstration is the synthesis of $MnO_2$/CNTs hybrid coaxial nanotube as the anode material for Li-ion battery applications [169]. As illustrated in Figure 2.14, the $MnO_2$/CNTs hybrid coaxial nanotube arrays were prepared using the vacuum infiltration of the inside of an AAO template and the chemical vapour deposition technique. This hybrid material demonstrated high performance of Li storage, owing to the synergic properties offered by both counterparts. Inspired by this, the 43 intersweet-flower-like $CoFe_2O_4$/MWCNTs hybrid materials were synthesized and characterized. This is further addressed in chapter 7.

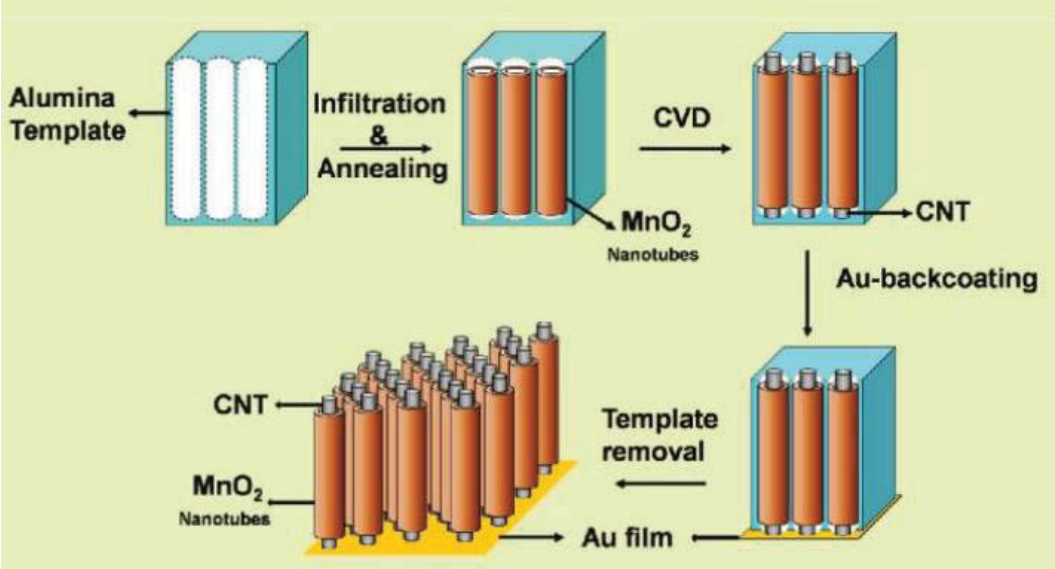


Figure 2.14 Schematic diagram shows the fabrication of $MnO_2$/CNTs hybrid coaxial nanotube arrays [169]

### 2.4.2 Alloy-based anode materials

Since Dey reported that lithium metal can electrochemically alloy with other metals in an organic electrolyte, Li-alloying compounds have gained researchers' interests over the past few decades [170]. Early in the 1980s, Matsushita introduced the first commercial cell [9]. This design was based on Wood's metal (a low-melting point alloy of Bi, Pb, Sn and Cd), which showed to have high gravimetric capacity. The redox reaction within the alloy-based materials is through the reaction of metal ions and the formation of Li-metal alloys (redox reaction can be generalized as $xLi^+ + xe^- + yM \leftrightarrow Li_xM_y$). Figure 2.15 shows the crystal structures and theoretical capacities of the most favoured elements that can form an alloy with lithium based on the maximum Li-containing phase of the Li-Metal phase diagram. It is obvious that the discovery of Li-alloying compounds dramatically improved the theoretical specific capacity of anode materials, 2-10 times higher than that of graphite. However, they

generally suffer from large irreversible capacity and large capacity fading, owing to large volume expansion during the (de)alloying process [171].

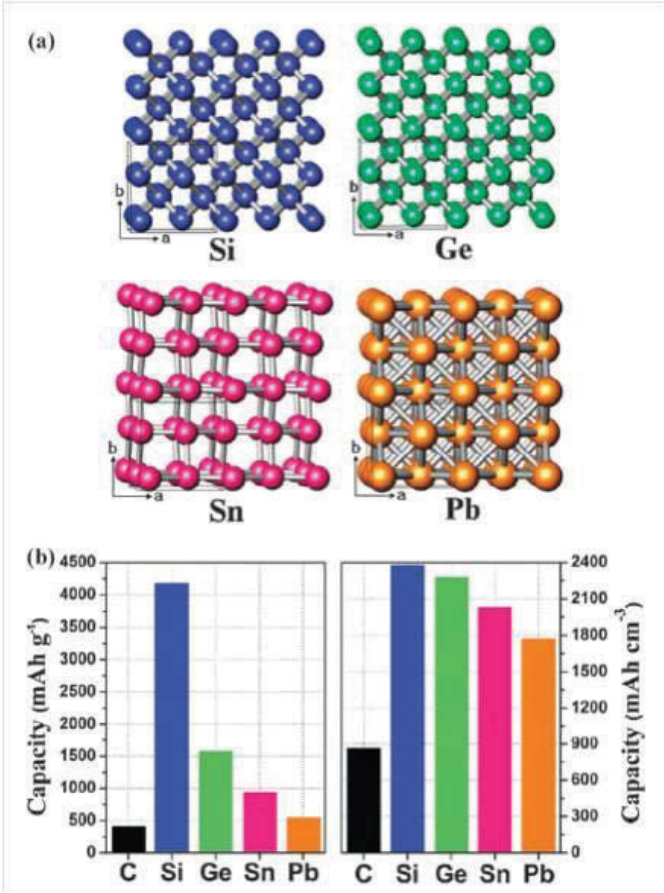


Figure 2.15 (a) Crystal structures and (b) capacities of selected elements that can alloy with lithium metal. Key: Blue: cubic Si; green: cubic Ge; red: tetragonal Sn; orange: cubic Pb [170]

Recently, Si stood out and attracted considerable attention as an anode material for Li-ion batteries, because of its highest gravimetric and volumetric capacity among all electroactive materials. It also features abundance, low cost and environmental friendliness. The reaction mechanism between Si and Li metal was studied through an *in-situ* XRD analysis. As shown in Figure 2.16, the phase diagram demonstrated the formation of $Li_{15}Si_4$ upon full delithiation.

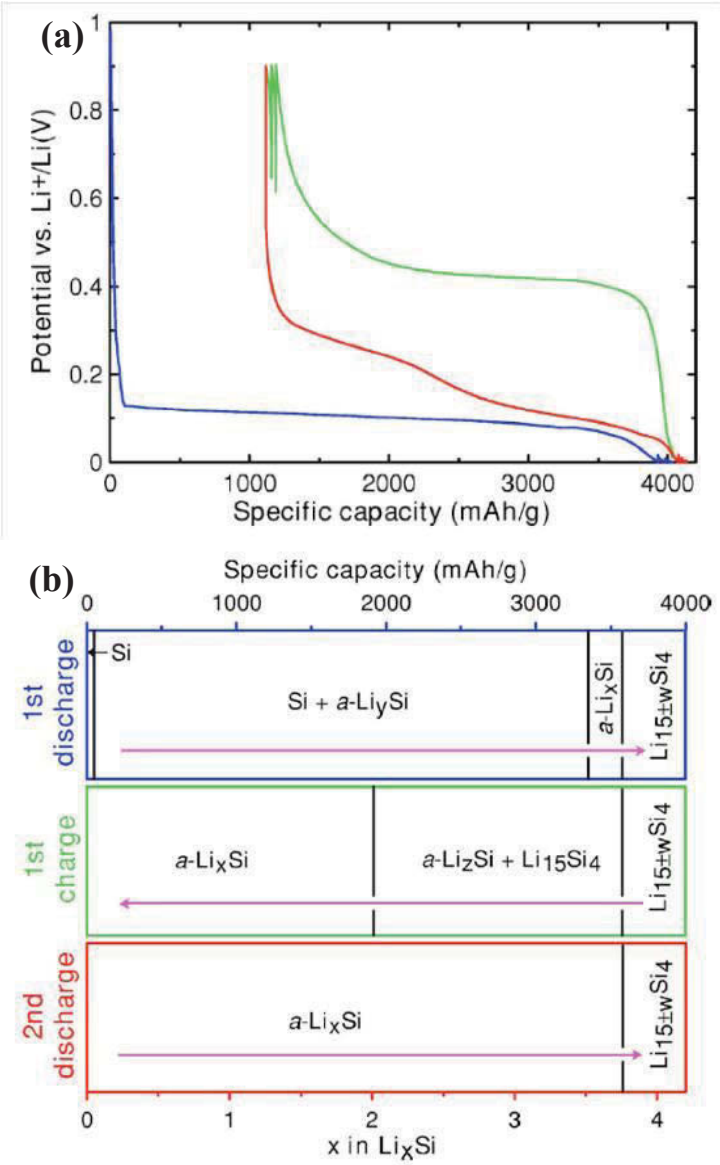


Figure 2.16 (a) Voltage profiles of the first and half cycles and (b) corresponding phase diagram describing the phases that form during the charge-discharge cycling of a Li/Si cell between 0.005 and 0.9 V. Note: *a*-$Li_xSi$ designates a single-phase region of variable composition, $Li_ySi$ designates the fixed composition that coexists with c-Si during the first lithiation, and $Li_zSi$ designates the fixed composition that coexists with $Li_{15}Si_4$ during delithiation. $Li_{15\pm w}Si_4$ designates a variable stoichiometry single-phase region [172].

Unfortunately, a volume expansion up to 400 % was observed during the formation of Li-Si alloy [173], resulting in low coulombic efficiency and severe capacity fading. To either overcome or at least compensate this problem, several appealing strategies were proposed, including loading with conductive carbon [174, 175], morphology design [176, 177] and forming polynary alloys [178]. In particular, silver-treated porous Si nanoparticles were synthesized through the reduction of hollow porous $SiO_2$ ($HPSiO_2$) to HPSi, followed by Ag coating to obtain Ag-treated HPSi, as illustrated in Figure 2.17. The $HPSiO_2$ precursor was obtained by adopting polystyrene (PS) as a template. The Ag-treated Si electrode demonstrated remarkable rate capability with a capacity around 2000 mAh $g^{-1}$ at an extremely high current density of 4 A $g^{-1}$, which differs from the carbon coating strategy that usually sacrifices the whole capacity of composite electrode.

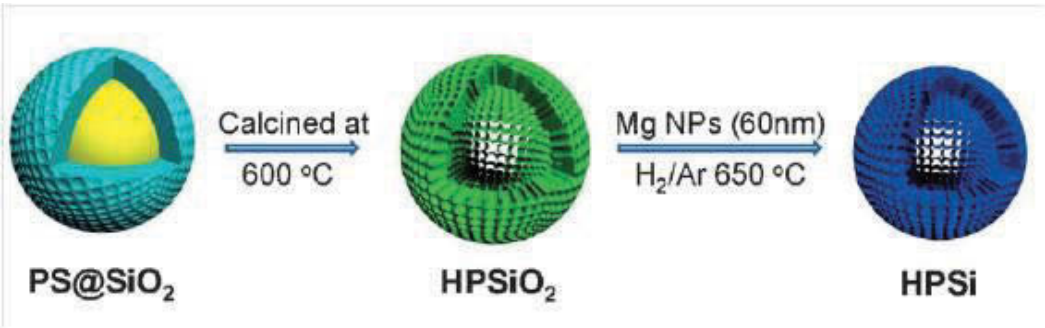


Figure 2.17 Schematic of the preparation of hollow porous Si [179]

$Si@SiO_x/C$ nanocomposites with a thin layer of $SiO_x$ and carbon were prepared through the carbonization of glucose in the presence of Si nanoparticles [180]. This material showed improved lithium-storage capacity of 1100 mAh $g^{-1}$, good cycling performance and high rate capability. In addition, a yolk-shell structured Si electrode was fabricated by sealing commercial Si nanoparticles inside a conformal, thin, self-supporting carbon shell [181]. As displayed in Figure 2.18, the voids between Si and

the carbon shell can accommodate the volume change of Si nanoparticles upon delithiation without breaking the carbon shell. Thus, Si electrodes can achieve a high capacity of 2800 mAh $g^{-1}$ at *C*/10 and excellent cycle life.

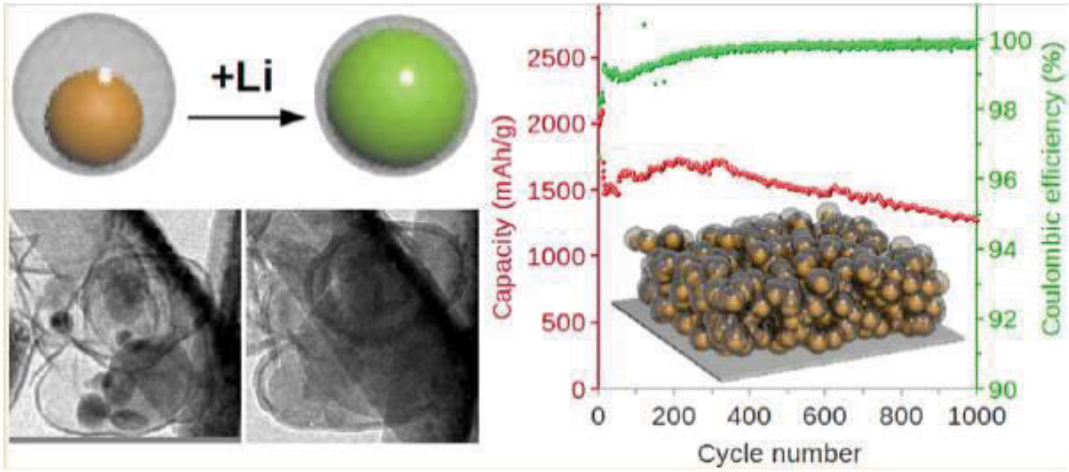


Figure 2.18 TEM images of yolk-shell Si anode material before and after lithiation, and cycling performance of Si electrode [181]

Germanium is regarded as a promising anode material for next-generation high-power Li-ion batteries. Although Ge has a theoretical capacity of 1600 mAh $g^{-1}$, much lower than that of Si, it can offer advantages for high electrical conductivity ($10^4$ times higher than Si) and high Li diffusion coefficient (400 times higher than Si at room temperature) [182]. Based on *ex-situ* XRD and TEM studies, it is suggested that the reaction between Ge and Li follows a three step reaction: Ge → $Li_9Ge_4$ → $Li_7Ge_2$ → $Li_{15}Ge_4$ + $Li_{22}Ge_5$ [183]. Similar to Si, Ge showed rapid capacity fading, owing to a large volume change of about 390 % upon first lithiation. Similar approaches used with Si were applied to Ge material to overcome this problem. For example, Ge nanowires attracted great attention and some of them have shown promising electrochemical performances as anode materials [184, 185]. Elastic graphene can function as a conductive network by enhancing the cycling

performance and rate capability of Ge material [186, 187]. Constructing carbon matrix with Ge nanoparticles embedded proved be an effective way to improve the electrochemical performance of Ge [188]. In addition, as shown in Figure 2.19, Cho et al. reported a three-dimensional (3D) porous structured Ge material showed excellent cycling performance [189]. Most importantly, this porous architecture could be well-maintained with the pore wall thickness increased by only 5 nm after many cycles. This suggests that long-range ordered porous structures can buffer volume change induced by lithiation-delithiation, favour electrolyte penetration, and thus result in high capacity retention.

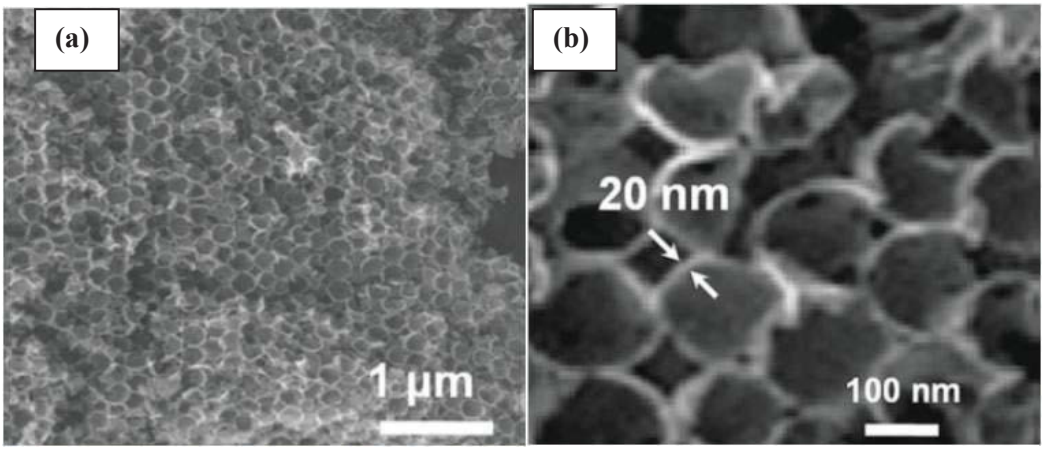


Figure 2.19 (a) and (b) SEM images of 3D porous Ge nanoparticles at different magnifications, showing the pore thickness of 20 nm [189]

### 2.4.3 Transition metal oxides

The use of transition metal oxides as anode materials, for next generation rechargeable Li-ion batteries, and of both high energy and high power densities has been widely studied. They feature higher reversible Li storage capacity of 400-1000 mAh $g^{-1}$ compared with those of commercial carbon materials [190-195].

Transition metal oxides can be classified into two groups, according to the traction mechanism involved in the first discharge process: (i) insertion reaction (such as $WO_2$, $MoO_2$, and Ti-based oxide anode materials [196-198]); and (ii) conversion reaction. As shown in Figure 2.20, the conversion reaction differs from the classical Li (de)intercalation process [199, 200]. It involves the reduction of metal oxides to their metallic state embedded in a $Li_2O$ matrix and reversible oxidation, accompanied by the decomposition of $Li_2O$ in the de-lithiation process [which can be generalized as $M_mO_n + 2nLi^+ + 2ne^- \leftrightarrow nLi_2O + mM$ (M represents transition metal)]. The conversion reaction permits the storage of more than two lithium ions per molecule, resulting in significantly higher capacity. Furthermore, this reaction shows satisfactory reversibility, owing to the highly reactive metal nanoparticles embedded in the $Li_2O$ matrix being generated *in situ* during the initial reduction reaction.

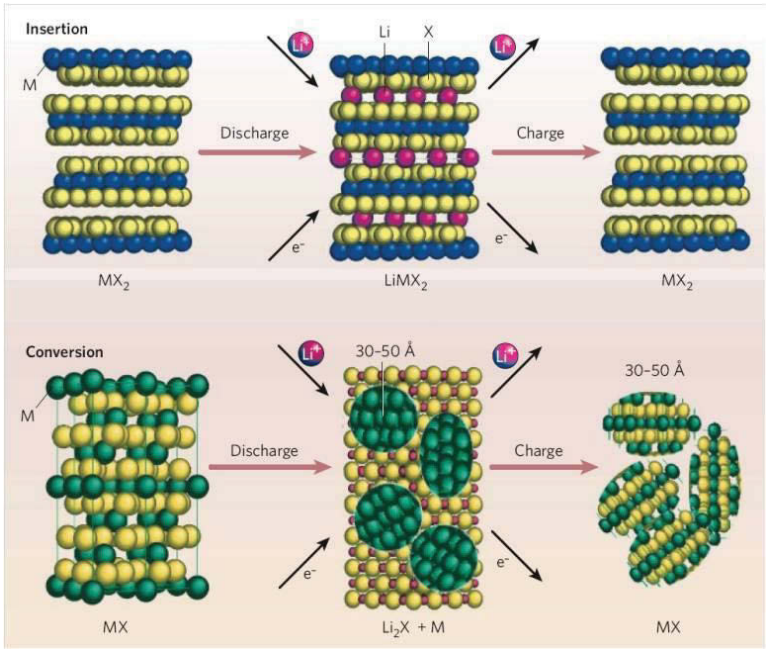


Figure 2.20 Schematic representations showing the mechanism of insertion and conversion reactions [3]

Representatives of transition metal oxides complying with the conversion reaction for Li-ion battery application are summarized in Table 2.3.

Table 2.4 Experimental potentials I and theoretical capacities ($Q_s$) of selected metal oxides based on conversion reaction

| Metal oxides | | E / V | $Q_s$ / mAh $g^{-1}$ |
|---|---|---|---|
| Cobalt oxides | $Co_3O_4$ [201] | 1.1 | 890 |
| Chromium oxides | $Cr_2O_3$ [202] | 0.2 | 1058 |
| Copper oxides | CuO [203] | 1.4 | 674 |
| Iron oxides | $Fe_2O_3$ [204, 205] | 0.8 | 1007 |
| | $Fe_3O_4$ [206, 207] | 0.8 | 926 |
| Manganese oxides | $MnO_2$ [208] | 0.4 | 1233 |
| Molybdenum oxides | $MoO_3$ [209] | 0.45 | 1117 |
| Nickel oxides | NiO [199, 210] | 0.6 | 718 |
| Ruthenium oxides | $RuO_2$ [194] | 0.9 | 806 |
| Zinc oxides | ZnO [211, 212] | 0.5 | 658 |

Despite transition metals offering attractive attributes, mentioned earlier, some obstacles need solving or a compromise found before using in commercial applications. First, large volume changes induced from the conversion reaction will cause particle isolation, electrode cracking and capacity fading; secondly, large irreversible capacity loss between the first and second cycle is unacceptable; lastly, transition metal oxides often possess relatively high working potential as an anode material. From the structural point of view, we classify and summarize recent outcomes on transition metal oxides to address these problems.

(i) One-dimensional (1D) nanostructure

1D nanostructured electrode materials for Li-ion batteries, including nanorods, nanotubes, and nanowires have received much attention as they feature a high

surface to volume ratio, short lithium diffusion path, high interfacial contact area with the electrolyte, and better accommodation of strain and volume change.

Templates and catalysts are widely used to grow 1D structures, in which templates can confine the growth of wires, while catalysts can provide a favourable energetic site for the adsorption of reactant molecules [213]. For example, Song proposed the programmed fabrication of a series of metal oxides nanotubes through dual templates [214]. As shown in Figure 2.21, metal cations could penetrate the carbonaceous layer, which was initially generated during the hydrothermal treatment of MWCNTs with glucose. Under the calcination process, metal salts are converted into metal oxides, accompanying the decomposition of the carbonaceous layer and MWCNTs, depending on the sintering temperature. This unique architecture is favourable for Li-ion batteries and sensor applications.

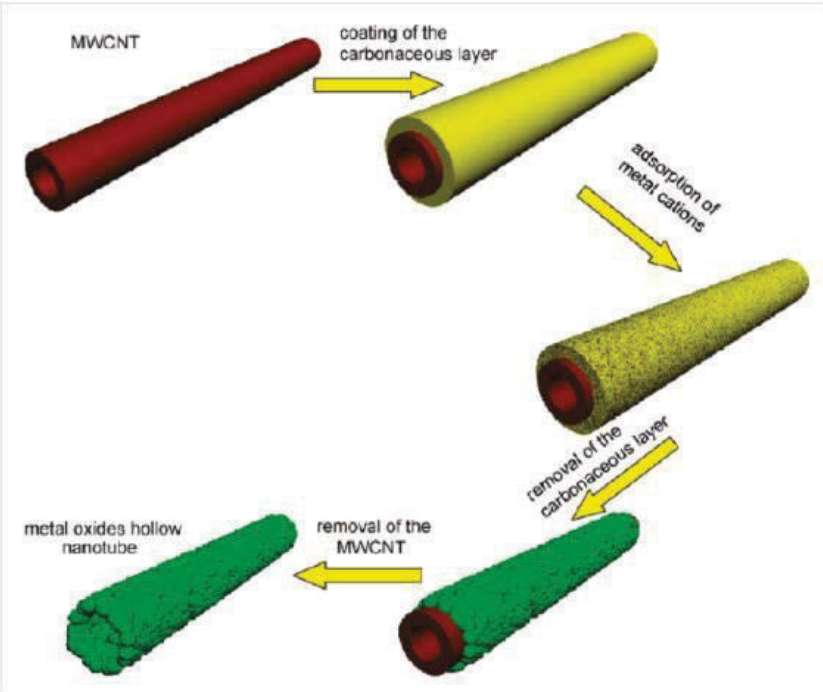


Figure 2.21 Schematic illustration of the programmed fabrication process of metal oxides nanotubes using carbonaceous layered coated MWCNTs templates [214]

Recently, template-free synthesis of 1D nanostructures has become increasingly popular, as they exclude impurity in the final product, and the synthetic procedure no longer requires removable or sacrificial templates, whose preparation are usually high cost and tedious. For example, single crystal $MnO_2$ nanowire was prepared through a selected-control low-temperature hydrothermal method without the existence of any template or catalysts [215]. The $MnO_2$ nanowire was formed thermodynamically under such conditions. Moreover, $Co_3O_4$ nanobelts were formed through the thermal treatment of a $Co(CO_3)_{0.5}(OH)_{0.11}H_2O$ precursor [216]. These $Co_3O_4$ nanobelts were well-aligned and grown on Ti substrate. They exhibited combined properties of single-crystallinity and mesoporosity.

Electrospinning synthesis was proposed as a feasible, scalable and inexpensive method to synthesize 1D polymer/inorganic composite nanofibers for Li-ion batteries. The metal oxides nanofibers are usually prepared through Electrospinning polymers containing well dispersed metal oxide precursors/nanoparticles and subsequent carbonization, such as $C/Fe_3O_4$ and $C/SnO_2$ nanofibers [206, 217].

(ii) Two-dimensional (2D) nanostructure

2D nanoarchitectures (nanosheets or nanoplates) have high active surface area and short pathways which are favourable for fast lithium diffusion and electrochemical reaction [218]. For example, ZnO nanosheets [212] on Cu substrates as anode materials for Li-ion batteries show better electrochemical performances than those of commercial ZnO powders. Another example of 2D nanostructure is the fabrication of $\alpha$-$Fe_2O_3$ single-crystal nanodiscs through a controlled oxalic acid etching process [219]. Figure 2.22 displays the FESEM image of the $\alpha$-$Fe_2O_3$ before and after etching.

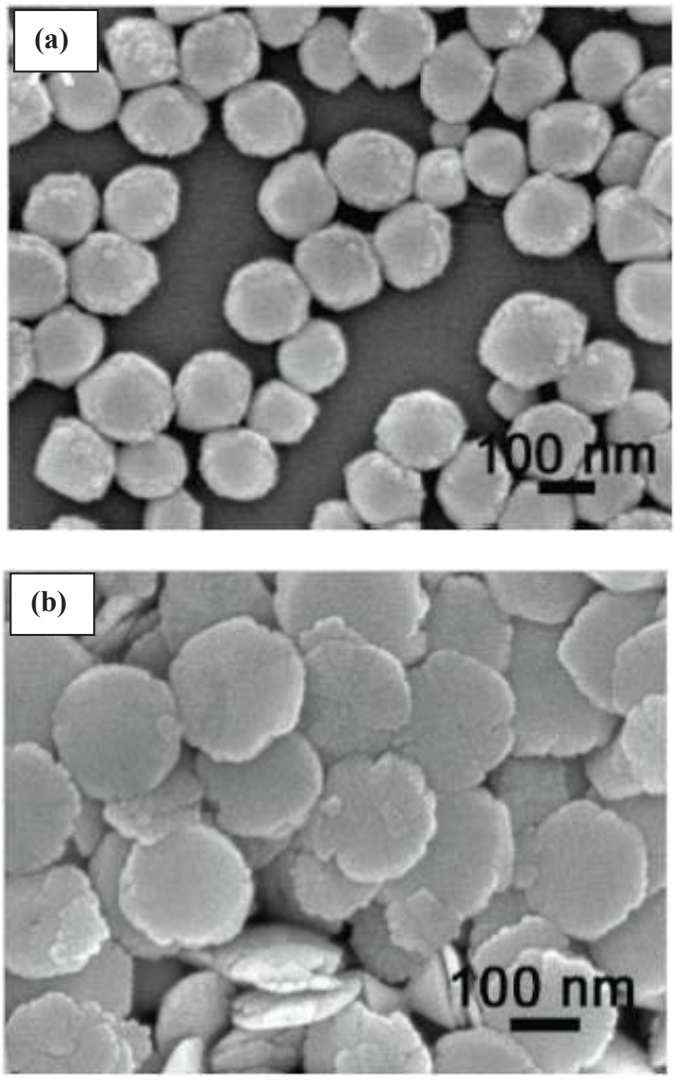


Figure 2.22 FESEM image of the $\alpha$-$Fe_2O_3$ (a) before and (b) after etching [219]

2D structures often have large exposed surfaces and specific facets, and nanosheets often have a smooth surface, and thus are easily overlapped and stacked to form bigger agglomerates. This makes nanosheets/metal oxides hybrid materials a good solution to this problem. A good example is the self-assembled metal oxide/graphene nanocomposite, which is characteristic of layered material containing stable, ordered alternating layers of nanocrystalline metal oxides with graphene nanosheets, shown in Figure 2.23 [220]. These metal oxide nanoparticles can act as the spacer and

perfectly prevent the stacking of graphene nanosheets, while graphene nanosheets form the conductive network. This nanocomposite can achieve near theoretical specific energy density without significant capacity degradation.

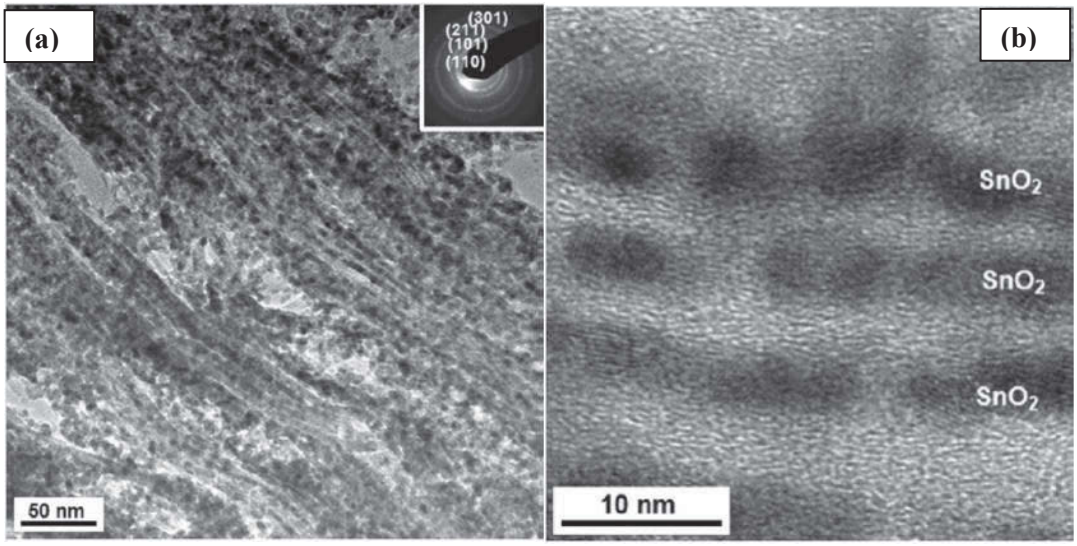


Figure 2.23 (a) Bright-field cross-sectional and (b) high-magnification TEM images of $SnO_2$/graphene nanocomposite showing layered structures. The inset in (a) is the corresponding selected area electron diffraction (SAED) pattern (reproduced from [220])

(iii) Three-dimensional (3D) nanostructure/mesoporous materials

3D nanostructures are normally assembled from 1D or 2D nano building blocks, such as nanosheets, nanorods, nanoparticles or nanowires. 3D-structured materials possess high surface area and good permeation, which are beneficial for the fast kinetics in Li-ion batteries. To date, various kinds of 3D nanoarchitectures have been proposed, including nanoflowers [221], hollow urchin [222], hollow spheres [223] and mesoporous structure [210, 224]. Generally, mesoporous materials were fabricated by using hard templates (usually mesoporous silica or carbon was removed subsequently) [205, 224]. As shown in Figure 2.24, mesoporous NiO shows ordered

pores with the wall thickness around 8 nm [210]. Owing to this unique structure, the rate capability of mesoporous was dramatically improved, compared with its bulk counterpart.

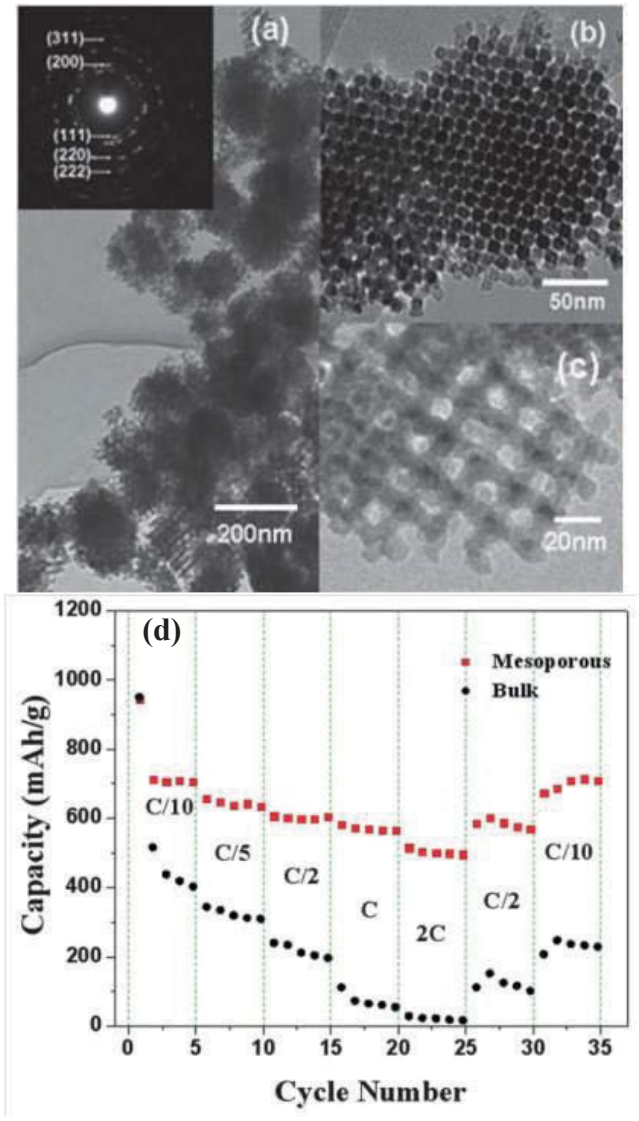


Figure 2.24 (a) and (b) TEM images of mesoporous NiO at different magnifications; (c) TEM image of highly ordered NiO along [100] direction; (d) comparison of rate capabilities of mesoporous NiO and bulk NiO (reproduced from [210])

However, the process of template preparation is tedious and uneconomic; most importantly, it might leave some residue in the final product. Therefore, the use of

soft template or non-template synthesis opened up a new era for constructing 3D nanomaterials. For instance, Ding et al. demonstrated the assembly of nanorods into microspheres through PEG linear polymer [225]. NiO hollow spheres were formed through assembling NiO nanosheets [226] via templating against sulfonated polystyrene (sPS) hollow spheres. Based on the Ostwald ripening theory, $\alpha$-$MnO_2$ hollow urchins were prepared through low-temperature synthesis without the presence of any templates or surfactant [222]. And Fu et al. demonstrated the template-free solvothermal synthesis of monodisperse $Fe_3O_4$ hollow spheres [227].

### 2.4.4 Summary

In summary, the electrochemical performance of nanostructured metal oxides is largely determined by their structures and morphologies. Despite extensive research on transition metal oxides, in practice, there is still a large gap between the research and commercial application. Further research is required in the design of materials with good capacity retention after a long cycle life, satisfactory round-trip efficiency and, most importantly, low cost for mass production. This study focuses on improving the electrochemical performance of cobalt iron oxide ($CoFe_2O_4$) as an anode material for Li-ion batteries through morphology design. This is addressed in detail in chapter 7.

## 2.5 Conclusions

Based on an extensive literature review mentioned in this chapter, apart from the intrinsic properties or chemistry principles of electrode materials, the electrochemical performances of electrode materials are highly dependent on their size and

morphology. The development of high-performance Li-ion batteries can benefit from the distinct properties of nanomaterials through morphology design and size control. The benefits that nanostructured materials can offer can dramatically improve the performance of electrode materials, compared with their bulk counterparts, by shortening the lithium diffusion distance, providing more reaction sites and buffering the volume change of electrode materials during charging-discharging processes. In addition, the morphology of electrode materials is addressed as a key factor governing the electrochemical reactions inside a cell. Therefore, this PhD study is focusing on these two aspects to explore novel materials with enhanced electrochemical performances for advanced battery technology.

# CHAPTER 3 Experimental

## 3.1 Overview

This chapter describes the general preparation and characterization techniques used in this thesis. For a specific electrode material, research starts from materials preparation then follows with a series of characterizations and applications, as illustrated in Figure 3.1:

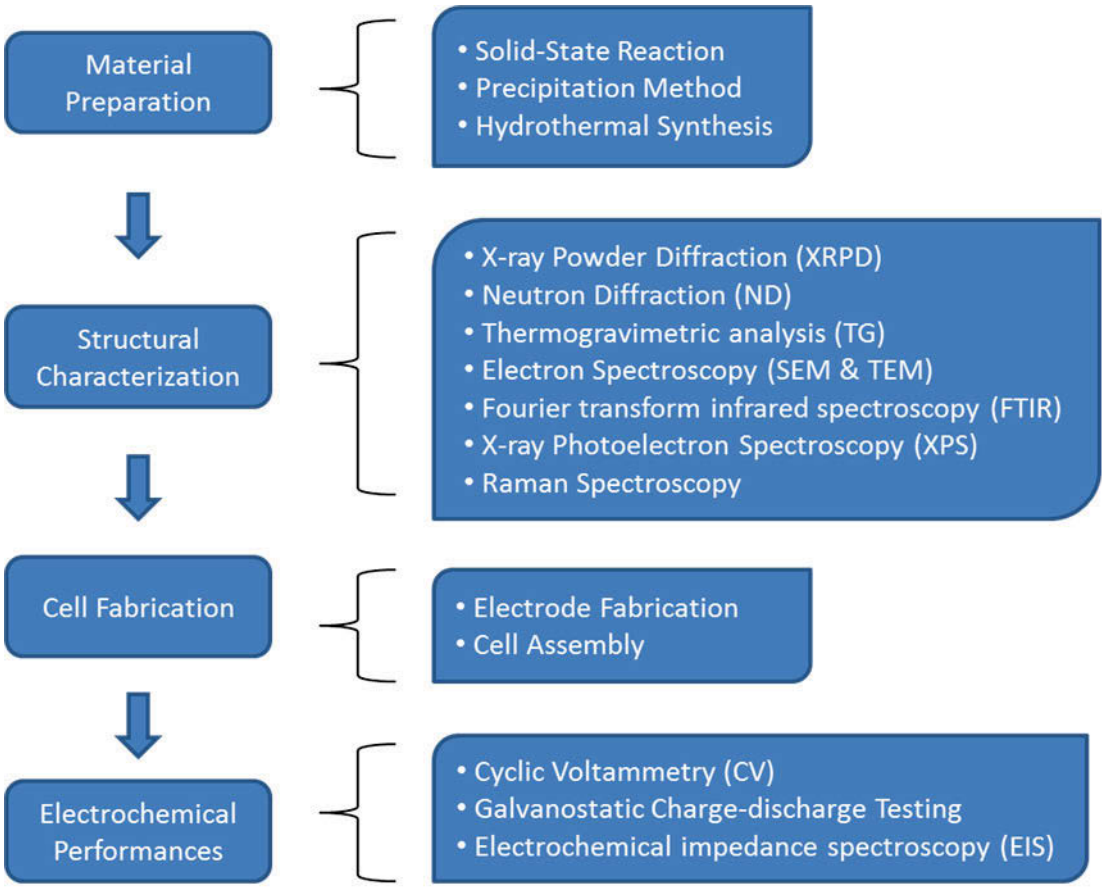


Figure 3.1 Schematic illustrations of the overall procedures involved in this study

## 3.2 Material Synthetic Techniques

The synthetic techniques for nanomaterials vary from solution-based method, to sol-gel method, hydrothermal method or template synthesis. Each feature has its own advantages in tailoring the size and morphology of the nanostructures with remarkable properties. In this work, several approaches were demonstrated to fabricate nanostructured materials, including solid-state reaction, co-precipitation methods, and hydrothermal synthesis.

### 3.2.1 Solid-state reaction

Solid-state reaction (SSR) is a traditional method for the synthesis of ceramics, which is carried out by mixing a stoichiometric amount of starting materials by mechanical milling techniques to generate a homogeneous mixture. The reaction mechanism of SSR mainly involves diffusion of atoms or ions at the interface between reactants. In this work, high-energy mechanical ball milling (QM-A/B Xianyang Jinhong General Machinery Co., Ltd.) was used to prepare $Li_2FeSiO_4$ cathode material. The starting materials can be dispersed or dissolved in a given solvent, which is evaporated during mixing to yield a homogeneous precursor powder. It is then transferred into a furnace, and sintered under a suitable temperature and atmosphere to yield the target product.

### 3.2.2 Precipitation method

Precipitation method in chemistry is the formation of a solid in a solution through chemical reaction between the soluble regents. When the reaction occurs in liquid, precipitate that formed can be further purified by centrifuge or filtration. This method is particularly suitable for synthesizing stoichiometric electrode materials containing several different elements for Li-ion batteries. A representative example is to prepare

the precursor of layer transition metal oxides $LiMn_xNi_yCo_zO_2$ (denoted as LMO). As demonstrated in Figure 3.2, the carbonate precursor prepared in this study can be formed through co-precipitation of the corresponding metal sulfates of Mn, Ni and Co. Two peristaltic pumps are used to introduce aqueous solutions of metal sources and precipitant simultaneously into the reactor under constant stirring and controlled temperature. After a certain reaction time, the resulting precipitates are filtered and washed with plenty of water.

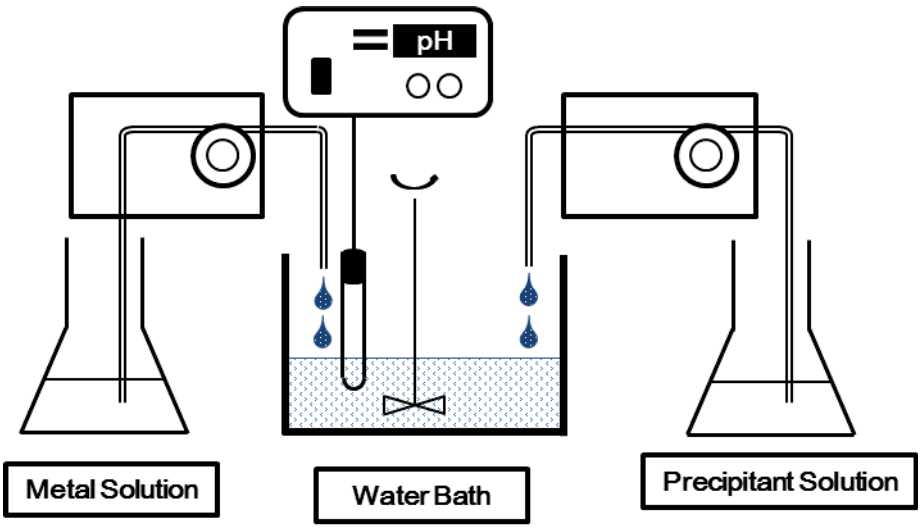


Figure 3.2 Diagram of the co-precipitation synthesis

The co-precipitation methods are introduced to prepare the precursors of nanosized $LiFePO_4$ and over-lithiated transition metal oxide cathode materials. The details are presented in Chapter 4 and Chapter 6.

### 3.2.3 Hydrothermal synthesis

Hydrothermal synthesis is a synthetic method to obtain crystallized substances from a high-temperature solution at a high vapour pressure [228]. This method can be adopted to prepare single crystals that depend on the solubility of chemicals in hot solution under high pressure. The crystal growth is performed inside an apparatus,

usually consisting of a steel vessel called an autoclave. Hydrothermal synthesis is also commonly used to prepare nanostructured materials, as it offers the following attributes [229]: it can create crystalline phases, which are unstable at the melting point temperatures; it is particularly suitable for the growth of crystals while maintaining good control over their morphology and composition; and the as-prepared compounds may have intriguing morphologies such as nanospheres, nanowires, nanotubes, and nanoflowers. Various strategies in the hydrothermal syntheses have been proposed, such as structure-directing agent technique, complexing, templating, nonaqueous solvothermal routes and induced growth through crystal seeds. The disadvantages of these methods are the need for expensive autoclaves, and that the *in-situ* monitoring of crystal growth is impossible. There are three methods when conducting a hydrothermal reaction: the temperature-difference method; the temperature-reduction technique; and the metastable-phase technique.

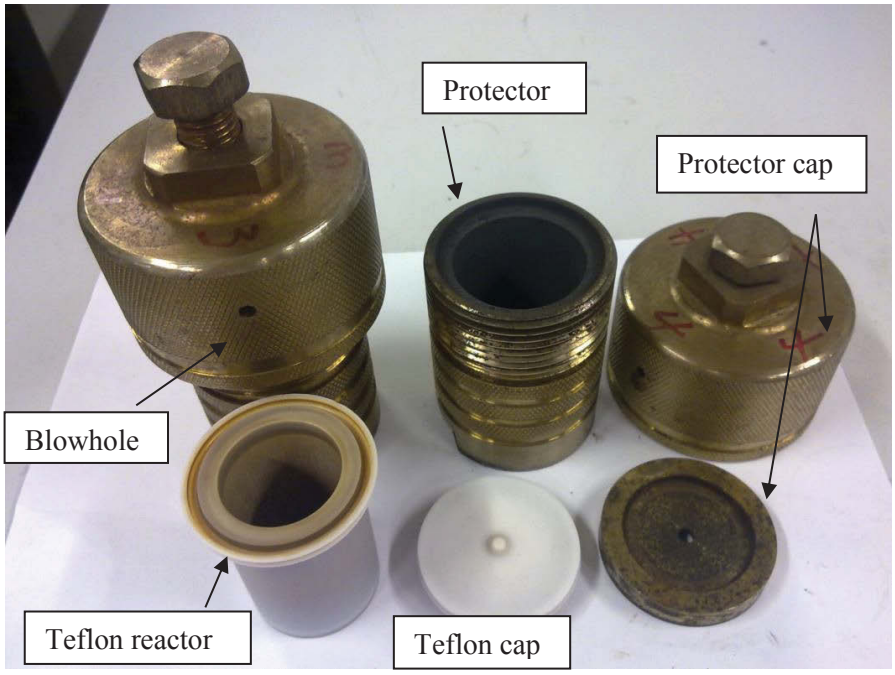


Figure 3.3 Autoclaves for hydrothermal synthesis

As shown in Figure 3.3, the autoclave used in this study consisted of a stainless steel vessel and a Teflon liner, with the capacity of 45 mL. A blowhole located at the top part of the protector released gas to avoid an explosion when the interior pressure was extremely high. Usually, the liquid volume in each experiment was controlled at 1/2-2/3 of the volume of the Teflon reactor.

## 3.3 Methods of Characterization

### 3.3.1 X-ray powder diffraction (XRPD)

X-ray powder diffraction (XRPD) is a characterization technique used for examining the intricate structure of materials. It is used in the determination of crystal structure, qualitative phase identification, quantitative phase analysis, particle size and the study of preferred orientation in crystals [230]. Because the wavelength of X-rays is comparable to the size of atoms, they are ideally suited for probing the structural arrangement of atoms and molecules in a wide range of materials. Each crystal has its unique characteristic X-ray diffraction pattern based on Bragg's law (Equation 3.1).

$$n\lambda = 2d\,sin\,\theta \qquad \text{(Eq. 3.1)}$$

Where $d$ is the interplanar spacing, $\theta$ is the Bragg angle, n is the order of reflection, and λ is the wavelength of the X-rays irradiation.

A diffraction pattern is obtained by measuring the intensity of scattered waves as a function of scattering angle. In a XRPD pattern, the peaks with very strong intensities are known as Bragg peaks, which satisfy the Bragg condition. The crystal size of materials is estimated using the Sherrer equation (Equation 3.2)

$$D = \kappa\lambda/\beta \cos\theta \qquad \text{(Eq. 3.2)}$$

Where κ is the shape factor (normally assigned a value of 0.89); λ is the wavelength of the X-rays irradiation; $\beta$ is the full width at half maximum (FWHM) of the diffraction peak; $\theta$ is the Bragg angle.

In this work, a Siemens D5000 diffractometer was used to obtain the X-ray powder diffraction pattern of the as-synthesized electrode materials. Samples were prepared by mounting the sample powder onto a low-background glass disk. As the XRPD test is non-destructive, the sample powder could be retrieved and used for further tests.

### 3.3.2 Neutron diffraction (ND)

Neutron diffraction is a technique to study the structural features of polycrystalline lithium materials [231]. Through 64 interswe the neutron diffraction data, it is possible to monitor any structure change of electrode materials on a molecular-scale during cycling. The basic principles of ionic mobility in solids and the Rietveld refinement method for neutron diffraction data can be studied. This would further help us in understanding the reaction mechanism within a specific electrochemical reaction. In this PhD work, NPD data were collected on the high intensity powder diffractometer, Wombat, at the Open Pool Australian Light-water (OPAL) reactor facility at the Australian Nuclear Science and Technology Organisation (ANSTO).

### 3.3.3 Field-emission scanning electron microscopy (FESEM)

A scanning electron microscope (SEM) is a type of electron microscope that images a sample by scanning it with a beam of electrons. The electrons interact with the atoms that make up the sample, producing signals that contain information about the sample's surface morphology. FESEM is often used to obtain high magnification

images to examine the details within nanostructured materials (around 1 nm in size). In this work, field-emission electron microscopy (FESEM, Zeiss Supra 55VP) was employed to characterize the morphology and surface structure of as-prepared electrode materials. Its high efficiency in-lens detector produces exceptional quality scanning electron images. The FESEM specimens can be prepared by spreading sample powder directly onto carbon tape or dropping the sample isopropanol solution onto silicon substrates, and then air drying.

### 3.3.4 Transmission electron microscopy (TEM)

Transmission electron microscopy (TEM) is a microscopy technique whereby a beam of electrons is transmitted through an ultra-thin specimen, interacting with the specimen as it passes through, and then an image is formed. High-resolution TEM is capable of imaging at a significantly high resolution, thus some fine features of nanomaterials, such as crystal orientation and electronic structure, can be observed [232]. In the electron diffraction ring pattern, each ring represents the electron diffraction from different lattice planes. The lattice planes were indexed by matching the calculated *d*, the inter-planer spacing, with the standard *d*-spacings from powder diffraction file (PDF) cards. In this work, transmission electron microscopy (TEM, JEOL JEM 2011) was employed to characterize the crystal structure of as-prepared materials. The TEM specimens were prepared by dropping the sample isopropanol solution onto a holey-carbon film on a copper grid by ultrasonication, and then air drying.

### 3.3.5 Thermogravimetric analysis (TGA) and differential scanning calorimetry (DSC)

Thermogravimetry is based on the continuous recording of the mass changes of a sample of material, as a function of a combination of temperature with time in a controlled atmosphere. The measurement is used to determine the thermal stabilities of materials as well as their compositional properties. The most common temperature profiles used in this work are: (1) selecting heating gas (air or high purity Argon), jumping to isotherm and holding at that temperature for a specific time to reach the thermal equilibrium; (2) ramping temperature at a constant rate; and (3) the cooling process.

Differential scanning calorimetry (DSC) is a thermoanalytical technique in which the difference in the amount of heat required to increase the temperature of a sample and reference is measured as a function of temperature. Throughout the experiment more or less heat will need to flow to the sample than the reference to maintain the temperature of both at the same temperature. Therefore, the phase transitions of a specific sample can be determined by whether it undergoes the endothermic (melting) or exothermic (crystallization) processes. By observing the difference in heat flow between the sample and the reference, the amount of heat absorbed or released during such transitions is measured by the differential scanning calorimeters [233]. Thus, DSC may be used to observe some phase changes, even subtle phase changes, which will be of benefit when determining glass transition temperature ($T_g$), melting temperature I, crystallization temperature ($T_c$) and solid-solid transitions. In our work, TGA-DSC (TA Instruments) was conducted with an SDT 2960 simultaneous analyser. For all testing, a platinum crucible was used to load sample powder. Usually, a 10-30 mg sample was needed, depending on the density of the sample.

### 3.3.6 Inductively coupled plasma-mass spectrometry (ICP)

The inductively coupled plasma mass spectrometry is a type of mass spectrometry, that allows the simultaneous detection of almost all elements of the periodic table at concentrations as low as one part in $10^{12}$ (part per trillion). This is achieved by ionizing the sample with inductively coupled plasma and then using a mass spectrometer to separate and quantify those ions [234]. In this study, an ICP-MS (Agilent Technologies 7500cs series) was used to analyse the sample. The sample was introduced into the ICP-MS via a micromist concentric 67 interswe (Glass expansion) and a Scott type double pass spray chamber cooled to 2 °C. The ICP operating parameters and the lens conditions were selected to 67 intersw the sensitivity of a 1 % $HNO_3$ : HCl solution containing 1 ng/mL of Li, Co, Y, Ce and Tl. Calibration curves were constructed and the results were analysed using Agilent Technologies Masshunter software.

### 3.3.7 Fourier transform infrared spectroscopy (FTIR)

Fourier transform infrared spectroscopy (FTIR) is a technique used to obtain an infrared spectrum of absorption of a solid, liquid or gas sample. The term Fourier transform infrared spectroscopy originates from the fact that a Fourier transform is required to convert the raw data into the actual spectrum. In this study, this technique was utilized to analyse any functional groups of the electrode materials. FTIR spectrum was obtained using a Nicolet Magna IR-6700 spectrometer with a DTGS KBr detector. The powder sample was dispersed in KBr discs and all spectra were obtained using 4 $cm^{-1}$ resolution and 64 scans at room temperature.

### 3.3.8 Raman spectroscopy

Raman spectroscopy provides information about molecular vibrations at the atomic scale in inorganic and organic compounds. Raman microscopy is also suited to the study of electrode materials for Li-ion batteries for the following reasons [235]. First, Raman analysis is non-destructive, giving the option of continued examination of the same electrode material. Second, most of the electrode materials, for example, carbonaceous compounds, transition metal oxides and phosphor-olivines, are Raman active materials. Third, Raman spectroscopy has demonstrated itself to be a powerful technique in the study of Li-ion batteries. It can provide information regarding local disorder, changes in bond length, bond angles, coordination, metal oxidation state and cation ordering, which is different from other techniques, such as XRPD, Neutron diffraction and FTIR. And finally, Ramen experiments can be performed without sample preparation, for example, sample coating or a controlled atmosphere. In this work, Raman spectroscopy was performed with a Jobin Yvon HR800 confocal Raman system with a laser wavelength of 632.81 nm on a 300 lines/mm grating at room temperature.

### 3.3.9 X-ray photoelectron spectroscopy (XPS)

X-ray photoelectron spectroscopy (XPS) is a quantitative spectroscopic technique that can measure the surface composition as well as electronic environment nondestructively within a material [236]. It is a surface sensitive spectroscopy technique that allows chemical identification of the elements in the top atomic layers of a sample. It is achieved by recording the binding energies of the electrons associated with these atoms. XPS has wide applications in analysing inorganic compounds, metal alloys, semiconductors, polymers, elements, catalysts, ceramics,

glasses, papers, inks and many others. In this study, XPS (Multilab-2000 Thermo Fisher Scientific) was used to examine the chemical states and binding energies of different elements in the electrode material. More details are presented in Chapter 4 and Chapter 5.

## 3.4 Cell Fabrication

The electrochemical properties of electrode materials were evaluated by assembling CR2032 coin cells or Swagelok cells inside an argon-filled glove box (Mbraun, Unilab, Germany).

### 3.4.1 Electrode fabrication

A mixture of active material, carbon black and polyvinylidene fluoride (PVDF) was added to N-methyl pyrrolidinone (NMP) solution to form a slurry (the ratio among them may have varied in different cases). Then the electrode was made by casting the slurry onto pre-weighted aluminum foil for cathode, or copper foil for anode, by using blade or spatula, and then vacuum dried at 100-110 °C overnight. After the electrode was dried, it was pressed at 1200 kg $cm^{-2}$ and weighed again before transferring it into an argon-filled glove box.

### 3.4.2 Cell assembly

The electrochemical characterization of electrode materials for Li-ion batteries were conducted on CR2032 coin cells or Swagelok cells, which were assembled in an argon-filled glove box using electrode materials as the cathode or anode materials, lithium foil as the counter electrode, and organic carbonates with lithium salts as the electrolyte. In this work, 1M $LiPF_6$ in a mixture of ethylene carbonate, diethyl

carbonate and dimethyl carbonate (EC: DEC: DMC = 1:1 or EC:DMC = 1:1 in some cases) was used. Celgard porous polypropylene membrane was used for all separators. The test cell configuration used in the study is shown in Figure 3.4.

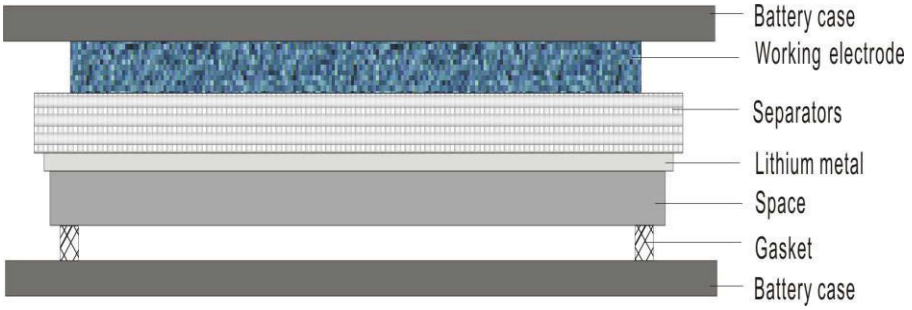


Figure 3.4 Basic configuration of testing cells

## 3.5 Electrochemical Measurements

Electrochemistry is a branch of chemistry that studies chemical reactions that take place in a solution at the interface of an electron conductor and an ionic conductor, and which involve electron transfer between the electrode and the electrolyte or species in solution. The electrochemical reaction occurring inside a battery system can create a voltage difference between the two electrodes, where oxidation and reduction reaction are happening.

### 3.5.1 Cyclic voltammetry

Cyclic voltammetry (CV) is a dynamic potentiodynamic electrochemical measurement for measuring redox events. Specifically, it can be used to study the electrochemical 70intersw of species diffusing to an electrode surface [237]. In a CV experiment, the working electrode potential is ramped linearly versus time, and the working electrode's potential ramp is reversed when CV reaches a set potential. This process can be repeated for several cycles during a single measurement. The CV

curve is obtained by plotting the current at the working electrode versus the applied voltage.

An ideal shape of CV curve for a reversible reaction (as shown in Figure 3.5) consists of two peaks opposite each other, as one process is anodic and the other is cathodic. Through 71interswe CV curves of a working electrode, information about solid-electrolyte interface (SEI) formation, redox potential and reversibility of a specific redox reaction occurring on the electrode interface can be obtained. SEI is typically formed on the surface of carbon materials, at voltages of about 0.8-0.9 V versus $Li^+$ [238]. This layer is electronically insulating, allowing $Li^+$ to permeate but preventing other electrolyte components. SEI plays an essential role in battery performance, as it can protect the electrode from further corrosion when in contact with the electrolyte. In this thesis, CV was conducted on an electrochemical workstation (CHI660C) at different scan rates and voltage ranges at room temperature.

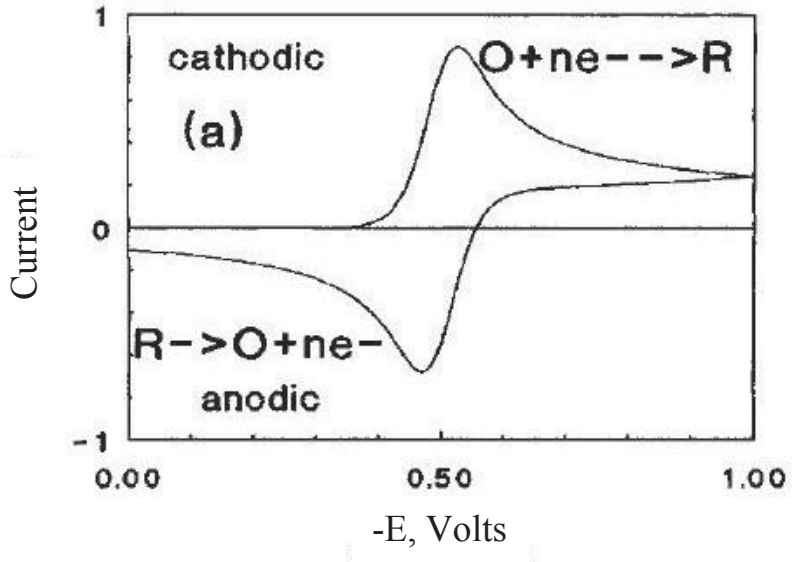


Figure 3.5 Ideal shapes of CV for a reversible, diffusion-controlled reaction [237]

### 3.5.2 Galvanostatic charge-discharge testing

Galvanostatic charge-discharge testing is a commonly used technique to determine the specific capacity, cyclability and coulombic efficiency of electrode materials for Li-ion batteries. Each Neware battery tester (Shenzhen Neware Co., Ltd) can manage tests of up to eight cells simultaneously and individually. Generally, each cell is cycled at a constant current within a certain voltage range, depending on the materials used. The controlling software (Neware BTS Battery Test System) can monitor the accumulated capacity on each cell upon each cycle. Then based on the specific mass of each electrode, the specific charge or discharge capacity of this electrode material can be calculated. When the cell is cycled for a certain cycle, the cyclability and coulombic efficiency can be obtained. More details are presented in the following chapters.

### 3.5.3 Electrochemical impedance spectroscopy

Electrochemical impedance spectroscopy (EIS) has been known to the electrochemistry community for more than a century. Electrochemical systems can be studied with methods based on measuring the impedance response of a system over a range of frequencies [239]. Initially, a small perturbation is applied to the cell system. This perturbation could be of applied potential or applied current. After that, the response to the applied perturbation can be recorded, which can differ in phase and amplitude from the applied signal. The EIS result could allow the analysis of the electrode process in relation to contributions from diffusion, kinetics, double layer, etc.

It is known that the overall cell impedance is a summation of resistance from all the components inside a cell. The impedance within a cell includes: (a) ohmic resistance ($R_\Omega$); (b) charge-transfer resistance ($R_{ct}$); (c) double-layer capacitance ($C_{dl}$) at the solid/liquid interface; and (d) Warburg impedance ($Z_w$). Charge-transfer resistance ($R_{ct}$) originates from the interface between the electrode and electrolyte, and becomes the major barrier to the kinetics of electrochemical reaction. Warburg impedance ($Z_w$) is attributed to the diffusion of ions. Capacitors in equivalent circuits in EIS experiments often do not behave ideally. Instead, they act like a constant phase element (CPE), probably owing to surface roughness.

Often, data obtained by EIS measurement is expressed graphically in a Nyquist plot. A typical Nyquist plot of the working electrode is shown in Figure 3.6.

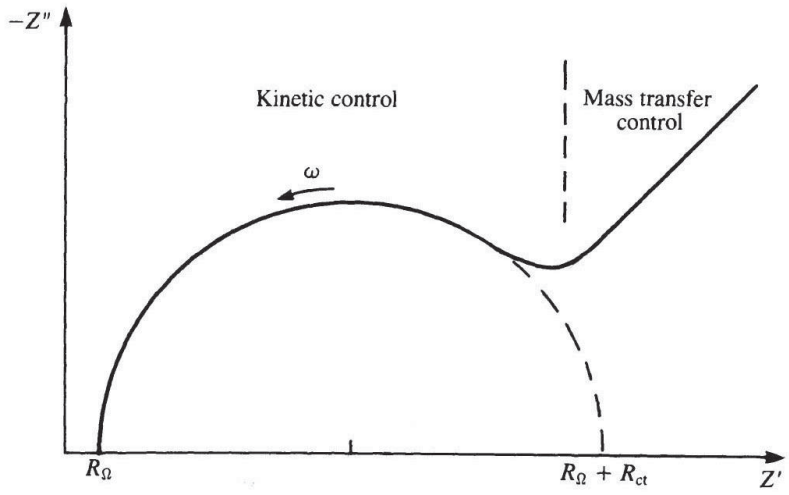


Figure 3.6 Typical Nyquist plot of a simple electrochemical system: $O + ne^- \rightarrow R$

The impedance spectra exhibit a depressed semicircle in the high-frequency range and a sloping line with almost the same gradient in the low-frequency range. The diameter of the semicircle in the medium frequency range could be assigned as $R_{ct}$, and $Z_w$ appears as a slope line with an angle of 45º. Based on the information

obtained from the Nyquist plot, a comparison is usually made between the electrochemical cell and an equivalent electrical circuit, which contains combinations of resistances and capacitances. In this study, EIS was measured on a PARSTAT 2273 Princeton Potentiostat in the frequency range of $10^{5}$-$10^{-2}$ Hz.

# CHAPTER 4 High Capacity Spherical Transition Metal Oxides as Cathode Materials for Li-ion Batteries

## 4.1 Introduction

These reported works have led to the optimization of the electrochemical properties of cathode materials. Recently, over-lithiated layered transition metal oxides have attracted considerable attention. They have higher specific capacity and better thermal stability than conventional layered cathode materials [45, 240].

Several approaches have been introduced to prepare layered transition metal oxides, and their practical specific capacity and capacity retention vary from synthetic procedures. Examples are solid-state reaction [241, 242], sol-gel [243, 244], and the microwave heating method [245]. Among them, the co-precipitation method became very popular, because of the advantages related to homogeneous cation distribution, high purity product and scalability for mass production [246]. Studies show that some variables, such as reaction time/temperature, pH value, stirring speed and the concentration of $NH^{3+}$ are essential in controlling the particle size and morphology of the precursor during the co-precipitation reaction [27, 247, 248]. Generally, two typical processes are involved in the synthetic procedure. The first step is to co-precipitate metal salts with precipitants to form the precursor $M(OH)_2$. The second step is to sinter a stoichiometric mixture of $M(OH)_2$ with a lithium source [248, 249]. However, Mn ions are precipitated as $Mn(OH)_2$ with the valence state of $2^+$, but

gradually oxidized to $Mn^{3+}$ (MnOOH) or $Mn^{4+}$ ($MnO_2$) in this hydroxide co-precipitation method [250]. Therefore, the preparation of a reproducible stoichiometric precursor is a challenge.

In this paper, ammonium carbonate was used to prepare spherical lithium transition metal oxide, $Li[Li_{0.24}Mn_{0.55}Co_{0.14}Ni_{0.07}]O_2$, using a co-precipitation method. This co-precipitation synthesis procedure was carried out under ambient atmosphere, which was markedly different from the commonly used hydroxide co-precipitation method carried out under Ar or $N_2$. Thus, our modified co-precipitation method shows potential for large-scale synthesis of these materials. The physical and structural characteristics and electrochemical properties of $Li[Li_{0.24}Mn_{0.55}Co_{0.14}Ni_{0.07}]O_2$ are subsequently systematically investigated.

## 4.2 Experimental

### 4.2.1 Preparation of spherical $Li[Li_{0.24}Mn_{0.55}Co_{0.14}Ni_{0.07}]O_2$

Step 1: Preparation of the transition metal acetate solution. Transition metal acetate solution (50 mL, 0.5 M) was prepared by dissolving a mixture of $Mn(CH_3COO)_2$, $Ni(CH_3COO)_2$ and $Co(CH_3COO)_2$ into 50 mL of distilled water. The total mole of transition metal acetate was 25 mmol and the mole ratio among Mn:Co:Ni was 0.55:0.14:0.07.

Step 2: The co-precipitation process. The transition metal acetate solution (50 mL, 0.5 M) and a solution of ammonium carbonate (50 mL, 0.5 M) were added simultaneously, via two peristaltic pumps, to a round-bottom flask containing distilled water (100 mL) at 40 °C with vigorous stirring. A rose-pink precipitate

emerged immediately upon stirring. After stirring for 15 h, the resulting precipitate was washed several times with distilled water and dried under a vacuum at 100 °C overnight. Finally, the as-prepared precursor $MCO_3$ (M = combination of Mn, Ni and Co) was ground together with a stoichiometric amount of LiOH $H_2O$, and then sintered at 900 °C in the air.

### 4.2.2 Materials characterization

XRPD data were collected in the $2\theta$ range of $10 \leq 2\theta \leq 80$ ° at a scan rate of 2 °/min. NPD data were subsequently collected on the high intensity powder diffractometer, Wombat. The sample was placed in a 6 mm vanadium can and data were collected between $20 \leq 2\theta \leq 130$ ° using $\lambda = 1.5418(1)$ for 15 minutes and 2.4107(1) Å for 30 minutes, with the wavelength determined using the NIST 660b $LaB_6$ standard reference material. Wombat has a 2D detector allowing data to be collected over the entire $2\theta$ range in one acquisition, and a higher resolution configuration was used for the $\lambda = 2.4107(1)$ Å data collection. Rietveld refinements were carried out using the GSAS [39] suite of programs with the EXPGUI [251] interface. To account for absorption in the NPD data, the Lobanov and Alte da Veiga absorption correction [41] was applied to the Rietveld model.

For elemental analysis, 1 mg of the sample was accurately weighed and dissolved in a mixture of 3 mL concentrated hydrochloric acid and 1 mL concentrated nitric acid. The solution was then diluted until the concentration reached 100 ng $mL^{-1}$ and it was analysed using an ICP-MS. The surface morphology and particle size distribution of $Li[Li_{0.24}Mn_{0.55}Co_{0.14}Ni_{0.07}]O_2$ were observed by FESEM and TEM. XPS was

performed to determine the valence state of the transition metal ions using twin Anode (Al Kα, h$\nu$ = 1486.6 eV) and monochromatic guns.

### 4.2.3 Electrochemical testing

Electrochemical properties of the $Li[Li_{0.24}Mn_{0.55}Co_{0.14}Ni_{0.07}]O_2$ cathode material were evaluated using Swagelok-type cells at room temperature. The Swagelok cells were fabricated inside an argon-filled glove box with layered oxide cathodes, metallic lithium anode, 1M $LiPF_6$ in 1:1 ethylene carbonate and dimethyl carbonate electrolyte, and a Celgard polypropylene separator. The cathodes were made by mixing 75 wt% active material, $Li[Li_{0.24}Mn_{0.55}Co_{0.14}Ni_{0.07}]O_2$, with 20 wt% carbon black and 5 wt% PVDF binder in NMP. The mixed slurry was casted onto a thin Al foil current collector with the cathode loading at about 1.1 mg $cm^{-2}$ and dried at 100 °C overnight. Galvanostatic charge-discharge and cycling tests were performed using a Neware battery tester at various *C* rates (1 *C* = 320 mA $g^{-1}$) in the voltage range of 2.0-4.8 V at room temperature.

## 4.3 Results and Discussion

### 4.3.1 Structural characteristics of $Li[Li_{0.24}Mn_{0.55}Co_{0.14}Ni_{0.07}]O_2$

The elemental analysis shows that the as-prepared sample has a chemical composition of $Li[Li_{0.24(3)}Mn_{0.54(8)}Co_{0.13(8)}Ni_{0.07(1)}]O_2$. This confirms the actual stoichiometry of the sample to be very close to the nominal value with the assumption that it is a pure single-phase compound. This also suggests that the ammonium carbonate can be used as the precipitant to replace the hydroxides. XRPD patterns of the (a) $MCO_3$ precursor and (b) as-prepared $Li[Li_{0.24}Mn_{0.55}Co_{0.14}Ni_{0.07}]O_2$

cathode material are shown in Figure 4.1. The precursor XRPD pattern (Figure 4.1 (a)) can be ascribed to the crystal structure typical of $MnCO_3$ (JCPDS 07-0268) and presumably owing to the combination of transition metals present in the precursor, the XRPD pattern shows slightly broad peak shapes. In contrast, the product diffraction pattern (Figure 4.1 (b)) displays a series of sharp diffraction peaks. On initial inspection, the product adopts a hexagonal layered α-$NaFeO_2$ structure (space group $R\bar{3}m$) characterized by the splitting of the (006)/(012) and (018)/(110) Bragg reflections, indicating a well-defined layered structure [252]. A few weak reflections observed around $2\Theta$ = 20-25° are in accordance with previous reports [63, 253].

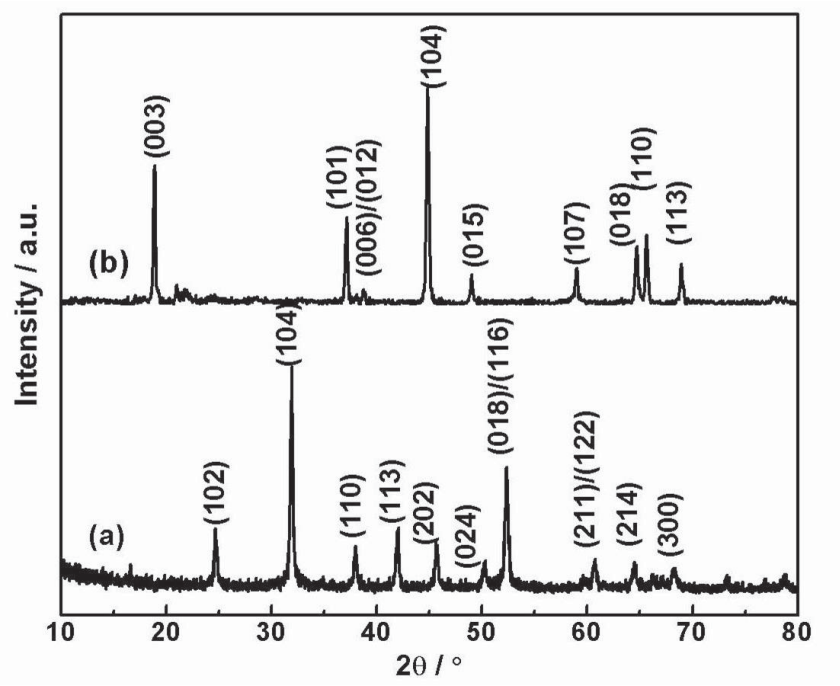


Figure 4.1 XRPD patterns of the (a) precursor $MCO_3$ and (b) $Li[Li_{0.24}Mn_{0.55}Co_{0.14}Ni_{0.07}]O_2$

NPD data collected at λ = 2.4107(1) Å (Figure 4.2 (a)) clearly shows the splitting of the (006) and (012) reflections, further confirming a layered structure as opposed to a spinel-type structure [42]. NPD data were then used to determine the transition metal

ordering within the product, taking advantage of the contrast offered by the nuclear scattering mechanism to the constituent cations in the product. Rietveld analysis was conducted using a modified model of $LiCo_{1/3}Mn_{1/3}Ni_{1/3}O_2$ [ICSD #171750] in $R\bar{3}m$ space-group symmetry that accounted for the used synthetic stoichiometric ratios. The lattice parameters were determined to be $a$ = 2.8386(2) and $c$ =14.1825(17) Å and the $c/a$ ratio of 4.996(7) is close to the previously reported values of related compounds [59]. Numerous permutations to the structural model were fitted against the data, but the best statistical fits with chemically and physically reasonable atomic displacement parameters and site-occupancy factors were found for the model presented in Table 4.1, and the fits to the data are shown in Figure 4.2. The final model shows no indication of nickel, or any other cation, with statistically significant occupation on the lithium site (3*a*), no evidence for lithium-ion vacancies, and the final refined cation occupancies lead to a composition of $Li[Li_{0.24(1)}Mn_{0.53(1)}Co_{0.14(1)}Ni_{0.07(1)}]O_2$.

Table 4.1 Crystallographic parameters of nominally $Li[Li_{0.24}Mn_{0.55}Ni_{0.07}Co_{0.14}]O_2$ determined from neutron powder diffraction data.

| Atom | Wyckoff position | $U_{iso}$ x 100 (Å$^2$) | Site occupancy factor |
|---|---|---|---|
| Li(1) | 3*a* | 4.4(3) | 1 |
| $Co^{3+}$ | 3*b* | 2.1(4)$^{\dagger}$ | 0.16(1)$^{-a}$ |
| $Mn^{4+}$ | 3*b* | 2.1(4)$^{\dagger}$ | 0.53(1)$^{a}$ |
| $Ni^{2+}$ | 3*b* | 2.1(4)$^{\dagger}$ | 0.07(1)$^{-b}$ |
| Li(2) | 3*b* | 2.1(4)$^{\dagger}$ | 0.24(1)$^{b}$ |
| O | 6*c* (*z* = 0.2404(2)) | 4.0(1) | 1 |

Refined composition $Li[Li_{0.24(1)}Mn_{0.53(1)}Ni_{0.07(1)}Co_{0.14(1)}]O_2$ in space group $R\bar{3}m$ with $a$ = 2.8386(2) and $c$ =14.1825(17) Å. The statistics of the fit were $R_p$ = 2.89 %, $wR_p$ = 3.92 %, $\chi^2$ = 1.63 for 20 variables.

$^{\dagger}$ Parameters constrained to be equal
$^{a,b}$ Constrained occupancies with either $^{a}$ or $^{b}$ refining during a procedure

The Rietveld model does not account for two broad non-overlapping reflections, observed in the NPD data, $2\theta$ = 45.2 º (which is equivalent to $2\theta$ = 70 º at λ = 2.4107(1) Å) and $2\theta$ = 104.3 º in the λ = 1.5418(1) Å dataset. There are two possible approaches to account for these reflections. The first is that excess lithium is used in the synthesis and the slight reduction in the refined manganese content relative to the expected value suggests the presence of the $Li_2MnO_3$ impurity phase, which may be owing to the weak reflections observed around 20 ≤ $2\theta$ ≤ 25 ° in the XRPD data (Figure 4.1 (b)). The inclusion of a highly constrained $Li_2MnO_3$ model into the Rietveld analysis results in a quantity of 10.7(15) wt% of $Li_2MnO_3$ in the as-prepared material (for simplicity, nominal formula $Li[Li_{0.24}Mn_{0.55}Co_{0.14}Ni_{0.07}]O_2$ was used for the following discussions). The second approach is to consider the broad reflections as superlattice reflections from a phase-pure layered compound where these reflections are associated with stacking faults along the *c*-axis direction (and/or cation ordering within layers) [253].

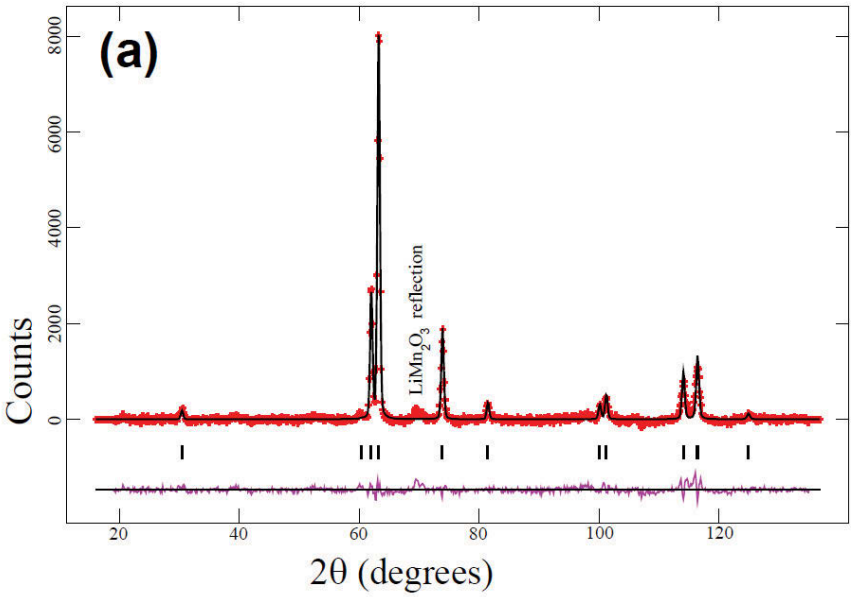

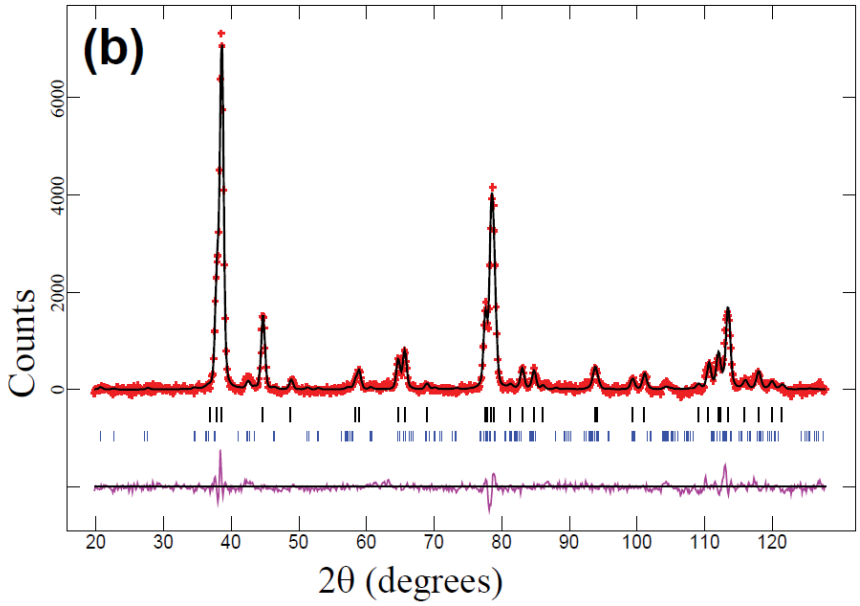


Figure 4.2 The Rietveld-refined fit of the $Li[Li_{0.24(1)}Mn_{0.53(1)}Ni_{0.07(1)}Co_{0.14(1)}]O_2$ model using NPD data at (a) $\lambda$ = 2.4107(1) Å and (b) $\lambda$ = 1.5418(1) Å. The red crosses represent collected data, the black line through the crosses the calculated Rietveld model, and the purple line below is the difference between the data and calculated model. The vertical black lines are reflection markers for $Li[Li_{0.24(1)}Mn_{0.53(1)}Ni_{0.07(1)}Co_{0.14(1)}]O_2$ (black) and $LiMn_2O_3$ [blue in (b)]. The statistics of the fit for (b) using a two-phase model were $R_p$ = 2.89%, $wR_p$ = 3.92%, $\chi^2$ = 1.63 for 20 variables.

To determine the approach that is representative of this sample, TEM analysis was conducted on the as-prepared $Li[Li_{0.24}Mn_{0.55}Co_{0.14}Ni_{0.07}]O_2$ sample. The HRTEM image Figure 4.3 (b) shows the presence of both $Li[Li_{0.24}Mn_{0.55}Co_{0.14}Ni_{0.07}]O_2$ and $Li_2MnO_3$ phases, with their assigned *d*-spacing values of 5.1 nm and 2.5 nm respectively. Similarly, the corresponding selected area electron diffraction (SAED) pattern show two sets of electron diffraction spots with minimal evidence of further superlattice reflections in the particles studied. This provides evidence that the two-

phase approach is valid. In addition, the fitting statistics of the two-phase structural model with a single-phase model using the neutron diffraction data at λ = 1.5418(1) Å were compared. In all attempted permutations, we find that the two-phase model shows a better fit to the data with a smaller number of parameters than the single-phase model. Where the statistics of the fit of the single-phase model approach the two-phase model, we find unrealistic atomic parameters in the single-phase model (e.g. negative ADPs). Moreover, the approximate average crystallite-size determined from peak-profile functions (particle-size broadening effect) was found to be around 120 nm using the higher resolution λ = 2.4107(1) Å NPD dataset, which is in accordance with the results from Figure 4.3 (a).

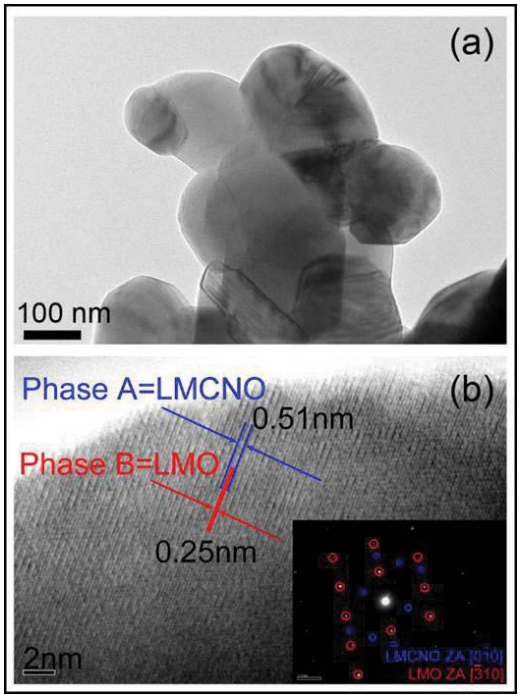


Figure 4.3 (a) TEM and (b) HRTEM images of $Li[Li_{0.24}Mn_{0.55}Co_{0.14}Ni_{0.07}]O_2$, the insert in (b) is the corresponding selected area electron diffraction pattern. The *d*-spacings and SAED pattern of the two phases are indicated (Phase A is $Li[Li_{0.24}Mn_{0.55}Co_{0.14}Ni_{0.07}]O_2$ and phase B is $Li_2MnO_3$)

### 4.3.2 Morphology and surface characteristics of the precursor and $Li[Li_{0.24}Mn_{0.55}Co_{0.14}Ni_{0.07}]O_2$

Morphologies of the metal carbonate precursor and final sintered product were examined by FESEM (Figure 4.4).

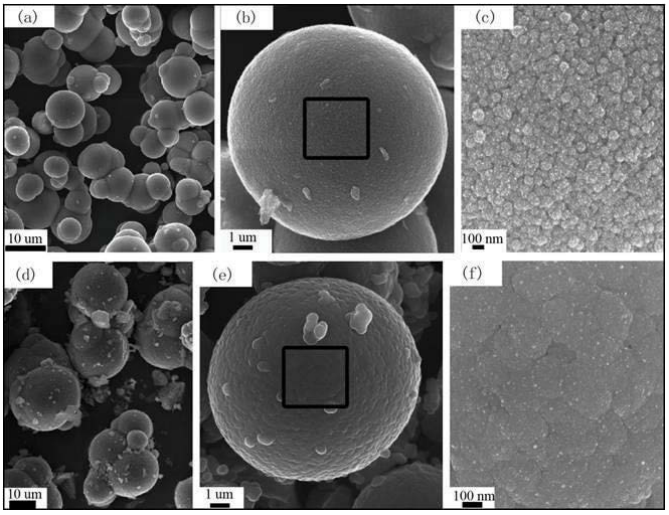


Figure 4.4 FESEM images of (a)-(c) precursor and (d)-(f) $Li[Li_{0.24}Mn_{0.55}Co_{0.14}Ni_{0.07}]O_2$ at different magnifications

As shown in Figure 4.4 (a), the precursor consists of spherical particles with a relatively narrow particle size distribution varying from 5 to 10 μm. Figure 4.4 (b) shows a typical spherical particle at higher magnification, with the enlarged view of the rectangular area shown in Figure 4.4 (c). Each spherical particle is composed of small primary particles. In particular, it is worth noting that these primary particles still have quasi-spherical shapes with the size around 100 nm. It is likely that these smaller primary particles were generated as soon as the materials were introduced into the co-precipitation system and acted as the nuclei. These newly-formed nuclei agglomerated to form bigger secondary particles during the stirring. Here, we illustrate that ammonium carbonate acted not only as the precipitant but also as the

complexing agent during the co-precipitation process. Figure 4.4 (d)-(f) reveal that after sintering, the spherical morphology of $Li[Li_{0.24}Mn_{0.55}Co_{0.14}Ni_{0.07}]O_2$ is maintained.

Valence states of the transition metal cations were analysed before and after calcinations using XPS on both the $MCO_3$ precursor and final product. The 2p core-level XPS spectra of Ni ions are shown in Figure 4.5 (a). For the spectrum of the precursor, Ni $2p_{3/2}$ and Ni $2p_{1/2}$ peaks at 856.66 eV and 874.68 eV correspond to $Ni^{2+}$, whereas a small peak at 862.2 eV is considered to be a satellite peak. Similarly, peaks found at 855.64 eV and 873.21 eV in the spectrum of the sintered product correspond to $Ni^{2+}$, where a satellite peak at 862 eV can also be detected. The appearance of satellite peaks could be ascribed to multiple splitting in the energy bands [254]. Figure 4.5 (b) displays the 2p core-level XPS spectra of Co ions in the precursor and the as-prepared $Li[Li_{0.24}Mn_{0.55}Co_{0.14}Ni_{0.07}]O_2$. The peak at 782.14 eV and 798.11 eV in the precursor can be assigned to $Co^{2+}$, while peaks with binding energies of 780.87 eV and 795.91 eV are attributed to $Co^{3+}$. In addition, as shown in Figure 4.5 (c), binding energies of Mn $2p_{3/2}$ and Mn $2p_{1/2}$ in the precursor are 642.12 eV and 654.18 eV, respectively; while slight shifts of the binding energy were found in the final sample. By comparing the binding energies of Mn $2p_{3/2}$ and Mn $2p_{1/2}$ in the present analysis and the literature reports [255], it can be concluded that Mn ions in the precursor and the final product are in +2 and +4 valence states respectively. In summary, the valence state of Ni, Co and Mn ions in the precursor are +2, indicating that ammonium carbonate as a precipitant does prevent $Mn^{2+}$ from oxidizing. After

high temperature calcinations, the valence states of Ni, Co and Mn in the final product have changed to +2, +3 and +4, respectively.

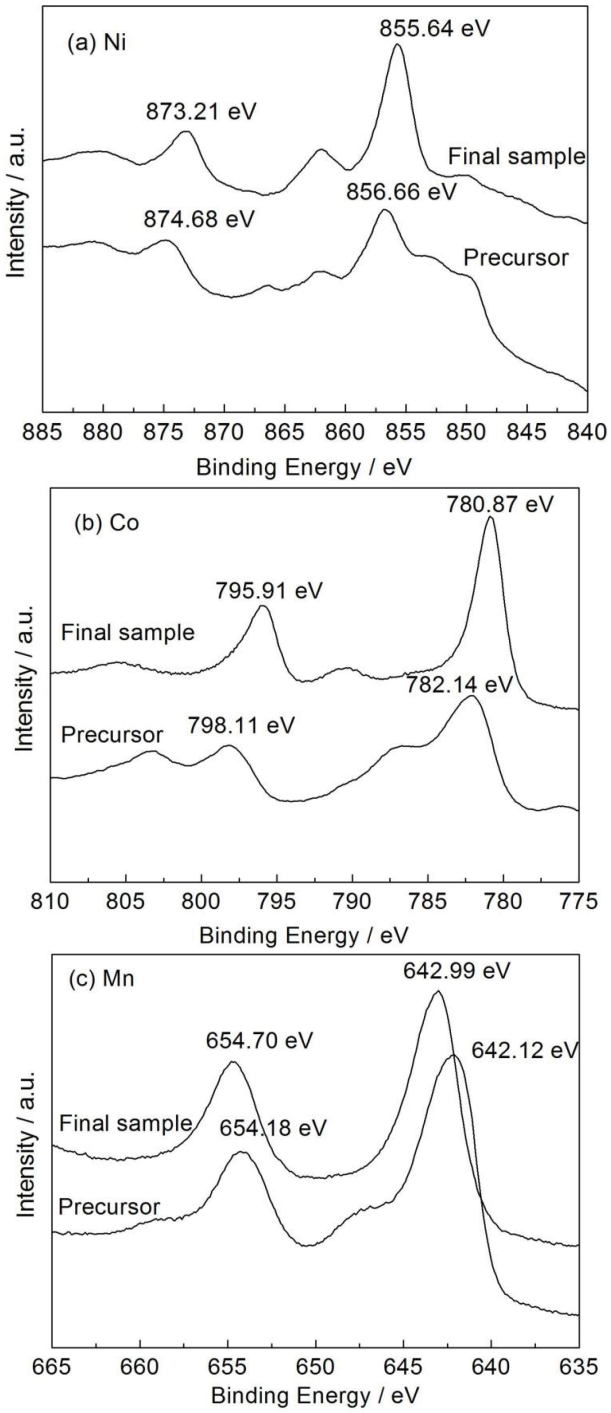


Figure 4.5 XPS 2p spectra of (a) Ni, (b) Co and (c) Mn ions of the precursor and $Li[Li_{0.24}Mn_{0.55}Co_{0.14}Ni_{0.07}]O_2$

### 4.3.3 Charge-discharge mechanisms of $Li[Li_{0.24}Mn_{0.55}Co_{0.14}Ni_{0.07}]O_2$ cathode materials

The theoretical capacity of $Li[Li_{0.24}Mn_{0.55}Co_{0.14}Ni_{0.07}]O_2$ is determined to be 375.6 mAh $g^{-1}$ based on the full extraction of lithium ions from this cathode material. Figure 4.6 shows the first and second charge-discharge profiles of $Li[Li_{0.24}Mn_{0.55}Co_{0.14}Ni_{0.07}]O_2$ cells in the voltage window of 2.0-4.8 V at *C*/20. As demonstrated in Figure 4.6, the as-prepared $Li[Li_{0.24}Mn_{0.55}Co_{0.14}Ni_{0.07}]O_2$ cathode material delivers an initial charge and discharge capacity of 311.8 and 264.6 mAh $g^{-1}$ respectively, resulting in an irreversible capacity loss ($C_{irr}$) of 47.2 mAh $g^{-1}$. The comparison in Table 4.2 shows that the as-prepared sample exhibits quite a low $C_{irr}$ value and high capacity retention, relative to similar compounds reported in the literature.

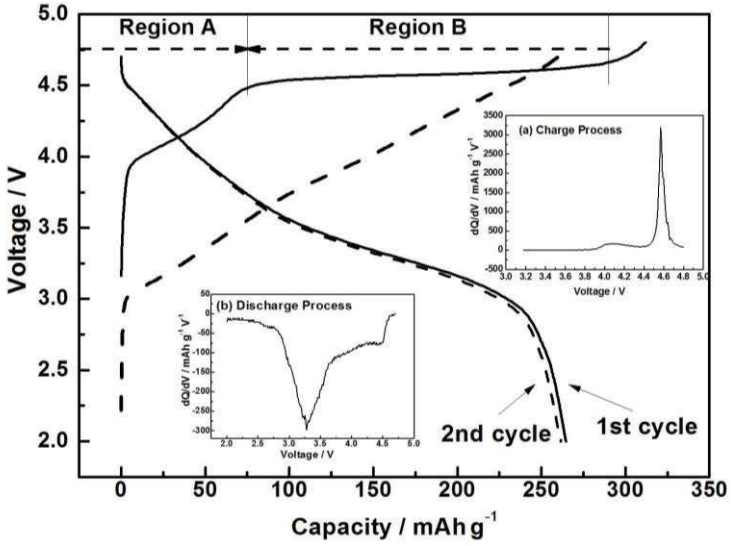


Figure 4.6 The first and the second charge-discharge profiles of $Li[Li_{0.24}Mn_{0.55}Co_{0.14}Ni_{0.07}]O_2$ cells with two insets showing the differential capacity plot of the initial (a) charge and (b) discharge process

Table 4.2 Comparison of the electrochemical cell data from relevant recent publications and results from this work

| Materials | Test condition [a] | Initial capacity (mAh $g^{-1}$) | | IRC [b] (mAh $g^{-1}$) | Capacity fade per cycle (%) | Refs |
|---|---|---|---|---|---|---|
| | | $Q_c$ | $Q_d$ | | | |
| $0.3Li_2MnO_3 \cdot 0.7\ Li\ Mn_{0.5}Ni_{0.5}O_2$ | 2.0-5.0 V | 352 | 287 | 65 | 1.04 | [46] |
| $Li_{1.17}Mn_{0.33}Co_{0.5}O_2$ | *C*/20 2.0-4.8 V | 333 | 269 | 64 | n/a | [49] |
| $Li_{1.14}Mn_{0.34}Co_{0.39}Ni_{0.13}O_2$ | | 316 | 233 | 83 | | |
| $Li_{1.2}Mn_{0.47}Co_{0.27}Ni_{0.06}O_2$ | | 334 | 254 | 80 | | |
| $Li_{1.1}Mn_{0.43}Co_{0.23}Ni_{0.23}O_2$ | *C*/20 2.0-4.8 V | 290 | 227 | 63 | 0.42 | [52] |
| $Li_{1.17}Mn_{0.58}Ni_{0.25}O_2$ | | 309 | 249 | 60 | 0.79 | |
| $Li_{1.2}Mn_{0.6}Ni_{0.2}O_2$ | 10 mA $g^{-1}$ 2.5-4.6 V | n/a | 267 | n/a | n/a | [53] |
| $Li_{1.2}Mn_{0.54}Co_{0.13}Ni_{0.13}O_2$ | *C*/20 2.0-4.8 V | 328 | 253 | 75 | 0.3 | [59] |
| $Li_{1.2}Mn_{0.54}Co_{0.13}Ni_{0.13}O_2$ | *C*/20 2.0-4.8 V | 332 | 252 | 80 | 0.24 | [56] |
| $Li_{1.2}Mn_{0.54}Co_{0.13}Ni_{0.13}O_2$ | 18 mA $g^{-1}$ 2.0-4.8 V | 325 | 249 | 75.5 | 0.37 | [62] |
| $Li_{1.2}Mn_{0.54}Co_{0.13}Ni_{0.13}O_2$ | *C*/5 2.0-4.8 V | 310 | 230 | 80 | 0.64 | [61] |
| $Li_{1.17}Mn_{0.58}Ni_{0.25}O_2$ | 12.5 mA $g^{-1}$ 2.0-4.8 V | n/a | 250 | n/a | 0.33 | [54] |
| $Li_{1.2}Mn_{0.6}Ni_{0.2}O_2$ | 20 mA $g^{-1}$ 2.0-4.8 V | n/a | 219 | n/a | n/a | [245] |
| $Li_{1.13}Mn_{0.37}Co_{0.4}Ni_{0.1}O_2$ | *C*/20 2.0-4.8 V | 320 | 239 | 81 | 0.63 | [60] |
| $Li_{1.2}Mn_{0.47}Co_{0.27}Ni_{0.06}O_2$ | | 334 | 254 | 80 | 0.63 | |
| $Li_{1.2}Mn_{0.56}Co_{0.07}Ni_{0.17}O_2$ | | 328 | 254 | 74 | 0.47 | |
| $Li_{1.16}Mn_{0.428}Co_{0.106}Ni_{0.306}]O_2$ | 20 mA $g^{-1}$ 2.0 -4.6 V | 291 | 203 | 87.7 | 0.1 | [256] |
| $Li_{1.24}Mn_{0.55}Co_{0.14}Ni_{0.07}]O_2$ | *C*/20 2.0-4.8 V | 311 | 264 | 47 | 0.19 | This work |

[a] All tests were carried out at room temperature
[b] Initial irreversible capacity

The electrochemical reaction of the first charge process can be divided into two dominant stages: region A and B; while the discharge process exhibits a sloping profile. The two insets (a) and (b) in Figure 4.6 show the corresponding differential capacity plot of the charge and discharge process respectively. Upon charging, a broad peak between 4.0 and 4.4 V and a sharp peak at 4.5 V were found, which are associated with the electrochemical reaction in region A and B respectively. Specifically, the sloping region A is attributed to the removal of lithium from the $Li[Li_{0.24}Mn_{0.55}Co_{0.14}Ni_{0.07}]O_2$ electrode with oxidation of transition metal ions (Co and Ni), with Mn remaining as $Mn^{4+}$. Region B exhibits a distinctly long voltage plateau at 4.5 V, and is mainly owing to the partial elimination of oxygen from the layered lattice as presumably $Li_2O$. This voltage plateau disappears in subsequent charge profiles, thereby revealing that the oxygen loss is an irreversible process. Similar phenomena found in previous reports demonstrated the redox reaction of $Li_2MnO_3$ in the initial charge-discharge process [257-259]. The dQ/dV plot of the discharge process shows a main peak at 3.3 V and a side peak at 4.5 V, corresponding to the reduction of Mn and Ni respectively.

To explain the origin of the high specific capacity for $Li[Li_{0.24}Mn_{0.55}Co_{0.14}Ni_{0.07}]O_2$ cathodes, XPS measurements were conducted of $Li[Li_{0.24}Mn_{0.55}Co_{0.14}Ni_{0.07}]O_2$ electrodes in the pristine, discharged and charged states. As shown in Figure 4.7 (a), upon charging, the core-level Ni $2p_{3/2}$ and Ni $2p_{1/2}$ XPS spectra move to higher binding energies, indicating the oxidation of $Ni^{2+}$ to $Ni^{4+}$. Upon discharging, the Ni $2p_{3/2}$ and Ni $2p_{1/2}$ peaks at 856.5 eV and 875.4 eV correspond to $Ni^{3+}$, implying the reduction of $Ni^{4+}$ to $Ni^{3+}$. Similar phenomena have been reported by Sivapakash [260], who also demonstrated further reduction of $Ni^{4+}$ to $Ni^{2+}$ when deeply

discharging the cathode to 1.45 V. Figure 4.7 (b) shows the XPS spectra of Co ions at different charge states. During the intercalation and deintercalation processes, the binding energy of Co $2p_{3/2}$ and Co $2p_{1/2}$ remains the same. However, during charging, there is a strong decrease in the satellite peak area, indicating the oxidation of $Co^{3+}$, and a similar satellite peak could be found in the discharged $Li[Li_{0.24}Mn_{0.55}Co_{0.14}Ni_{0.07}]O_2$ electrode, showing the reversibility of this process [261]. As illustrated in Figure 4.7 (c), the binding energies of Mn $2p_{3/2}$ and Mn $2p_{1/2}$ in the charged electrode are found to be at 643.15 eV and 654.82 eV, which are remarkably close to the values found in the pristine electrode. This reveals that the valence state of Mn ions does not change during the charge process. On the contrary, obvious shifts of Mn $2p_{3/2}$ and Mn $2p_{1/2}$ peaks can be found in the XPS spectrum of the discharged electrode, with the binding energies at 641.8 eV and 653.8 eV respectively. This phenomenon corresponds with the reduction of $Mn^{4+}$ to $Mn^{3+}$, illustrating that $Li_2MnO_3$ (shown to exist by the use of the two-phase model) can participate in the charge-discharge process, and the specific capacity of $Li[Li_{0.24}Mn_{0.55}Co_{0.14}Ni_{0.07}]O_2$ is remarkably increased by the $Mn^{4+}/Mn^{3+}$ couple. This conclusion is also supported by the existence of the strong reduction peak centred at 3.3 V in the differential plots.

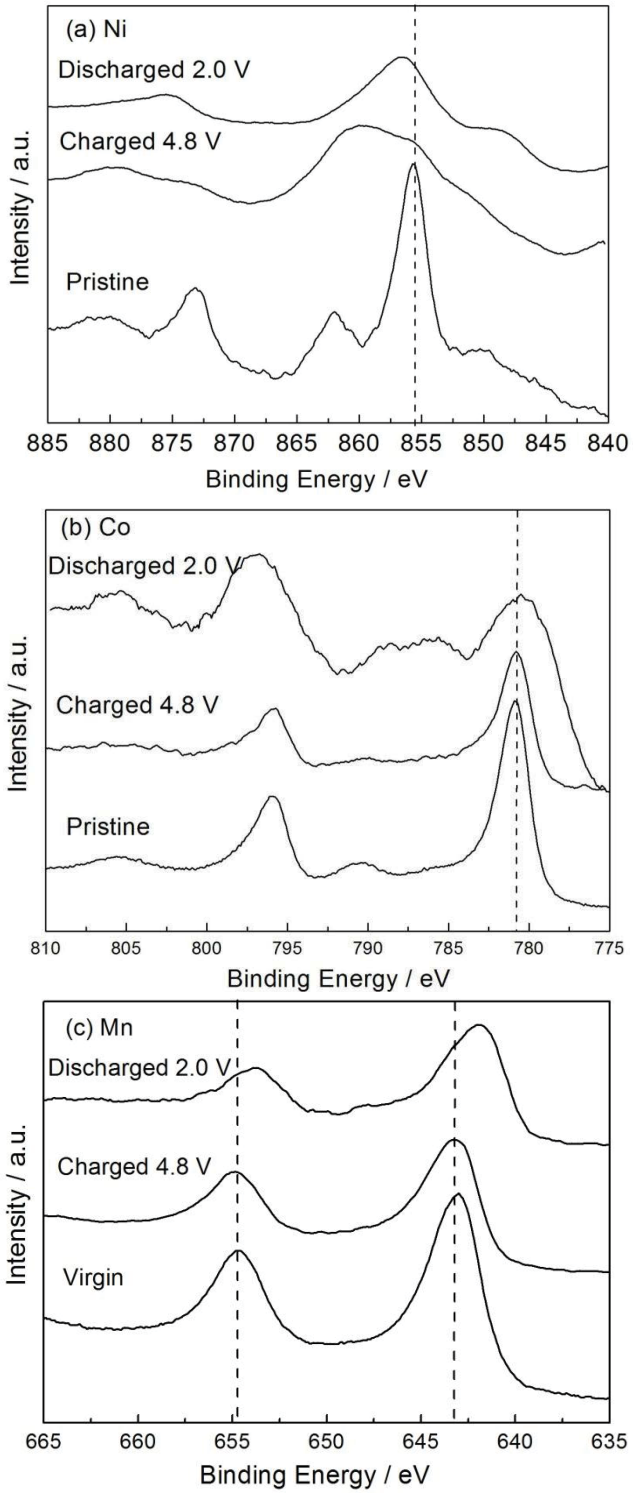


Figure 4.7 XPS 2p spectra of (a) Ni, (b) Co and (c) Mn ions of $Li[Li_{0.24}Mn_{0.55}Co_{0.14}Ni_{0.07}]O_2$ electrode at pristine, fully charged and discharged states

### 4.3.4 Electrochemical performance of $Li[Li_{0.24}Mn_{0.55}Co_{0.14}Ni_{0.07}]O_2$ cathode materials

Figure 4.8 presents the cycling performance and rate capability of the $Li[Li_{0.24}Mn_{0.55}Co_{0.14}Ni_{0.07}]O_2$ cathode material.

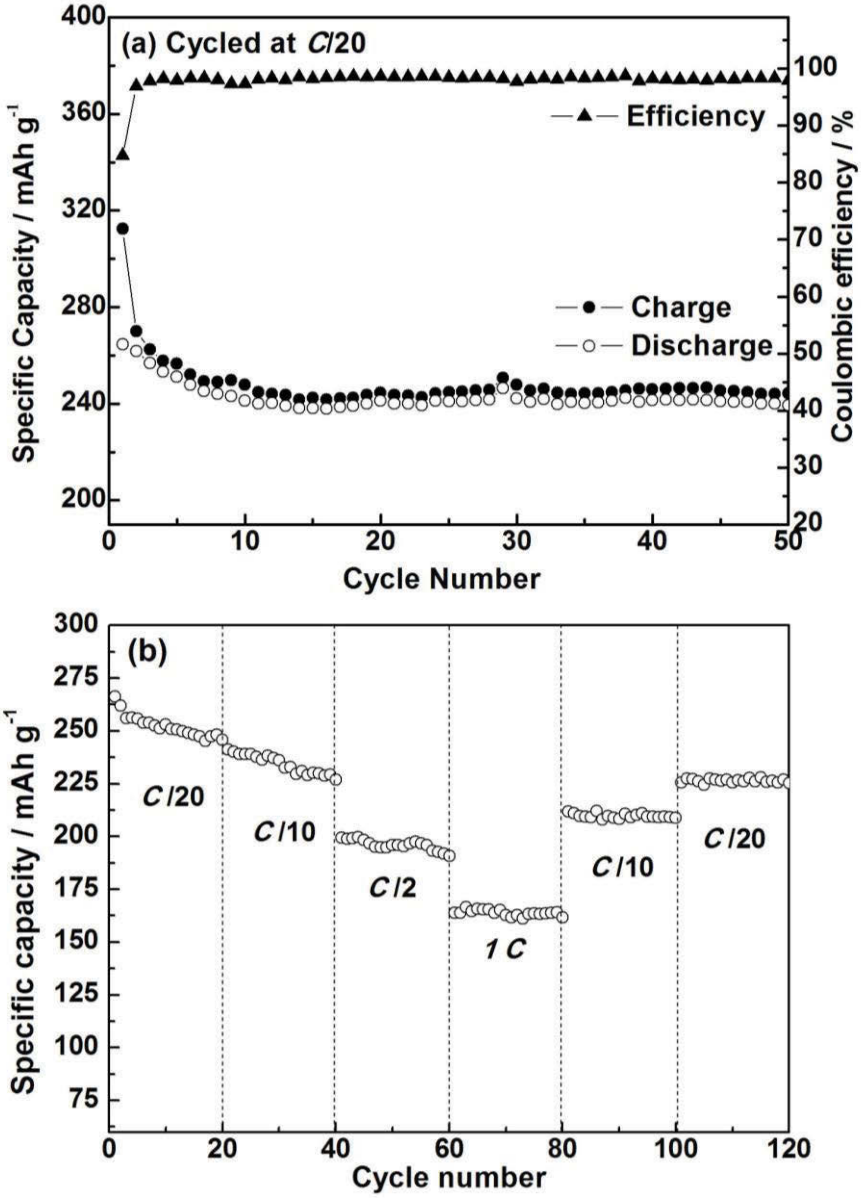


Figure 4.8 (a) Cycling and (b) rate performance of $Li[Li_{0.24}Mn_{0.55}Co_{0.14}Ni_{0.07}]O_2$ cells in the voltage range of 2.0-4.8 V

As shown in Figure 4.8 (a), the $Li[Li_{0.24}Mn_{0.55}Co_{0.14}Ni_{0.07}]O_2$ cell exhibits excellent cycling stability and reversibility, with a capacity retention of 90.4 % and an average coulombic efficiency of 98 % after 50 cycles. The rate performance of the $Li[Li_{0.24}Mn_{0.55}Co_{0.14}Ni_{0.07}]O_2$ cell subjected to 20 charge-discharge cycles at different *C*-rates are shown in Figure 4.8 (b). This material exhibits a high capacity retention and good rate capability, particularly at higher *C*-rates. The discharge capacities of the $Li[Li_{0.24}Mn_{0.55}Co_{0.14}Ni_{0.07}]O_2$ cell are 245.8, 227, 190.9 and 161.8 mAh $g^{-1}$ after 20 cycles at *C*/20, *C*/10, *C*/2 and 1 *C* respectively. In addition, when a lower *C*-rate was applied, the specific capacity of $Li[Li_{0.24}Mn_{0.55}Co_{0.14}Ni_{0.07}]O_2$ cathode material can be recovered, reaching 208.9 and 225.2 mAh $g^{-1}$ at *C*/10 and *C*/20 respectively. The outstanding electrochemical performance of the spherical $Li[Li_{0.24}Mn_{0.55}Co_{0.14}Ni_{0.07}]O_2$ cathode material might be attributed to its well-controlled morphology that originates from the co-precipitation method.

## 4.4 Conclusions

A modified co-precipitation method was used to synthesize spherical $Li[Li_{0.24}Mn_{0.55}Co_{0.14}Ni_{0.07}]O_2$ particles with a controlled size in the range of 5-10 μm, which are highly applicable as cathode materials in lithium-ion batteries. Rietveld analysis indicates a layered structure with lattice parameters $a$ = 2.8386(2) and $c$ = 14.1825(17) Å. A single mixed cation site (3*b*) is found with no evidence of lithium-ion vacancies resulting in a final refined composition of $Li[Li_{0.24(1)}Mn_{0.53(1)}Co_{0.14(1)}Ni_{0.07(1)}]O_2$, which is consistent with the nominal formula. XPS and SEM analysis suggest that ammonium carbonate has a significant effect on controlling the morphology of the precursor as well as preventing the transition metal

ions from oxidation. $Li[Li_{0.24}Mn_{0.55}Co_{0.14}Ni_{0.07}]O_2$ cathode materials exhibit quite low irreversible capacity loss, high specific capacity, satisfactory cyclability and rate capability, which is suitable for large-scale application. The presence of the secondary $Li_2MnO_3$ phase in the final product, revealed by Rietveld and TEM analysis, transforms this electrode into a composite system, with each component contributing to the high specific capacity of the synthesized $Li[Li_{0.24}Mn_{0.55}Co_{0.14}Ni_{0.07}]O_2$ cathode material.

# CHAPTER 5 Lithium Iron Phosphate as Cathode Material for Li-ion Batteries

## 5.1 Introduction

In electrical and hybrid electrical vehicles (Evs/HEVs), backup power systems and other energy storage devices, $LiFePO_4$ has fulfilled most of the principal requirements, i.e. non-toxicity, low cost, safety, higher power/energy density, excellent rate capability and long cycle life [262, 263]. However, lithium iron phosphate suffers from two main disadvantages: low electronic conductivity and slow lithium ion diffusion coefficient [87], resulting in poor electrochemical performance, especially poor rate capability. In order to successfully utilize lithium iron phosphate as cathode material in Li-ion batteries for Evs/HEVs or other high power applications, researchers have been committed to developing better solutions to optimize its properties. Among these techniques, coating or embedding with conductive layers, particularly from carbon [76, 94], has stood out as a reliable method to improve its electronic conductivity. With regard to the carbon effects, more attention has been focused on how to perfect the carbon coating layer using different primary carbon sources and how to achieve the most efficient coating method, because this conductive layer undoubtedly plays an important role in improving conductivity and facilitating the delithiation and lithiation processes [77, 264]. However, when carbon contributed as part of the cathode materials, would decrease the theoretical capacity of cathode material, many researchers have tried to reduce the carbon content to reach higher energy density and tap density [85, 265].

Doeff et al. [266] reported that the morphology and characteristic of residual carbon can affect the electrochemical performance of $LiFePO_4$. For instance, the higher content of carbon $sp^2$ character in the coating, the better are the electrochemical properties that can be expected. Recently, there are many reports on the synthesis of $LiFePO_4$ by using polymeric additive (PA), including polyaniline (Pan) [92], polypyrrole (Ppy) [93], polyethylene [95] and polyetheramine [267]. These polymer additives not only possess electrochemical activity by themselves, but also form a carbonaceous deposit on the surfaces of particles, to suppress the crystal growth and the content of impurity phase ($Li_3Fe_2(PO_4)_3$). Therefore, polymers have become an ideal substitute for other carbon sources in the synthesis of $LiFePO_4$.

In addition, the low Li-ion diffusion rate can be overcome by particle size minimization, because a shorter lithium ion transport length and lower electrode resistance can be achieved [102, 119]. In this regard, several methods have been proposed to minimize the particle size of $LiFePO_4$, for instance, sintering at lower temperature [87], chemical vapour deposition [98], mechanical activation [119, 125], co-precipitation in an aqueous medium [268, 269] and hydrothermal synthesis [270].

Based on the previous research work, we believe the electrochemical performance of $LiFePO_4$ can be improved by forming a conductive layer, while simultaneously minimizing their particle size. In this paper, the co-precipitation method was chosen as the synthetic method for the precursor, because of the feasibility of controlling the morphology and the accessibility of cheap raw materials. At the same time, aniline monomer, a highly conductive polymer, was chosen as the carbon source during polymerization. Nanocrystalline $LiFePO_4$ with carbon coating layer was prepared by a reduction process.

## 5.2 Experimental

### 5.2.1 Material synthesis

$FePO_4$/Pan (polyaniline) composite was synthesized through a spontaneous precipitation and polymerization in an aqueous solution. Typically, stoichiometric $NH_4H_2PO_4$ (0.4671 g), aniline monomer (200 μl) and HCl (37 %, equimolar with aniline) were dissolved in 50 mL distilled water. Then, $H_2O_2$ (4 mL, 50 wt%) and $FeSO_4$ $7H_2O$ (1.1233 g) were dissolved in 50 ml $H_2O$ then added to the above-mentioned solution under vigorous stirring at room temperature, and a black precipitate emerged. After stirring for 5 h, the resultant precipitant was washed three times with distilled water, filtered and dried at 50 ºC overnight in a vacuum. To synthesize $LiFePO_4$, $LiCH_3COO$ (0.1 mol), as-prepared $FePO_4$/Pan precursor (0.1 mol), and L-ascorbic acid (VC, 0.06 mol) were dispersed in ethanol and ultrasonicated for 30 min. After stirring the suspension for 5 h at 60 °C, the alcohol-insoluble amorphous precipitate was separated by filtration, washed with distilled water and dried at 50 °C overnight in a vacuum. Finally, crystalline $LiFePO_4$ was obtained by sintering the amorphous $LiFePO_4$ at 350 ºC for 5 h, and then at 650 ºC for 15 h.

### 5.2.2 Physical and structural characterization

TG-DSC was conducted to determine the sample's carbon content between 35 ºC and 800 °C at a heating rate of 5 °C $min^{-1}$ under argon atmosphere. XPRD was conducted to determine the phase of the precursors and the as-prepared $LiFePO_4$. Raman spectroscopy was performed to confirm the presence of residue carbon. XPS was

performed to confirm the oxidation state in the final product. The surface morphology and particle size distribution were observed using FESEM and TEM.

### 5.2.3 Electrochemical testing

The electrochemical characterization of $LiFePO_4$ was conducted on CR2032 coin cells, which were assembled in an argon-filled glove box using $LiFePO_4$ as the cathode material, lithium foil as the counter electrode, and 1M $LiPF_6$ in a mixture of EC: DMC = 1:1 as the electrolyte. After dispersing 80 wt% active material, 12 wt% carbon black, and 8 wt% PVDF in NMP to form a slurry, the cathode was made by spreading the slurry onto Al foil. After vacuum drying at 110 °C, the coated electrodes were pressed at 1200 kg $cm^{-2}$. CV was conducted in the voltage range of 2.5-4.2 V at different scan rates. The galvanostatic charge-discharge tests were performed at various current densities in the range of 2.0-4.2 V at room temperature.

## 5.3 Results and Discussion

### 5.3.1 Structural analysis and surface characterization of the as-prepared $LiFePO_4$

The XRPD patterns of the as-obtained $FePO_4$ are shown in Figure 5.1. The diffraction line (a) indicates that the $FePO_4$ as initially prepared by the co-precipitation method is completely amorphous without any peaks. After heat-treating at 450 °C, one major broad peak at the $2\theta$ of 25.9 º can be detected in the diffraction line (b), which means that the precursor has begun to dehydrate, but still remains amorphous; while after sintering at 650 ºC, as shown in the diffraction line (c), a series of diffraction peaks has emerged. The highest intensity peak, at the $2\theta$ of 25.9 º, can be assigned to anhydrous $FePO_4$ with a hexagonal structure (JCPDS card No. 29-

0715) [263], indicating that amorphous $FePO_4$ has transformed into crystalline phase after heat treated at an elevated temperature.

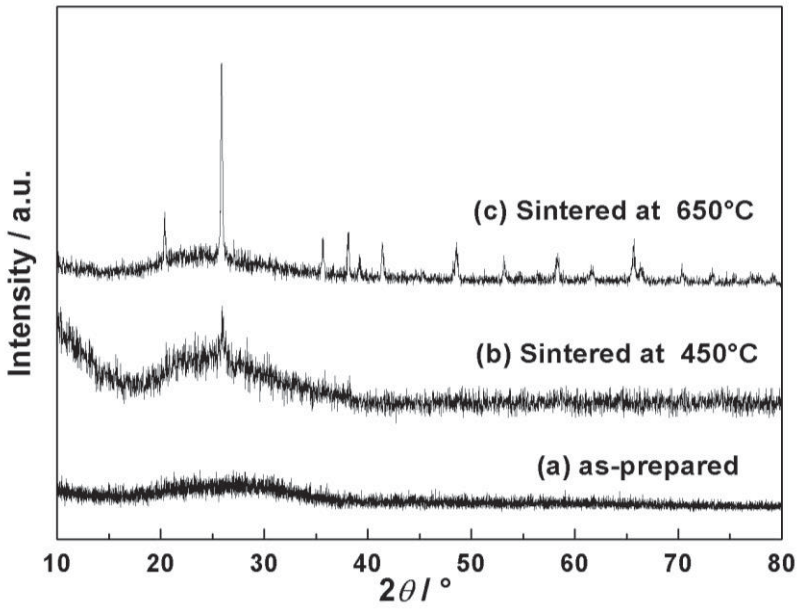


Figure 5.1 XRPD patterns of the amorphous $FePO_4$ and crystallized $FePO_4$ sintered at different temperatures

The TG-DSC curves of $LiFePO_4$ precursor are displayed in Figure 5.2 showing two obvious weight losses. The first weight loss occurred between room temperature and 150 °C, which is associated with the loss of physical absorption water in the as-prepared $LiFePO_4$. Furthermore, the second weight loss at around 170 °C to 350 °C, indicated the carbonization of polyaniline and might involve the decomposition of some residue of organic chemicals. No appreciable weight loss can be found over the temperature range from 350 °C to 450 °C, but an exothermic peak is visible at 438 °C in the DSC curve, which is related to the crystallization of this compound.

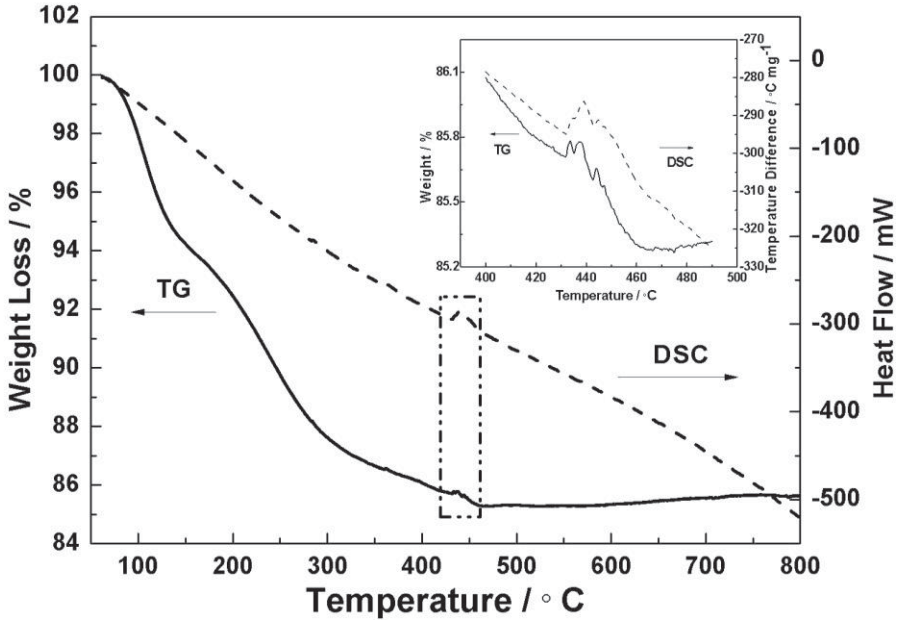


Figure 5.2 TG-DSC curves of $LiFePO_4$ precursor measured at a heating rate of 5 ºC $min^{-1}$ in the Ar flow between RT and 800 ºC with a zoom-in area as an insert

Figure 5.3 shows the XRPD patterns of $LiFePO_4$ with a Raman spectrum as an inset. No peaks can be found in the diffraction line (a), which means the as-prepared $LiFePO_4$ has emerged in amorphous form. After sintering at 650 °C for 15 h, a series of sharp and symmetric diffraction peaks can be detected in the diffraction line (b), which indicates that the $LiFePO_4$ is now highly crystallized and can be well indexed to ordered orthorhombic olivine structured $LiFePO_4$ (JCPDS card No. 40-1499, space group Pmnb (62)). The lattice parameters calculated by MDI. Jade.5.0 are a = 5.985 nm, b = 10.306 nm, c = 4.681 nm, and V = 288.76 $nm^3$, which are quite close to the results of a previous report [268]. In addition, there is no diffraction peak of carbon in the final sample. In order to confirm the existence of the residual carbon, Raman spectroscopy was performed, as shown in the inset in Figure 5.3. Two bands

in the range of 1110-1480 $cm^{-1}$ and 1480-1720 $cm^{-1}$ are attributed to the D-band and G-band of carbon respectively, which reveals that the carbon was amorphous.

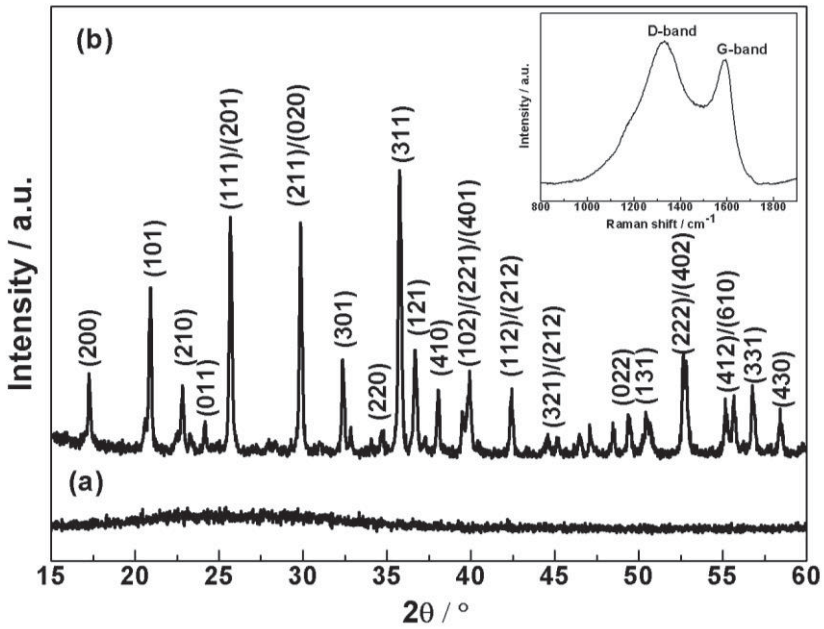


Figure 5.3 XRPD patterns of amorphous precursor (a), crystallized $LiFePO_4$ (b) and Raman spectrum of $LiFePO_4$ as an inset

The oxidation state of Fe in $LiFePO_4$ was examined by the XPS measurement. As shown in Figure 5.4, the binding energies (BE) of O1s, C1s, P2p, and Li1s were determined to be 531.2 eV, 284.4 eV, 133.4 eV, and 55.6 eV respectively. Especially in the enlarged spectrum of Fe2p, shown as the inset in Figure 4.4, one obvious peak and one satellite peak can be found at BE of 710.9 eV and 723.8 eV respectively, which correspond to Fe 2p3/2 and Fe 2p1/2 in $LiFePO_4$ [86]. Therefore, based on the XRPD and XPS results, $LiFePO_4$ with high crystallinity and phase purity has been successfully synthesized.

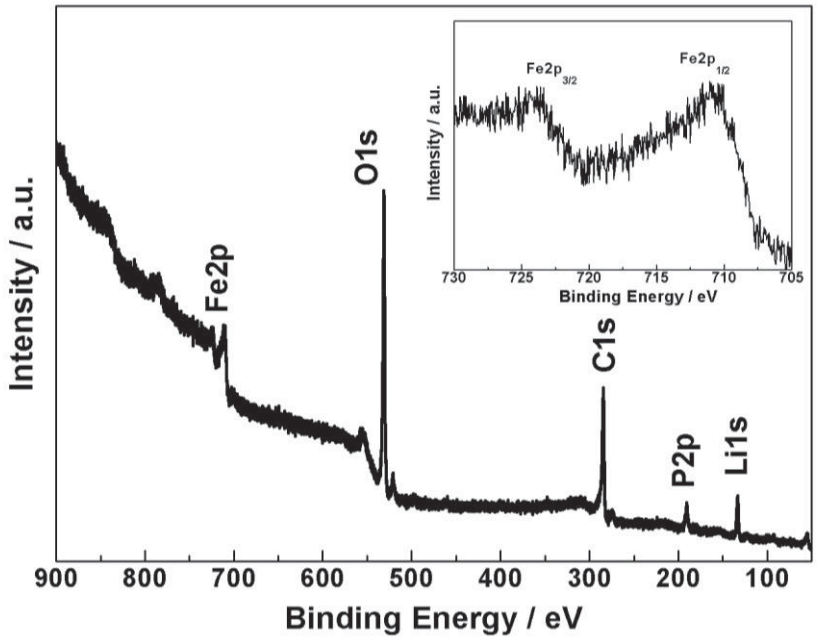


Figure 5.4 XPS pattern of $LiFePO_4$ and a high-resolution XPS Fe2p spectrum as an inset

### 5.3.2 FESEM and TEM observations of the as-prepared $LiFePO_4$

The FESEM images of $LiFePO_4$ (Figure 5.5) shows that the ultra-fine primary particles (a size in the range 40-50 nm) have agglomerated to form larger secondary particles (with a size about 100-110 nm). Figure 5.5 (b) clearly demonstrates that each secondary particle contains several primary particles and is wrapped in a thin layer of carbon. We believe that this layer was generated during the sintering process because of the carbonization of polyaniline. In order to further identify the structure of $LiFePO_4$, TEM observation was performed. Figure 5.6 (a) exhibits a large particle cluster with uniform agglomerated nanoparticles and Figure 5.6 (b) demonstrates that the typical particle size of $LiFePO_4$ is around 40-50 nm, with a continuous thin layer covering each particle, which is in agreement with the FESEM results. Selected-area electron diffraction (SAED), inset in Figure 5.6 (b), reveals that the as-prepared

$LiFePO_4$ is highly crystalline. The enlarged image of selected area in Figure 5.6 (b) is shown in Figure 5.6 (c). The high-resolution TEM images have confirmed that each crystallite is spheroidal and fully coated by a carbon layer with a thickness ranging from 3-5 nm (indicated by arrows). Another zoom-in area in Figure 5.6 (d) also confirms the morphology of as-prepared $LiFePO_4$. Here, it is 103interswee that the conductive carbon layer is continuous, not only covering each primary crystallite, but also outside of the agglomerated particles, so that it forms an efficient pathway for the lithiation and delithiation of lithium ions.

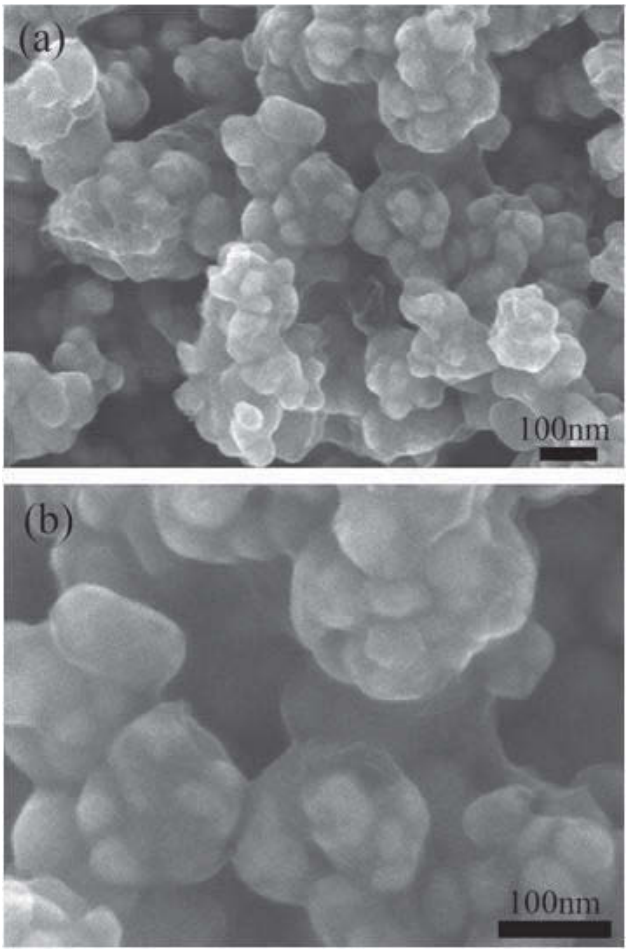


Figure 5.5 FESEM images of $LiFePO_4$ after sintered at 650 °C for 15 h at different magnifications

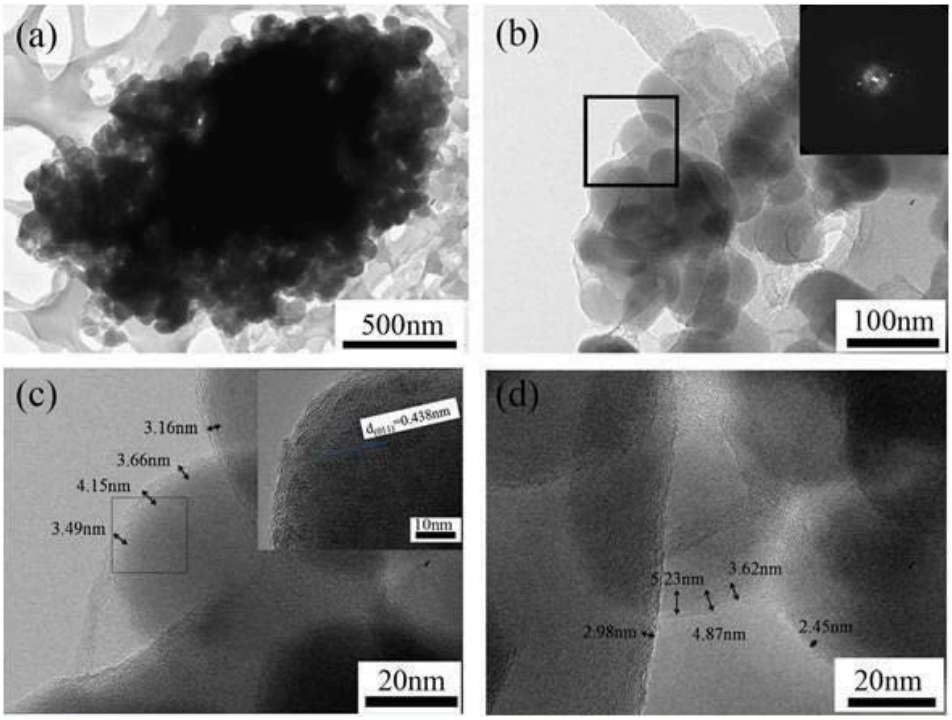


Figure 5.6 TEM images of (a) $LiFePO_4$; (b) enlarged TEM image of spherical $LiFePO_4$ particles with a SAED as an inset; (c) zoom-in image of selected-area in (b) with enlarged d-spacing as an inset; (d) selected-area TEM image for $LiFePO_4$ containing several primary crystallites

### 5.3.3 Electrochemical properties of the as-prepared $LiFePO_4$

In order to investigate the electrochemical properties of $LiFePO_4$, a series of electrochemical tests were performed. Figure 5.7 (a) shows the first five cycles of CV curves of $LiFePO_4$ composite in the voltage range 2.5-4.2 V at the scan rate of 0.1 mV $s^{-1}$ at room temperature. Negligible peak position shift can be found in the first oxidation peak compared with the subsequent four cycles, which indicates that $LiFePO_4$ has excellent coulombic efficiency and reversible capability. In Figure 5.7 (b), a series of redox peaks between 3.2 V and 3.8 V are assigned to $Fe^{2+/3+}$ at different scan rates. When the scan rate is increased gradually from 0.2 mV $s^{-1}$ to 5

mV $s^{-1}$, the corresponding extraction and insertion of lithium ions can still be observed, which indicates superior rate performance of this material.

As shown in Figure 5.7 I, $LiFePO_4$ can deliver 150 mAh $g^{-1}$ initial discharge capacity with negligible capacity loss after 50 cycles at the 1 *C* between 2.0-4.2 V. These curves present a long and flat voltage plateau, and exhibit excellent cycling stability with small voltage difference between charge and discharge process. The cycling capability of $LiFePO_4$ with increasing *C*-rates between 2.0-4.2 V is presented in Figure 5.7 (d). The discharge capacity of $LiFePO_4$ is 149 mAh $g^{-1}$ at 0.1 *C*. Furthermore, at higher *C*-rates (0.2 *C*, 1 *C*, 2 *C* and 5 *C*) the discharge capacities are 145, 150, 134 and 127 mAh $g^{-1}$ respectively, corresponding to a capacity retention of 97.3 %, 100 %, 90 % and 85.2 %, compared with the capacity at a rate of 0.1 *C*. The discharge capacity slightly deteriorates at the rate of 5 *C* as a function of cycle number; however, $LiFePO_4$ can be regenerated after being charge-discharged at lower *C*-rates again, and capacity return to 145 mAh $g^{-1}$ at 0.2 *C*. This was further confirmed that by coating $LiFePO_4$ with a continuous conductive carbon layer through in-situ polymerization, this ultra-fine $LiFePO_4$ composite can exhibit excellent electrochemical properties.

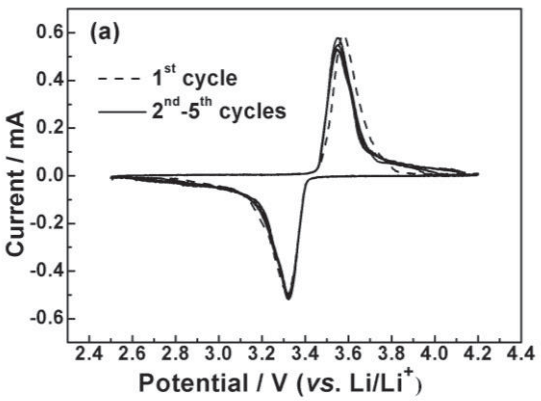


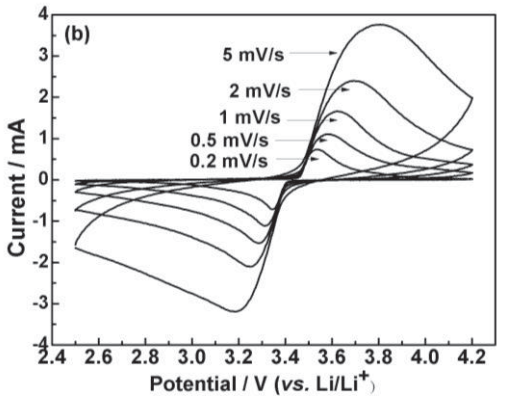

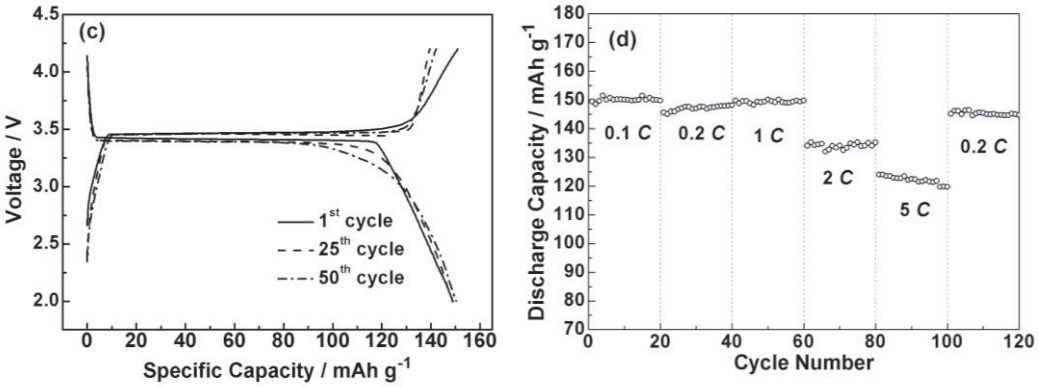


Figure 5.7 Electrochemical properties of the as-prepared $LiFePO_4$ (a) Cyclic voltammetry tests for the first five cycles at the scan rate 0.1 mV $s^{-1}$ in the potential window 2.5-4.2 V; (b) Cyclic voltammetry tests at different scan rates in the potential window 2.5-4.2 V; (c) Charge-discharge curves at different cycle number at 1 *C*-rate; (d) Cycle capability at different discharge rates

## 5.4 Conclusions

Nanosize $LiFePO_4$ was synthesized by co-precipitation combined with in-situ polymerization. During the co-precipitation process, aniline monomers were polymerized and covered the surface of each newly-formed $FePO_4$ particle, thus hindering the further growth of nuclei. Even though, the $LiFePO_4$ was sintered at 650 °C for 15 h, the primary particle size of $LiFePO_4$ was still controlled within 40-50 nm, with a continuous carbon coating layer. The as-prepared $LiFePO_4$ delivered an initial discharge capacity of 150 mAh $g^{-1}$ at the rate of 1 *C* and exhibited excellent capacity retention and cycling stability at higher *C*-rates.

# CHAPTER 6 An Investigation of Carbon Coating on the Electrochemical Performances of Lithium Iron Silicate for Li-ion Batteries

## 6.1 Introduction

Recently, $Li_2FeSiO_4$ as an alternative cathode material for Li-ion batteries started to attract the attention of researchers, owing to its several advantages related to natural abundance, safety and non-toxicity. Several methods have been proposed to synthesize $Li_2FeSiO_4$, including solid-state reaction [136, 158], sol-gel [144, 271], hydrothermal method [149, 272], Pechini synthesis [138] and microwave-solvothermal synthesis [142].

Recently, some novel synthetic routes were proposed to prepare nanosized $Li_2FeSiO_4$ with high purity. For instance, $Li_2FeSiO_4$/C nanoparticles were synthesized through the combustion of reaction mixtures [273]. Sucrose was used as the carbon source and $Fe(NO_3)_3$ and $SiO_2$ were the reagents. The whole reaction can be expressed as $2LiNO_3 + Fe(NO_3)_3 + SiO_2 + xC_{12}H_{22}O_{11} \rightarrow Li_2FeSiO_4 + 2.5N_2 + 12xCO_2 + 11xH_2O$. This material achieved stable cycling performance at 2 *C*. Moreover, $Li_2FeSiO_4$/C nanocomposites were synthesized by a combination of spray pyrolysis and wet ball-milling [274].

$Li_2FeSiO_4$ suffers from low specific conductivity ($6\times10^{-14}$ S $cm^{-1}$) and slow lithium diffusion. Based on this, carbon-coating strategy could be an efficient way to enhance the electronic conductivity of pristine $Li_2FeSiO_4$. In this study, pristine and carbon-coated $Li_2FeSiO_4$/C cathode materials were prepared via a modified ball-

milling method, which is an efficient and cost-effective method to synthesize nanomaterials. The glycolic acid was used as the carbon source. The structure and electrochemical properties of pristine and $Li_2FeSiO_4$/C materials were systematically investigated.

## 6.2 Experimental

### 6.2.1 Material synthesis

Stoichiometric amounts of $Li_2CO_3$, $FeC_2O_4$ $2H_2O$, and $SiO_2$ were dispersed in a water-ethanol mixture (50:50 in volume). The mixture was ultrasonically treated for 30 min and refluxed at 70 °C for 12 h. After cooling to room temperature, the mixture was ball-milled with 5 wt% of glycolic acid in acetone for 16 h. Following the evaporation of acetone, the homogenous mixture was sintered at 700 °C for 10 h in argon flow. For the preparation of pristine $Li_2FeSiO_4$, all procedures were the same except that no carbon source was added in the ball-milling process.

### 6.2.2 Physical characterization and electrochemical testing

The phase purity was determined by XRPD. Raman spectroscopy was performed with a Jobin Yvon HR800 confocal Raman system with a laser wavelength of 632.81 nm on a 300 lines/mm grating at room temperature. Surface morphology and particle size distribution of as-obtained samples were analysed by using FESEM and TEM. Electrochemical characterizations of the pristine and $Li_2FeSiO_4$/C cathode materials were evaluated by assembling CR2032 coin cells in an argon-filled glove box. $Li_2FeSiO_4$ electrode was used as the working electrode, and Li foil was the counter and reference electrode. The electrolyte was prepared by dissolving 1 M $LiPF_6$ in EC:

DMC = 1:1. The electrodes were made by dispersing 70 wt% active material, 20 wt% carbon black, and 10 wt% PVDF in NMP to form a slurry. The slurry was then spread onto Al foil. The coated electrodes were dried at 100 °C in a vacuum oven overnight. The galvanostatic charge-discharge tests were performed at room temperature on a Neware battery tester at different *C*-rates between 1.5-4.8 V. EIS was measured in the frequency range of $10^5$-$10^{-2}$ Hz.

## 6.3 Results and Discussion

### 6.3.1 Structural analysis of $Li_2FeSiO_4$/C

Figure 6.1 shows the XRPD patterns of the $Li_2FeSiO_4$ and $Li_2FeSiO_4$/C materials.

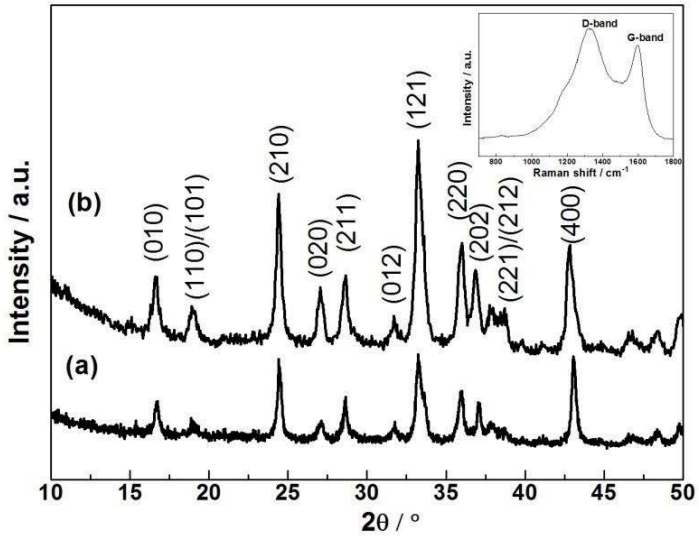


Figure 6.1 XRPD patterns of (a) $Li_2FeSiO_4$ and (b) $Li_2FeSiO_4$/C and Raman spectrum of $Li_2FeSiO_4$/C as an inset

Sharp and symmetric diffraction peaks can be detected in both samples, indicating that both samples are well crystallized and can be indexed to orthorhombic phase with the space group of $Pmn2_1$. In addition, there is no diffraction peak of carbon in

the diffraction line (b). In order to confirm the nature of carbon, the Raman spectrum is presented as the inset in Figure 6.1. The D-band and G-band of carbon reveal that the carbon layer was amorphous.

### 6.3.2 FESEM and TEM observations of $Li_2FeSiO_4$/C

The morphologies of the $Li_2FeSiO_4$ and $Li_2FeSiO_4$/C samples are shown in Figure 6.2 (a) and (b) respectively. As shown in Figure 6.2 (a) small primary particles of pristine $Li_2FeSiO_4$ tend to form large agglomerates during heat treatment; while $Li_2FeSiO_4$/C exhibits better uniformity with the secondary particle size in the range 200-300 nm.

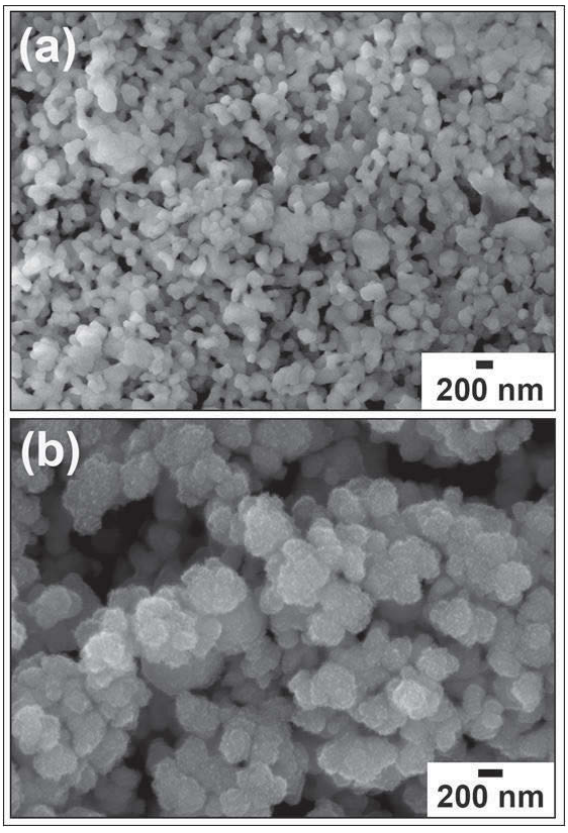


Figure 6.2 FESEM images of (a) $Li_2FeSiO_4$ and (b) $Li_2FeSiO_4$/C

TEM analysis was conducted to confirm the existence of the carbon layer on the $Li_2FeSiO_4$/C. Figure 6.3 (a) and (b) display TEM images of a typical particle cluster

and the enlarged view of the $Li_2FeSiO_4$/C respectively. Figure 6.3 (a) clearly demonstrates that the $Li_2FeSiO_4$/C consists of nanosized particles with good uniformity. An enlarged TEM image in Figure 6.3 (b) indicates that the crystal size of $Li_2FeSiO_4$/C is in the range 20-40 nm. The inset in Figure 6.3 (b) confirms the presence of a carbon layer with the thickness of about 1.5-3 nm (indicated by arrows). During the sintering process, glycolic acid as the carbon source can inhibit particle growth and agglomeration by forming a conductive carbon layer simultaneously on the surface of individual particles.

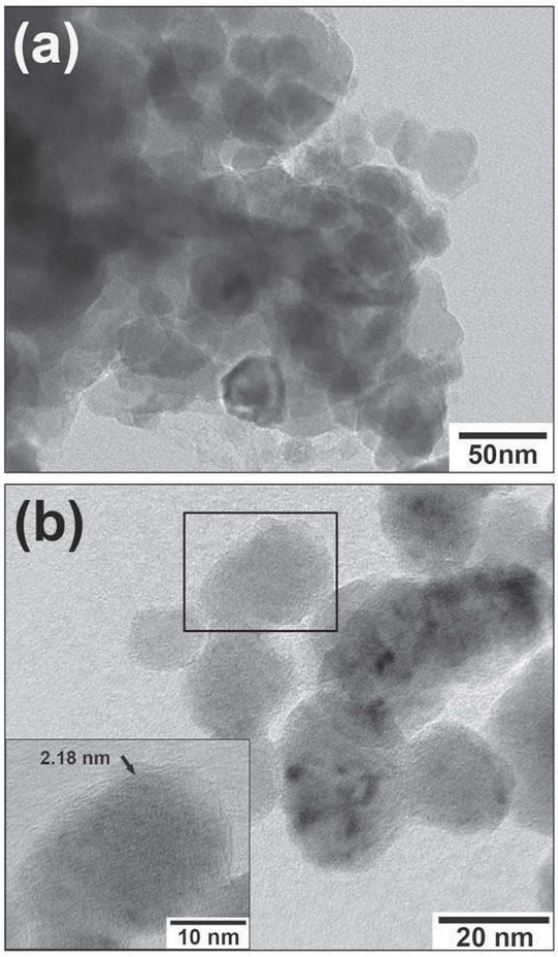


Figure 6.3 TEM images of $Li_2FeSiO_4$/C at different magnifications (a) and (b). The inset in (b) is the zoom-in nanoparticles shown in the rectangular area

### 6.3.3 Electrochemical properties of $Li_2FeSiO_4$/C

Figure 6.4 (a) compares the charge-discharge curves of the $Li_2FeSiO_4$ and $Li_2FeSiO_4$/C cathode materials. An obvious shift of the potential plateau from 3.2 V in the initial charge to 2.9 V in the second charge is identified for both samples. This phenomenon is consistent with the previous reports [133]. The initial discharge capacities of the pristine and $Li_2FeSiO_4$/C are 137 mAh $g^{-1}$ and 148 mAh $g^{-1}$ respectively. It should be noted that $Li_2FeSiO_4$/C material shows an improved initial columbic efficiency (86 %) over pristine $Li_2FeSiO_4$ (77 %). Figure 6.4 (b) shows the cycling performances of the $Li_2FeSiO_4$ and $Li_2FeSiO_4$/C cathode materials at various *C*-rates when cycled between 1.5 V and 4.8 V. Clearly, $Li_2FeSiO_4$/C exhibits much better capacity retention and rate capability than $Li_2FeSiO_4$. At 0.1 *C*, $Li_2FeSiO_4$ and $Li_2FeSiO_4$/C cells exhibit the capacity retention of 78.6 % and 90 % over the first 20 cycles respectively. The $Li_2FeSiO_4$/C cathode material can deliver a specific capacity of 127 mAh $g^{-1}$ and 111 mAh $g^{-1}$ at 0.2 *C* and 1 *C* respectively, with negligible capacity loss. Overall, the electrochemical performance of the $Li_2FeSiO_4$/C cathode material is superior to that of the pristine $Li_2FeSiO_4$, in terms of electrochemical stability and reversible capacity. This suggests that electrochemical properties of $Li_2FeSiO_4$ are significantly improved by coating a carbon layer. The conductive carbon layer may not only suppress the particle growth of $Li_2FeSiO_4$ during calcinations, but also improve the conductivity of the $Li_2FeSiO_4$ cathode material.

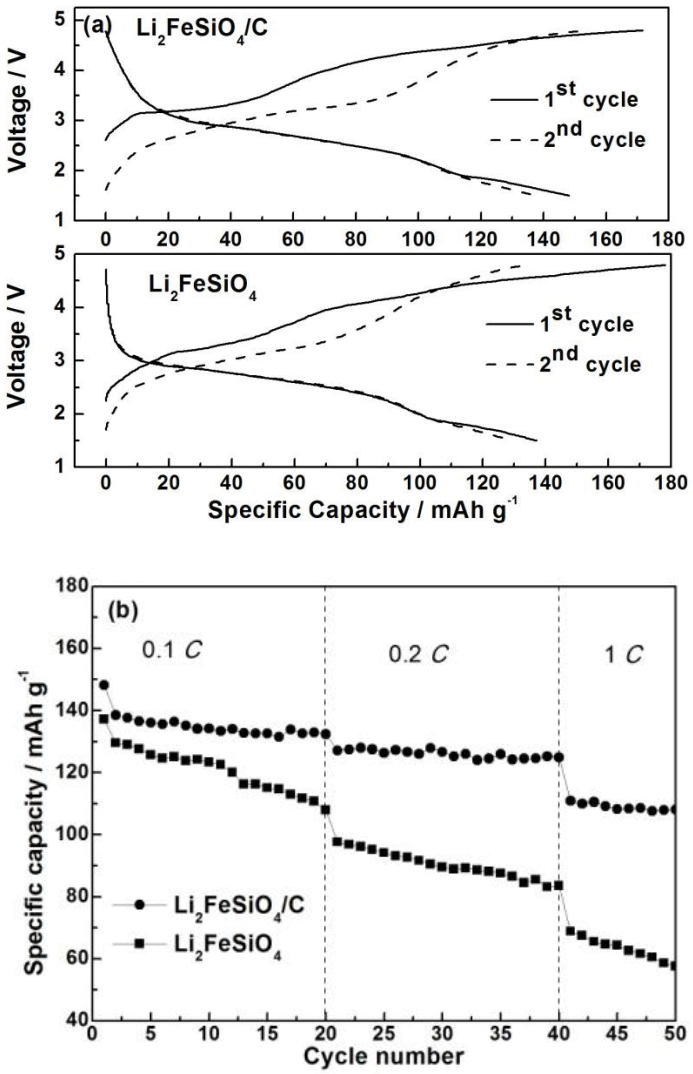


Figure 6.4 (a) Charge-discharge profiles and (b) cyclic performances of $Li_2FeSiO_4$ and $Li_2FeSiO_4$/C

In order to understand the improved electrochemical performance of the $Li_2FeSiO_4$/C, an AC impedance measurement was carried out for both pristine and $Li_2FeSiO_4$/C electrodes at a 50 % state of charge (SOC). As shown in Figure 6.5, the impedance spectra exhibit a depressed semicircle in the high-frequency range and a sloping line with almost the same gradient in the low-frequency range. The intercept at *Z*' axis in high frequency corresponds to the ohmic resistance ($R_\Omega$). The semicircles are

attributed to the charge transfer resistance, while the sloping lines correspond to the typical Warburg 114intersw. Based on this, an equivalent circuit model is given in the inset in Figure 6.5. In the equivalent circuit model, $R_{\Omega}$ refers to the ohmic resistance between the working electrode and the reference electrode, $R_{ct}$ represents the charge transfer resistance, which can be determined by the value of the semicircle on the $Z$' axis, and $CPE_{ct}$ is the constant phase-angle element depicting the non-ideal capacitance of the double layer. $R_s$ refers to the resistance for the lithium ion diffusion in the surface layer, $CPE_w$ is the constant phase-angle element describing the non-ideal capacitance of the surface layer, and $Z_w$ is the Warburg impedance [158]. In this work, the $R_{\Omega}$ values are negligible for both cathode materials. However, $R_{ct}$ values are 350 Ω and 560 Ω for the $Li_2FeSiO_4$/C and pristine $Li_2FeSiO_4$ electrode respectively. Therefore, carbon layer decreases the charge transfer resistance in the $Li_2FeSiO_4$/C cell, indicating an enhancement in the kinetics of lithium-ion diffusion and charge transfer reaction.

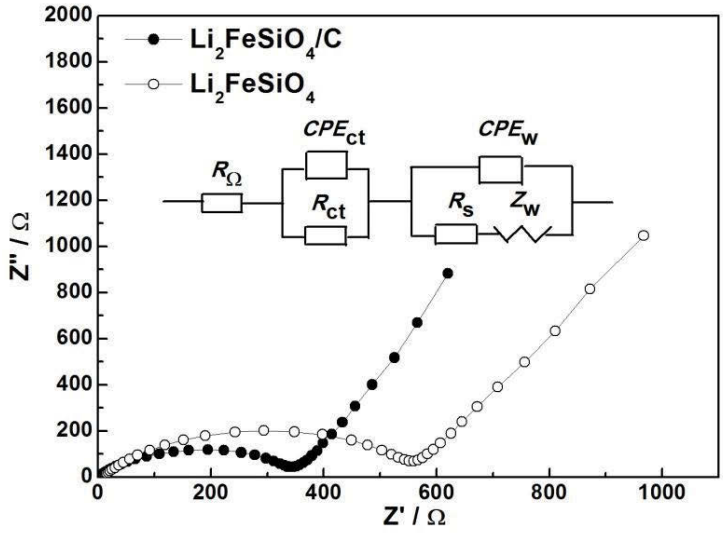


Figure 6.5 EIS plots of $Li_2FeSiO_4$ and $Li_2FeSiO_4$/C acquired at 50 % SOC with the equivalent circuit as an inset

## 6.4 Conclusions

$Li_2FeSiO_4$/C cathode materials exhibit improved rate capability and cycling performance compared with pristine $Li_2FeSiO_4$. TEM analysis demonstrates that the coating of a nanolayer carbon (1.5-3 nm in thickness) on the $Li_2FeSiO_4$/C cathode material has been realized by the carbonization of glycolic acid during calcination. EIS analysis indicates that the improvement of the electrochemical properties of $Li_2FeSiO_4$/C can be ascribed to the decrease in the charge transfer resistance. $Li_2FeSiO_4$/C could be used as a potential cathode material for Li-ion batteries.

# CHAPTER 7 Design of Cobalt Iron Oxide as High-performance Anode Material for Li-ion Batteries

## 7.1 Part I Synthesis of $CoFe_2O_4$ Hollow Spheres

### 7.1.1 Introduction

The spinel ferrite ($CoFe_2O_4$) features high saturation magnetization, high coercivity and excellent chemical stability, which leads to wide applications in drug-delivery, magnetic response imaging and high-density magnetic storage [275, 276]. $CoFe_2O_4$ has been investigated as an anode material for Li-ion batteries because of its high theoretical capacity of 916 mAh $g^{-1}$ (8 mole Li per mole of $CoFe_2O_4$ can be involved according to the conversion reaction $CoFe_2O_4 + 8Li^+ + 8e^- \leftrightarrow Co + 2Fe + 4Li_2O$) with promising stable electrochemical properties [277, 278].

Several approaches have been developed for the synthesis of $CoFe_2O_4$. These include sol-gel [279, 280], macroporous synthesis [281] reverse micelles procedure [282], freeze-drying [283], co-precipitation method [284] and thermolysis [285]. In general, those $CoFe_2O_4$ materials exhibited an initial capacity in the range of 800-1300 mAh $g^{-1}$. However, they generally suffer from large irreversible capacity, relatively poor cyclability and low rate capability, owing to severe particle aggregation and large volume change during cycling. Recently, Li *et.al* reported the application of a macroporous $CoFe_2O_4$ as anode material that delivered an initial specific capacity of

1782 mAh $g^{-1}$ [192]. However, this material demonstrated relatively poor capacity retention.

It is well accepted that the reactivity of electrode materials in Li-ion batteries relies on the lithium reaction pathway and the capability of lithium diffusion [195, 286]. Therefore, the dimension and morphology of the electrode material could play an important role in improving the electrochemical performance. In particular, nanomaterials, theoretically, can deliver high reversible capacity and good cycling performance by providing a large surface area and short pathway for lithium ion transport. Based on previous reports, hollow nanostructured materials have shown their unique physical and chemical properties [222, 275, 287]. As the anode material for Li-ion batteries, the uniformed hollow nanostructure could facilitate the solid-state diffusion of Li-ions in the transition metal oxide by providing larger solid-liquid reaction interface area than the bulk counterpart. In the first part, we report the synthesis of cobalt ferrous oxide with a uniform morphology and a hollow nanoarchitecture by a hydrothermal method. The electrochemical performance of $CoFe_2O_4$ nanospheres have been systematically investigated through cyclic voltammetry and galvanostatic charge/discharge cycling.

### 7.1.2 Experimental

#### 7.1.2.1 Material synthesis

Non-aqueous hydrothermal method was employed for the synthesis of $CoFe_2O_4$ nanospheres. In a typical synthetic procedure, 0.005 mol of $CoCl_2$ $6H_2O$ and 0.01 mol of $FeCl_3$ were added into 35 mL ethylene glycol. After that, 0.09 mol urea was added and the mixture was stirred for 2 h until the complete dissolution of solid

reagents. The solution was transferred into a Teflon-lined autoclave and the reaction temperature was maintained at 200 °C for a given duration. After cooling to room temperature, the resulting black precipitates were washed with distilled water and ethanol several times, and then were dried in a vacuum oven at 80 °C overnight. Three different samples of $CoFe_2O_4$ were prepared under different reaction times. For simplicity, these samples were assigned M6, M12 and M24 for the reaction duration of 6 h, 12 h and 24 h respectively.

#### 7.1.2.2 Material characterizations

XRPD was performed to determine the phase of the as-prepared $CoFe_2O_4$ using a Siemens D5000 Diffractometer with Cu Kα radiation (λ = 0.15406 nm) in the $2\theta$ range of 10-80° at a scan rate of 2 ° $min^{-1}$. In order to prepare electrodes for *ex-situ* XRPD measurement, multiple identical Swagelok Cells were discharged or charged to different voltages, and then were disassembled in an argon-filled glove box. The electrodes were recovered and washed thoroughly with DEC to remove lithium salt and any impurities, and then dried at 80 °C in vacuum. For *ex-situ* XRPD measurements, the signals from electrodes were collected at different discharge and charge states along with Cu substrate. FESEM and TEM were used to analyse the surface morphology, particle size distribution and crystal structure of $CoFe_2O_4$.

#### 7.1.2.3 Electrochemical testing

Electrochemical properties of $CoFe_2O_4$ material were evaluated by assembling the Swagelok Cells in a glove box. The electrode was made by dispersing 55 wt% $CoFe_2O_4$ with 30 wt% carbon black and 15 wt% polyvinylidene fluoride (PVDF) binder in *N*-methyl pyrrolidione (NMP). Lithium foil was used as the counter

electrode. The electrolyte was 1M $LiPF_6$ in 1:1 EC:DMC. Cyclic voltammetry was collected on $CoFe_2O_4$ cells at 0.1 mV $s^{-1}$ at room temperature on CHI660C. The cells were galvanostatically charged and discharged on a Neware battery tester at various *C*-rates in the voltage range 0.01-3.0 V.

### 7.1.3 Results and discussion

Figure 7.1 shows the XRPD patterns of the $CoFe_2O_4$ (M6, M12 and M24) nanospheres and the standard XRPD pattern of cubic $CoFe_2O_4$ (JCPDS Card No. 22-1086).

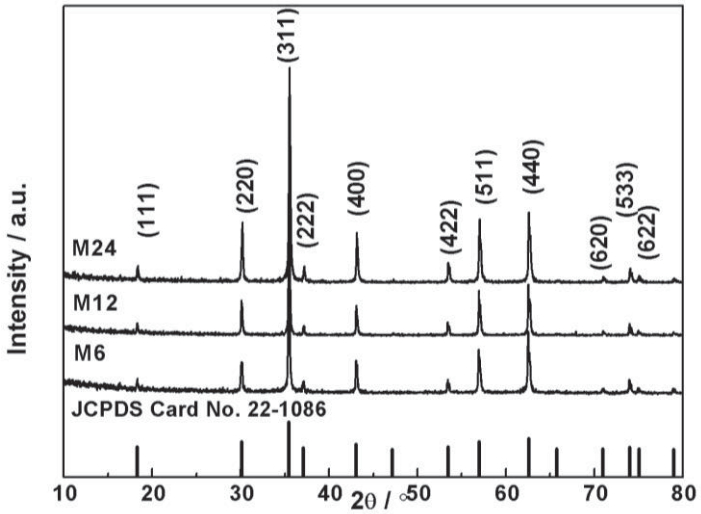


Figure 7.1 XRPD patterns of $CoFe_2O_4$ nanospheres (samples M6, M12 and M24) and the standard XRPD pattern of the cubic $CoFe_2O_4$

The sharp diffraction peaks and high intensity indicate the good crystallinity of the three as-prepared $CoFe_2O_4$ samples. All diffraction peaks can be indexed to the standard single phase cubic $CoFe_2O_4$ structure, which confirms the formation of pure compound. For the sample M12, the value of the lattice parameter was calculated to be a = 0.8391 nm, which is in good agreement with the database value of 0.8392 nm (JCPDS Card No. 22-1086).

The influence of reaction time on morphologies of the as-prepared $CoFe_2O_4$ is examined by FESEM analysis and shown in Figure 7.2.

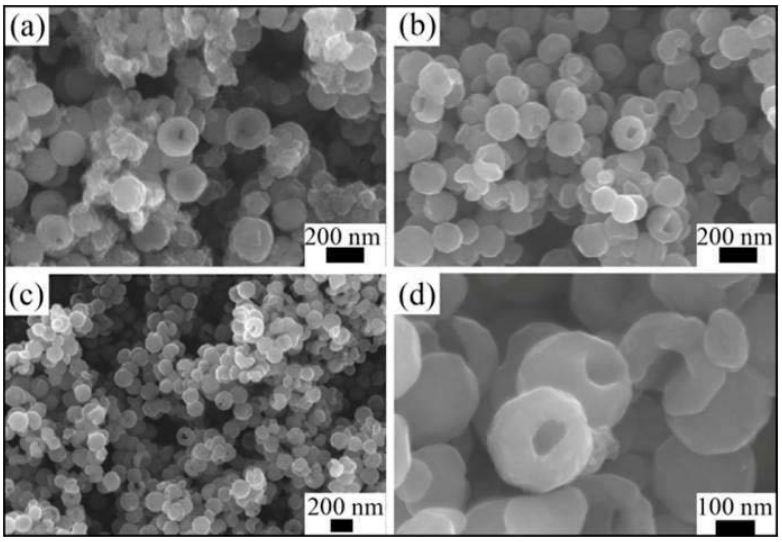


Figure 7.2 FESEM images of the as-prepared $CoFe_2O_4$ nanospheres (a) M6, (b) and (d) M12, (c) M24

For the M6 sample, some $CoFe_2O_4$ flocculence mixed with nanospheres were presented (as shown in Figure 7.2 (a)). When the reaction time proceeded to 12 h and 24 h, as shown in Figure 7.2 (b) and (c), more nanospheres formed. This suggests that longer reaction time is favourable for the complete formation of $CoFe_2O_4$ nanospheres. By 120interswe the individual nanospheres of sample M12 in Figure 7.2 (d), we can identify that $CoFe_2O_4$ nanospheres have a hollow architecture with the average outer diameter of 200-300 nm and the wall thickness of 100 nm. The formation of these hollow $CoFe_2O_4$ nanospheres can be explained by the well-known Ostwald Ripening process [195]. $CO_2$ bubbles resulting from the thermal decomposition of urea could induce the hollow nanostructure, in which small $CoFe_2O_4$ nanoparticles generated in the reaction could aggregate around the $CO_2$-

liquid interface. As the reaction proceeded, $CoFe_2O_4$ nanospheres with hollow cavities were formed.

TEM analysis and selected-area electron diffraction (SAED) pattern were carried out to determine the microstructure of the as-prepared $CoFe_2O_4$ nanospheres. As shown in Figure 7.3 (a) and (b), the sample consists of nanospheres with the uniform particle size of about 200-300 nm. All the SAED rings (the inset in Figure 7.3 (b)) can be readily indexed to the cubic crystal structure, which confirms the $CoFe_2O_4$ phase. From the image of an individual particle (Figure 7.3 (c)), it indicates that $CoFe_2O_4$ consists of nanocrystals containing small internal pores. This architecture is an ideal framework required for the fast electron transfer and lithium diffusion. Figure 7.3 (d) shows the lattice resolved HRTEM image of the $CoFe_2O_4$ nanocrystal, in which the (220) crystal planes with 0.297 nm *d*-spacing have been indexed.

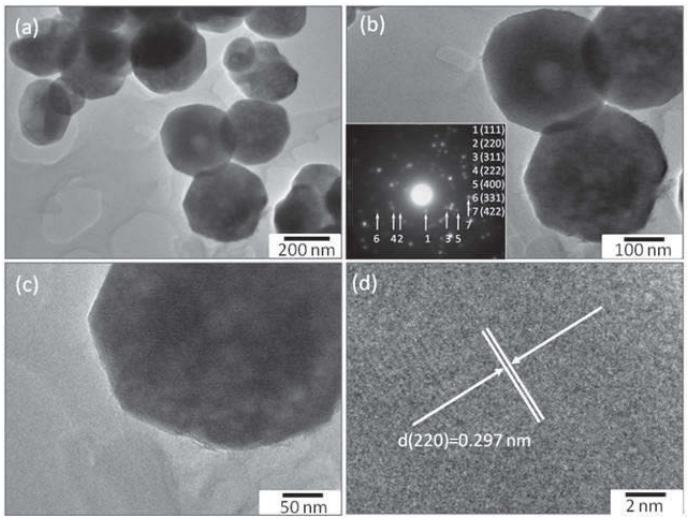


Figure 7.3 TEM images of the M12 $CoFe_2O_4$ sample at different magnifications. (a) and (b) are low magnification TEM images. (c) A high magnification TEM view of a $CoFe_2O_4$ nanosphere. (d) A lattice resolved HRTEM image of a $CoFe_2O_4$ nanocrystal. The inset in (b) is the corresponding selected area electron diffraction patterns

Figure 7.4 shows the cyclic voltammograms (CV) of the $CoFe_2O_4$ electrode for the first three cycles at a scan rate of 0.1 mV $s^{-1}$ in the voltage range 0.01-3 V versus $Li/Li^+$.

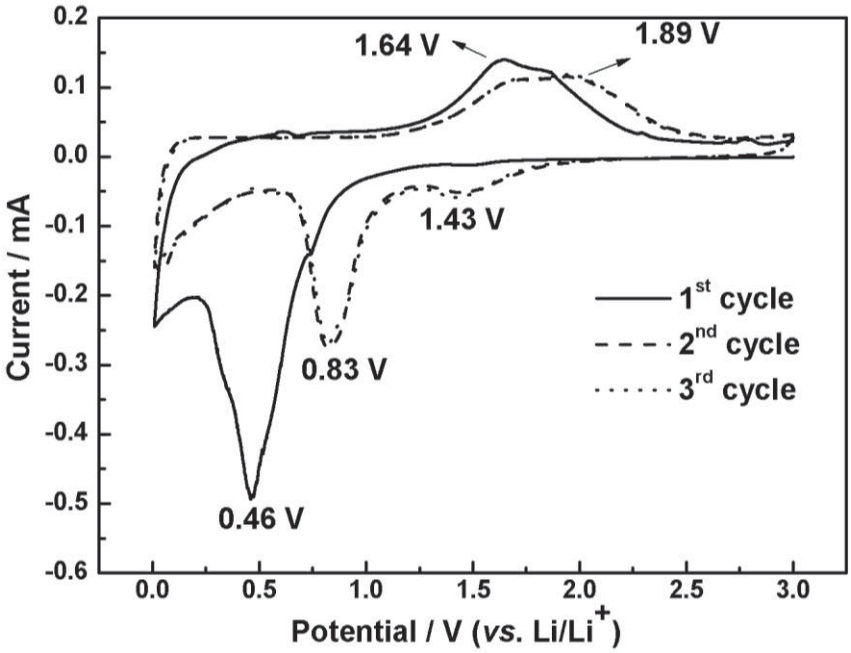


Figure 7.4 Cyclic voltammograms of the M12 sample electrode at a scan rate of 0.1 mV $s^{-1}$ between 0.01 and 3 V (vs. $Li/Li^+$)

In the first cathodic polarization process, the sharp peak at 0.46 V corresponds to the reduction of $Fe^{3+}$ and $Co^{2+}$ to their metallic states and the formation of $Li_2O$, accompanied by the decomposition of organic electrolyte to form a solid electrolyte interphase (SEI) layer. It is well known that the SEI layer (an organic polymeric layer) usually forms at the electrode/electrolyte interphase by the reduction of electrolyte [288]. In the subsequent cathodic scans, two cathodic peaks located at 0.83 V and 1.43 V can be attributed to the reductive reaction of $Fe_2O_3$ and CoO to Fe and Co metal respectively. The decrease of the redox peak intensity implies that the capacity decreases after the first cycle. In the first anodic cycle, a main broad peak

centred at 1.64 V is related to the oxidation of metallic iron and cobalt to $Fe^{3+}$ and $Co^{2+}$, which shifts to about 1.89 V after the second cycle. It should be noted that the peak intensity and integrated area during the anodic and cathodic polarization process remained almost unchanged in the second and third scanning cycles, indicating the good electrochemical reversibility of the $CoFe_2O_4$ nanosphere electrode.

In order to understand the reaction mechanism during the first lithium intercalation and deintercalation processes, the *ex-situ* XRPD was conducted on the $CoFe_2O_4$ electrodes at different discharge and charge states (as illustrated in Figure 7.5). The XRPD pattern of the pristine $CoFe_2O_4$ is also presented as the reference. By 123interswe the XRPD patterns of the pristine $CoFe_2O_4$ and the $CoFe_2O_4$ electrode discharged to 1.2 V, no clear phase transition was observed, which indicates that there is no electrochemical reaction occurred above 1.2 V. The XRPD pattern of electrodes discharged to 0.5 V and 0.01 V were featureless, and only diffraction peaks of Cu substrate were observed. This indicates that when the electrode was discharged to 0.5 V, the reduction and amorphization of the $CoFe_2O_4$ material was fully reached. The XRPD pattern of the fully charged electrode also lacks the characteristic diffraction peaks of $CoFe_2O_4$. The same phenomena were found in the initial charge/discharge process of $NiCo_2O_4$ and $ZnCo_2O_4$ materials [190, 289]. Previous studies have shown reduced metal nanoparticles in transition metal oxides embedded into $Li_2O$ matrix to form a homogeneous composite, with the $Li_2O$ nanoparticles being surrounded by a solid electrolyte interface [199].

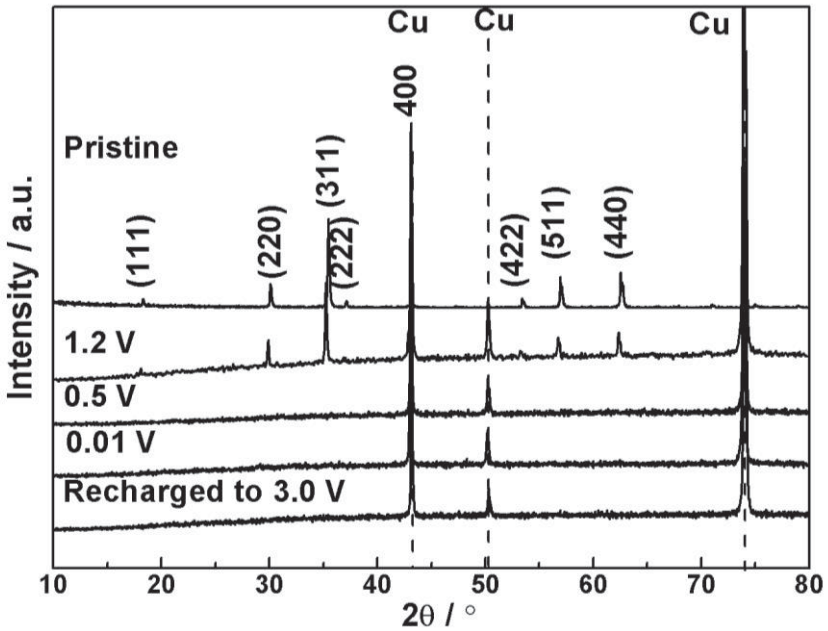


Figure 7.5 *Ex-situ* XRPD patterns of the $CoFe_2O_4$ nanosphere electrode (the sample M12) at different discharge and charge states. The diffraction peaks due to the copper substrate are indicated by dash lines

Figure 7.6 (a) shows the charge/discharge profiles of the $CoFe_2O_4$ nanosphere electrodes in first, second and 50$^{th}$ cycles. The electrode shows a typical charge-discharge 124intersw for transition metal anode materials [199]. The voltage profile of the $CoFe_2O_4$ anode material in the first cycle comprises a sharp slope in the initial stage of the discharge, a flat voltage plateau at 0.8 V, followed by a gentle slope until 0.01 V. The discharge capacity obtained above 0.8 V is 939 mAh $g^{-1}$ and corresponds to 8.2 mol Li per mol of $CoFe_2O_4$, which is slightly higher than the theoretical capacity of 916 mAh $g^{-1}$ (8 mol Li per mol of $CoFe_2O_4$, according to the equation [192, 279]: $CoFe_2O_4 + 8Li^+ + 8e^- \leftrightarrow Co + 2Fe + 4Li_2O$). When discharged to 0.01 V, the $CoFe_2O_4$ electrode exhibits a quite high discharge capacity of 2264 mAh $g^{-1}$, which is much higher than the theoretical value. The large excess capacity could be

ascribed to the decomposition of organic electrolytes in the voltage range 0.05-0.8 V and the amorphization of the nanocrystalline $CoFe_2O_4$ when the cell voltage reaches 0.01 V. Similar phenomena have been observed in the discharge process of other transition metal oxides [289, 290]. The possibility of interfacial storage in nanocrystalline could also contribute to the large excess capacity observed in this material [205, 291].

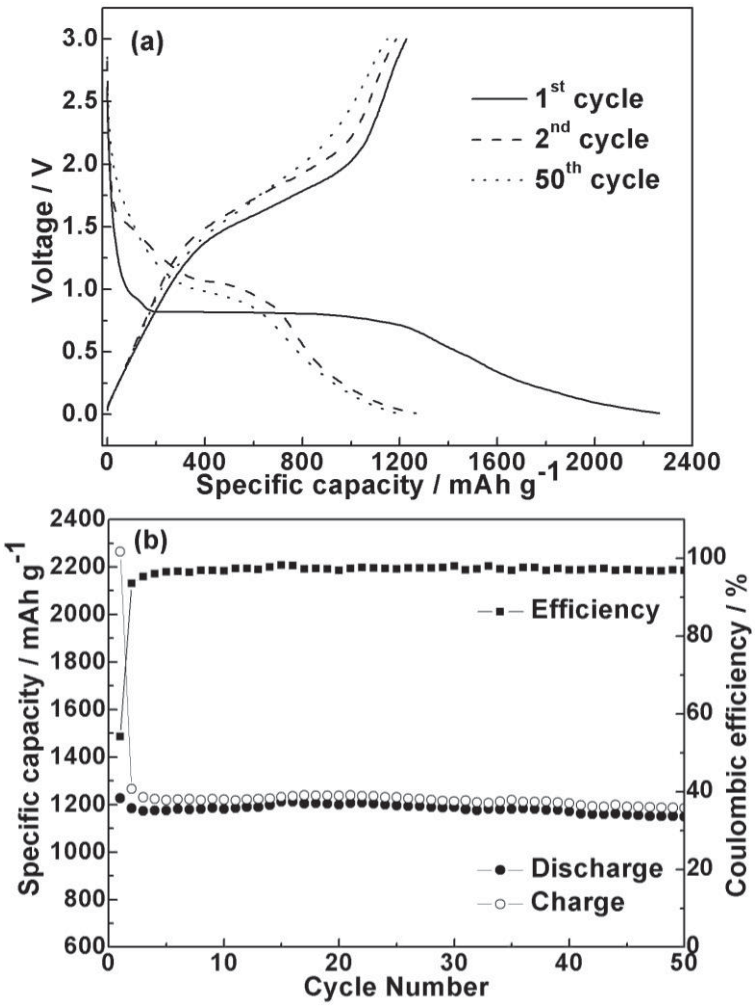


Figure 7.6 (a) Charge-discharge profiles of the $CoFe_2O_4$ nanosphere electrode (the sample M12) in the first, second and 50$^{th}$ cycles. (b) Cycling performance of the M12 electrode between 0.01 and 3 V at 0.1 *C*

As shown in Figure 7.6 (a), difference of the voltage profiles of $CoFe_2O_4$ between the first discharge process and the subsequent cycles indicates different redox reactions. This finding is consistent with the results found in CV and *ex-situ* XRPD measurements. 11 mol Li per mol of $CoFe_2O_4$ can be reversed in the second cycle that gives the reversible capacity of 1266 mAh $g^{-1}$. To the best of our knowledge, the lithium storage capacity is the highest value compared with the previous reports [192, 279, 282, 292]. Furthermore, the discharge capacity of $CoFe_2O_4$ maintained 1185 mAh $g^{-1}$ after 50 cycles, indicating the superior electrochemical stability of $CoFe_2O_4$ nanosphere anode material. Figure 7.6 (b) shows the cycling performance of the $CoFe_2O_4$ electrode up to 50 cycles, with a discharge capacity retention of 93.6 % and an average columbic efficiency of 97.13 %.

The rate capability of hollow $CoFe_2O_4$ nanospheres was tested at room temperature for four different current densities, corresponding to the *C* value of 0.1 *C*, 0.2 *C*, 0.5 *C* and 1 *C* (in this study, 1 *C* = 900 mAh $g^{-1}$). Ten cycles were carried out on each *C* rate in the voltage range 0.01-3 V. As shown in Figure 7.7, the $CoFe_2O_4$ nanosphere electrode delivered the discharge capacities of 1249, 1194 and 1133 mAh $g^{-1}$ at 0.1 *C*, 0.2 *C* and 0.5 *C* respectively. At these *C*-rates, the capacity is reasonably stable. Even though a slight capacity decrease could be found at 1 *C*, the cell still delivered a reversible discharge capacity of higher than 1000 mAh $g^{-1}$This is three-fold higher than the carbonaceous materials and also much higher than previous reports on transitional metal oxides $Mfe_2O_4$ (M = Co, Ni or Zn) [190, 195, 278, 279]. When decreasing the *C*-rate from 1 *C* to 0.1 *C*, 94.5 % of the initial capacity at 0.1 *C* can be recovered. The $CoFe_2O_4$ nanosphere electrode shows similar discharge profiles under various *C*-rates, suggesting the fast lithium diffusion during the redox reaction (the

inset in Figure 7.7). The good rate capability could be ascribed to the well-constructed hollow structure of $CoFe_2O_4$ nanospheres. In addition, TEM analysis determined that each nanosphere is composed of tiny nanocrystals, with a porous architecture. Therefore, hollow $CoFe_2O_4$ nanospheres provide the possibility of a more efficient diffusion of lithium ions and facile penetration of electrolytes in Li-ion batteries [222].

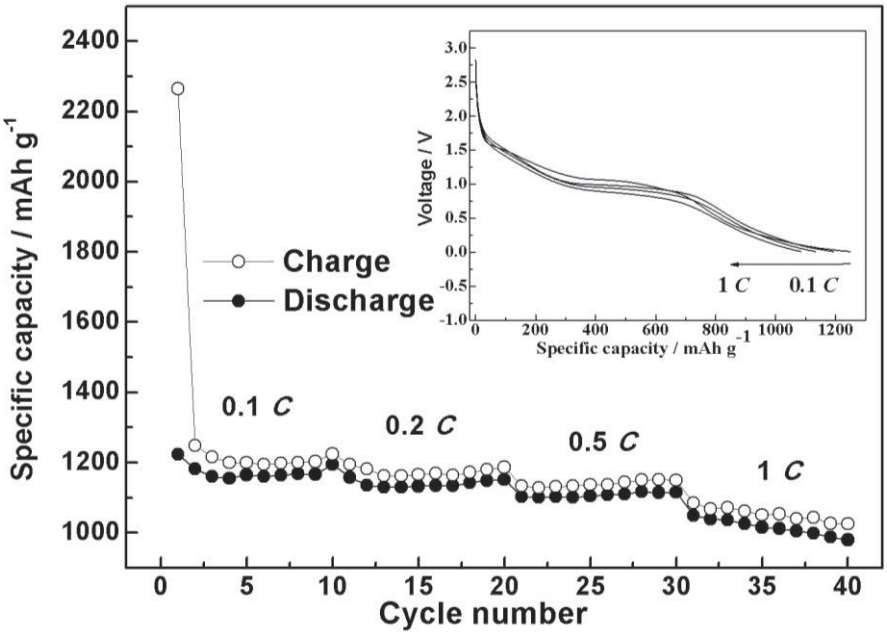


Figure 7.7 Cyclability of the M12 $CoFe_2O_4$ nanosphere electrode at various *C*-rates. The discharge profiles of $CoFe_2O_4$ in the first cycle at each *C*-rate are shown in the inset

### 7.1.4 Conclusions

Hollow $CoFe_2O_4$ nanospheres with the outer diameter 200-300 nm and wall thickness 100 nm were synthesized by a one-step hydrothermal method. XRPD and TEM characterizations confirmed the phase purity of cubic $CoFe_2O_4$. The electrochemical properties of $CoFe_2O_4$ nanospheres were evaluated though cyclic

voltammetry and galvanostatic charge/discharge cycling tests. The $CoFe_2O_4$ nanosphere electrode exhibited a reversible lithium storage capacity of 1266 mAh $g^{-1}$ at 0.1 *C*. High coulombic efficiency of 97.13 % and capacity retention of 93.6 % was achieved for the as-prepared $CoFe_2O_4$ nanospheres, indicating the excellent electrochemical reversibility and stability. Furthermore, $CoFe_2O_4$ demonstrated good rate capability with a reversible discharge capacity of higher than 1000 mAh $g^{-1}$ at 1 *C*, which is far higher than the commercial graphite anode in Li-ion batteries. The as-prepared $CoFe_2O_4$ nanospheres can be applied as a high capacity anode material for Li-ion batteries.

## 7.2 Part II Synthesis of Wintersweet-flower-like $CoFe_2O_4$/MWCNTs Hybrid Material

### 7.2.1 Introduction

As an anode material for Li-ion batteries, CNTs can offer a lower potential and accommodate more Li-ions than other carbonaceous material, such as carbon black, graphene or mesoporous carbon [293]. However, one serious drawback is that pristine CNTs easily entangle each other to form agglomerates, resulting in poor dispersibility and low lithium storage capability. Recently, hybrid materials, such as metal oxides combined with carbonaceous materials, have been proposed as a competitive strategy for developing of novel materials for high-performance Li-ion batteries. It is believed that hybrids can display some synergistic properties, which compensate for some disadvantages from the counterpart. Examples are metal oxides/graphene [192, 220, 294, 295], metal oxides/carbon sphere [296], and metal oxides/mesoporous carbon hybrids [224, 297]. All of these have demonstrated some improvements in electrochemical properties. In particular, CNTs have been used as electrode modifiers for Li-ion batteries in combination with $SnO_2$ [298-300], $TiO_2$ [301], $MnO_2$ [302, 303], NiO [304], CuO [168], $Fe_2O_3$ [305, 306], $Fe_3O_4$ [307], and $CeO_2$ [308]. For the reason that CNTs not only provide fast electron transfer during the lithiation-delithiation process, but also contribute to the discharge capacity [309]. However, it remains a challenge to synthesize electrode materials with high initial

discharge capacity, high columbic efficiency, good cyclic performance and high rate capability.

Herein, $CoFe_2O_4$ nanocrystals were synthesized by a hydrothermal reaction. To prevent the agglomeration of nanosized $CoFe_2O_4$, multiwall carbon nanotubes (MWCNTs) were added, both as the frameworks to anchor $CoFe_2O_4$ nanocrystals and as an efficient conducting network to facilitate the fast electron transport. Conversely, $CoFe_2O_4$ nanoclusters anchored on MWCNTs can also effectively separate entangled MWCNTs through the formation of the 130intersweet-flower-like nanoarchitecture. The electrochemical performances of the $CoFe_2O_4$/MWCNTs hybrid materials have been systematically investigated through cyclic voltammetry, galvanostatic charge/discharge cycling and electrochemical impedance spectroscopy.

### 7.2.2 Experimental

#### 7.2.2.1 Material synthesis

$CoFe_2O_4$/MWCNTs hybrid material was synthesized by a hydrothermal method. MWCNTs were purchased from Sigma Aldrich (outer diameter 110-170 nm, length 5-9 μm). In a typical procedure, anhydrous $FeCl_3$ (0.1254 g) and $CoCl_2$ $6H_2O$ (0.0892 g) were dissolved in ethylene glycol (EG, 10 mL), followed by the addition of diethylenetriamine (DETA, 2.5 mL). Then, KOH solution (0.187 g KOH in 5 mL EG) was added to the above solution. A clear brown solution was formed after stirring for 10 mins. Afterwards, MWCNTs (30 mg) were well dispersed into EG (10 mL) by treatment with an ultrasonic probe for 10 mins, and then the resulting suspension was charged into the above brown solution. After another 10 mins stirring, the mixture was transferred into a Teflon-lined autoclave and the reaction

temperature was maintained at 180 °C for 10 h. After cooling to room temperature, the resulting black precipitates were rinsed with distilled water and ethanol in a vacuum filtration apparatus. The final products were obtained after drying the precipitate at 80 °C under vacuum overnight. For comparison, the pristine $CoFe_2O_4$ sample was prepared according to the above procedure but without adding MWCNTs, and another batch of $CoFe_2O_4$/MWCNTs hybrid material was prepared without adding DETA.

#### 7.2.2.2 Characterization

XRPD data were collected on a Siemens D5000 Diffractometer with Cu Kα radiation ($\lambda = 0.15405$ nm) in the $2\theta$ range $10 \leq 2\theta \leq 80$ ° at a scan rate of 2 ° $min^{-1}$. FTIR spectrum was obtained using a Nicolet Magna IR-6700 spectrometer with a DTGS KBr detector. The powder of the $CoFe_2O_4$/MWCNTs hybrid material was dispersed in KBr discs and all spectra were obtained using 4 $cm^{-1}$ resolution and 64 scans at room temperature. TG was conducted on a SDT 2960 simultaneous analyser between 35 °C and 1000 °C at a heating rate of 10 °C $min^{-1}$ under air atmosphere. FESEM and TEM were applied to observe the surface morphology and crystal structure of the as-prepared materials. FESEM and TEM specimens were prepared by dropping the sample isopropanol solution onto silicon and copper substrates, respectively.

#### 7.2.2.3 Electrochemical testing

The electrochemical properties of pristine MWCNTs, $CoFe_2O_4$ and $CoFe_2O_4$/MWCNTs hybrid material were evaluated by assembling CR2032 coin cells inside an argon-filled glove box. For all cells, lithium foil was used as the counter electrode, and the electrolyte was a solution of 1M $LiPF_6$ in a mixture of EC:

DEC: DMC = 1:1:1. The pristine MWCNTs, $CoFe_2O_4$ and $CoFe_2O_4$/MWCNTs hybrid material were used as the active materials in different cells. A mixture of 80 wt% active material, 10 wt% carbon black and 10 wt% PVDF were dispersed in NMP to form a slurry. CV was conducted in the voltage range 0.01-3 V at a scan rate of 0.1 mV $s^{-1}$. Cells were galvanostatically charged and discharged at various current densities in the voltage range 0.01-3.0 V. EIS was carried out in the frequency range of $10^5$-$10^{-2}$ Hz.

### 7.2.3 Results and discussion

#### 7.2.3.1 Characterization of $CoFe_2O_4$/MWCNTs Hybrid Material

Figure 7.8 shows the XRPD patterns of $CoFe_2O_4$/MWCNTs hybrid material, pristine $CoFe_2O_4$, and the standard XRPD pattern of cubic $CoFe_2O_4$.

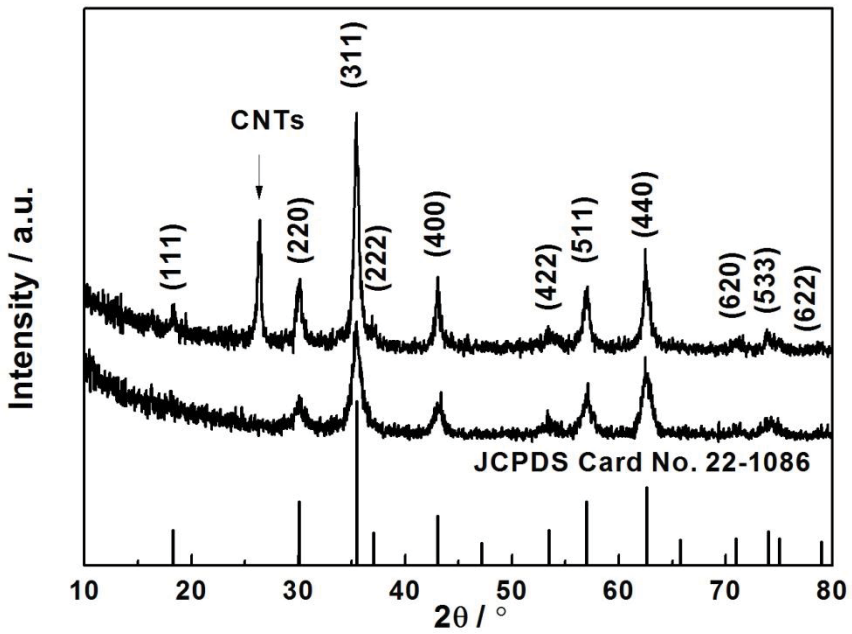


Figure 7.8 XRPD patterns of (a) $CoFe_2O_4$/MWCNTs hybrid material and (b) pristine $CoFe_2O_4$. The standard XRPD pattern of the cubic $CoFe_2O_4$ is presented on the bottom

Both samples can be indexed to the cubic structure of $CoFe_2O_4$ with the *Fd*3m (227) space group (JCPDS Card No. 22-1086). The diffraction peak appeared at $2\theta = 26.4$ ° in the diffraction line (a) is derived from CNTs [310]. The XRPD patterns clearly confirm that the hybrid material consists of MWCNTs and well-crystallized $CoFe_2O_4$. The broad diffraction peaks indicate the nanocrystalline nature of $CoFe_2O_4$.

Figure 7.9 (a) shows the FTIR spectrum of $CoFe_2O_4$/MWCNTs hybrid material. The broad peak at 3407 $cm^{-1}$ corresponds with O-H stretching vibrations of ethylene glycol (EG) or possibly absorbed water molecules. Two weak peaks at 2919 $cm^{-1}$ and 2849 $cm^{-1}$ are characteristic of asymmetrical and symmetrical stretchings of methylene ($CH_2$) groups [311]. The absorption bands at 1634 $cm^{-1}$ and 1045 $cm^{-1}$ are attributed to the N-H bend vibration and C-N stretch vibration from diethylenetriamine (DETA). Meanwhile, the in-plane bend vibration of the 133intersw group is located at 1386 $cm^{-1}$. In addition, the strong adsorption peak at 578 $cm^{-1}$ is associated with the metal-oxygen stretch vibration of $CoFe_2O_4$. The FTIR spectrum demonstrates that small amounts of DETA and EG exist in the final product, which is further confirmed by the TG analysis, as shown in Figure 7.9 (b). The first weight loss of 1.0 wt% (region A) occurred at 110 °C and can mainly be ascribed to the loss of physically absorbed moisture. The second weight loss of 2.5 wt% from 110 °C to 350 °C is due to the decomposition of DETA (region B), followed by the 37.5 wt% weight loss (region C) at 350-700 °C, which is associated with the decomposition of MWCNTs. Based on TG analysis, the hybrid material consists of 59 wt% $CoFe_2O_4$ and 37.5 wt% MWCNTs.

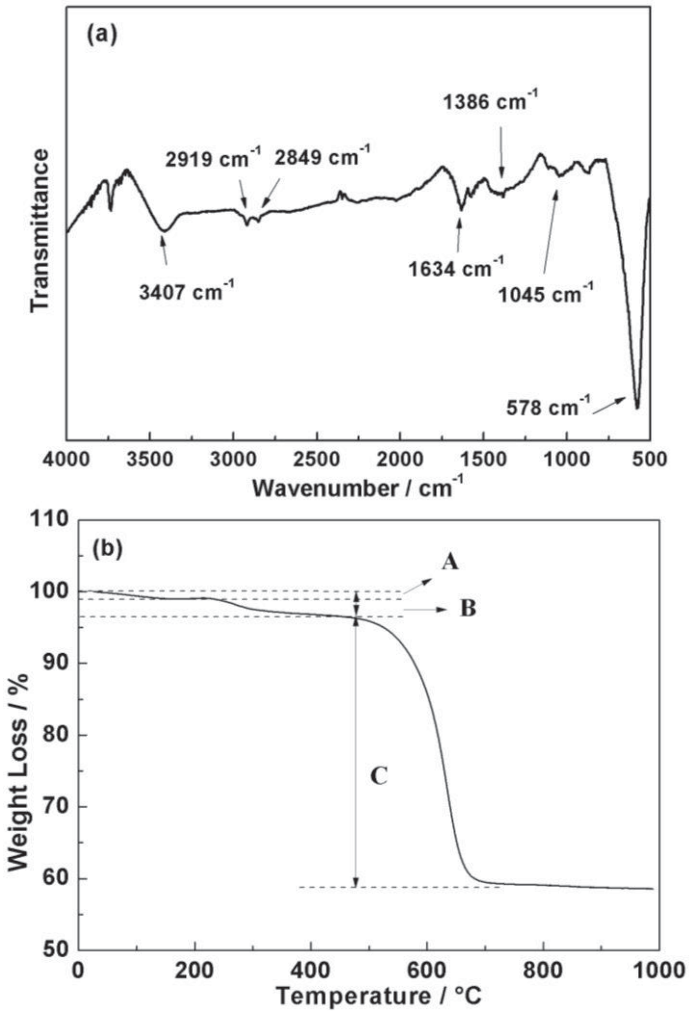


Figure 7.9 (a) FTIR spectrum and (b) TG curves of $CoFe_2O_4$/MWCNTs hybrid material

7.2.3.2 Morphology of $CoFe_2O_4$/MWCNTs Hybrid Material

Figure 7.10 shows the FESEM images of the as-prepared $CoFe_2O_4$/MWCNTs hybrid material at different magnifications. The low-magnification FESEM image in Figure 7.10 (a) shows well-separated MWCNTs anchored with $CoFe_2O_4$ quasi-spheres, which mimic the 134intersweet flowers in nature. As observed from the enlarged FESEM images (Figure 7.10 (b) and (c)), these quasi-spherical $CoFe_2O_4$ nanoclusters have an average size of about 200 nm. Figure 7.10 (d) further clearly demonstrates

that the $CoFe_2O_4$ nanoclusters are firmly anchored to individual carbon nanotubes, which helps to separate the entangled MWCNTs. In the case of pristine $CoFe_2O_4$ (Figure 7.11), even though the mean size of primary particles is quite small, large agglomerates formed under the same synthetic conditions. Therefore, the presence of MWCNTs is essential to suppress the growth of $CoFe_2O_4$ nanoparticles and prevent the agglomeration of the $CoFe_2O_4$ nanoparticles.

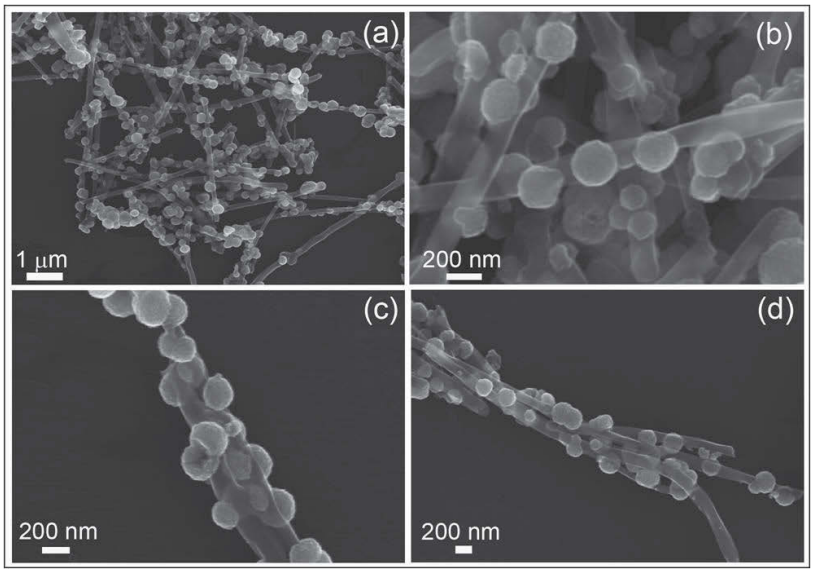


Figure 7.10 (a) Low-magnification FESEM image, and (b-d) high-magnification FESEM images of the as-prepared $CoFe_2O_4$/MWCNTs hybrid material

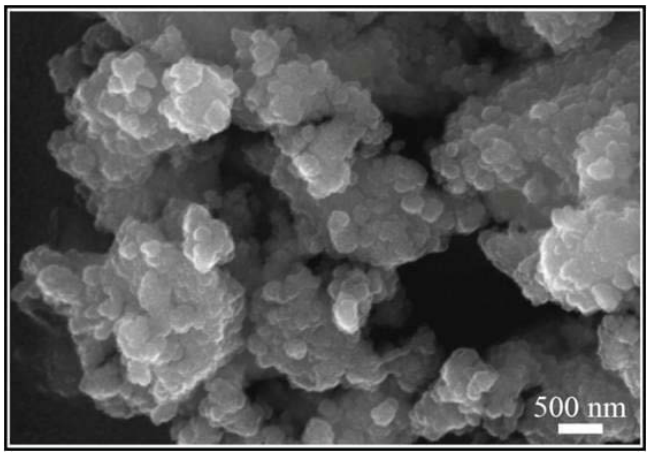


Figure 7.11 FESEM image of the pristine $CoFe_2O_4$ without adding MWCNTs

TEM images and selected-area electron diffraction (SAED) patterns (shown in Figure 7.12) were collected to determine the crystal structure of the as-prepared $CoFe_2O_4$/MWCNTs hybrid material.

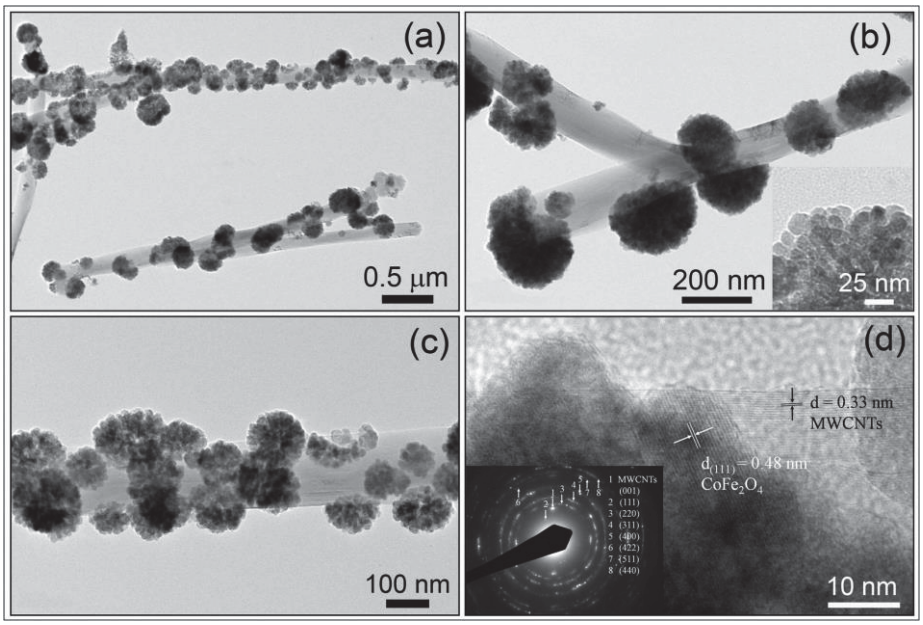


Figure 7.12 (a) Low-magnification TEM image, and (b) and (c) high-magnification TEM images of $CoFe_2O_4$/MWCNTs hybrid material. (d) Lattice resolved HR-TEM image of $CoFe_2O_4$ nanoparticles and MWCNTs. The inset in (b) is an enlarged $CoFe_2O_4$ nanocluster, indicative of the size of the primary $CoFe_2O_4$ nanocrystal. The inset in (d) is the SAED pattern of $CoFe_2O_4$/MWCNTs hybrid material. 1 MWCNTs (001), 2 (111), 3(220), 4 (311), 5 (400), 6 (422), 7 (511), 8 (440)

Figure 7.12 (a) shows a panoramic view of the $CoFe_2O_4$/MWCNTs hybrid material, with quasi-spherical $CoFe_2O_4$ nanoclusters evenly spread along each carbon nanotube. The high-magnification TEM images of $CoFe_2O_4$/MWCNTs in Figure 7.12 (b) and (c) display the typical 136 intersweet flower buds-on-branches morphology. It can be seen that $CoFe_2O_4$ nanoclusters are firmly anchored to MWCNTs without any loose $CoFe_2O_4$ nanoparticles, even after prolonged sonication

during the preparation of the TEM specimen. This finding suggests the strong adhesion of $CoFe_2O_4$ nanoparticles to MWCNTs. From the magnified image of an individual $CoFe_2O_4$ nanocluster (Figure 7.12 (b) inset), the primary crystal size of $CoFe_2O_4$ can be determined to be around 5-10 nm. Figure 7.12 (d) shows a lattice-resolved HR-TEM image of the $CoFe_2O_4$/MWCNTs hybrid material. The 0.48 nm lattice fringe corresponds to the (111) crystal planes of $CoFe_2O_4$, while the 0.33 nm lattice fringe arises from the (001) planes of MWCNTs. As shown in the inset in Figure 7.12 (d), the first SAED ring can be readily indexed to MWCNTs of the (001) planes. The rest of the SAED rings have been fully indexed to the cubic structure of $CoFe_2O_4$ phase.

In the hydrothermal synthetic process, DETA as a strong coordinating agent can coordinate with metal ions ($Fe^{3+}$ and $Co^{2+}$) to form stable complexes, which reduce the concentration of free metal ions in the solution and slow the further growth of nuclei. As Zhu *et al.* reported, "When a relatively high temperature and vapour pressure built up in the autoclave, the complex decomposed and released DETA. The newly formed crystallites had a strong tendency to attach to the MWCNTs, and started to form nanospheres, driven by the minimization of interfacial energy and magnetic dipole-dipole interaction" [227]. Based on Zhu's work, it is believed that such a ligand can form a layer on the surface of newly formed $CoFe_2O_4$ nanocrystals and further assist their assembly into nanoclusters. FTIR analysis also confirms the existence of DETA in the final hybrid material. When DETA was not added to the hydrothermal reaction system, the obtained $CoFe_2O_4$ product had a large particle size and was not uniform (Figure 7.13). Therefore, the presence of DETA plays an important role in the synthesis of 137 intersweet-flower-like $CoFe_2O_4$/MWCNTs

hybrid material. In addition, based on our experiments, if the loading ratio between $CoFe_2O_4$ and MWCNTs is increased, $CoFe_2O_4$ nanoparticles grow and aggregate outside the carbon nanotubes (Figure 7.14). Therefore, the loading mass of $CoFe_2O_4$ on MWCNTs is also crucial for the formation of 138 intersweet-flower-like architecture.

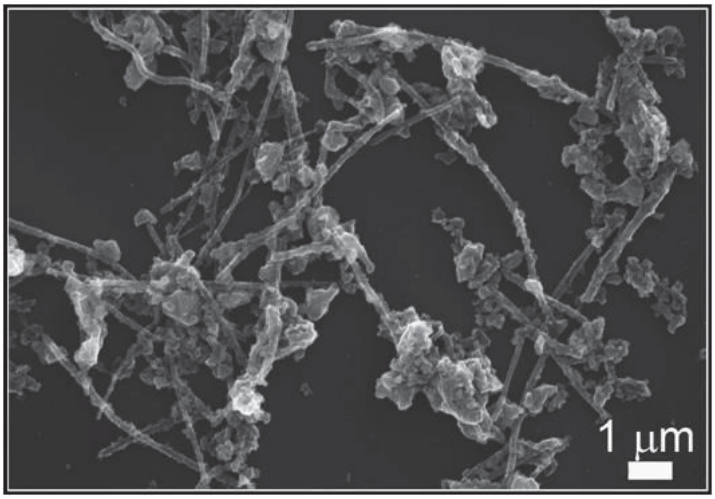


Figure 7.13 FESEM image of the $CoFe_2O_4$/MWCNTs hybrid material without adding DETA

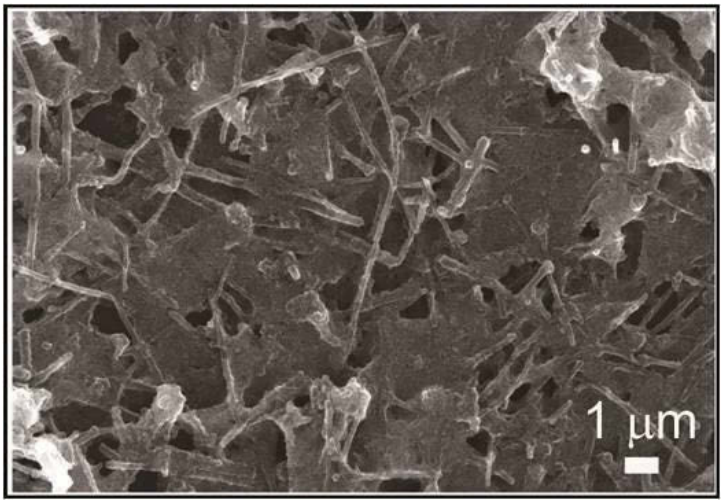


Figure 7.14 FESEM image of the $CoFe_2O_4$/MWCNTs hybrid material with increased loading mass of $CoFe_2O_4$ on MWCNTs

7.2.3.3 Electrochemical Performances of the $CoFe_2O_4$/MWCNTs Hybrid Electrode

Figure 7.15 (a) shows the CV of the $CoFe_2O_4$/MWCNTs electrode at a scan rate of 0.1 mV $s^{-1}$ in the voltage range 0.01-3 V *vs.* $Li/Li^+$. There is a significant difference in the CV profiles of $CoFe_2O_4$/MWCNTs hybrid material between the first discharge process and the subsequent cycles, indicating the different reaction mechanisms. The same phenomenon has been observed in the CV profiles of the pristine $CoFe_2O_4$ electrode, shown in Figure 7.15 (b). This finding is consistent with the previous reports [278, 312]. In Figure 7.15 (a), in the first cycle, the sharp peak centred at 0.62 V in the cathodic polarization process corresponds to the reduction of $Fe^{3+}$ and $Co^{2+}$ to their metallic states and the formation of $Li_2O$, accompanying by the decomposition of organic electrolyte to form a solid electrolyte interphase (SEI) layer [312]. The reduction process can be formulated as $CoFe_2O_4 + 8Li^+ + 8e^- \leftrightarrow Co + 2Fe + 4Li_2O$. A main broad peak centred at 1.63 V, in the anodic polarization process, is related to the multistep oxidation of metallic Fe and Co to $Fe^{3+}$ and $Co^{2+}$. The reaction can be expressed as $Co + 2Fe + 4Li_2O \leftrightarrow CoO + Fe_2O_3 + 8Li$. In the subsequent scans, two peaks located at 0.75 V and 1.36 V can be attributed to the multistep electrochemical reactions, and the anodic peak slightly shifts to a higher potential compared with the initial one. The decrease of the redox peak intensities and integrated areas between the first scan and the subsequent cycles implies the irreversible capacity loss in the initial lithiation-delithiation process. However, it should be noted that all redox peaks remained almost unchanged between the second and third cycles, indicating the good electrochemical reversibility of the $CoFe_2O_4$/MWCNTs electrode. On the contrary, the peak intensities and integrate

areas of the redox peaks for the pristine $CoFe_2O_4$ electrode continued to decrease (shown in Figure 7.15 (b)), suggesting the poor electrochemical reversibility.

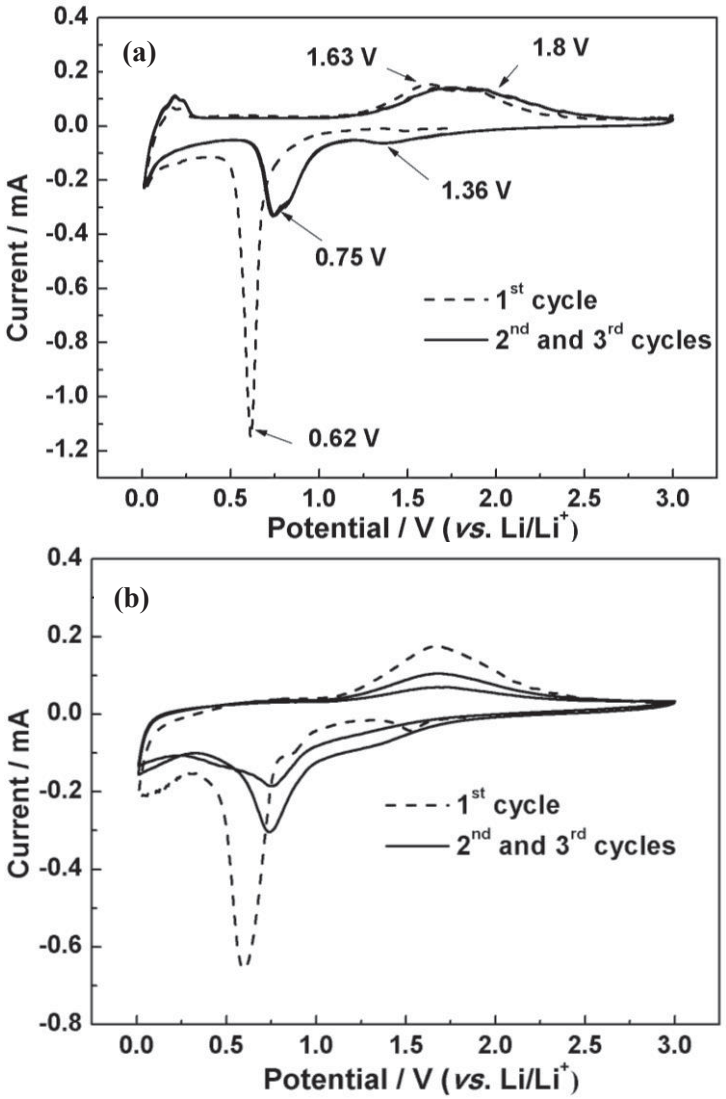


Figure 7.15 Cyclic voltammograms of the (a) $CoFe_2O_4$/MWCNTs and (b) pristine $CoFe_2O_4$ electrode at a scan rate of 0.1 mV $s^{-1}$ between 0.01 and 3 V (vs. $Li/Li^+$)

Figure 7.16 shows galvanostatic charge-discharge and cycling performances of the $CoFe_2O_4$/MWCNTs hybrid material, pristine MWCNTs, and $CoFe_2O_4$. As shown in Figure 7.16 (a), the charge-discharge curves feature the typical properties of carbon nanotubes [163]. The initial charge and discharge capacities of pristine MWCNTs

are 369 and 523 mAh $g^{-1}$. Figure 7.16 (b), (c) shows the charge-discharge profiles of the pristine $CoFe_2O_4$ and $CoFe_2O_4$/MWCNTs electrodes in the first, second and 50$^{th}$ cycles respectively. Both the voltage profiles in the first cycle show a sharp slope in the initial stage of the discharge, a flat voltage plateau at about 0.86 V and a long slope until 0.01 V. When discharged to 0.01 V, the initial discharge capacities of the pristine $CoFe_2O_4$ and $CoFe_2O_4$/MWCNTs hybrid electrodes are 1427 and 1016 mAh $g^{-1}$, which are much higher than the corresponding calculated theoretical value of 916 and 705 mAh $g^{-1}$ respectively. The large excess capacities could be ascribed to the decomposition of organic electrolytes in the voltage range 0.05-0.8 V. Interfacial storage in nanocrystalline materials could also contribute to the large excess capacity [291]. Meanwhile, the initial charge capacity of the as-prepared hybrid material is 740 mAh $g^{-1}$, corresponding to a high initial columbic efficiency of 72.8 %. It should be noted that the $CoFe_2O_4$/MWCNTs hybrid material showed a better initial columbic efficiency than those of previously reported $SnO_2$-CNT (42 %) [298], NiO/MWCNT (66.45 %) [304], CuO-CNT (50 %) [168], CNT/$Fe_3O_4$ (67 %) [307], $MnO_2$/CNT (< 50 %) [169], and the pristine $CoFe_2O_4$ (56.6 %). As shown in Figure 7.16 (b), the discharge capacity of the pristine $CoFe_2O_4$ electrode rapidly drops to 822 mAh $g^{-1}$ in the second cycle. However, the $CoFe_2O_4$/MWCNTs electrode demonstrated a much better reversibility for lithium storage than the pristine $CoFe_2O_4$ electrode. It gives a reversible discharge capacity of 800 mAh $g^{-1}$ in the second cycle. Furthermore, the $CoFe_2O_4$/MWCNTs electrode exhibited an excellent cycling performance. The electrode maintained a capacity of 823 mAh $g^{-1}$ after 50 cycles, with a capacity retention of nearly 100 % (Figure 7.16 (d)), whereas the

capacity retentions of pure MWCNTs and $CoFe_2O_4$ are 85.5 % and 12.4 % respectively.

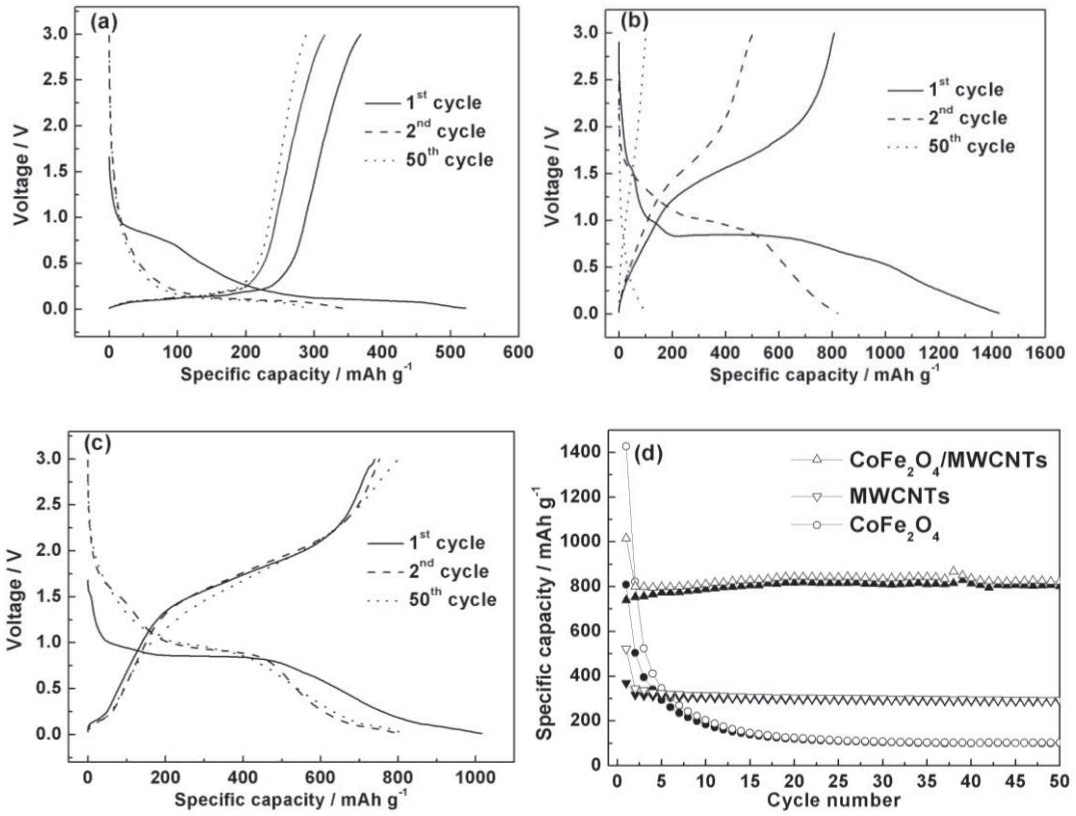


Figure 7.16 Charge-discharge profiles of (a) pristine MWCNTs, (b) pristine $CoFe_2O_4$, and (c) $CoFe_2O_4$/MWCNTs hybrid material for the first, second, and 50$^{th}$ cycles between 0.01 and 3 V. (d) Cycling performances of pristine MWCNTs, $CoFe_2O_4$, and $CoFe_2O_4$/MWCNTs electrodes. All cells are cycled at a current density of 45 mA $g^{-1}$. The charge capacities are presented as solid symbols, while discharge capacities are shown as hollow symbols

The rate capabilities of $CoFe_2O_4$/MWCNTs hybrid material, pristine $CoFe_2O_4$ and MWCNTs electrodes were tested under various current densities. Ten cycles were carried out on each current density in the voltage range 0.01-3 V at room temperature. As shown in Figure 7.17, the $CoFe_2O_4$/MWCNTs electrode delivers the discharge

capacities of 792 and 804 mAh $g^{-1}$ after 10 cycles at the current densities of 45 and 90 mAh $g^{-1}$ respectively. Comparatively, the reversible capacity of the pure $CoFe_2O_4$ electrode quickly drops from 218 to 127 mAh $g^{-1}$. At higher current densities of 180, 450, 900 and 1800 mAh $g^{-1}$, the reversible capacities of the $CoFe_2O_4$/MWCNTs electrode are 809, 765, 539 and 359 mAh $g^{-1}$ respectively. The pristine $CoFe_2O_4$ electrode exhibits a very low reversible capacity of less than 100 mAh $g^{-1}$ under the same charge-discharge conditions (note: the cyclic test at the current density of 1800 mAh $g^{-1}$ for pristine $CoFe_2O_4$ cells was not carried out, because of the failure of the cell).

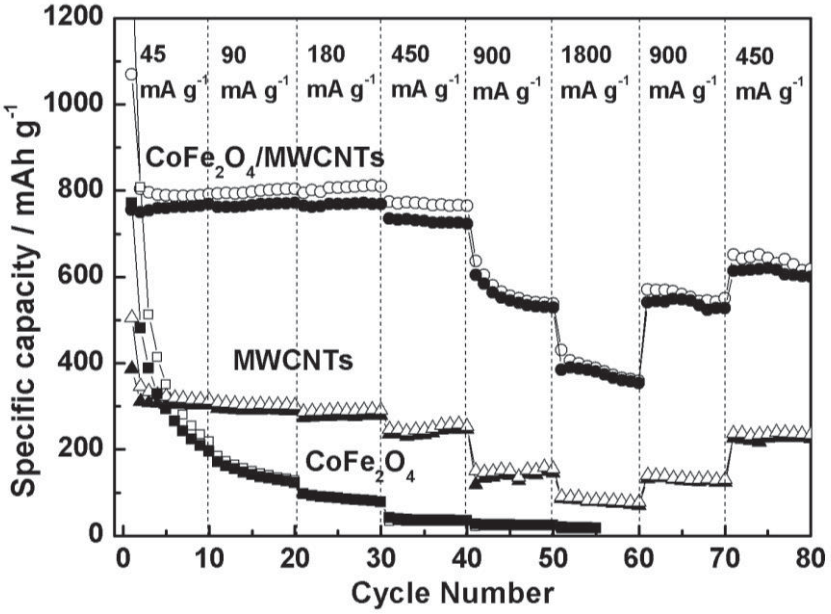


Figure 7.17 Cyclabilities of $CoFe_2O_4$/MWCNTs hybrid material, pristine MWCNTs, and pristine $CoFe_2O_4$ electrodes between 0.01 and 3 V at various current densities. The charge capacities are presented as solid symbols, while discharge capacities are shown as hollow symbols

The poor rate capability of pristine $CoFe_2O_4$ cells could be attributed to the severe aggregation of nanoparticles and the low electronic conductivity. The

$CoFe_2O_4$/MWCNTs electrode also presents similar discharge profiles when the current is increased (Figure 7.18), suggesting the fast lithium diffusion in the electrode. In addition, the $CoFe_2O_4$/MWCNTs electrode can recover high capacity when the current densities are reversed to a low value. We also observed that the pristine MWCNTs electrode exhibited relatively poor rate performance, with the reversible capacities lower than 300 mAh $g^{-1}$ after 20 cycles. Furthermore, the $CoFe_2O_4$/MWCNTs hybrid materials exhibited excellent cyclability at high current densities (Figure 7.19). Overall, the $CoFe_2O_4$/MWCNTs hybrid material shows a much improved rate capability than pristine $CoFe_2O_4$, pristine MWCNTs, $Co_3O_4$/graphene [192], $SnO_2$-CNT [298], CuO-CNT [168] and $SnO_2$-graphene nanocomposites [313].

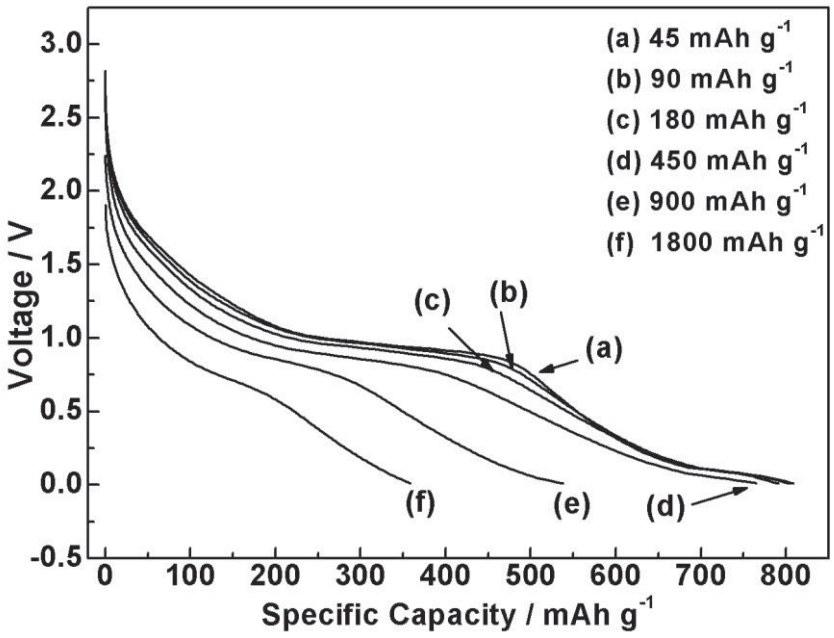


Figure 7.18 Discharge profiles of the $CoFe_2O_4$/MWCNTs electrode between 0.01 and 3 V at various current densities

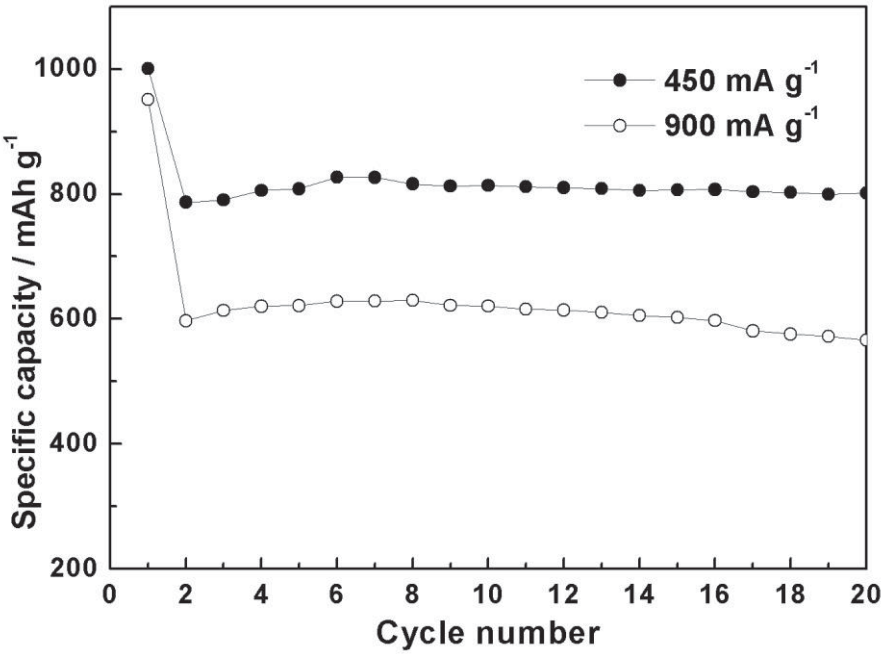


Figure 7.19 Cycling performances of the $CoFe_2O_4$/MWCNTs electrode between 0.01 and 3 V at higher current densities

The enhanced electrochemical properties of $CoFe_2O_4$/MWCNTs hybrid material can be ascribed to the unique 145intersweet-flower-like nanoarchitecture. The $CoFe_2O_4$ nanocrystals contributed to the increase in Li storage; while the carbon nanotube network can accommodate the volume variation induced by the redox reaction of $CoFe_2O_4$ with Li, as well as form a perfect framework for easy access of Li-ions and fast electron transport. In addition, TEM analysis confirmed that each porous $CoFe_2O_4$ nanocluster consists of nanocrystals with the sizes 5-10 nm, which enables the possibility of a more efficient diffusion of lithium ions, large reaction areas, facile penetration of electrolytes and extra charge storage. The AC impedance spectra (Figure 7.20) further identified the fast charge transfer inside the $CoFe_2O_4$/MWCNTs cell, which is evidenced by much smaller electron transfer resistance than in the pristine $CoFe_2O_4$ cell.

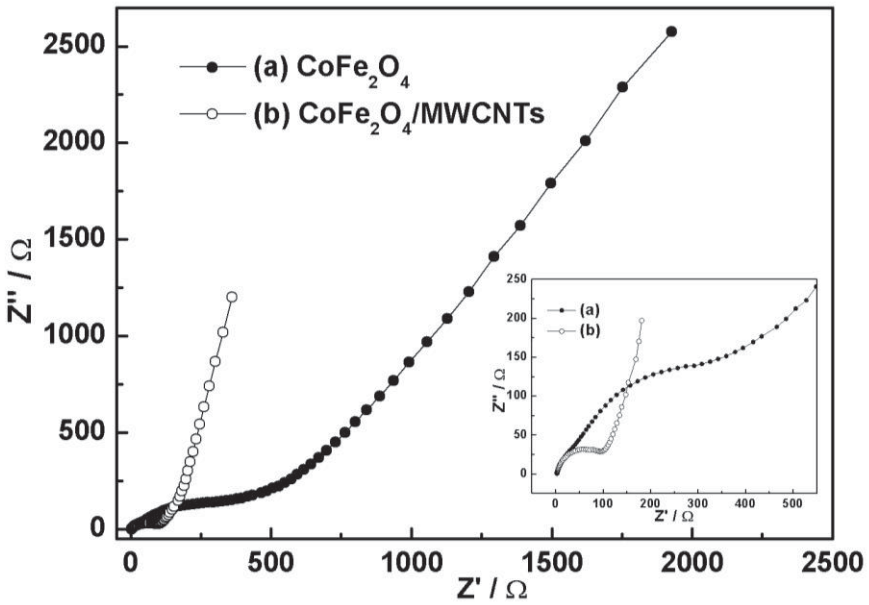


Figure 7.20 AC impedance spectra of pristine $CoFe_2O_4$ and the $CoFe_2O_4$/MWCNTs cells. Both cells were subjected to 20 cycles between 0.01-3 V at the current density of 45 mA $g^{-1}$ and then measured in a frequency range from $10^{-2}$ Hz to $10^5$ Hz. The inset shows the zoom-in the area of the high frequency range. The intercepts of the high frequency semicircles on the X axis demonstrate the corresponding electron transfer resistance

The FESEM images of the $CoFe_2O_4$/MWCNTs electrodes before and after the cycling test further confirmed the structure stability of this hybrid material (Figure 7.21). Therefore, the overall electrochemical performance can be efficiently improved by forming the unique hybrid nanoarchitecture.

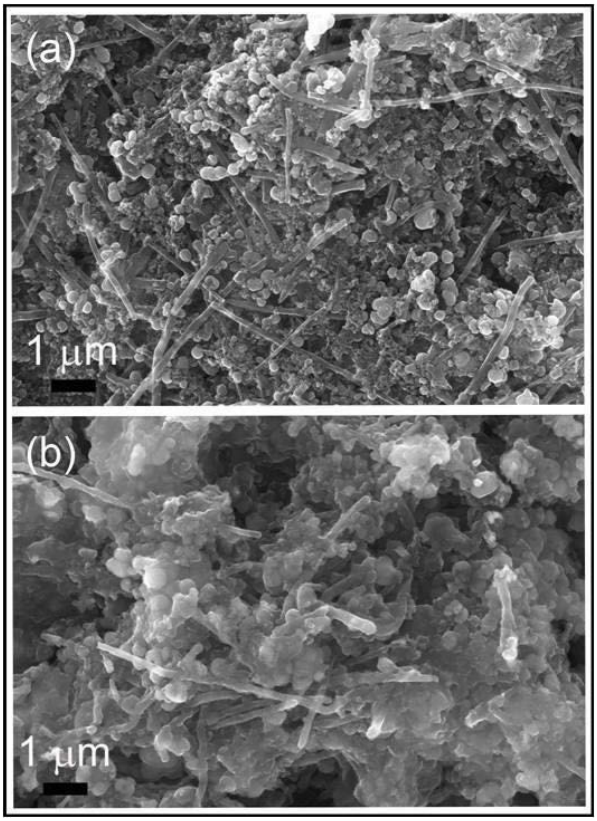


Figure 7.21 FESEM images of the $CoFe_2O_4$/MWCNTs electrode (a) before and (b) after long-term charge-discharge test

### 7.2.4 Conclusions

The $CoFe_2O_4$/MWCNTs hybrid material was prepared by a hydrothermal method. FESEM and TEM characterizations confirmed that $CoFe_2O_4$ nanoclusters were anchored on individual carbon nanotubes, resembling the 147intersweet flower buds-on-branches nanoarchitecture. Each $CoFe_2O_4$ nanocluster consists of tiny nanocrystals with a size of 5-10 nm. This unique nanoarchitecture leads to double effects in suppressing the growth of $CoFe_2O_4$ crystals and separating the agglomeration of MWCNTs. The electrochemical properties of $CoFe_2O_4$/MWCNTs hybrid material have been fully evaluated through a series of electrochemical tests. The $CoFe_2O_4$/MWCNTs hybrid material exhibited a high reversible capacity, stable

cycling performance and a high rate capability for lithium storage. The good electrochemical performance of $CoFe_2O_4$/MWCNTs hybrid material could be credited to the synergistic effect, with contributions from $CoFe_2O_4$ nanocrystals and MWCNTs. On the one hand, the MWCNTs matrix can effectively cushion the volume change of $CoFe_2O_4$ nanocrystals during the lithiation and de-lithiation process and provide electronic conductivity for the insulating $CoFe_2O_4$. On the other hand, $CoFe_2O_4$ nanocrystals contribute high capacity for lithium storage. This strategy could also be applied to prepare other hybrid materials for high energy Li-ion batteries.

# CHAPTER 8 Conclusions and Outlook

## 8.1 Conclusions

In this thesis, several approaches were demonstrated in the design of nanostructured electrode materials for Li-ion batteries. The electrochemical properties of these materials were systematically evaluated. The relationship among the synthetic procedure, morphology and final practical applications have been studied, which will help to understand the rationale and principles within an electrochemical system, and as a guide to further design a better battery system. Some additional considerations on materials for rechargeable batteries are the following:

1) Alloy-based materials, particularly Si and Ge, provide extremely high capacity, which opens a new era for high-performance Li-ion batteries with high energy/power density. However, problems associated with volume expansion and contraction during de-lithiation/lithiation need to be negotiated before any mass production or even commercialization. Therefore, attention must be paid on this area.
2) Graphene as an anode material for Li-ion batteries has attracted considerable attention recently, as it features unique 2D architecture, allowing fast electron transfer. Studies have shown that graphene composite material demonstrated improved electrochemical performances over its pristine counterparts. Without doubt, this direction will provide lots of opportunities in improving battery technology.

3) Fundamental research into sodium-ion batteries is needed, as they provide an alternative to Li-ion batteries, with the advantage that they have natural abundance and low cost.

## 8.2 Outlook

Compared with technologies in Lead-acid batteries and Ni-H batteries, rechargeable Li-ion batteries are still in the infant stage. Searching for thinner, lighter, greener, more efficient and durable batteries motivates continuous improvements in battery technology. From both the chemistry and engineering prospective, such improvements should arise from the following aspects:

1) Nanostructured material with specified morphology, could improve battery performance by providing numerous active sites and facile electronic/ionic transfer and diffusion. It is necessary to understand the mechanisms of lithium storage in nanomaterials and the kinetic transport on the surface of the electrode and electrolyte.
2) Applications of nanotechnology in energy storage areas are in the research stage. The mass production of nanomaterials is not straightforward or economic. Some novel synthetic strategies (top-down and bottom-up) have been developed to fabricate novel nanostructures [314, 315]. This may shed light on the synthesis of nanostructured electrode materials for Li-ion batteries.
3) The performance of rechargeable batteries not only depends essentially on the thermodynamics and kinetics of the electrochemical reaction involved in the whole system, but also on the external energy management system. Therefore, the knowledge required in a battery system encompasses fields of

electrochemistry, materials chemistry, physics, engineering, surface science and electronics. A better battery system could be developed and thus meet consumers' demands by integrating multi-discipline knowledge and techniques from these areas.

# REFERENCES


1. F.Y. Cheng, J. Liang, Z.L. Tao and J. Chen, Functional materials for rechargeable batteries. *Advanced Materials*, (2011). **23**(15): p. 1695-1715.
2. D. Linden and B.R. Thomas, eds. *Handbook of batteries*. 3rd ed. 2002, McGraw-Hill.
3. M. Armand and J.M. Tarascon, Building better batteries. *Nature*, (2008). **451**(7179): p. 652-657.
4. Z.L. Gong and Y. Yang, Recent advances in the research of polyanion-type cathode materials for Li-ion batteries. *Energy & Environmental Science*, (2011). **4**(9): p. 3223-3242.
5. Y. Wang and G.Z. Cao, Developments in nanostructured cathode materials for high-performance lithium-ion batteries. *Advanced Materials*, (2008). **20**(12): p. 2251-2269.
6. J. Chen and F.Y. Cheng, Combination of lightweight elements and nanostructured materials for batteries. *Accounts of Chemical Research*, (2009). **42**(6): p. 713-723.
7. G.-A. Nazri and G. Pistoia, *Lithium batteries: science and technology*. 2009: Springer.
8. A. Yoshino, The birth of the lithium-ion battery. *Angewandte Chemie-International Edition*, (2012). **51**(24): p. 5798-5800.
9. J.M. Tarascon and M. Armand, Issues and challenges facing rechargeable lithium batteries. *Nature*, (2001). **414**(6861): p. 359-367.
10. H. Kim and J. Cho, Superior lithium electroactive mesoporous Si@carbon core-shell nanowires for lithium battery anode material. *Nano Letters*, (2008). **8**(11): p. 3688-3691.
11. K. Mizushima, P.C. Jones, P.J. Wiseman and J.B. Goodenough, $Li_xCoO_2$: A new cathode material for batteries of high energy density. *Materials Research Bulletin*, (1980). **15**(6): p. 783-789.
12. E. Antolini, $LiCoO_2$: formation, structure, lithium and oxygen nonstoichiometry, electrochemical behaviour and transport properties. *Solid State Ionics*, (2004). **170**(3-4): p. 159-171.
13. E.-D. Jeong, M.-S. Won and Y.-B. Shim, Cathodic properties of a lithium-ion secondary battery using $LiCoO_2$ prepared by a complex formation reaction. *Journal of Power Sources*, (1998). **70**(1): p. 70-77.

14. Y. Li, C. Wan, Y. Wu, C. Jiang and Y. Zhu, Synthesis and characterization of ultrafine $LiCoO_2$ powders by a spray-drying method. *Journal of Power Sources*, (2000). **85**(2): p. 294-298.
15. P.N. Kumta, D. Gallet, A. Waghray, G.E. Blomgren and M.P. Setter, Synthesis of $LiCoO_2$ powders for lithium-ion batteries from precursors derived by rotary evaporation. *Journal of Power Sources*, (1998). **72**(1): p. 91-98.
16. F. Jiao, K.M. Shaju and P.G. Bruce, Synthesis of nanowire and mesoporous low-temperature $LiCoO_2$ by a post-templating reaction. *Angewandte Chemie-International Edition*, (2005). **44**(40): p. 6550-6553.
17. X.X. Li, F.Y. Cheng, B. Guo and J. Chen, Template-synthesized $LiCoO_2$, $LiMn_2O_4$, and $LiNi_{0.8}Co_{0.2}O_2$ nanotubes as the cathode materials of lithium ion batteries. *Journal of Physical Chemistry B*, (2005). **109**(29): p. 14017-14024.
18. M. Thackeray, Lithium-ion batteries - An unexpected conductor. *Nature Materials*, (2002). **1**(2): p. 81-82.
19. R. Alcantara, P. Lavela, J.L. Tirado, E. Zhecheva and R. Stoyanova, SPES, Li-6 MAS NMR, and $Ni^{3+}$ EPR evidence for the formation of $Co^{2+}$-containing spinel phases in $LiCoO_2$ cycled electrode materials. *Journal of Electroanalytical Chemistry*, (1998). **454**(1-2): p. 173-181.
20. J. Cho, Y.J. Kim and B. Park, Novel $LiCoO_2$ cathode material with $Al_2O_3$ coating for a Li ion cell. *Chemistry of Materials*, (2000). **12**(12): p. 3788-3791.
21. J. Cho, J.G. Lee, B. Kim and B. Park, Effect of $P_2O_5$ and $AlPO_4$ coating on $LiCoO_2$ cathode material. *Chemistry of Materials*, (2003). **15**(16): p. 3190-3193.
22. H. Miyashiro, A. Yamanaka, M. Tabuchi, S. Seki, M. Nakayama, Y. Ohno, Y. Kobayashi, Y. Mita, A. Usami and M. Wakihara, Improvement of degradation at elevated temperature and at high state-of-charge storage by $ZrO_2$ coating on $LiCoO_2$. *Journal of the Electrochemical Society*, (2006). **153**(2): p. A348-A353.
23. G. Li, Z.X. Yang and W.S. Yang, Effect of $FePO_4$ coating on electrochemical and safety performance of $LiCoO_2$ as cathode material for Li-ion batteries. *Journal of Power Sources*, (2008). **183**(2): p. 741-748.
24. J.R. Dahn, U. von Sacken and C.A. Michal, Structure and electrochemistry of $Li_{1\pm y}NiO_2$ and a new $Li_2NiO_2$ phase with the $Ni(OH)_2$ structure. *Solid State Ionics*, (1990). **44**(1–2): p. 87-97.

25. N.Q. Ye, C.J. Liu and S.Y. Shen, Drawbacks and improve ways of $LiNiO_2$ as a cathode material for lithium ion batteries. *Journal of Inorganic Materials*, (2004). **19**(6): p. 1217-1224.
26. M.S. Whittingham, Lithium batteries and cathode materials. *Chemical Reviews*, (2004). **104**(10): p. 4271-4302.
27. P. He, H.R. Wang, L. Qi and T. Osaka, Electrochemical characteristics of layered $LiNi_{1/3}Co_{1/3}Mn_{1/3}O_2$ and with different synthesis conditions. *Journal of Power Sources*, (2006). **160**(1): p. 627-632.
28. F. Capitaine, P. Gravereau and C. Delmas, A new variety of $LiMnO_2$ with a layered structure. *Solid State Ionics*, (1996). **89**(3–4): p. 197-202.
29. Z.X. Wang, Y.C. Sun, L.Q. Chen and X.J. Huang, Electrochemical characterization of positive electrode material $LiNi_{1/3}Co_{1/3}Mn_{1/3}O_2$ and compatibility with electrolyte for lithium-ion batteries. *Journal of the Electrochemical Society*, (2004). **151**(6): p. A914-A921.
30. Y. Idemoto, Y. Takanashi and N. Kitamura, Dependence of property, crystal structure and electrode characteristics on Li content for $Li_xNi_{0.8}Co_{0.2}O_2$ as a cathode active material for Li secondary battery. *Journal of Power Sources*, (2009). **189**(1): p. 269-278.
31. K.S. Lee, S.T. Myung, J.S.M. Moon and Y.K. Sun, Particle size effect of $Li[Ni_{0.5}Mn_{0.5}]O_2$ prepared by co-precipitation. *Electrochimica Acta*, (2008). **53**(20): p. 6033-6037.
32. B. Zhang, G. Chen, P. Xu and Z. Lv, Effect of ultrasonic irradiation on the structure and electrochemical properties of cathode material $LiNi_{0.5}Mn_{0.5}O_2$ for lithium batteries. *Solid State Ionics*, (2007). **178**(19-20): p. 1230-1234.
33. T. Ohzuku and Y. Makimura, Layered lithium insertion material of $LiNi_{1/2}Mn_{1/2}O_2$: A possible alternative to $LiCoO_2$ for advanced lithium-ion batteries. *Chemistry Letters*, (2001)(8): p. 744-745.
34. Y.K. Sun, S.T. Myung, B.C. Park, J. Prakash, I. Belharouak and K. Amine, High-energy cathode material for long-life and safe lithium batteries. *Nature Materials*, (2009). **8**(4): p. 320-324.
35. I. Belharouak, Y.K. Sun, J. Liu and K. Amine, $Li(Ni_{1/3}Co_{1/3}Mn_{1/3})O_2$ as a suitable cathode for high power applications. *Journal of Power Sources*, (2003). **123**(2): p. 247-252.

36. N. Yabuuchi and T. Ohzuku, Novel lithium insertion material of $LiCo_{1/3}Ni_{1/3}Mn_{1/3}O_2$ for advanced lithium-ion batteries. *Journal of Power Sources*, (2003). **119–121**(0): p. 171-174.

37. B.J. Hwang, Y.W. Tsai, D. Carlier and G. Ceder, A combined computational/experimental study on $LiNi_{1/3}Co_{1/3}Mn_{1/3}O_2$. *Chemistry of Materials*, (2003). **15**(19): p. 3676-3682.

38. R. Guo, P.F. Shi, X.Q. Cheng and C.Y. Du, Synthesis and characterization of carbon-coated $LiNi_{1/3}Co_{1/3}Mn_{1/3}O_2$ cathode material prepared by polyvinyl alcohol pyrolysis route. *Journal of Alloys and Compounds*, (2009). **473**(1-2): p. 53-59.

39. Y.G. Liang, X.Y. Han, X.W. Zhou, J.T. Sun and Y.H. Zhou, Significant improved electrochemical performance of $Li(Ni_{1/3}Co_{1/3}Mn_{1/3})O_2$ cathode on volumetric energy density and cycling stability at high rate. *Electrochemistry Communications*, (2007). **9**(5): p. 965-970.

40. K.M. Shaju and P.G. Bruce, Macroporous $Li(Ni_{1/3}Co_{1/3}Mn_{1/3})O_2$: A high-power and high-energy cathode for rechargeable lithium batteries. *Advanced Materials*, (2006). **18**(17): p. 2330-2334.

41. Z.D. Huang, X.M. Liu, S.W. Oh, B.A. Zhang, P.C. Ma and J.K. Kim, Microscopically porous, interconnected single crystal $LiNi_{1/3}Co_{1/3}Mn_{1/3}O_2$ cathode material for Lithium ion batteries. *Journal of Materials Chemistry*, (2011). **21**(29): p. 10777-10784.

42. Z.H. Lu, L.Y. Beaulieu, R.A. Donaberger, C.L. Thomas and J.R. Dahn, Synthesis, structure, and electrochemical behavior of $LiNi_xLi_{1/3-2x/3}Mn_{2/3-x/3}O_2$. *Journal of the Electrochemical Society*, (2002). **149**(6): p. A778-A791.

43. K. Numata and S. Yamanaka, Preparation and electrochemical properties of layered lithium-cobalt-manganese oxides. *Solid State Ionics*, (1999). **118**(1-2): p. 117-120.

44. J. Bareno, C.H. Lei, J.G. Wen, S.H. Kang, I. Petrov and D.P. Abraham, Local structure of layered oxide electrode materials for lithium-ion batteries. *Advanced Materials*, (2010). **22**(10): p. 1122-1127.

45. M.M. Thackeray, S.H. Kang, C.S. Johnson, J.T. Vaughey, R. Benedek and S.A. Hackney, $Li_2MnO_3$-stabilized $LiMO_2$ (M = Mn, Ni, Co) electrodes for lithium-ion batteries. *Journal of Materials Chemistry*, (2007). **17**(30): p. 3112-3125.

46. C.S. Johnson, J.S. Kim, C. Lefief, N. Li, J.T. Vaughey and M.M. Thackeray, The significance of the $Li_2MnO_3$ component in 'composite' $xLi_2MnO_3 \cdot (1 -$

x)$LiMn_{0.5}Ni_{0.5}O_2$ electrodes. *Electrochemistry Communications*, (2004). **6**(10): p. 1085-1091.

47. A.D. Robertson and P.G. Bruce, Mechanism of Electrochemical Activity in $Li_2MnO_3$. *Chemistry of Materials*, (2003). **15**(10): p. 1984-1992.
48. J.-S. Kim, C.S. Johnson, J.T. Vaughey, M.M. Thackeray, S.A. Hackney, W. Yoon and C.P. Grey, Electrochemical and structural properties of $xLi_2M'O_3 \cdot (1-x)LiMn_{0.5}Ni_{0.5}O_2$ electrodes for lithium batteries (M' = Ti, Mn, Zr; $0 \leq x \leq 0.3$). *Chemistry of Materials*, (2004). **16**(10): p. 1996-2006.
49. T.A. Arunkumar, Y. Wu and A. Manthiram, Factors influencing the irreversible oxygen loss and reversible capacity in layered $Li[Li_{1/3}Mn_{2/3}]O_2-Li[M]O_2$ (M = $Mn_{0.5-y}Ni_{0.5-y}Co_{2y}$ and $Ni_{1-y}Co_y$) solid solutions. *Chemistry of Materials*, (2007). **19**(12): p. 3067-3073.
50. J. Kikkawa, T. Akita, M. Tabuchi, K. Tatsumi and M. Kohyama, Participation of oxygen in charge/discharge reactions in $Li_{1.2}Mn_{0.4}Fe_{0.4}O_2$: evidence of removal/reinsertion of oxide ions. *Journal of the Electrochemical Society*, (2011). **158**(6): p. A760-A768.
51. M. Jiang, B. Key, Y.S. Meng and C.P. Grey, Electrochemical and structural study of the layered, "Li-excess" lithium-ion battery electrode material $Li[Li_{1/9}Ni_{1/3}Mn_{5/9}]O_2$. *Chemistry of Materials*, (2009). **21**(13): p. 2733-2745.
52. Y. Wu and A. Manthiram, High capacity, surface-modified layered Li $Li_{(1-x)/3}Mn_{(2-x)/3}Ni_{x/3}Co_{x/3}O_2$ cathodes with low irreversible capacity loss. *Electrochemical and Solid State Letters*, (2006). **9**(5): p. A221-A224.
53. Y.J. Kang, J.H. Kim, S.W. Lee and Y.K. Sun, The effect of $Al(OH)_3$ coating on the $Li[Li_{0.2}Ni_{0.2}Mn_{0.6}]O_2$ cathode material for lithium secondary battery. *Electrochimica Acta*, (2005). **50**(24): p. 4784-4791.
54. Y. Wu and A. Manthiram, Effect of $Al^{3+}$ and $F^-$ doping on the irreversible oxygen loss from layered $Li[Li_{0.17}Mn_{0.58}Ni_{0.25}]O_2$ cathodes. *Electrochemical and Solid State Letters*, (2007). **10**(6): p. A151-A154.
55. Q.Y. Wang, J. Liu, A.V. Murugan and A. Manthiram, High capacity double-layer surface modified $Li[Li_{0.2}Mn_{0.54}Ni_{0.13}Co_{0.13}]O_2$ cathode with improved rate capability. *Journal of Materials Chemistry*, (2009). **19**(28): p. 4965-4972.
56. J. Liu and A. Manthiram, Functional surface modifications of a high capacity layered $Li[Li_{0.2}Mn_{0.54}Ni_{0.13}Co_{0.13}]O_2$ cathode. *Journal of Materials Chemistry*, (2010). **20**(19): p. 3961-3967.

57. J. Liu, Q.Y. Wang, B. Reeja-Jayan and A. Manthiram, Carbon-coated high capacity layered $Li[Li_{0.2}Mn_{0.54}Ni_{0.13}Co_{0.13}]O_2$ cathodes. *Electrochemistry Communications*, (2010). **12**(6): p. 750-753.

58. J. Liu, B. Reeja-Jayan and A. Manthiram, Conductive surface modification with aluminum of high capacity layered $Li[Li_{0.2}Mn_{0.54}Ni_{0.13}Co_{0.13}]O_2$ cathodes. *Journal of Physical Chemistry C*, (2010). **114**(20): p. 9528-9533.

59. Y. Wu, A.V. Murugan and A. Manthiram, Surface modification of high capacity layered $Li[Li_{0.2}Mn_{0.54}Ni_{0.13}Co_{0.13}]O_2$ cathodes by $AlPO_4$. *Journal of the Electrochemical Society*, (2008). **155**(9): p. A635-A641.

60. Y. Wu and A. Manthiram, Effect of surface modifications on the layered solid solution cathodes $(1 - z)Li[Li_{1/3}Mn_{2/3}]O_2$-$(z)Li[Mn_{0.5 - y}Ni_{0.5 - y}Co_{2y}]O_2$. *Solid State Ionics*, (2009). **180**(1): p. 50-56.

61. J.M. Zheng, Z.R. Zhang, X.B. Wu, Z.X. Dong, Z. Zhu and Y. Yang, The effects of $AlF_3$ coating on the performance of $Li[Li_{0.2}Mn_{0.54}Ni_{0.13}Co_{0.13}]O_2$ positive electrode material for lithium-ion battery. *Journal of the Electrochemical Society*, (2008). **155**(10): p. A775-A782.

62. J.M. Zheng, J. Li, Z.R. Zhang, X.J. Guo and Y. Yang, The effects of $TiO_2$ coating on the electrochemical performance of $Li[Li_{0.2}Mn_{0.54}Ni_{0.13}Co_{0.13}]O_2$ cathode material for lithium-ion battery. *Solid State Ionics*, (2008). **179**(27-32): p. 1794-1799.

63. Z.Q. Deng and A. Manthiram, Influence of cationic substitutions on the oxygen loss and reversible capacity of lithium-rich layered oxide cathodes. *Journal of Physical Chemistry C*, (2011). **115**(14): p. 7097-7103.

64. J. Gao and A. Manthiram, Eliminating the irreversible capacity loss of high capacity layered $Li[Li_{0.2}Mn_{0.54}Ni_{0.13}Co_{0.13}]O_2$ cathode by blending with other lithium insertion hosts. *Journal of Power Sources*, (2009). **191**(2): p. 644-647.

65. J. Gao, J. Kim and A. Manthiram, High capacity $Li[Li_{0.2}Mn_{0.54}Ni_{0.13}Co_{0.13}]O_2$-$V_2O_5$ composite cathodes with low irreversible capacity loss for lithium ion batteries. *Electrochemistry Communications*, (2009). **11**(1): p. 84-86.

66. M. Winter, J.O. Besenhard, M.E. Spahr and P. Novák, Insertion Electrode Materials for Rechargeable Lithium Batteries. *Advanced Materials*, (1998). **10**(10): p. 725-763.

67. M.M. Thackeray, Structural considerations of layered and spinellithiatied oxides for lithium ion batteries. *Journal of the Electrochemical Society*, (1995). **142**(8): p. 2558-2563.

68. E. Hosono, T. Kudo, I. Honma, H. Matsuda and H.S. Zhou, Synthesis of single crystalline spinel $LiMn_2O_4$ nanowires for a lithium ion battery with high power density. *Nano Letters*, (2009). **9**(3): p. 1045-1051.

69. S. Lim and J. Cho, PVP-Assisted $ZrO_2$ coating on $LiMn_2O_4$ spinel cathode nanoparticles prepared by $MnO_2$ nanowire templates. *Electrochemistry Communications*, (2008). **10**(10): p. 1478-1481.

70. S.T. Myung, S. Komaba, N. Kumagai, H. Yashiro, H.T. Chung and T.H. Cho, Nano-crystalline $LiNi_{0.5}Mn_{1.5}O_4$ synthesized by emulsion drying method. *Electrochimica Acta*, (2002). **47**(15): p. 2543-2549.

71. M. Kunduraci and G.G. Amatucci, Synthesis and characterization of nanostructured 4.7 V $Li_xMn_{1.5}Ni_{0.5}O_4$ spinels for high-power lithium-ion batteries. *Journal of the Electrochemical Society*, (2006). **153**(7): p. A1345-A1352.

72. J.C. Arrebola, A. Caballero, M. Cruz, L. Hernan, J. Morales and E.R. Castellon, Crystallinity control of a nanostructured $LiNi_{0.5}Mn_{1.5}O_4$ spinet via polymer-assisted synthesis: A method for improving its rate capability and performance in 5 V lithium batteries. *Advanced Functional Materials*, (2006). **16**(14): p. 1904-1912.

73. M.S. Islam, R. Dominko, C. Masquelier, C. Sirisopanaporn, A.R. Armstrong and P.G. Bruce, Silicate cathodes for lithium batteries: alternatives to phosphates? *Journal of Materials Chemistry*, (2011). **21**(27): p. 9811-9818.

74. M. de Dompablo, J.M. Gallardo-Amores, J. Garcia-Martinez, E. Moran, J.M. Tarascon and M. Armand. *Is it possible to prepare olivine-type $LiFeSiO_4$? A joint computational and experimental investigation*. in *16th International Conference on Solid State Ionics*. 2007. Shanghai, People's Republic of China.

75. A.K. Padhi, K.S. Nanjundaswamy and J.B. Goodenough, Phospho-olivines as positive-electrode materials for rechargeable lithium batteries. *Journal of the Electrochemical Society*, (1997). **144**(4): p. 1188-1194.

76. W. Xing-Long, J. Ling-Yan, C. Fei-Fei, G. Yu-Guo and W. Li-Jun, $LiFePO_4$ nanoparticles embedded in a nanoporous carbon matrix: superior cathode material for electrochemical energy-storage devices. *Advanced Materials*, (2009). **21**(25-26): p. 2710-2714.

77. H. Joachin, T.D. Kaun, K. Zaghib and J. Prakash, Electrochemical and thermal studies of carbon-coated $LiFePO_4$ cathode. *Journal of the Electrochemical Society*, (2009). **156**(6): p. A401-A406.

78. L.X. Yuan, Z.H. Wang, W.X. Zhang, X.L. Hu, J.T. Chen, Y.H. Huang and J.B. Goodenough, Development and challenges of $LiFePO_4$ cathode material for lithium-ion batteries. *Energy & Environmental Science*, (2011). **4**(2): p. 269-284.

79. J.J. Wang and X.L. Sun, Understanding and recent development of carbon coating on $LiFePO_4$ cathode materials for lithium-ion batteries. *Energy & Environmental Science*, (2012). **5**(1): p. 5163-5185.

80. S.Y. Chung, J.T. Bloking and Y.M. Chiang, Electronically conductive phospho-olivines as lithium storage electrodes. *Nature Materials*, (2002). **1**(2): p. 123-128.

81. A. Yamada, H. Koizumi, N. Sonoyama and R. Kanno, Phase change in $Li_xFePO_4$. *Electrochemical and Solid State Letters*, (2005). **8**(8): p. A409-A413.

82. P.P. Prosini, M. Lisi, D. Zane and M. Pasquali, Determination of the chemical diffusion coefficient of lithium in $LiFePO_4$. *Solid State Ionics*, (2002). **148**(1–2): p. 45-51.

83. R. Amin, J. Maier, P. Balaya, D.P. Chen and C.T. Lin, Ionic and electronic transport in single crystalline $LiFePO_4$ grown by optical floating zone technique. *Solid State Ionics*, (2008). **179**(27–32): p. 1683-1687.

84. H. Huang, S.C. Yin and L.F. Nazar, Approaching theoretical capacity of $LiFePO_4$ at room temperature at high rates. *Electrochemical and Solid State Letters*, (2001). **4**(10): p. A170-A172.

85. Z.H. Chen and J.R. Dahn, Reducing carbon in $LiFePO_4$/C composite electrodes to maximize specific energy, volumetric energy, and tap density. *Journal of the Electrochemical Society*, (2002). **149**(9): p. A1184-A1189.

86. F. Yu, J.J. Zhang, Y.F. Yang and G.Z. Song, Up-scalable synthesis, structure and charge storage properties of porous microspheres of $LiFePO_4$@C nanocomposites. *Journal of Materials Chemistry*, (2009). **19**(48): p. 9121-9125.

87. L. Wang, G.C. Liang, X.Q. Ou, X.K. Zhi, J.P. Zhang and J.Y. Cui, Effect of synthesis temperature on the properties of $LiFePO_4$/C composites prepared by carbothermal reduction. *Journal of Power Sources*, (2009). **189**(1): p. 423-428.

88. D. Lepage, C. Michot, G.X. Liang, M. Gauthier and S.B. Schougaard, A soft chemistry approach to coating of $LiFePO_4$ with a conducting polymer. *Angewandte Chemie-International Edition*, (2011). **50**(30): p. 6884-6887.

89. K. Saravanan, M.V. Reddy, P. Balaya, H. Gong, B.V.R. Chowdari and J.J. Vittal, Storage performance of $LiFePO_4$ nanoplates. *Journal of Materials Chemistry*, (2009). **19**(5): p. 605-610.

90. Y.H. Huang and J.B. Goodenough, High-rate $LiFePO_4$ lithium rechargeable battery promoted by electrochemically active polymers. *Chemistry of Materials*, (2008). **20**(23): p. 7237-7241.

91. W. Yonggang, W. Yarong, H. Eiji, W. Kaixue and Z. Haoshen, The design of a $LiFePO_4$ carbon nanocomposite with a core-shell structure and its synthesis by an in situ polymerization restriction method. *Angewandte Chemie International Edition*, (2008). **47**(39): p. 7461-7465.

92. L. Gangtie, Y. Xiaohua, W. Lei, L. Zhaohui and Z. Ji, An investigation of the electrochemical performance of polyaniline coated $LiFePO_4$ materials. *Polymers for Advanced Technologies*, (2009). **20**(6): p. 576-580.

93. S.Y. Chen, B. Gao, L.H. Su, C.H. Mi and X.G. Zhang, Electrochemical properties of $LiFePO_4$/C synthesized using polypyrrole as carbon source. *Journal of Solid State Electrochemistry*, (2009). **13**(9): p. 1361-1366.

94. A.V. Murugan, T. Muraliganth and A. Manthiram, Rapid microwave-solvothermal synthesis of phospho-olivine nanorods and their coating with a mixed conducting polymer for lithium ion batteries. *Electrochemistry Communications*, (2008). **10**(6): p. 903-906.

95. A. Fedorkova, H.D. Wiemhofer, R. Orinakova, A. Orinak, M.C. Stan, M. Winter, D. Kaniansky and A.N. Alejos, Improved lithium exchange at $LiFePO_4$ cathode particles by coating with composite polypyrrole-polyethylene glycol layers. *Journal of Solid State Electrochemistry*, (2009). **13**(12): p. 1867-1872.

96. H.M. Xie, R.S. Wang, J.R. Ying, L.Y. Zhang, A.F. Jalbout, H.Y. Yu, G.L. Yang, X.M. Pan and Z.M. Su, Optimized $LiFePO_4$-polyacene cathode material for lithium-ion batteries. *Advanced Materials*, (2006). **18**(19): p. 2609-2613.

97. Y.H. Nien, J.R. Carey and J.S. Chen, Physical and electrochemical properties of $LiFePO_4$/C composite cathode prepared from various polymer-containing precursors. *Journal of Power Sources*, (2009). **193**(2): p. 822-827.

98. B. Zhao, Y. Jiang, H. Zhang, H. Tao, M. Zhong and Z. Jiao, Morphology and electrical properties of carbon coated $LiFePO_4$ cathode materials. *Journal of Power Sources*, (2009). **189**(1): p. 462-466.

99. Y.H. Huang, K.S. Park and J.B. Goodenough, Improving lithium batteries by tethering carbon-coated $LiFePO_4$ to polypyrrole. *Journal of the Electrochemical Society*, (2006). **153**(12): p. A2282-A2286.

100. N. Ravet, M. Gauthier, K. Zaghib, J.B. Goodenough, A. Mauger, F. Gendron and C.M. Julien, Mechanism of the $Fe^{3+}$ reduction at low temperature for $LiFePO_4$ synthesis from a polymeric additive. *Chemistry of Materials*, (2007). **19**(10): p. 2595-2602.

101. M. Gaberscek, R. Dominko and J. Jamnik, Is small particle size more important than carbon coating? An example study on $LiFePO_4$ cathodes. *Electrochemistry Communications*, (2007). **9**(12): p. 2778-2783.

102. C. Delacourt, P. Poizot, S. Levasseur and C. Masquelier, Size effects on carbon-free $LiFePO_4$ powders. *Electrochemical and Solid State Letters*, (2006). **9**(7): p. A352-A355.

103. Y.-D. Cho, G.T.-K. Fey and H.-M. Kao, The effect of carbon coating thickness on the capacity of $LiFePO_4$/C composite cathodes. *Journal of Power Sources*, (2009). **189**(1): p. 256-262.

104. J.R. Ying, M. Lei, C.Y. Jiang, C.R. Wan, X.M. He, J.J. Li, L. Wang and J.G. Ren, Preparation and characterization of high-density spherical $Li_{0.97}Cr_{0.01}FePO_4$/C cathode material for lithium ion batteries. *Journal of Power Sources*, (2006). **158**(1): p. 543-549.

105. N. Recham, J.N. Chotard, J.C. Jumas, L. Laffont, M. Armand and J.M. Tarascon, Ionothermal synthesis of Li-based fluorophosphates electrodes. *Chemistry of Materials*. **22**(3): p. 1142-1148.

106. X.J. Chen, G.S. Cao, X.B. Zhao, J.P. Tu and T.J. Zhu, Electrochemical performance of $LiFe_{1-x}V_xPO_4$/carbon composites prepared by solid-state reaction. *Journal of Alloys and Compounds*, (2008). **463**(1-2): p. 385-389.

107. S.-h. Wu, M.-S. Chen, C.-J. Chien and Y.-P. Fu, Preparation and characterization of $Ti^{4+}$-doped $LiFePO_4$ cathode materials for lithium-ion batteries. *Journal of Power Sources*, (2009). **189**(1): p. 440-444.

108. G. Wang, Y. Cheng, M.M. Yan and Z.Y. Jiang, $Li_{0.99}Ti_{0.01}FePO_4$/C composite as cathode material for lithium ion battery. *Journal of Solid State Electrochemistry*, (2007). **11**(4): p. 457-462.

109. N. Jayaprakash and N. Kalaiselvi, On the electrochemical behavior of $LiM_XFe_{1-X}PO_4$ [M = Cu, Sn; X=0.02] anodes - An approach to enhance the anode performance of $LiFePO_4$. *Electrochemistry Communications*, (2007). **9**(4): p. 620-628.

110. M.R. Yang and W.H. Ke, The doping effect on the electrochemical properties of $LiFe_{0.95}M_{0.05}PO_4$ (M=$Mg^{2+}$, $Ni^{2+}$, $Al^{3+}$, or $V^{3+}$) as cathode materials for lithium-ion cells. *Journal of the Electrochemical Society*, (2008). **155**(10): p. A729-A732.

111. H. Gwon, D.-H. Seo, S.-W. Kim, J. Kim and K. Kang, Combined first-principle calculations and experimental study on multi-component olivine cathode for lithium rechargeable batteries. *Advanced Functional Materials*, (2009). **19**(20): p. 3285-3292.

112. N.N. Bramnik, K. Nikolowski, C. Baehtz, K.G. Bramnik and H. Ehrenberg, Phase transitions occurring upon lithium insertion−extraction of $LiCoPO_4$. *Chemistry of Materials*, (2007). **19**(4): p. 908-915.

113. S.K. Martha, J. Grinblat, O. Haik, E. Zinigrad, T. Drezen, J.H. Miners, I. Exnar, A. Kay, B. Markovsky and D. Aurbach, $LiMn_{0.8}Fe_{0.2}PO_4$: an advanced cathode material for rechargeable lithium batteries. *Angewandte Chemie-International Edition*, (2009). **48**(45): p. 8559-8563.

114. H.L. Wang, Y. Yang, Y.Y. Liang, L.F. Cui, H.S. Casalongue, Y.G. Li, G.S. Hong, Y. Cui and H.J. Dai, $LiMn_{1-x}Fe_xPO_4$ nanorods grown on graphene sheets for ultrahigh-rate-performance lithium ion batteries. *Angewandte Chemie-International Edition*, (2011). **50**(32): p. 7364-7368.

115. S.M. Oh, S.T. Myung, J.B. Park, B. Scrosati, K. Amine and Y.K. Sun, Double-structured $LiMn_{0.85}Fe_{0.15}PO_4$ coordinated with $LiFePO_4$ for rechargeable lithium batteries. *Angewandte Chemie-International Edition*, (2012). **51**(8): p. 1853-1856.

116. Y.S. Hu, Y.G. Guo, R. Dominko, M. Gaberscek, J. Jamnik and J. Maier, Improved electrode performance of porous $LiFePO_4$ using $RuO_2$ as an oxidic nanoscale interconnect. *Advanced Materials*, (2007). **19**(15): p. 1963-1966.

117. C.S. Li, S.Y. Zhang, F.Y. Cheng, W.Q. Ji and J. Chen, Porous $LiFePO_4$/NiP composite nanospheres as the cathode materials in rechargeable lithium ion batteries. *Nano Research*, (2008). **1**(3): p. 242-248.

118. K.T. Lee and K.S. Lee, Electrochemical properties of $LiFe_{0.9}Mn_{0.1}PO_4/Fe_2P$ cathode material by mechanical alloying. *Journal of Power Sources*, (2009). **189**(1): p. 435-439.

119. G.T.K. Fey, Y.G. Chen and H.M. Kao. *Electrochemical properties of $LiFePO_4$ prepared via ball-milling*. in *14th International Meeting on Lithium Batteries*. 2008. Tianjin, People's Republic of China.

120. C.-Z. Lu, G.T.-K. Fey and H.-M. Kao, Study of $LiFePO_4$ cathode materials coated with high surface area carbon. *Journal of Power Sources*, (2009). **189**(1): p. 155-162.

121. B. Ellis, W.H. Kan, W.R.M. Makahnouk and L.F. Nazar, Synthesis of nanocrystals and morphology control of hydrothermally prepared $LiFePO_4$. *Journal of Materials Chemistry*, (2007). **17**(30): p. 3248-3254.

122. K. Dokko, S. Koizumi, H. Nakano and K. Kanamura, Particle morphology, crystal orientation, and electrochemical reactivity of $LiFePO_4$ synthesized by the hydrothermal method at 443 K. *Journal of Materials Chemistry*, (2007). **17**(45): p. 4803-4810.

123. M.K. Devaraju and I. Honma, Hydrothermal and solvothermal process towards development of $LiMPO_4$ (M = Fe, Mn) nanomaterials for lithium-ion batteries. *Advanced Energy Materials*, (2012). **2**(3): p. 284-297.

124. R. Dominko, M. Bele, J.M. Goupil, M. Gaberscek, D. Hanzel, I. Arcon and J. Jamnik, Wired porous cathode materials: a novel concept for synthesis of $LiFePO_4$. *Chemistry of Materials*, (2007). **19**(12): p. 2960-2969.

125. M. Konarova and I. Taniguchi, Physical and electrochemical properties of $LiFePO_4$ nanoparticles synthesized by a combination of spray pyrolysis with wet ball-milling. *Journal of Power Sources*, (2009). **194**(2): p. 1029-1035.

126. N. Recham, L. Dupont, M. Courty, K. Djellab, D. Larcher, M. Armand and J.M. Tarascon, Ionothermal synthesis of tailor-made $LiFePO_4$ powders for Li-ion battery applications. *Chemistry of Materials*, (2009). **21**(6): p. 1096-1107.

127. C.M. Doherty, R.A. Caruso, B.M. Smarsly and C.J. Drummond, Colloidal crystal templating to produce hierarchically porous $LiFePO_4$ electrode materials for high power lithium ion batteries. *Chemistry of Materials*, (2009). **21**(13): p. 2895-2903.

128. S.Y. Lim, C.S. Yoon and J.P. Cho, Synthesis of nanowire and hollow $LiFePO_4$ cathodes for high-performance lithium batteries. *Chemistry of Materials*, (2008). **20**(14): p. 4560-4564.

129. J.M. Tarascon, N. Recham, M. Armand, J.N. Chotard, P. Barpanda, W. Walker and L. Dupont, Hunting for better Li-based electrode materials via low temperature inorganic synthesis. *Chemistry of Materials*. **22**(3): p. 724-739.

130. F. Zhou, M. Cococcioni, K. Kang and G. Ceder, The Li intercalation potential of $LiMPO_4$ and $LiMSiO_4$ olivines with M = Fe, Mn, Co, Ni. *Electrochemistry Communications*, (2004). **6**(11): p. 1144-1148.

131. R. Dominko, I. Arcon, A. Kodre, D. Hanzel and M. Gaberscek. *In-situ XAS study on $Li_2MnSiO_4$ and $Li_2FeSiO_4$ cathode materials*. in *14th International Meeting on Lithium Batteries*. 2008. Tianjin, People's Republic of China.

132. A. Nyten, A. Abouimrane, M. Armand, T. Gustafsson and J.O. Thomas, Electrochemical performance of $Li_2FeSiO_4$ as a new Li-battery cathode material. *Electrochemistry Communications*, (2005). **7**(2): p. 156-160.

133. A. Nyten, S. Kamali, L. Haggstrom, T. Gustafsson and J.O. Thomas, The lithium extraction/insertion mechanism in $Li_2FeSiO_4$. *Journal of Materials Chemistry*, (2006). **16**(23): p. 2266-2272.

134. A.R. West and F.P. Glasser, Preparation and crystal chemistry of some tetrahedral $Li_3PO_4$-type compounds. *Journal of Solid State Chemistry*, (1972). **4**(1): p. 20-28.

135. C. Eames, A.R. Armstrong, P.G. Bruce and M.S. Islam, Insights into changes in voltage and structure of $Li_2FeSiO_4$ polymorphs for lithium-ion batteries. *Chemistry of Materials*, (2012). **24**(11): p. 2155-2161.

136. K. Zaghib, A.A. Salah, N. Ravet, A. Mauger, F. Gendron and C.M. Julien, Structural, magnetic and electrochemical properties of lithium iron orthosilicate. *Journal of Power Sources*, (2006). **160**(2): p. 1381-1386.

137. H.J. Guo, K.X. Xiang, X. Cao, X.H. Li, Z.X. Wang and L.M. Li, Preparation and characteristics of $Li_2FeSiO_4$/C composite for cathode of lithium ion batteries. *Transactions of Nonferrous Metals Society of China*, (2009). **19**(1): p. 166-169.

138. R. Dominko, $Li_2MSiO_4$ (Fe and/or Mn) cathode materials. *Journal of Power Sources*, (2008). **184**(2): p. 462-468.

139. K.C. Kam, T. Gustafsson and J.O. Thomas, Synthesis and electrochemical properties of nanostructured $Li_2FeSiO_4$/C cathode material for Li-ion batteries. *Solid State Ionics*, (2011). **192**(1): p. 356-359.

140. P.J. Zuo, T. Wang, G.Y. Cheng, X.Q. Cheng, C.Y. Du and G.P. Yin, Effects of carbon on the structure and electrochemical performance of $Li_2FeSiO_4$ cathode materials for lithium-ion batteries. *Rsc Advances*, (2012). **2**(17): p. 6994-6998.

141. Z.P. Yan, S. Cai, L.J. Miao, X. Zhou and Y.M. Zhao, Synthesis and characterization of in situ carbon-coated $Li_2FeSiO_4$ cathode materials for lithium ion battery. *Journal of Alloys and Compounds*, (2012). **511**(1): p. 101-106.

142. T. Muraliganth, K.R. Stroukoff and A. Manthiram, Microwave-solvothermal synthesis of nanostructured $Li_2MSiO_4$/C (M = Mn and Fe) cathodes for lithium-ion batteries. *Chemistry of Materials*, (2010). **22**(20): p. 5754-5761.

143. S. Zhang, C. Deng and S.Y. Yang, Preparation of nano-$Li_2FeSiO_4$ as cathode material for lithium-ion batteries. *Electrochemical and Solid State Letters*, (2009). **12**(7): p. A136-A139.

144. Z.L. Gong, Y.X. Li, G.N. He, J. Li and Y. Yang, Nanostructured $Li_2FeSiO_4$ electrode material synthesized through hydrothermal-assisted sol-gel process. *Electrochemical and Solid-state Letters*, (2008). **11**(5): p. A60-63.

145. D. Ensling, M. Stjerndahl, A. Nyten, T. Gustafsson and J.O. Thomas, A comparative XPS surface study of $Li_2FeSiO_4$/C cycled with LiTFSI- and $LiPF_6$-based electrolytes. *Journal of Materials Chemistry*, (2009). **19**(1): p. 82-88.

146. A. Nyten, M. Stjerndahl, H. Rensmo, H. Siegbahn, M. Armand, T. Gustafsson, K. Edstrom and J.O. Thomas, Surface characterization and stability phenomena in $Li_2FeSiO_4$ studied by PES/XPS. *Journal of Materials Chemistry*, (2006). **16**(34): p. 3483-3488.

147. M. Nadherna, R. Dominko, D. Hanzel, J. Reiter and M. Gaberscek, Electrochemical Behavior of $Li_2FeSiO_4$ with Ionic Liquids at Elevated Temperature. *Journal of the Electrochemical Society*, (2009). **156**(7): p. A619-A626.

148. I. Belharouak, A. Abouimrane and K. Amine, Structural and electrochemical characterization of $Li_2MnSiO_4$ cathode material. *Journal of Physical Chemistry C*, (2009). **113**(48): p. 20733-20737.

149. R. Dominko, M. Bele, M. Gaberscek, A. Meden, M. Remskar and J. Jamnik, Structure and electrochemical performance of $Li_2MnSiO_4$ and $Li_2FeSiO_4$ as potential Li-battery cathode materials. *Electrochemistry Communications*, (2006). **8**(2): p. 217-222.

150. R. Dominko, M. Bele, A. Kokalj, M. Gaberscek and J. Jamnik. *$Li_2MnSiO_4$ as a potential Li-battery cathode material*. in *13th International Meeting on Lithium Batteries*. 2006. Biarritz, France.

151. W.G. Liu, Y.H. Xu and R. Yang, Synthesis, characterization and electrochemical performance of $Li_2MnSiO_4$/C cathode material by solid-state reaction. *Journal of Alloys and Compounds*, (2009). **480**(2): p. L1-L4.

152. C. Deng, S. Zhang, B.L. Fu, S.Y. Yang and L. Ma, Characterization of $Li_2MnSiO_4$ and $Li_2FeSiO_4$ cathode materials synthesized via a citric acid assisted sol-gel method. *Materials Chemistry and Physics*. **120**(1): p. 14-17.

153. Y.X. Li, Z.L. Gong and Y. Yang. *Synthesis and characterization of $Li_2MnSiO_4$/C nanocomposite cathode material for lithium ion batteries*. in *13th International Meeting on Lithium Batteries*. 2006. Biarritz, France.

154. A. Kokalj, R. Dominko, G. Mali, A. Meden, M. Gaberscek and J. Jamnik, Beyond one-electron reaction in Li cathode materials: Designing $Li_2Mn_xFe_{1-x}SiO_4$. *Chemistry of Materials*, (2007). **19**(15): p. 3633-3640.

155. C. Deng, S. Zhang and S.Y. Yang, Effect of Mn substitution on the structural, morphological and electrochemical behaviors of $Li_2Fe_{1-x}Mn_xSiO_4$ synthesized via citric acid assisted sol-gel method. *Journal of Alloys and Compounds*, (2009). **487**(1-2): p. L18-L23.

156. Z.L. Gong, Y.X. Li and Y. Yang, Synthesis and characterization of $Li_2Mn_xFe_{1-x}SiO_4$ as a cathode material for lithium-ion batteries. *Electrochemical and Solid State Letters*, (2006). **9**(12): p. A542-A544.

157. Y. Chung, S. Yu, M.S. Song, S.S. Kim and W.I. Cho, Structural and electrochemical properties of $Li_2Mn_{0.5}Fe_{0.5}SiO_4$/C cathode nanocomposite. *Bulletin of the Korean Chemical Society*, (2011). **32**(12): p. 4205-4209.

158. L.M. Li, H.J. Guo, X.H. Li, Z.X. Wang, W.J. Peng, K.X. Xiang and X. Cao. *Effects of roasting temperature and modification on properties of $Li_2FeSiO_4$/C cathode*. in *$14^{th}$ International Meeting on Lithium Batteries*. 2008. Tianjin, People's Republic of China.

159. H. Hao, J.B. Wang, J.L. Liu, T. Huang and A.S. Yu, Synthesis, characterization and electrochemical performance of $Li_2FeSiO_4$/C cathode materials doped by vanadium at Fe/Si sites for lithium ion batteries. *Journal of Power Sources*, (2012). **210**: p. 397-401.

160. C. de las Casas and W.Z. Li, A review of application of carbon nanotubes for lithium ion battery anode material. *Journal of Power Sources*, (2012). **208**: p. 74-85.

161. H. Shioyama, The interactions of two chemical species in the interlayer spacing of graphite. *Synthetic Metals*, (2000). **114**(1): p. 1-15.

162. S. Iijima, Helical microtubules of graphitic carbon. *Nature*, (1991). **354**(6348): p. 56-58.

163. E. Frackowiak and F. Beguin, Electrochemical storage of energy in carbon nanotubes and nanostructured carbons. *Carbon*, (2002). **40**(10): p. 1775-1787.

164. A.J.S. Ahammad, J.J. Lee and M.A. Rahman, Electrochemical sensors based on carbon nanotubes. *Sensors*, (2009). **9**(4): p. 2289-2319.

165. R.H. Baughman, A.A. Zakhidov and W.A. de Heer, Carbon nanotubes - the route toward applications. *Science*, (2002). **297**(5582): p. 787-792.

166. A.C. Dillon, Carbon nanotubes for photoconversion and electrical energy storage. *Chemical Reviews*, (2010). **110**(11): p. 6856-6872.

167. H. Shimoda, B. Gao, X.P. Tang, A. Kleinhammes, L. Fleming, Y. Wu and O. Zhou, Lithium intercalation into opened single-wall carbon nanotubes: Storage capacity and electronic properties. *Physical Review Letters*, (2002). **88**(1).

168. S.F. Zheng, J.S. Hu, L.S. Zhong, W.G. Song, L.J. Wan and Y.G. Guo, Introducing dual functional CNT networks into CuO nanomicrospheres toward superior electrode materials for lithium-ion batteries. *Chemistry of Materials*, (2008). **20**(11): p. 3617-3622.

169. A.L.M. Reddy, M.M. Shaijumon, S.R. Gowda and P.M. Ajayan, Coaxial $MnO_2$/carbon nanotube array electrodes for high-performance lithium batteries. *Nano Letters*, (2009). **9**(3): p. 1002-1006.

170. C.M. Park, J.H. Kim, H. Kim and H.J. Sohn, Li-alloy based anode materials for Li secondary batteries. *Chemical Society Reviews*, (2010). **39**(8): p. 3115-3141.

171. A.S. Arico, P. Bruce, B. Scrosati, J.M. Tarascon and W. Van Schalkwijk, Nanostructured materials for advanced energy conversion and storage devices. *Nature Materials*, (2005). **4**(5): p. 366-377.

172. J. Li and J.R. Dahn, An in situ X-ray diffraction study of the reaction of Li with crystalline Si. *Journal of the Electrochemical Society*, (2007). **154**(3): p. A156-A161.

173. U. Kasavajjula, C.S. Wang and A.J. Appleby, Nano- and bulk-silicon-based insertion anodes for lithium-ion secondary cells. *Journal of Power Sources*, (2007). **163**(2): p. 1003-1039.

174. G.X. Wang, J.H. Ahn, J. Yao, S. Bewlay and H.K. Liu, Nanostructured Si-C composite anodes for lithium-ion batteries. *Electrochemistry Communications*, (2004). **6**(7): p. 689-692.

175. R.D. Cakan, M.M. Titirici, M. Antonietti, G.L. Cui, J. Maier and Y.S. Hu, Hydrothermal carbon spheres containing silicon nanoparticles: synthesis and lithium storage performance. *Chemical Communications*, (2008)(32): p. 3759-3761.

176. J. Cho, Porous Si anode materials for lithium rechargeable batteries. *Journal of Materials Chemistry*, (2010). **20**(20): p. 4009-4014.

177. H. Kim, B. Han, J. Choo and J. Cho, Three-dimensional porous silicon particles for use in high-performance lithium secondary batteries. *Angewandte Chemie-International Edition*, (2008). **47**(52): p. 10151-10154.

178. H. Dong, X.P. Ai and H.X. Yang, Carbon/Ba-Fe-Si alloy composite as high capacity anode materials for Li-ion batteries. *Electrochemistry Communications*, (2003). **5**(11): p. 952-957.

179. D.Y. Chen, X. Mei, G. Ji, M.H. Lu, J.P. Xie, J.M. Lu and J.Y. Lee, Reversible lithium-ion storage in silver-treated nanoscale hollow porous silicon particles. *Angewandte Chemie-International Edition*, (2012). **51**(10): p. 2409-2413.

180. Y.S. Hu, R. Demir-Cakan, M.M. Titirici, J.O. Muller, R. Schlogl, M. Antonietti and J. Maier, Superior storage performance of a Si@$SiO_x$/C nanocomposite as anode material for lithium-ion batteries. *Angewandte Chemie-International Edition*, (2008). **47**(9): p. 1645-1649.

181. N. Liu, H. Wu, M.T. McDowell, Y. Yao, C.M. Wang and Y. Cui, A yolk-shell design for stabilized and scalable Li-ion battery alloy anodes. *Nano Letters*, (2012). **12**(6): p. 3315-3321.

182. J. Graetz, C.C. Ahn, R. Yazami and B. Fultz, Nanocrystalline and thin film germanium electrodes with high lithium capacity and high rate capabilities. *Journal of the Electrochemical Society*, (2004). **151**(5): p. A698-A702.

183. S. Yoon, C.M. Park and H.J. Sohn, Electrochemical characterizations of germanium and carbon-coated germanium composite anode for lithium-ion batteries. *Electrochemical and Solid State Letters*, (2008). **11**(4): p. A42-A45.

184. Y.D. Ko, J.G. Kang, G.H. Lee, J.G. Park, K.S. Park, Y.H. Jin and D.W. Kim, Sn-induced low-temperature growth of Ge nanowire electrodes with a large lithium storage capacity. *Nanoscale*, (2011). **3**(8): p. 3371-3375.

185. M.H. Seo, M. Park, K.T. Lee, K. Kim, J. Kim and J. Cho, High performance Ge nanowire anode sheathed with carbon for lithium rechargeable batteries. *Energy & Environmental Science*, (2011). **4**(2): p. 425-428.

186. D.J. Xue, S. Xin, Y. Yan, K.C. Jiang, Y.X. Yin, Y.G. Guo and L.J. Wan, Improving the electrode performance of Ge through Ge@C core-shell nanoparticles and graphene networks. *Journal of the American Chemical Society*, (2012). **134**(5): p. 2512-2515.

187. J.S. Cheng and J. Du, Facile synthesis of germanium-graphene nanocomposites and their application as anode materials for lithium ion batteries. *Crystengcomm*, (2012). **14**(2): p. 397-400.

188. H. Lee, H. Kim, S.G. Doo and J. Cho, Synthesis and optimization of nanoparticle Ge confined in a carbon matrix for lithium battery anode material. *Journal of the Electrochemical Society*, (2007). **154**(4): p. A343-A346.

189. M.H. Park, K. Kim, J. Kim and J. Cho, Flexible dimensional control of high-capacity Li-ion-battery anodes: from 0D hollow to 3D porous germanium nanoparticle assemblies. *Advanced Materials*, (2010). **22**(3): p. 415-418.

190. Y. Sharma, N. Sharma, G.V. Subba Rao and B.V.R. Chowdari, Nanophase $ZnCo_2O_4$ as a high performance anode material for Li-ion batteries. *Advanced Functional Materials*, (2007). **17**(15): p. 2855-2861.

191. X.Y. Wang, X.F. Zhou, K. Yao, J.G. Zhang and Z.P. Liu, A $SnO_2$/graphene composite as a high stability electrode for lithium ion batteries. *Carbon*, (2011). **49**(1): p. 133-139.

192. Z.S. Wu, W.C. Ren, L. Wen, L.B. Gao, J.P. Zhao, Z.P. Chen, G.M. Zhou, F. Li and H.M. Cheng, Graphene anchored with $Co_3O_4$ nanoparticles as anode of lithium ion batteries with enhanced reversible capacity and cyclic performance. *Acs Nano*, (2010). **4**(6): p. 3187-3194.

193. Y. Sharma, N. Sharma, G.V.S. Rao and B.V.R. Chowdari, Lithium recycling behaviour of nano-phase-$CuCo_2O_4$ as anode for lithium-ion batteries. *Journal of Power Sources*, (2007). **173**(1): p. 495-501.

194. P. Balaya, H. Li, L. Kienle and J. Maier, Fully reversible homogeneous and heterogeneous Li storage in $RuO_2$ with high capacity. *Advanced Functional Materials*, (2003). **13**(8): p. 621-625.

195. Y.F. Deng, Q.M. Zhang, S.D. Tang, L.T. Zhang, S.N. Deng, Z.C. Shi and G.H. Chen, One-pot synthesis of $ZnFe_2O_4$/C hollow spheres as superior anode materials for lithium ion batteries. *Chemical Communications*, (2011). **47**(24): p. 6828-6830.

196. J.S. Chen, D. Luan, C.M. Li, F.Y.C. Boey, S. Qiao and X.W. Lou, $TiO_2$ and $SnO_2$@$TiO_2$ hollow spheres assembled from anatase $TiO_2$ nanosheets with enhanced lithium storage properties. *Chemical Communications*, (2010). **46**(43): p. 8252-8254.

197. J.S. Chen, Y.L. Tan, C.M. Li, Y.L. Cheah, D.Y. Luan, S. Madhavi, F.Y.C. Boey, L.A. Archer and X.W. Lou, Constructing hierarchical spheres from large ultrathin anatase $TiO_2$ nanosheets with nearly 100% exposed (001) facets for fast reversible

lithium storage. *Journal of the American Chemical Society*, (2010). **132**(17): p. 6124-6130.

198. B.K. Guo, X.P. Fang, B. Li, Y.F. Shi, C.Y. Ouyang, Y.S. Hu, Z.X. Wang, G.D. Stucky and L.Q. Chen, Synthesis and lithium storage mechanism of ultrafine $MoO_2$ nanorods. *Chemistry of Materials*, (2012). **24**(3): p. 457-463.
199. P. Poizot, S. Laruelle, S. Grugeon, L. Dupont and J.M. Tarascon, Nano-sized transition-metaloxides as negative-electrode materials for lithium-ion batteries. *Nature*, (2000). **407**(6803): p. 496-499.
200. K.L. Lee, J.Y. Jung, S.W. Lee, H.S. Moon and J.W. Park, Electrochemical characteristics of a-Si thin film anode for Li-ion rechargeable batteries. *Journal of Power Sources*, (2004). **129**(2): p. 270-274.
201. Y.M. Kang, M.S. Song, J.H. Kim, H.S. Kim, M.S. Park, J.Y. Lee, H.K. Liu and S.X. Dou, A study on the charge-discharge mechanism of $Co_3O_4$ as an anode for the Li ion secondary battery. *Electrochimica Acta*, (2005). **50**(18): p. 3667-3673.
202. J. Hu, H. Li and X.J. Huang, $Cr_2O_3$-based anode materials for Li-ion batteries. *Electrochemical and Solid State Letters*, (2005). **8**(1): p. A66-A69.
203. X.P. Gao, J.L. Bao, G.L. Pan, H.Y. Zhu, P.X. Huang, F. Wu and D.Y. Song, Preparation and electrochemical performance of polycrystalline and single crystalline CuO nanorods as anode materials for Li ion battery. *Journal of Physical Chemistry B*, (2004). **108**(18): p. 5547-5551.
204. H. Kitaura, K. Takahashi, F. Mizuno, A. Hayashi, K. Tadanaga and M. Tatsumisago, Preparation of alpha-$Fe_2O_3$ electrode materials via solution process and their electrochemical properties in all-solid-state lithium batteries. *Journal of the Electrochemical Society*, (2007). **154**(7): p. A725-A729.
205. B. Sun, J. Horvat, H.S. Kim, W.S. Kim, J. Ahn and G.X. Wang, Synthesis of mesoporous alpha-$Fe_2O_3$ nanostructures for highly sensitive gas sensors and high capacity anode materials in lithium ion batteries. *Journal of Physical Chemistry C*, (2010). **114**(44): p. 18753-18761.
206. L. Wang, Y. Yu, P.C. Chen, D.W. Zhang and C.H. Chen, Electrospinning synthesis of C/$Fe_3O_4$ composite nanofibers and their application for high performance lithium-ion batteries. *Journal of Power Sources*, (2008). **183**(2): p. 717-723.
207. H. Liu, G.X. Wang, J.Z. Wang and D. Wexler, Magnetite/carbon core-shell nanorods as anode materials for lithium-ion batteries. *Electrochemistry Communications*, (2008). **10**(12): p. 1879-1882.

208. J.Z. Zhao, Z.L. Tao, J. Liang and J. Chen, Facile synthesis of nanoporous gamma-$MnO_2$ structures and their application in rechargeable Li-ion batteries. *Crystal Growth & Design*, (2008). **8**(8): p. 2799-2805.

209. S.-H. Lee, Y.-H. Kim, R. Deshpande, P.A. Parilla, E. Whitney, D.T. Gillaspie, K.M. Jones, A.H. Mahan, S. Zhang and A.C. Dillon, Reversible lithium-ion insertion in molybdenum oxide nanoparticles. *Advanced Materials*, (2008). **20**(19): p. 3627-3632.

210. H. Liu, G.X. Wang, J. Liu, S.Z. Qiao and H.J. Ahn, Highly ordered mesoporous NiO anode material for lithium ion batteries with an excellent electrochemical performance. *Journal of Materials Chemistry*, (2011). **21**(9): p. 3046-3052.

211. J.P. Liu, Y.Y. Li, R.M. Ding, J. Jiang, Y.Y. Hu, X.X. Ji, Q.B. Chi, Z.H. Zhu and X.T. Huang, Carbon/ZnO nanorod array electrode with significantly improved lithium storage capability. *Journal of Physical Chemistry C*, (2009). **113**(13): p. 5336-5339.

212. X.H. Huang, X.H. Xia, Y.F. Yuan and F. Zhou, Porous ZnO nanosheets grown on copper substrates as anodes for lithium ion batteries. *Electrochimica Acta*, (2011). **56**(14): p. 4960-4965.

213. J. Hu, T.W. Odom and C.M. Lieber, Chemistry and physics in one dimension: synthesis and properties of nanowires and nanotubes. *Accounts of Chemical Research*, (1999). **32**(5): p. 435-445.

214. L.S. Zhang, L.Y. Jiang, C.Q. Chen, W. Li, W.G. Song and Y.G. Guo, Programmed fabrication of metal oxides nanostructures using dual templates to spatially disperse metal oxide nanocrystals. *Chemistry of Materials*, (2010). **22**(2): p. 414-419.

215. X. Wang and Y.D. Li, Selected-control hydrothermal synthesis of alpha- and beta-$MnO_2$ single crystal nanowires. *Journal of the American Chemical Society*, (2002). **124**(12): p. 2880-2881.

216. Y. Wang, H. Xia, L. Lu and J.Y. Lin, Excellent performance in lithium-ion battery anodes: rational synthesis of $Co(CO_3)_{0.5}(OH)\cdot 0.11H_2O$ nanobelt array and its conversion into mesoporous and single-crystal $Co_3O_4$. *Acs Nano*, (2010). **4**(3): p. 1425-1432.

217. J.H. Kong, S.Y. Wong, Y. Zhang, H.R. Tan, X. Li and X.H. Lu, One-dimensional carbon-$SnO_2$ and $SnO_2$ nanostructures via single-spinneret electrospinning: tunable morphology and the underlying mechanism. *Journal of Materials Chemistry*, (2011). **21**(40): p. 15928-15934.

218. J.H. Liu and X.W. Liu, Two-dimensional nanoarchitectures for lithium storage. *Advanced Materials*, (2012). **24**(30): p. 4097-4111.

219. J.S. Chen, T. Zhu, X.H. Yang, H.G. Yang and X.W. Lou, Top-down fabrication of alpha-$Fe_2O_3$ single-crystal nanodiscs and microparticles with tunable porosity for largely improved lithium storage properties. *Journal of the American Chemical Society*, (2010). **132**(38): p. 13162-13164.

220. D.H. Wang, R. Kou, D. Choi, Z.G. Yang, Z.M. Nie, J. Li, L.V. Saraf, D.H. Hu, J.G. Zhang, G.L. Graff, J. Liu, M.A. Pope and I.A. Aksay, Ternary self-assembly of ordered metal oxide-graphene nanocomposites for electrochemical energy storage. *Acs Nano*, (2010). **4**(3): p. 1587-1595.

221. Q. Gao, A.W. Zhao, Z.B. Gan, W.Y. Tao, D. Li, M.F. Zhang, H.Y. Guo, D.P. Wang, H.H. Sun, R.R. Mao and E.H. Liu, Facile fabrication and growth mechanism of 3D flower- like $Fe_3O_4$ nanostructures and their application as SERS substrates. *Crystengcomm*, (2012). **14**(14): p. 4834-4842.

222. B.X. Li, G.X. Rong, Y. Xie, L.F. Huang and C.Q. Feng, Low-temperature synthesis of alpha-$MnO_2$ hollow urchins and their application in rechargeable $Li^+$ batteries. *Inorganic Chemistry*, (2006). **45**(16): p. 6404-6410.

223. Y. Wang, F.B. Su, J.Y. Lee and X.S. Zhao, Crystalline carbon hollow spheres, crystalline carbon-$SnO_2$ hollow spheres, and crystalline $SnO_2$ hollow spheres: Synthesis and performance in reversible Li-ion storage. *Chemistry of Materials*, (2006). **18**(5): p. 1347-1353.

224. S.M. Zhu, H.A. Zhou, M. Hibino, I. Honma and M. Ichihara, Synthesis of $MnO_2$ nanoparticles confined in ordered mesoporous carbon using a sonochemical method. *Advanced Functional Materials*, (2005). **15**(3): p. 381-386.

225. X.F. Zhou, S.Y. Chen, D.Y. Zhang, X.F. Guo, W.P. Ding and Y. Chen, Microsphere organization of nanorods directed by PEG linear polymer. *Langmuir*, (2006). **22**(4): p. 1383-1387.

226. S.J. Ding, T. Zhu, J.S. Chen, Z.Y. Wang, C.L. Yuan and X.W. Lou, Controlled synthesis of hierarchical NiO nanosheet hollow spheres with enhanced supercapacitive performance. *Journal of Materials Chemistry*, (2011). **21**(18): p. 6602-6606.

227. L.P. Zhu, H.M. Xiao, W.D. Zhang, G. Yang and S.Y. Fu, One-pot template-free synthesis of monodisperse and single-crystal magnetite hollow spheres by a simple solvothermal route. *Crystal Growth & Design*, (2008). **8**(3): p. 957-963.

228. S.H. Feng and R.R. Xu, New materials in hydrothermal synthesis. *Accounts of Chemical Research*, (2001). **34**(3): p. 239-247.

229. K. Byrappa and T. Adschiri, Hydrothermal technology for nanotechnology. *Progress in Crystal Growth and Characterization of Materials*, (2007). **53**(2): p. 117-166.

230. D.M. Poojary and A. Clearfield, Application of X-ray powder diffraction techniques to the solution of unknown crystal structures. *Accounts of Chemical Research*, (1997). **30**(10): p. 414-422.

231. M. Catti, *Lithium Ion Materials for Energy Applications: Structural Properties from Neutron Diffraction*. Neutron Applications in Earth, Energy and Environmental Sciences, ed. L. Liang, R. Rinaldi, and H. Schober. 2009. 439-460.

232. Z.L. Wang, New developments in transmission electron microscopy for nanotechnology. *Advanced Materials*, (2003). **15**(18): p. 1497-1514.

233. C.H. Spink, *Differential scanning Calorimetry*, in *Biophysical Tools for Biologists: Vol 1 in Vitro Techniques*, J.J. Correia and H.W. Detrich, Editors. 2008. p. 115-141.

234. R.S. Houk and J.J. Thompson, Inductively coupled plasma mass-spectrometry. *Mass Spectrometry Reviews*, (1988). **7**(4): p. 425-461.

235. R. Baddour-Hadjean and J.P. Pereira-Ramos, Raman microspectrometry applied to the study of electrode materials for lithium batteries. *Chemical Reviews*, (2010). **110**(3): p. 1278-1319.

236. N.H. Turner and J.A. Schreifels, Surface analysis: X-ray photoelectron spectroscopy and auger electron spectroscopy. *Analytical Chemistry*, (2000). **72**(12): p. 99R-110R.

237. J.F. Rusling and S.L. Suib, Characterizing materials with cyclic voltammetry. *Advanced Materials*, (1994). **6**(12): p. 922-930.

238. S. Flandrois and B. Simon, Carbon materials for lithium-ion rechargeable batteries. *Carbon*, (1999). **37**(2): p. 165-180.

239. C.M.A. Brett and A.M.O. Brett, *Electrochemistry principles, methods, and applications*. 1993, Oxford, New York, Tokyo: Oxford University Press.

240. S.K. Martha, J. Nanda, G.M. Veith and N.J. Dudney, Electrochemical and rate performance study of high-voltage lithium-rich composition: $Li_{1.2}Mn_{0.525}Ni_{0.175}Co_{0.1}O_2$. *Journal of Power Sources*, (2012). **199**: p. 220-226.

241. J.J. Liu, W.H. Qiu, L.Y. Yu, G.H. Zhang, H.L. Zhao and T. Li, Studies on the low-heating solid-state reaction method to synthesize $LiNi_{1/3}Co_{1/3}Mn_{1/3}O_2$ cathode materials. *Journal of Power Sources*, (2007). **174**(2): p. 701-704.

242. L. Tan and H.W. Liu, High rate charge-discharge properties of $LiNi_{1/3}Co_{1/3}Mn_{1/3}O_2$ synthesized via a low temperature solid-state method. *Solid State Ionics*, (2010). **181**(33-34): p. 1530-1533.

243. Y.-K. Lin and C.-H. Lu, Preparation and electrochemical properties of layer-structured $LiNi_{1/3}Co_{1/3}Mn_{1/3-y}Al_yO_2$. *Journal of Power Sources*, (2009). **189**(1): p. 353-358.

244. Y.H. Ding, P. Zhang, Y. Jiang and D.S. Gao, Effect of rare earth elements doping on structure and electrochemical properties of $LiNi_{1/3}Co_{1/3}Mn_{1/3}O_2$ for lithium-ion battery. *Solid State Ionics*, (2007). **178**(13-14): p. 967-971.

245. Q.W. Peng, Z.Y. Tang, L.Q. Zhang and X.J. Li, Synthesis of layered $Li_{1.2+x}[Ni_{0.25}Mn_{0.75}]_{0.8-x}O_2$ materials ($0 \leq x \leq 4/55$) via a new simple microwave heating method and their electrochemical properties. *Materials Research Bulletin*, (2009). **44**(11): p. 2147-2151.

246. X. Luo, X. Wang, L. Liao, X. Wang, S. Gamboa and P.J. Sebastian, Effects of synthesis conditions on the structural and electrochemical properties of layered $LiNi_{1/3}Co_{1/3}Mn_{1/3}O_2$ cathode material via the hydroxide co-precipitation method LIB SCITECH. *Journal of Power Sources*, (2006). **161**(1): p. 601-605.

247. M.H. Lee, Y. Kang, S.T. Myung and Y.K. Sun, Synthetic optimization of $LiNi_{1/3}Co_{1/3}Mn_{1/3}O_2$ via co-precipitation. *Electrochimica Acta*, (2004). **50**(4): p. 939-948.

248. K.K. Cheralathan, N.Y. Kang, H.S. Park, Y.J. Lee, W.C. Choi, Y.S. Ko and Y.K. Park, Preparation of spherical $LiNi_{0.80}Co_{0.15}Mn_{0.05}O_2$ lithium-ion cathode material by continuous co-precipitation. *Journal of Power Sources*, (2010). **195**(5): p. 1486-1494.

249. F. Zhou, X.M. Zhao, A. van Bommel, A.W. Rowe and J.R. Dahn, Coprecipitation synthesis of $Ni_xMn_{1-x}(OH)_2$ mixed hydroxides. *Chemistry of Materials*, (2010). **22**(3): p. 1015-1021.

250. T.H. Cho, S.M. Park, M. Yoshio, T. Hirai and Y. Hideshima, Effect of synthesis condition on the structural and electrochemical properties of $Li[Ni_{1/3}Mn_{1/3}Co_{1/3}]O_2$ prepared by carbonate co-precipitation method. *Journal of Power Sources*, (2005). **142**(1-2): p. 306-312.

251. H.T. Brian, EXPGUI, a graphical user interface for GSAS. *Journal of Applied Crystallography*, (2001). **34**(2): p. 210-213.

252. K.M. Shaju, G.V. Subba Rao and B.V.R. Chowdari, Performance of layered $Li(Ni_{1/3}Co_{1/3}Mn_{1/3})O_2$ as cathode for Li-ion batteries. *Electrochimica Acta*, (2002). **48**(2): p. 145-151.

253. N. Yabuuchi, K. Yoshii, S.T. Myung, I. Nakai and S. Komaba, Detailed studies of a high-capacity electrode material for rechargeable batteries, $Li_2MnO_3$-$LiCo_{1/3}Ni_{1/3}Mn_{1/3}O_2$. *Journal of the American Chemical Society*, (2011). **133**(12): p. 4404-4419.

254. K. Amine, H. Tukamoto, H. Yasuda and Y. Fujita, A new three-volt spinel $Li_{1+x}Mn_{1.5}Ni_{0.5}O_4$ for secondary lithium batteries. *Journal of the Electrochemical Society*, (1996). **143**(5): p. 1607-1613.

255. S.K. Martha, H. Sclar, Z. Szmuk Framowitz, D. Kovacheva, N. Saliyski, Y. Gofer, P. Sharon, E. Golik, B. Markovsky and D. Aurbach, A comparative study of electrodes comprising nanometric and submicron particles of $LiNi_{0.50}Mn_{0.50}O_2$, $LiNi_{0.33}Mn_{0.33}Co_{0.33}O_2$, and $LiNi_{0.40}Mn_{0.40}Co_{0.20}O_2$ layered compounds. *Journal of Power Sources*, (2009). **189**(1): p. 248-255.

256. J.-H. Lim, H. Bang, K.-S. Lee, K. Amine and Y.-K. Sun, Electrochemical characterization of $Li_2MnO_3$-$Li[Ni_{1/3}Co_{1/3}Mn_{1/3}]O_2$-$LiNiO_2$ cathode synthesized via co-precipitation for lithium secondary batteries. *Journal of Power Sources*, (2009). **189**(1): p. 571-575.

257. J.-H. Jeong, B.-S. Jin, W.-S. Kim, G. Wang and H.-S. Kim, The influence of compositional change of $0.3Li_2MnO_3 \cdot 0.7LiMn_{1-x}Ni_yCo_{0.1}O_2$ ($0.2 \leq x \leq 0.5$, $y = x - 0.1$) cathode materials prepared by co-precipitation. *Journal of Power Sources*, (2011). **196**(7): p. 3439-3442.

258. A.R. Armstrong, M. Holzapfel, P. Novák, C.S. Johnson, S.-H. Kang, M.M. Thackeray and P.G. Bruce, Demonstrating oxygen loss and associated structural reorganization in the lithium battery cathode $Li[Ni_{0.2}Li_{0.2}Mn_{0.6}]O_2$. *Journal of the American Chemical Society*, (2006). **128**(26): p. 8694-8698.

259. Z.H. Lu and J.R. Dahn, Understanding the anomalous capacity of $Li/Li[Ni_xLi_{1/3-2x/3}Mn_{2/3-x/3}]O_2$ cells using in situ X-ray diffraction and electrochemical studies. *Journal of the Electrochemical Society*, (2002). **149**(7): p. A815-A822.

260. S. Sivaprakash and S.B. Majumder, Spectroscopic analyses of $0.5Li[Ni_{0.8}Co_{0.15}Zr_{0.05}]O_2$-$0.5Li[Li_{1/3}Mn_{2/3}]O_2$ composite cathodes for lithium rechargeable batteries. *Solid State Ionics*, (2010). **181**(15-16): p. 730-739.

261. L. Daheron, R. Dedryvere, H. Martinez, M. Menetrier, C. Denage, C. Delmas and D. Gonbeau, Electron transfer mechanisms upon lithium deintercalation from $LiCoO_2$ to $CoO_2$ investigated by XPS. *Chemistry of Materials*, (2008). **20**(2): p. 583-590.

262. Y. Wang, J. Wang, J. Yang and Y. Nuli, High-rate $LiFePO_4$ electrode material synthesized by a novel route from $FePO_4 \cdot 4H_2O$. *Advanced Functional Materials*, (2006). **16**(16): p. 2135-2140.

263. P.P. Prosini, M. Carewska, S. Scaccia, P. Wisniewski, S. Passerini and M. Pasquali, A new synthetic route for preparing $LiFePO_4$ with enhanced electrochemical performance. *Journal of the Electrochemical Society*, (2002). **149**(7): p. A886-A890.

264. I. Belharouak, C. Johnson and K. Amine, Synthesis and electrochemical analysis of vapor-deposited carbon-coated $LiFePO_4$. *Electrochemistry Communications*, (2005). **7**(10): p. 983-988.

265. V. Pallomares, A. Goni, I.G. de Muro, I. de Meatza, M. Bengoechea, I. Cantero and T. Rojo, Influence of carbon content on $LiFePO_4$/C samples synthesized by freeze-drying process. *Journal of the Electrochemical Society*, (2009). **156**(10): p. A817-A821.

266. M.M. Doeff, Y.Q. Hu, F. McLarnon and R. Kostecki, Effect of surface carbon structure on the electrochemical performance of $LiFePO_4$. *Electrochemical and Solid State Letters*, (2003). **6**(10): p. A207-A209.

267. C. Sisbandini, D. Brandell, T. Gustafsson and L. Nyholm, The mechanism of capacity enhancement in $LiFePO_4$ cathodes through polyetheramine coating. *Journal of the Electrochemical Society*, (2009). **156**(9): p. A720-A725.

268. B.F. Wang, Y.L. Qiu and S.Y. Ni, Ultrafine $LiFePO_4$ cathode materials synthesized by chemical reduction and lithiation method in alcohol solution. *Solid State Ionics*, (2007). **178**(11-12): p. 843-847.

269. J.C. Zheng, X.H. Li, Z.X. Wang, H.J. Guo and S.Y. Zhou. *$LiFePO_4$ with enhanced performance synthesized by a novel synthetic route*. in *Meeting of the International-Battery-Material-Association*. 2007. Shenzhen, People's Repubic of China.

270. Z.L. Wang, S.R. Su, C.Y. Yu, Y. Chen and D.G. Xia. *Synthesises, characterizations and electrochemical properties of spherical-like $LiFePO_4$ by hydrothermal method*. in *Meeting of the International-Battery-Material-Association*. 2007. Shenzhen, People's Republic of China.

271. Z.M. Zheng, Y. Wang, A. Zhang, T.R. Zhang, F.Y. Cheng, Z.L. Tao and J. Chen, Porous $Li_2FeSiO_4$/C nanocomposite as the cathode material of lithium-ion batteries. *Journal of Power Sources*, (2012). **198**: p. 229-235.

272. M. Zhang, Q.P. Chen, Z.X. Xi, Y.G. Hou and Q.L. Chen, One-step hydrothermal synthesis of $Li_2FeSiO_4$/C composites as lithium-ion battery cathode materials. *Journal of Materials Science*, (2012). **47**(5): p. 2328-2332.

273. M. Dahbi, S. Urbonaite and T. Gustafsson, Combustion synthesis and electrochemical performance of $Li_2FeSiO_4$/C cathode material for lithium-ion batteries. *Journal of Power Sources*, (2012). **205**: p. 456-462.

274. B. Shao and I. Taniguchi, Synthesis of $Li_2FeSiO_4$/C nanocomposite cathodes for lithium batteries by a novel synthesis route and their electrochemical properties. *Journal of Power Sources*, (2012). **199**: p. 278-286.

275. Y.D. Meng, D.R. Chen and X.L. Jiao, Synthesis and characterization of $CoFe_2O_4$ hollow spheres. *European Journal of Inorganic Chemistry*, (2008)(25): p. 4019-4023.

276. Z.T. Chen and L. Gao, Synthesis and magnetic properties of $CoFe_2O_4$ nanoparticles by using PEG as surfactant additive. *Materials Science and Engineering B-Solid State Materials for Advanced Technology*, (2007). **141**(1-2): p. 82-86.

277. Y.-N. NuLi and Q.-Z. Qin, Nanocrystalline transition metal ferrite thin films prepared by an electrochemical route for Li-ion batteries. *Journal of Power Sources*, (2005). **142**(1-2): p. 292-297.

278. Y.-Q. Chu, Z.-W. Fu and Q.-Z. Qin, Cobalt ferrite thin films as anode material for lithium ion batteries. *Electrochimica Acta*, (2004). **49**(27): p. 4915-4921.

279. P. Lavela and J.L. Tirado, $CoFe_2O_4$ and $NiFe_2O_4$ synthesized by sol-gel procedures for their use as anode materials for Li ion batteries. *Journal of Power Sources*, (2007). **172**(1): p. 379-387.

280. P. Lavela, G.F. Ortiz, J.L. Tirado, E. Zhecheva, R. Stoyanova and S. Ivanova, High-performance transition metal mixed oxides in conversion electrodes: a combined spectroscopic and electrochemical study. *The Journal of Physical Chemistry C*, (2007). **111**(38): p. 14238-14246.

281. Z.H. Li, T.P. Zhao, X.Y. Zhan, D.S. Gao, Q.Z. Xiao and G.T. Lei, High capacity three-dimensional ordered macroporous $CoFe_2O_4$ as anode material for lithium ion batteries. *Electrochimica Acta*, (2010). **55**(15): p. 4594-4598.

282. C. Vidal-Abarca, P. Lavela and J.L. Tirado, On the role of faradaic and capacitive contributions in the electrochemical performance of $CoFe_2O_4$ as conversion anode for Li-ion cells. *Solid State Ionics*, (2010). **181**(13-14): p. 616-622.

283. P. Lavela, J.L. Tirado, M. Womes and J.C. Jumas, Elucidation of capacity fading on $CoFe_2O_4$ conversion electrodes for lithium batteries based on Fe-57 mossbauer spectroscopy. *Journal of the Electrochemical Society*, (2009). **156**(7): p. A589-A594.

284. X. Yang, X. Wang and Z. Zhang, Electrochemical properties of submicron cobalt ferrite spinel through a co-precipitation method. *Journal of Crystal Growth*, (2005). **277**(1-4): p. 467-470.

285. Y.H. Jin, S.D. Seo, H.W. Shim, K.S. Park and D.W. Kim, Synthesis of core/shell spinel ferrite/carbon nanoparticles with enhanced cycling stability for lithium ion battery anodes. *Nanotechnology*, (2012). **23**(12).

286. Y.G. Guo, Y.S. Hu and J. Maier, Synthesis of hierarchically mesoporous anatase spheres and their application in lithium batteries. *Chemical Communications*, (2006)(26): p. 2783-2785.

287. X. Xu and S.A. Asher, Synthesis and utilization of monodisperse hollow polymeric particles in photonic crystals. *Journal of the American Chemical Society*, (2004). **126**(25): p. 7940-7945.

288. R. Dedryvère, S. Laruelle, S. Grugeon, P. Poizot, D. Gonbeau and J.M. Tarascon, Contribution of X-ray photoelectron spectroscopy to the study of the electrochemical reactivity of CoO toward lithium. *Chemistry of Materials*, (2004). **16**(6): p. 1056-1061.

289. R. Alcántara, M. Jaraba, P. Lavela and J.L. Tirado, $NiCo_2O_4$ spinel: first report on a transition metal oxide for the negative electrode of sodium-ion batteries. *Chemistry of Materials*, (2002). **14**(7): p. 2847-2848.

290. H. Zhao, Z. Zheng, K.W. Wong, S. Wang, B. Huang and D. Li, Fabrication and electrochemical performance of nickel ferrite nanoparticles as anode material in lithium ion batteries. *Electrochemistry Communications*, (2007). **9**(10): p. 2606-2610.

291. J. Jamnik and J. Maier, Nanocrystallinity effects in lithium battery materials Aspects of nano-ionics. Part IV. *Physical Chemistry Chemical Physics*, (2003). **5**(23): p. 5215-5220.

292. C. Vidal-Abarca, P. Lavela and J.L. Tirado, A (57)Fe Mossbauer spectroscopy study of cobalt ferrite conversion electrodes for Li-ion batteries. *Journal of Power Sources*, (2011). **196**(16): p. 6978-6981.

293. W.X. Chen, J.Y. Lee and Z. Liu, Electrochemical lithiation and de-lithiation of carbon nanotube-$Sn_2Sb$ nanocomposites. *Electrochemistry Communications*, (2002). **4**(3): p. 260-265.

294. D. Wang, D. Choi, J. Li, Z. Yang, Z. Nie, R. Kou, D. Hu, C. Wang, L.V. Saraf, J. Zhang, I.A. Aksay and J. Liu, Self-assembled $TiO_2$–graphene hybrid nanostructures for enhanced Li-ion insertion. *Acs Nano*, (2009). **3**(4): p. 907-914.

295. Y. Zhao, J. Li, Y. Ding and L. Guan, Enhancing the lithium storage performance of iron oxide composites through partial substitution with $Ni^{2+}$ or $Co^{2+}$. *Journal of Materials Chemistry*, (2011). **21**(47): p. 19101-19105.

296. J.S. Zhou, H.H. Song, X.H. Chen, L.J. Zhi, S.Y. Yang, J.P. Huo and W.T. Yang, Carbon-encapsulated metal oxide hollow nanoparticles and metal oxide hollow nanoparticles: a general synthesis strategy and its application to lithium-ion batteries. *Chemistry of Materials*, (2009). **21**(13): p. 2935-2940.

297. A.B. Fuertes, M. Sevilla, T. Valdes-Solis and P. Tartaj, Synthetic route to nanocomposites made up of inorganic nanoparticles confined within a hollow mesoporous carbon shell. *Chemistry of Materials*, (2007). **19**(22): p. 5418-5423.

298. J.G. Ren, J.B. Yang, A. Abouimrane, D.P. Wang and K. Amine, $SnO_2$ nanocrystals deposited on multiwalled carbon nanotubes with superior stability as anode material for Li-ion batteries. *Journal of Power Sources*, (2011). **196**(20): p. 8701-8705.

299. W.-Q. Han and A. Zettl, Coating single-walled carbon nanotubes with tin oxide. *Nano Letters*, (2003). **3**(5): p. 681-683.

300. X.B. Meng, Y. Zhong, Y.F. Sun, M.N. Banis, R.Y. Li and X.L. Sun, Nitrogen-doped carbon nanotubes coated by atomic layer deposited $SnO_2$ with controlled morphology and phase. *Carbon*, (2011). **49**(4): p. 1133-1144.

301. B. Liu and H.C. Zeng, Carbon nanotubes supported mesoporous mesocrystals of anatase $TiO_2$. *Chemistry of Materials*, (2008). **20**(8): p. 2711-2718.

302. X. Jin, W. Zhou, S. Zhang and G.Z. Chen, Nanoscale microelectrochemical cells on carbon nanotubes. *Small*, (2007). **3**(9): p. 1513-1517.

303. X. Xie and L. Gao, Characterization of a manganese dioxide/carbon nanotube composite fabricated using an in situ coating method. *Carbon*, (2007). **45**(12): p. 2365-2373.

304. C.H. Xu, J. Sun and L.A. Gao, Large scale synthesis of nickel oxide/multiwalled carbon nanotube composites by direct thermal decomposition and their lithium storage properties. *Journal of Power Sources*, (2011). **196**(11): p. 5138-5142.

305. Z. Wang, D. Luan, S. Madhavi, Y. Hu and X.W. Lou, Assembling carbon-coated α-$Fe_2O_3$ hollow nanohorns on the CNT backbone for superior lithium storage capability. *Energy & Environmental Science*, (2012). **5**(1): p. 5252-5256.

306. S.L. Chou, J.Z. Wang, Z.X. Chen, H.K. Liu and S.X. Dou, Hollow hematite nanosphere/carbon nanotube composite: mass production and its high-rate lithium storage properties. *Nanotechnology*, (2011). **22**(26): p. 265401.

307. Y. He, L. Huang, J.S. Cai, X.M. Zheng and S.G. Sun, Structure and electrochemical performance of nanostructured $Fe_3O_4$/carbon nanotube composites as anodes for lithium ion batteries. *Electrochimica Acta*, (2010). **55**(3): p. 1140-1144.

308. R. Zhang, L. Li, L. Chen, G. Zhang and K.Y. Shi, N-doped carbon nanotubes synthesized in high yield and decorated with $CeO_2$ and $SnO_2$ nanoparticles. *Journal of Alloys and Compounds*, (2011). **509**(35): p. 8620-8624.

309. W.D. Zhang, B. Xu and L.C. Jiang, Functional hybrid materials based on carbon nanotubes and metal oxides. *Journal of Materials Chemistry*, (2010). **20**(31): p. 6383-6391.

310. W.Z. Li, C.H. Liang, W.J. Zhou, J.S. Qiu, Z.H. Zhou, G.Q. Sun and Q. Xin, Preparation and characterization of multiwalled carbon nanotube-supported platinum for cathode catalysts of direct methanol fuel cells. *Journal of Physical Chemistry B*, (2003). **107**(26): p. 6292-6299.

311. H.X. Wu, G. Liu, X. Wang, J.M. Zhang, Y. Chen, J.L. Shi, H. Yang, H. Hu and S.P. Yang, Solvothermal synthesis of cobalt ferrite nanoparticles loaded on multiwalled carbon nanotubes for magnetic resonance imaging and drug delivery. *Acta Biomaterialia*, (2011). **7**(9): p. 3496-3504.

312. Y. Wang, D. Su, A. Ung, J.-h. Ahn and G. Wang, Hollow $CoFe_2O_4$ nanospheres as a high capacity anode material for lithium ion batteries. *Nanotechnology*, (2012). **23**(5): p. 055402.

313. L.S. Zhang, L.Y. Jiang, H.J. Yan, W.D. Wang, W. Wang, W.G. Song, Y.G. Guo and L.J. Wan, Mono dispersed $SnO_2$ nanoparticles on both sides of single layer graphene sheets as anode materials in Li-ion batteries. *Journal of Materials Chemistry*, (2010). **20**(26): p. 5462-5467.

314. A.R. Tao, J.X. Huang and P.D. Yang, Langmuir-blodgettry of nanocrystals and nanowires. *Accounts of Chemical Research*, (2008). **41**(12): p. 1662-1673.

315. Q.B. Xu, R.M. Rioux, M.D. Dickey and G.M. Whitesides, Nanoskiving: a new method to produce arrays of nanostructures. *Accounts of Chemical Research*, (2008). **41**(12): p. 1566-1577.

# NOMENCLATURE

| Abbreviation/Symbols | Full name |
|---|---|
| $2\Theta$ | XRPD peak position |
| Ar | Argon |
| BE | Binding energy |
| $C$ | $C$-rate |
| $C_{dl}$ | Double-layer capacitance |
| $CPE_{ct}$ | Constant phase-angle element |
| $CPE_{w}$ | Phase-angle element for the non-ideal capacitance of the surface layer |
| CV | Cyclic Voltammetry |
| $d$ | Interfacial spacing |
| DETA | diethylenetriamine |
| DEC | Diethyl carbonate |
| DFT | Density functional theory |
| DMC | Dimethyl carbonate |
| DSC | Differential scanning calorimetry |
| EC | Ethylene carbonate |
| EIS | Electrochemical impedance spectroscopy |
| eV | Electron volt |
| EV | Electric vehicles |
| FESEM | Filed-emission scanning electronic spectroscopy |
| FT-IR | Fourier transform infrared |

| | |
|---|---|
| g | Gram |
| h | Hour |
| HEV | Hybrid electric vehicles |
| HRTEM | High-resolution transmission electronic spectroscopy |
| Hz | Hertz |
| *I* | Intensity |
| JCPDS | Joint committee on powder diffraction standards |
| K | Kelvin |
| LiTFSI | Lithium bis(trifluoromethylsulfonyl)imide |
| LMO | Layered metal oxide |
| Li-ion battery | Lithium ion battery |
| M | Molar concentration |
| mAh $g^{-1}$ | Milli ampere hour per gram |
| min | Minute |
| mm | Millimeter |
| MWCNT | Multiwall carbon nanotube |
| n | Number of moles |
| NCM | $LiNi_{1/3}Co_{1/3}Mn_{1/3}O_2$ |
| ND | Neutron diffraction |
| nm | nanometer |
| NMP | N-methyl pyrrolidinone |
| NMR | Nuclear magnetic resonances |
| OCV | Open circuit voltage |

| | |
|---|---|
| PA | Polymeric additive |
| Pan | Polyaniline |
| PEDOT | Poly(3,4-ethylenedioxythiophene) |
| PEG400 | Polyethylene glycol 400 |
| PMMA | poly(methyl methacrylate) |
| PPy | Polypyrrole |
| PS | Polystyrene |
| PVA | Polyvinyl alcohol |
| PVDF | Polyvinylidene fluoride |
| $R_{ct}$ | Charge transfer resistance |
| $R_s$ | Lithium ion diffusion resistance |
| $R_\Omega$ | Ohmic resistance |
| SAED | Selected-area electron diffraction |
| SEI | Solid electrolyte interphase |
| SHE | Standard hydrogen electrode |
| SOC | State of charge |
| sPS | Sulfonated polystyrene |
| SSR | Solid state reaction |
| TEM | Transmission electronic spectroscopy |
| TGA | Thermogravimetric analysis |
| TMO | Transition metal oxide |
| VC | L-ascorbic acid |
| VGCF | Vapour-phase-grown carbon fiber |

| | |
|---|---|
| XAS | X-ray adsorption spectroscopy |
| XPS | X-ray photoelectron spectroscopy |
| XRPD | X-ray powder diffraction |
| $Z_w$ | Warburg impedance |
| μm | Micrometer |
| σ | Electronic conductivity |
| ° | Degree |
| Ω | Ohm |
| °C | Degree Celsius |
| λ | Wavelength |

# LIST OF MATERIALS AND CHEMICALS

| Chemical Name/Materials | Formula | Grade, % | Supplier |
|---|---|---|---|
| Acetone | $CH_3COCH_3$ | 99 | Sigma-Aldrich |
| Ammonium carbonate | $(NH_4)_2CO_3$ | 99 | Sigma-Aldrich |
| Ammonium phosphate monobasic | $NH_4H_2PO_4$ | 98.5 | Sigma-Aldrich |
| Aniline | $C_6H_5NH_2$ | 99 | Sigma-Aldrich |
| Carbon black | C | 100 | Sigma-Aldrich |
| Cobalt acetate | $Co(CH_3COO)_2$ | 98 | Sigma-Aldrich |
| Cobalt chloride hexahydrate | $CoCl_2\ H_2O$ | 99 | Sigma-Aldrich |
| Diethyl carbonate | $C_2H_5O(CO)OC_2H_5$ | 99 | Sigma-Aldrich |
| Diethylenetriamine | $H_2N(CH_2)_2NH(CH_2)_2NH_2$ | 99 | Sigma-Aldrich |
| Dimethyl carbonate | $(CH_3)_2CO_3$ | 99 | Sigma-Aldrich |
| Ethanol | $CH_3CH_2OH$ | 95 | Chem Supply |
| Ethylene carbonate | $(CH_2)_2CO3$ | 99 | Sigma-Aldrich |
| Ethylene glycol | $HO(CH_2)_2OH$ | 99.8 | Chem Supply |
| Ferrous sulfate heptahydrate | $FeSO_4\ 7H_2O$ | 99 | Sigma-Aldrich |
| Glycolic acid | $HOCOCH_2OH$ | 99 | Fluka |
| Hydrochloric acid | HCl | 37 | Aldrich |
| Hydrogen peroxide solution | $H_2O_2$ | 50 | Sigma-Aldrich |
| Iron(III) chloride, anhydrous | $FeCl_3$ | 97 | Sigma-Aldrich |
| Iron(II) oxalate dehydrate | $FeC_2O_4\ 2H_2O$ | 99 | Aldrich |
| Isopropanol | $CH_3OHCH_3$ | 99.5 | Chem Supply |
| L-ascorbic acid | $C_6H_8O_6$ | 99 | Sigma-Aldrich |
| Lithium acetate | $LiCH_3CO_2$ | 100 | Sigma-Aldrich |

| | | | |
|---|---|---|---|
| Lithium carbonate | $Li_2CO_3$ | 99.9 | Sigma-Aldrich |
| Lithium hexafluorophosphate | $LiPF_6$ | 99.99 | Sigma-Aldrich |
| Lithium hydroxide | LiOH | 98 | Sigma-Aldrich |
| Manganese acetate | $Mn(CH_3CO_2)_2$ | 99 | Sigma-Aldrich |
| MWCNT | C | 99.99 | Sigma-Aldrich |
| Nickel acetate | $Ni(CH_3CO_2)_2$ | 99 | Sigma-Aldrich |
| Nitric acid | $HNO_3$ | 68 | Aldrich |
| N-methyl pyrrolidinone (NMP) | $C_5H_9NO$ | 99.5 | Aldrich |
| Polypropylene separator | $(C_3H_6)_n$ | 100 | Celgard |
| Polyvinylidene fluoride (PVDF) | $(C_2H_2F_2)_n$ | 99 | Aldrich |
| Potassium bromide (FT-IR grade) | KBr | 99 | Sigma-Aldrich |
| Potassium hydroxide | KOH | 90 | Sigma-Aldrich |
| Silicon dioxide | $SiO_2$ | 100 | Nanopowder |
| Urea | $H_2NCONH_2$ | 98 | Sigma-Aldrich |

# PUBLICATIONS

1. Anjon Kumar Mondal, Bei Wang, Dawei Su, Ying Wang, Xiaogang Zhang and Guoxiu Wang, "Graphene/$MnO_2$ Hybrid Nanosheets as High Performance Electrode Materials for Supercapacitors", **Journal of Power Sources, Submitted.**
2. Qi Liu, Lili Yu, Ying Wang, Josip-Horvat, Mei-Ling Cheng and Guoxiu Wang, "Manganese Based Layered Coordination Polymer: Synthesis, Structural Characterization, Magnetic Property and Electrochemical Performance in Lithium Ion Batteries", **Inorganic Chemistry, Accepted.**
3. Ying Wang, Dawei Su and Guoxiu Wang, "The Effect of Carbon Coating on the Electrochemical Performance of Nanosized $Li_2FeSiO_4$ Cathode Materials", **2nd International Advances in Applied Physics & Materials Science Congress**, **Accepted**.
4. Bing Sun, Ying Wang, Bei Wang, Hyun-Soo Kim, Woo-Seong Kim and Guoxiu Wang, "Porous $LiFePO_4$/C Microspheres as High-power Cathode Materials for Lithium Ion Batteries", **Journal of Nanoscience and Nanotechnology**, **Accepted**.
5. Bei Wang, Ying Wang, Bing Sun, Paul Munroe and Guoxiu Wang, "Coral-like $V_2O_5$ Nanowhiskers as High-Capacity Cathode Materials for Lithium-ion Batteries", **RSC Advances**, **2013**, *3*, 5069-5075.
6. Ying Wang, Dawei Su, and Guoxiu Wang, "$SnO_2$@MWCNTs Nanocomposites for Reversible Sodium-ion Battery Applications", **Electrochemistry Communications, 2013**, *29*, 8-11.
7. Ying Wang, Neeraj Sharma, Dawei Su, David Bishop, Hyojun Ahn and Guoxiu Wang, "High Capacity Spherical $Li[Li_{0.24}Mn_{0.55}Co_{0.14}Ni_{0.07}]O_2$ Cathode Materials for Lithium Ion Batteries", **Solid State Ionics, 2013**, *233*, 12-19.
8. Ying Wang, Jinsoo Park, Bing Sun, Hyojun Ahn and Guoxiu Wang, "Wintersweet-

Flower-Like $CoFe_2O_4$/MWCNTs Hybrid Material for High-Capacity Reversible Lithium Storage", **Chemistry an Asian Journal**, **2012,** *7*, 1940-1946.

9. Ying Wang, Dawei Su, Alison Ung, Jung-ho Ahn and Guoxiu Wang, "Hollow CoFe2O4 Nanospheres as a High Capacity Anode Material for Lithium Ion Batteries", **Nanotechnology**, **2012,** *23*, 055402.
10. Anjon Kumar Mondal, Bei Wang, Dawei Su, Ying Wang, Xiaogang Zhang and Guoxiu Wang, "Preparation and Enhanced Electrochemical Performance of $MnO_2$ Nanosheets for Supercapacitors", **Journal of the Chinese Chemical Society**, **2012,** *59*, 1275-1279.
11. Ying Wang, Bing Sun, Jinsoo Park, Woo-Seong Kim, Hyun-Soo Kim and Guoxiu Wang, "Morphology Control and Electrochemical Properties of Nanosize LiFePO4 Cathode Material Synthesized by Co-precipitation Combined with *In Situ* Polymerization", **Journal of Alloys and Compounds, 2011,** *509*, 1040-1044.
12. Bei Wang, Ying Wang, Jinsoo Park, Hyojun Ahn and Guoxiu Wang, "*In situ* Synthesis of $Co_3O_4$/graphene Nanocomposite Material for Lithium-ion Batteries and Supercapacitors with High Capacity and Supercapacitance", **Journal of Alloys and Compounds, 2011,** *509*, 7778-7783.
13. Guoxiu Wang, Bei Wang, Jinsoo Park, Ying Wang, Bing Sun and Jane Yao, "Highly Efficient and Large-scale Synthesis of Graphene by Electrolytic Exfoliation", **Carbon, 2009,** *47*, 3242-3246.